Cumming, Alan V. (2008) *Aspects of mirrors and suspensions for advanced gravitational wave detectors.*
PhD thesis.

http://theses.gla.ac.uk/468/

Copyright and moral rights for this thesis are retained by the author

A copy can be downloaded for personal non-commercial research or study, without prior permission or charge

This thesis cannot be reproduced or quoted extensively from without first obtaining permission in writing from the Author

The content must not be changed in any way or sold commercially in any format or medium without the formal permission of the Author

When referring to this work, full bibliographic details including the author, title, awarding institution and date of the thesis must be given

Glasgow Theses Service
http://theses.gla.ac.uk/
theses@gla.ac.uk

Aspects of mirrors and suspensions for advanced gravitational wave detectors

Alan V. Cumming M. Sci.

Department of Physics & Astronomy,

University of Glasgow.

Presented as a thesis for the degree of Ph.D. in the University of Glasgow, University Avenue, Glasgow, G12 8QQ.

© Alan V. Cumming 2008

"…did I turn that soldering iron off in 215…..?!?!"

- Alan Cumming, many, many times during 2004, 2005, 2006, 2007…

Contents

Contents i

List of figures viii

List of tables xvii

Acknowledgements xix

Preface xxi

Summary xxiv

Chapter 1 Gravitational Wave Detection 1

1.2 Properties and nature of Gravitational Waves 3
1.3 Gravitational Wave Sources 5
1.3.1 Burst Sources 5
1.3.1.1 Supernovae 5
1.3.1.2 Coalescing Compact Binaries 7
1.3.2 Periodic Sources 8
1.3.2.1 Pulsars 8
1.3.2.2 Low-Mass X-Ray Binaries 9
1.3.3 Stochastic Background Radiation 9
1.4 Experimental Gravitational Wave Detectors 10
1.4.1 Ground Based Resonant Bar Detectors 10
1.4.2 Laser Interferometry 11
1.4.2.1 Delay Line Interferometry 14
1.4.2.2 Fabry-Perot Interferometry 14
1.4.2.3 Power and Signal Recycling 15
1.5 Interferometric Detector Noise Sources 16
1.5.1 Quantum Noise – Photon Shot Noise 17

1.5.2 Quantum Noise – Radiation Pressure 18
1.5.3 Standard Quantum Limit 19
1.5.4 Seismic Noise 20
1.5.5 Gravity Gradient Noise 23
1.5.6 Thermal Noise 23
1.5.6.1 Brownian Thermal Noise 23
1.5.6.2 Thermorefractive Noise and Thermoelastic Noise 24
1.5.7 Noise Spectra 25
1.6 Operational Interferometric Detectors 25
1.6.1 LIGO Detector Network 26
1.6.2 GEO600 27
1.6.3 VIRGO 29
1.6.4 TAMA300 30
1.7 Second Generation interferometric gravitational wave detectors 30
1.7.1 Enhanced and Advanced LIGO 31
1.7.2 GEO-HF 32
1.7.3 Advanced VIRGO 32
1.8 Third Generation Interferometric Gravitational Wave Detectors 33
1.9 Space Based Detectors 33
1.10 Conclusions 34
Chapter 2 Thermal Displacement Noise 36
2.1 Introduction 36
2.2 Brownian Motion 37
2.3 Einstein and Dissipation 38
2.4 Forms of Damping 39
2.4.1 External Damping 39
2.4.2 Internal Damping 39
2.5 Mechanical Loss Factor ϕ 43
2.6 Thermoelastic Noise 44
2.6.1 Thermoelastic Noise in Suspension Fibres 45
2.6.2 Thermoelastic Noise in Test Mass Mirrors 46
2.7 Noise Spectra as a Function of Mechanical Loss 46
2.7.1 Single Resonance Systems 46
2.7.2 Multi-Resonance Systems 49
2.8 Mirror Suspension Modes 49

2.8.1 Internal Modes of the Test Mass....50
2.8.2 Modes of Suspension Elements....50
2.8.2.1 Pendulum Modes....50
2.8.2.2 Mechanical Loss of a Pendulum Suspension....51
2.8.2.3 Violin Modes....54
2.8.2.4 Bounce, Pitch, Yaw and Roll Modes....56
2.9 Low Loss Suspension Materials....57
2.9.1 Empirical Models of Mechanical Loss of Fused Silica....57
2.9.2 Other Suitable Materials....58
2.9.2.1 Sapphire....58
2.9.2.2 Silicon....59
2.10 Conclusions....60
Chapter 3 Characterisation of mirror suspension fibres....61
3.1 Introduction....61
3.2 First Generation Detector Suspensions....62
3.2.1 Initial LIGO Mirror Suspensions....62
3.2.2 GEO600 Mirror Suspensions....63
3.3 Suspension Design Requirements for Advanced LIGO....65
3.4 Ribbon Suspension Fibres....67
3.5 CO_2 Laser Production of Ribbon Fibres....73
3.5.1 CO_2 Laser Pulling Machine....75
3.5.2 Pulling Machine Control....77
3.6 Ribbon Characterisation....80
3.6.1 Dimensional Characterisation of Laser Pulled Fibres....81
3.6.1.1 Characterising Fibres for GEO600....82
3.6.1.2 Preliminary Concepts....83
3.6.1.3 Scanner....83
3.6.1.4 Imaging by Web-camera – 1st Prototype....86
3.6.1.5 Imaging by Web-camera – 2nd Prototype - Dual Camera System....89
3.6.1.6 Profiler Final Development....91
3.6.1.7 Machine Capabilities and Testing....95
3.6.2 Proof Load Testing of Laser Pulled Ribbons....98
3.6.3 Vertical Bounce Frequency of Laser Pulled ribbons....99
3.6.3.1 Experimental Bounce Testing....99
3.6.3.2 Calibration....100

3.7 Characterisation of Typical Advanced LIGO Suspension Ribbons 102
3.7.1 Profiling 102
3.7.2 Proof Load Testing 106
3.7.3 Bounce Frequencies 107
3.8 Conclusions 108
Chapter 4 FE Analysis of Advanced LIGO pendulum suspensions 109
4.1 FEA Modelling Techniques in ANSYS 110
4.1.1 Creating Masses and Ribbons in ANSYS 110
4.1.2 Importing Ribbon Dimension Data into ANSYS 113
4.1.3 Extracting the Bending Point 114
4.2 Calculating the dilution factor 116
4.2.1 Verifying the Technique 118
4.2.2 Checking Solution Convergence 123
4.3 Single Ribbon/Fibre Models 126
4.3.1 Single Ribbon/Fibre with No Neck 126
4.3.2 Single Ribbon/Fibre with Linear Taper Neck of 7.5mm Length 126
4.3.3 Single Ribbon/Fibre with Linear Taper Neck of 15 mm Length 129
4.3.4 Discussion 132
4.3.5 Dilution as a Function of Taper Length 133
4.4 Advanced LIGO Models 135
4.4.1 No Necks, Simple Ears 135
4.4.2 Linear Tapered Necks 138
4.4.3 Real Necks 142
4.4.4 Real Necks, Real Ears 145
4.4.5 Discussion 147
4.5 Improving Thermal Noise Performance 147
4.5.1 Tapered Fibres 147
4.5.2 Tapered Fibre with Ear Representation 149
4.5.3 Real Tapered Fibre 151
4.6 Evaluation of all Mechanical Loss Mechanisms in Real Ribbons/Fibres 153
4.7 Conclusions 159
Chapter 5 Test Mass Mirror Coatings 160
5.1 Test Mass Mirror Coatings 160
5.2 Measuring Mechanical Loss of Test Mass Samples 161
5.3 Experimental Measurement of the Mechanical Loss of a Mirror Coating 162

5.3.1 Samples 162
5.3.2 Experimental Mechanical Loss Measurement Setup 164
5.3.2.1 Test Mass Suspension 164
5.3.2.2 Detection System 166
5.3.2.3 Interferometer Signal Correction Apparatus 171
5.3.2.4 Data acquisition 175
5.3.3 Calculation of Coating Loss 176
5.3.4 Extracting Energy Ratios from ANSYS 178
5.3.5 Composite Material Properties 179
5.3.6 Mode Shapes and Frequencies 182
5.4 Mechanical Loss of Doped Tantala Coatings 183
5.5 Conclusions 185
Chapter 6 Mechanical Loss of Diffractive Mirrors 187
6.1 Interferometry Using Diffractive Optics 187
6.1.1 Introduction 187
6.1.2 Diffractive Interferometer Configurations 188
6.1.3 Advantages of Diffractive Interferometry 189
6.1.4 Diffractive Samples 190
6.2 Mechanical Loss Measurements of Diffractive Samples by Fibre Suspension 192
6.2.1 FEA Modelling of the Substrates 192
6.2.2 Sample Suspensions Used in Measurement 193
6.2.3 Measured Losses 197
6.3 Measurements by Nodal Support 200
6.3.1 Design 200
6.3.2 Nodal Support Initial Testing and Development 201
6.4 Sample Surface Quality 204
6.5 Mechanical Loss of Sample With Diffractive Surface 214
6.6 Mechanical Loss of Diffractive Optics with Reflective Optical Coating 215
6.7 Conclusions and Future Work 218
Chapter 7 Conclusions 220
Appendix A CO_2 Laser Pulling Machine LabVIEW Control Program 224
A.1 CO_2 Laser Machine Control 224
A.2 Front Panel 225
A.3 Block Diagram 226
A.3.1 Main Diagram and Idle State 226

A.3.2 Startup Zero State....230
A.3.3 Stabilise State....231
A.3.4 Open Shutter State....232
A.3.5 Enable Enables State....233
A.3.6 Pull State....234
A.3.7 Close Shutter State....235
A.3.8 Zero Voltages and Stop State....236
A.3.9 Disable Enables State....237
A.3.10 Alert and Prompt State....238
A.3.11 End Pull Overrun State....239
A.3.12 Reset State....240
A.3.13 Reset 2 State....241
A.3.14 Exit State....242
A.4 Input Voltage Dataset....242
Appendix B Dimensional Characterisation Machine LabVIEW Measurement and Control Program 245
B.1 Program Front Panel....245
B.2 Block Diagram....249
B.2.1 Main Diagram and Measurement State....249
B.2.2 Motor Off State....253
B.2.3 Motor On, Counting Distance State....254
B.2.4 Motor On State....255
B.2.5 Reset Message State....256
B.2.6 Idle State....257
B.2.7 File Setup State....258
B.2.8 Snap for Neck Scan State....259
B.2.9 Neck Scan Top State....260
B.2.10 Initial Count State....261
B.2.11 Reset State....265
B.2.12 Exit state....267
B.2.13 Live Video State....268
B.2.14 Next State....271
B.2.15 Record Data State....272
B.2.16 Graph State....273
Appendix C Installation of Ribbon Characterisation Equipment at LASTI, LIGO Test Facility 274

Appendix D LabVIEW Program for Producing Command Line ANSYS Code 275
D.1 Front Panel 275
D.2 Block Diagram 275
Appendix E LabVIEW Exponential Voltage Decay Program 278
E.1 Exponential Decay Drive of Function Generator 278
E.1.1 Front Panel 278
E.1.2 Block Diagram 278
Appendix F LabVIEW Data Acquisition and Mechanical Loss Calculation Program 279
F.1 Front Panel 279
F.2 Block Diagram 279
F.2.1 Main Diagram and Idle State 279
F.2.2 Start State 282
F.2.3 Data Acquisition State 283
F.2.4 Calculation of Q Value / Mechanical Loss State 285
F.2.5 Iteration Mark State 286
F.2.6 Recording of Ringdown State 287
F.2.7 Start2 State 288
F.2.8 Exit State 289
Bibliography 290

List of figures

Figure 1.1 A loop of test mass particles, showing the effects of a gravitational wave which interacts with the loop at normal incidence. 4

Figure 1.2 Schematic diagram of a basic Michelson interferometer..... 12

Figure 1.3 Effect on a ring of free test mass particles of the passage of a singularly polarised (h_+) gravitational wave of period T (travelling perpendicular to the plane containing the masses) (top) and a Michelson interferometer (bottom). If made free to move the interferometer's end mirrors act like the particles in the ring, and cause a detectable differential arm length change..... 13

Figure 1.4 Delay line interferometers a. Delay line using folding mirrors b. Herriot delay line using input mirrors with small gaps for entering and exiting beams..... 14

Figure 1.5 Interferometry using Fabry-Perot cavities in the interferometer arms 15

Figure 1.6a. Michelson interferometer with Fabry-Perot arm cavities and power recycling mirror at the input of the interferometer b. Michelson interferometer with Fabry-Perot arm cavities and signal recycling mirror at the output of the interferometer 16

Figure 1.7 Transfer function of a 1 Hz pendulum 22

Figure 1.8 Theoretical sensitivity and noise sources for the GEO600 interferometric gravitational wave detector (described in the coming section), tuned to 250Hz, showing the contributions of the various noise sources. Noise sources marked "TN" are thermal noise sources, which will be discussed further in Chapter 2. 25

Figure 1.9 LIGO 4km arm length detectors at Hanford, Washington (left) and Livingston, Louisiana (right). The Hanford instrument shares its infrastructure with a smaller with a 2km interferometer..... 26

Figure 1.10 Strain sensitivities of LIGO detectors at Hanford (LHO) and Livingston (LLO) during the first 5 data taking runs 27

Figure 1.11 Aerial view of the GEO600 detector with 600 m long perpendicular arms, at Ruthe, Germany..... 28

Figure 1.12 Strain sensitivities of GEO600 detector during the first 5 data taking runs28

Figure 1.13 VIRGO detector, Cascina, Italy *29*

Figure 1.14 Sensitivity of VIRGO during the first data taking run, October 2007...... *30*

Figure 1.15a. Orbit of the three LISA spacecraft b. Artist's impression of the three LISA spacecraft *34*

Figure 2.1 Simple representation of an anelastic material, with a single relaxation process. *40*

Figure 2.2 Typical Mode shapes of an Initial LIGO 10.7 kg test mass. *50*

Figure 2.3 a. Pendulum modes for 2 wire pendulum b. Bending occurring at top only c. Bending occurring both top and bottom..... *54*

Figure 2.4 Bounce, roll, yaw and pitch modes of a test mass suspension *56*

Figure 2.5 Vertical bounce mode coupling into arm length change (and hence displacement thermal noise) of a long interferometer arm...... *57*

Figure 3.1 a. Initial LIGO test mass suspension and frame b. Cutaway drawing showing suspension wire loop and clamp *62*

Figure 3.2a. GEO600 test mass triple suspension b. GEO600 reaction chain, showing electrostatic drive *64*

Figure 3.3a. GEO600 monolithic stage under construction b. Fused silica ears and fibres on GEO600 test mass...... *64*

Figure 3.4 Advanced LIGO monolithic suspension (left, showing one of the two metal masses and the fused silica lower stage). Insets show detail of the ears and ribbon fibres. *66*

Figure 3.5 Frequency dependence of thermoelastic loss in ribbon and fibre, showing different locations of the thermoelastic peak...... *69*

Figure 3.6 Thermoelastic noise at 10 Hz, when nonlinear effects are taken into account *72*

Figure 3.7a. Flame pulling machine, as used to produced fibres for GEO600 mirror suspensions b. Flame heating of silica..... *74*

Figure 3.8a. Drawing of CO_2 laser pulling machine b. Close up of laser beam delivery point and motorised carriage arrangement..... *76*

Figure 3.9 Laser bench showing motorised beam dump and power monitoring..... *77*

Figure 3.10 Schematic diagram of laser pulling machine control program...... *78*

Figure 3.11 Characterisation procedures for Advanced LIGO ribbons...... *81*

Figure 3.12 Construction of early prototype ribbon cartridge.The ribbon was pulled on the pulling machine in the clamps shown, and the L-shaped stiffening bars

were attached to the clamps in-situ. The complete rigid cartridge was then removed from the pulling machine as a single unit..... 84

Figure 3.13 Image of early laser pulled ribbon neck section made using flatbed scanner. Ribbon shows very thin section after the initial neck, which was due to initial pulling problems with laser machine 84

Figure 3.14 Measurement by LabVIEW edge detection program 85

Figure 3.15 Firewire web camera used for imaging 86

Figure 3.16 Proof-of-concept web-camera based dimensional characterisation setup. a. view of camera and ribbon cartridge b. Complete setup from different angle showing mobility of imaging head..... 87

Figure 3.17 LabVIEW imaging and measurement showing ribbon as imaged by firewire web-cam. The contrast change visible toward the bottom of the image was later attributed to a lens misalignment..... 88

Figure 3.18 Profiler under development, showing initial test upgrade to use dual cameras. Ribbon was not contained in the cartridge for these tests, as the cartridge design precluded the use of both cameras simultaneously..... 90

Figure 3.19 a. Construction of revised ribbon cartridge, showing the ribbon held in "fuse" holsters, and stiffening bars relocated to the corners of the revised clamps. b. Ribbon removal from the clamps to allow proof and bounce testing after profiling..... 92

Figure 3.20 Finalised ribbon profiling machine, showing cartridge with ribbon installed in top and bottom loose clamp holders, which have coarse alignment and rotation adjustability built in. Fine adjustment and focus is achieved with the cameras as is shown. 93

Figure 3.21 Repeatability of width of test ribbon neck and segment of thin section..... 96

Figure 3.22 Repeatability of thickness of test ribbon neck and segment of thin section 97

Figure 3.23 a. Proof test machine b. Close up of hydraulic mass lifter..... 98

Figure 3.24 a. Ribbon bounce tester b. Close up of mass, detector and exciter..... 100

Figure 3.25 Ribbon profile of oversize Advanced LIGO ribbon. Average dimensions do not include the neck regions..... 103

Figure 3.26 Ribbon profile of Advanced LIGO ribbon with approximately correct cross section. Average dimensions do not include the neck regions..... 104

Figure 3.27 Neck profile of the shortest neck achieved.. Inset shows photograph of the actual ribbon width..... 106

Figure 3.28a 12.5 kg mass in proof tester. b. mass hanging on loaded ribbon showing stretch of ribbon (mass is seen hanging lower than in the first picture due to stretching) 107

Figure 4.1 Steps taken in building a solid element model in ANSYS. Keypoints define vertices of the block, lines joining keypoints define the edges allowing a volume to be created. Nodes mesh this volume, with (in this case) each node being located at the vertex of an element. 111

Figure 4.2 Steps used in building a beam element ribbon in ANSYS. Keypoints are defined along the ribbon length, these being linked by lines. Meshing these lines gives an array of nodes along the ribbon length, and cross sections are defined to give the ribbon its shape. 112

Figure 4.3 Schematic showing process of producing a neck model of a real ribbon.. Ribbon (left) is characterised in the profiler giving data shown in blue curve (only width data shown for clarity). Red data points are those chosen to create cross sections in ANSYS. Image on right shows the resulting ribbon model in ANSYS. 114

Figure 4.4 Schematic showing bending length and bending points of a pendulum fibre. 115

Figure 4.5a. Schematic diagram of pendulum bending (in red) and method of extracting the bending point b. Example of bending in a 15mm long taper neck in ANSYS 116

Figure 4.6 Single ribbon FEA ANSYS model, suspending mass of 10kg, with ideal ribbon containing no end necks. Insets to the right show the equivalent circular fibre as modelled by R. Kumar 119

Figure 4.7 a. Longitudinal pendulum mode considered in the ribbon pendulum analysis, showing bending occurring in thin dimension. Wireframe shows pendulum equilibrium position b. Side view of longitudinal pendulum mode. 120

Figure 4.8 Strain energy distribution for top 3 mm of ribbon and fibre with no necks 122

Figure 4.9 Strain energy distribution for bottom 3 mm of ribbon and fibre with no necks 122

Figure 4.10 a. Theoretical system b. System as modelled in ANSYS, showing additional bending (exaggerated for clarity) and pitching of the finite sized mass. 123

Figure 4.11 Convergence of dilution using a 10 kg mass constructed from beam elements 124

Figure 4.12 Convergence of dilution using a 10 kg mass constructed from solid elements 125

Figure 4.13 a. Linear taper neck used in FE models, with cross sectional area identical to circular fibre. b. Linear taper neck with actual start dimension of 5 x 0.5 mm. c. Comparison circular fibre, as modelled by R. Kumar. b. and c. have identical cross sectional area throughout. 127

Figure 4.14 a. Stress distribution in 8.4 x 0.84 mm start dimension ribbon neck showing 3D and side views. MX denotes the position of maximum stress b. Stress distribution in 5 x 0.5 mm start dimension ribbon neck showing 3D and side

views c. Stress distribution in circular fibre. Inset shows that the stress is more localised at the end of the neck..... 128

Figure 4.15 Bending strain energy discribution in 7.5 mm linear taper necks 129

Figure 4.16 a. Linear tapered ribbon neck of 15mm b. Comparison neck as modelled by R. Kumar 130

Figure 4.17 a. Stress concentration in 15 mm long linear taper ribbon neck. b. Ribbon viewed from side, showing stress concentration through its thickness. c. Comparison circular fibre, showing a more localised stress concentration, with maximum located at the end of the neck section. 131

Figure 4.18 Bending strain energy discribution in 15 mm linear taper necks 132

Figure 4.19 Graph showing dilution as a function of linear taper neck length for both ribbon and fibre, where cross sectional areas are identical through the taper. 134

Figure 4.20 Graph showing dilution as a function of linear taper neck length for both ribbon and fibre where the start dimension of the ribbon is taken as the real life 5 x 0.5 mm. 134

Figure 4.21 Simple model of Advanced LIGO suspensions, using simplified ears, and ideal no-necked ribbons/fibres..... 136

Figure 4.22 a. 3D view of longitudinal pendulum mode for Advanced LIGO b. side view of longitudinal pendulum mode showing mass ramaining horizontal due to its inertia 137

Figure 4.23 a. Advanced LIGO model with 7.5 mm linear taper necks b. equivalent circular fibre model 139

Figure 4.24 a. Advanced LIGO model with 15 mm linear taper necks b. equivalent circular fibre model 139

Figure 4.25 Strain energy distribution for a single ribbon/fibre in Advanced LIGO 4 ribbon/fibre model, with ribbon/fibre having 7.5 mm long linear tapered necks..... 141

Figure 4.26 Strain energy distribution for a single ribbon/fibre in Advanced LIGO 4 ribbon/fibre model, with ribbon/fibre having 15 mm long linear tapered necks..... 141

Figure 4.27 Advanced LIGO models using real ribbon profiles. a. shows the oversized ribbon, b. shows the thinner ribbon 142

Figure 4.28 Strain energy distributions for the real ribbons characterised in Chapter 3 143

Figure 4.29 Advanced LIGO model for real short neck characterised in section 3.7.1, (see Figure 3.27)..... 144

Figure 4.30 Strain energy distribution for Advanced LIGO model for real short neck characterised in section 3.7.1, (see Figure 3.27). *145*

Figure 4.31 Advanced LIGO model using accurate models of the real ears, and also the best ribbon neck profile obtained from the data from section 3.7.1. ..... *146*

Figure 4.32a. Tapered fibre ANSYS model b.Stress in bending of tapered fibre showing bending contained in thicker 805 μm diameter section of fibre *148*

Figure 4.33 Strain energy distribution for tapered fibre. Inset shows the small peak in strain energy observed due to a small additional bend occurring at the transition to 400 μm diameter. *149*

Figure 4.34a. Tapered fibre model with ear representation b. Some stress occurs in the weld region. *150*

Figure 4.35 Strain energy distribution for tapered fibre and ear representation. *151*

Figure 4.36 Real tapered fibre (top), ANSYS model (centre) and profile (plotted). *152*

Figure 4.37 Strain energy distribution for real tapered fibre *153*

Figure 4.38 Schematic ANSYS model of fibre (side view of fibre), showing approximation of elements to constant diameter sections. *156*

Figure 4.39 Mechanical loss contribution of surface and thermoelastic loss for real circular tapered fibre *157*

Figure 4.40 Mechanical loss spectra of real ribbon, real tapered fibre and baseline ribbon *158*

Figure 5.1 Coated test mass sample, with coating on top face. *163*

Figure 5.2 Side view of test mass sling suspension, showing clamping block, clamp with hollowed faces, mass, drive plate and catcher. *165*

Figure 5.3 Experimental setup for measurement of mechanical loss of test mass samples. *166*

Figure 5.4 Photo of interferometer showing the beam paths around the optical bench of the interferometer. Beam exiting to the right incidents the front face of the test mass within the vacuum tank. *167*

Figure 5.5 Plot showing raw ringdown data (red), and the exponential ringdown envelope from which the Q-factor of the resonance is calculated. The data shows a sinusoidal variation in amplitude, of the type that is discussed below. *168*

Figure 5.6 Laser intensity variation as a function of time for He-Ne laser used in interferometric loss measurements *170*

Figure 5.7 Variation in amplitude of a recorder ringdown as compared to the variation in intensity of laser power over the same period of 750 seconds. *171*

Figure 5.8 Recording and correcting of a ringdown envelope. a. Recorded ringdown envelope showing fluctuation in both ring down (green) and the recording of the constant amplitude 10kHz signal (grey). b. Ringdown envelope after normalisation by 10 kHz signal (black) is a much closer fit to the injected signal (red). The fit line for the black data is not shown for clarity..... 173

Figure 5.9a. Typical poor dataset showing a fluctuation and peak in the ringdown envelope after 40s, likely caused by a varying alignment in the interferometer. b. The corrected data shows near perfect exponential form. 174

Figure 5.10a. Very poor dataset from a ringdown taken when significant vibration in laboratory. b. After correction, the corrected dataset is still very usable... 175

Figure 5.11 Application of a coating surface to a FEA model of the test mass sample in ANSYS. 179

Figure 5.12 ANSYS derived mode shapes for 76.2 mm (3") diameter and 25.4 mm (1") thick test mass sample. Relative displacement vector sums $U = \sqrt{x^2 + y^2 + z^2}$ *are shown in dimensionless units. 182*

Figure 5.13 Measured mechanical losses of different 30 layer coatinged silica test mass samples manufactured by CSIRO 183

Figure 6.1 Typical grating configurations a. Diffraction from grating surface showing reflected beam m=0, and first order m=1 diffracted beam b. All reflective Michelson interferometer c. Fabry-Perot cavity formed with grating in 1st order Littrow configuration d. Fabry-Perot cavity formed with grating in 2nd order Littrow configuration 188

Figure 6.2 a. 2-D Optical profiles of diffraction grating on silica disk substrate, used in the experiments detailed in this chapter b. 3D image of same region c. Surface profile along dashed line 191

Figure 6.3 S.E.M. image of cross section of diffractive substrate with 30 layer silica-tantala coating stack (only 28 layers visible). 192

Figure 6.4 ANSYS FEA model mode shapes of silica disks. Relative displacement vector sums $U = \sqrt{x^2 + y^2 + z^2}$ *are shown in dimensionless units. 193*

Figure 6.5 Seven silica suspensions used to investigate mechanical loss of silica disk.. 194

Figure 6.6 Suspension of silica disk, showing blade spring isolation and intermediate isolation mass 195

Figure 6.7 a. Suspension 6 with disk held from a single 3 cm fibre, and upper isolation mass held from thread. b. close up of clamping and double thread loop.... 196

Figure 6.8 a. Suspension 7 with disk held in monolithic suspension. b. Isolation mass held by fibre from clamped ear. 197

Figure 6.9 Measured mechanical loss using fibre suspensions..... 198

Figure 6.10 Close up of disk weld point showing deformation near the weld and vapour deposition around the weld point..... 199

Figure 6.11 Design concept for nodal support using tensioned thread to support thin disks..... 201

Figure 6.12a. First test nodal suspension using 3 threads b. electrostatic drive plate held behind sample..... 201

Figure 6.13 Comparison of different suspension materials and configurations..... 202

Figure 6.14 Cross section of thread/wire at contact point. 202

Figure 6.15 Revised nodal support with rubber damping o-rings between legs and base, and lead blocks..... 203

Figure 6.16 Mechanical loss changes when lead blocks added on top of clamping structure..... 204

Figure 6.17 Comparison of lowest measured losses for different production batches of disks..... 205

Figure 6.18 Comparison of measured losses with points where suspension wires contact flame polished..... 206

Figure 6.19 Flame polishing of disk edge Inset: Close up of heating of edge showing area heated and proximity and angle of gas torch..... 207

Figure 6.20 Mechanical losses for disk with and without flame polished edges..... 208

Figure 6.21 Comparison of ratio of energy in disk edge to measured mechanical loss for outermost 2.5 mm of disk edge. 209

Figure 6.22 Comparison of ratio of energy in disk edge to measured mechanical loss for outermost 270 μm of disk edge. 210

Figure 6.23 SEM image of 1.7 mm cross section of batch 1 disk, showing rough surface. 211

Figure 6.24 SEM image of 1.7 mm cross section of a production batch 2 disk, showing rough surface with more features compared to batch 1 disks. 211

Figure 6.25 SEM image of 1.7 mm cross section of production batch 1 disk, with edge flame polished. The rough surface at top of image is a scribe line, used to verify that image was correctly focussed. The small circular feature visible at the centre bottom of the image is a small chip in the disk edge that left a depression after flame polishing 211

Figure 6.26 FFT analysis of disk edge images..... 212

Figure 6.27 Images used in RMS deviation calculation, Batch 1 disk, Batch 2 disk, flame polished disk 213

Figure 6.28 Comparison of measured losses of blank disk with vapour deposits, pristine blank disk, and diffractive disk. 215

Figure 6.29 Measured coating loss values for three silica disks from two different production batches, with one diffractive sample. 217

List of tables

Table 3.1 Repeatability tests of profiler measurement system – test 1 repeated the measurement with no change made to a good focus, test 2 refocussed the image for each repetition. *95*

Table 3.2 Bounce testing of steel suspension wire *101*

Table 3.3 Vertical bounce frequency measurements for Advanced LIGO ribbons *107*

Table 4.1 Dilution results for simple single ribbon/fibre holding 10 kg, showing *121*

Table 4.2 Dilution factors for 7.5 mm taper necked fibres and ribbons *127*

Table 4.3 Dilution factors for 15 mm taper necked fibres and ribbons *130*

Table 4.4 Summary of dilution factors for non-necked and taper necked ribbons and fibres *132*

Table 4.5 Dilution comparison for Advanced LIGO longitudinal pendulum mode *137*

Table 4.6 Dilution values for linear tapered neck ribbons and fibres. *140*

Table 4.7 Dilution values for real ribbons characterised in Chapter 3 ..... *143*

Table 4.8 Comparison of dilution when bending strain energy in ears is introduced... *146*

Table 4.9 Summary of ribbon dilution factors for Advanced LIGO models *147*

Table 5.1 Composition of high index layers of three CSIRO coated samples. *163*

Table 5.2 Properties of individual constituent materials of the coating samples *180*

Table 5.3 Composite material properties of high refractive index layers of doped coatings *181*

Table 5.4 Thicknesses of the individual high and low index layers, and of complete coating *181*

Table 5.5 Effective material properties of 30 layer doped coatings. *181*

Table 5.6 Ratios of the elastic energy contained in the coating to the total elastic energy in both substrate and coating for the three doped mass samples. Convergence of the solutions was found to be similar to the convergence of the models studied in Chapter 4..... 184

Table 5.7 Coating losses for doped coatings, with undoped tantala / silica coating loss also shown. 184

Table 5.8 Residual coating losses for doped coatings, with undoped tantala / silica residual coating loss also shown. 184

Table 6.1 Details of the seven disc suspensions used in measurements..... 194

Table 6.2 RMS about mean of the average brightness values (structure height) for three different disk edge images..... 213

Table 6.3 Measured coating losses for silica disks (Note, disks B and D were blank samples, not involved in the coating process). 218

Acknowledgements

Academic staff in the Institute for Gravitational Research that deserve thanks include my supervisors Prof. Jim Hough, Dr. Harry Ward and Prof. Sheila Rowan for both the opportunity to join their research group, and their prudent guidance and help through the course of my postgraduate research. Additional thanks to Dr. Caroline Cantley and latterly Dr. Mark Barton, as well as Prof. Ken Strain for their assistance and guidance as part of the laser pulling machine project. Thanks extend to PPARC, and latterly STFC, for provision of funding for the research undertaken.

Lab and office colleges Iain Martin, Alastair Heptonstall and Stuart Reid deserve special thanks. Iain for sharing an office with me for the entire length of my PhD with endless conversations, support when nothing worked and general friendship; Alastair for his approachable down to earth manner and conversations on anything 4 wheeled (particularly Alfa and Saab mentalism); and Stuart for some great laughs (usually involving a knackered white Honda and a fire break) and excellent advice in equal measures. Knowledge accrued from both Alastair and Stuart was indispensable in explaining many of my confused queries, both practical and theoretical during my PhD.

Group technicians Colin Craig and Stephen Craig also deserve particular recognition. Their experience and expertise proved valuable in assembly of all the experiments constructed during the research, and their down to earth humour and chat made the lab experimental work an enjoyable activity. Thanks also extend to engineer Russell

Jones, whose expertise with Solidworks was invaluable and Russell was a pleasure to work with.

Other group members that deserve thanks include officemates, Eleanor, Karen (for random conversation about cats, fire, tall buildings, hamsters, postal frolics and the Snowman), Marielle, Frank (for saying nothing about the picture of a Spitfire above his desk), Peter, Rahul and Riccardo (for excessive use of the phrase “high definition”). Personal thanks to the Kev (for still managing to be my friend despite fleeing physics) and the tall man with the spectacles (for being somewhere else almost all of the time). Unexpected thanks also extend Microsoft Word for (somewhat surprisingly) only crashing to a point of losing anything once in process of writing this document – a rare treat of reliability.

Final and most heartfelt thanks must go to my parents and grandparents without whose support, in every respect, I would not have achieved anything.

Preface

This thesis documents research work undertaken from October 2004 to April 2008 on characterising aspects of mirror suspensions for advanced gravitational wave detectors.

In Chapter 1 gravitational waves are introduced and their nature is discussed, and potential sources are reviewed. Detection schemes are also discussed along with an introduction to a variety of limiting noise sources. Current interferometric detectors and their sensitivities are introduced, together with future upgrades that are envisaged. This chapter is based on published literature.

Chapter 2 comprises a discussion of aspects of thermal noise, and how it can be quantified together with the way it affects gravitational wave detector sensitivity. Mechanical losses of suspension elements are linked to displacement noise within the detectors, and sources of dissipation are discussed. This chapter is based on published literature.

The suspension technology envisaged for the future Advanced LIGO detector is the focus of Chapter 3. Comparison with current detector suspensions is given, together with the motivation for the Advanced LIGO suspension design using ribbon suspension fibres. Ribbons were produced using a CO_2 laser pulling machine constructed by Dr. A. Heptonstall, Dr. M. Barton, Dr. G. Cagnoli, Dr C. Cantley and Mr R. Jones, with control programming written by the author, including laser stabilisation control by Dr. M. Barton. Construction of a ribbon/fibre dimensional characterisation machine and

authoring of the control software was conducted by the author with assistance from Mr. R. Jones, with initial advice from Dr. C. Cantley, Dr. D. Crooks, Dr. A. Heptonstall. Construction of the bounce test machine and proof load tester were carried out with assistance from Dr. W. Cunningham and Dr. C. Torrie.

Chapter 4 presents finite element modelling of rectangular ribbon and circular cross section suspension fibres as characterised in chapter 3. Work was carried out jointly with Mr. R. Kumar, with analysis of the rectangular cross section ribbons being carried out by the author; with circular cross section fibres being studied by Mr. R. Kumar. Advice was provided by Dr. C. Torrie, Dr. W. Cunningham, Prof. J. Hough and Prof. S. Rowan. Work at the end of this chapter on the mechanical loss of tapered fibres was carried out in conjunction with Dr. A. Heptonstall.

Chapter 5 contains measurements performed jointly by the author and Dr. P. Murray on test mass samples coated with doped tantalum pentoxide, silica and titania on their front faces. Construction of the interferometric readout system was undertaken by the author with the assistance of Dr. P. Sneddon and the advice of Prof. J. Hough, Prof. S. Rowan, and Dr. S. Reid. Residual coating loss calculations were performed by Dr. P. Murray.

In Chapter 6 measurements of the mechanical loss of thin disk samples with diffraction gratings in addition to optical coatings on their surfaces are presented. The measurements of the samples and analysis of the results were carried out by the author. Fabrication of the fibre suspensions was carried out by Dr. A. Heptonstall. Design and construction of the nodal support was undertaken by the author after consultation with Prof. J. Hough and Prof. V. Mitrofanov. Surface measurements in the SEM were undertaken by the author with instruction and assistance of Dr. W. Cunningham.

Advice was given throughout by Prof J. Hough, Prof. S. Rowan, Dr. A. Heptonstall, Dr. S. Reid and Dr. W. Cunningham.

Appendix A gives the LabVIEW program code written by the author to control the laser pulling machine described in chapter 3.

Appendix B gives the LabVIEW program code written by the author for measurement and control of the dimensional characterisation machine described in chapter 3

Appendix C shows the ribbon/fibre characterisation equipment installed at the LIGO "LASTI" test facility in Boston.

Appendix D gives the LabVIEW program code written by the author to generate command line script for use in the finite element analysis program ANSYS, as discussed in chapter 4.

Appendix E gives the LabVIEW program code written by the author to generate an exponentially decaying voltage used in checking the functionality of the interferometer correction setup constructed in chapter 5.

Appendix F gives the LabVIEW program code written by the author to record the ringdown data and calculate the mechanical loss of test mass samples, as described in chapter 5.

Summary

Gravitational waves were first predicted by Albert Einstein's Theory of General Relativity, published in 1916. These waves are perturbations in the curvature of space-time. Indirect evidence of their existence has been obtained via observations of binary pulsar system inspirals by Hulse and Taylor. Research is now focussed on achieving direct detection of gravitational waves, giving a new way of observing astronomical events in the universe.

Gravitational waves are quadrupole in nature, causing tidal strains in space. The weak nature of gravity means that the magnitude of these strains is very small. Only astronomical scale sources are likely to produce waves of sufficient amplitude to be detected on earth. In the frequency band of a few Hz to a few kHz, the expected strain amplitude for violent sources is of the order of 10^{-22}. Detection is most likely to be achieved using long baseline interferometer detectors.

Currently several such detectors are in operation worldwide, including the GEO600 detector, built in a collaboration involving the Institute for Gravitational Research at the University of Glasgow, the Albert Einstein Institute (Hannover and Golm), and the University of Cardiff. In America the LIGO detector network has three large interferometric detectors - two of 4 km arm length and one with 2 km arms. In Italy a European collaboration has constructed the 3 km VIRGO detector. Currently GEO600 and LIGO have undertaken 5 data taking science runs with the most recent year long

run, also involving VIRGO, concluding in November 2007. No detections have yet been confirmed, but analysis on the results of the most recent GEO600/LIGO/VIRGO run is ongoing.

These detectors are now operating at, or close to their design sensitivities, so research is focussed on reduction of various noise sources by upgrading of the detectors. One important noise source is thermal noise (both Brownian and thermo-elastic) - a limiting factor at midband frequencies. Reduction of mechanical loss in mirrors and their suspensions will help lessen the impact of thermal noise in future detectors.

The research detailed in this thesis was aimed at reducing thermal noise. In particular, it covers work undertaken to investigate the mechanical loss of suspension ribbons and fibres, test mass mirror coatings and also diffractive surfaces on test masses to evaluate their suitability for employment in future advanced gravitational wave detectors.

Upgrade of LIGO to "Advanced LIGO" will aim to reduce thermal noise by implementing mirror suspension techniques pioneered in GEO600. Specifically, it was initially proposed that test masses be suspended from silica ribbon fibres, a key choice that will be re-evaluated in this thesis. Ribbons (or fibres) will be fabricated by a CO_2 laser pulling machine being developed in Glasgow, with control programming being undertaken by the author.

Characterising the dimensions, strength and vertical bounce frequencies of the ribbons is important to confirm their suitability for use in detector mirror suspensions. A dimensional characterisation machine was constructed to measure the ribbon's cross sectional dimensions, with emphasis being placed on achieving high resolution in the ribbon neck regions, where the most bending occurs. Also, a bounce testing machine was constructed to experimentally measure the ribbon's vertical bounce frequency.

Finally a proof load test was constructed to verify that ribbons could support the required weight. Results showed that ribbons could be fabricated successfully with the required strength and bounce frequency, though shaping of the cross section still requires further research to achieve the optimum.

In a pendulum system most of the energy is stored as gravitational potential energy rather than bending energy of the suspension fibres or ribbons. Thus the effective loss of the suspension fibres/ribbons is reduced or "diluted" and thermal noise is lower than may be naively expected. Dilution of the mechanical loss of the pendulum suspensions was investigated using finite element modelling. Methods for importing data from the dimensional characterisation machine were developed, and it was observed that the dilution resulting from ribbon suspensions was not as high as had been initially expected, with bending in the neck region of the ribbon being seen to significantly reduce dilution. It was observed that the rectangular ribbons had inferior dilution to equivalent cross section circular fibres for necks of the length typically being produced. A typical 7.5 mm necked ribbon was seen to have a dilution 1.5 times lower than an equivalent fibre, despite the ribbons having 3.3 times greater dilution with no necks. Ribbons were only seen to have this superior dilution for very short necks. Bending in the necks resulted in an increased amount of bending strain energy occurring which caused the lower dilution factors. Additionally, bending occurring in the ears that join the fibres or ribbons to the masses was seen to further reduce the dilution. In the light of low dilution factors, reduction (ideally nulling) of thermoelastic noise was studied. Reduction in thermal noise in this way is proposed through use of tapered fibres, which showed that a lower overall noise level than that from the baseline ribbons planned for Advanced LIGO can be achieved, despite lower dilution factors. In the light of this work tapered fibres have now been adopted as the baseline for Advanced LIGO.

Measurements of test mass mirror samples showed that the mechanical loss of mirror coatings can be significantly reduced by doping the high refractive index layer, with reduction of up to a factor of 2.5 in measured mechanical loss observed, when compared to equivalent undoped coatings. In order to perform these measurements an interferometric read out system was constructed.

Future detectors will use higher laser powers which may cause thermal distortions in transmissive optical components. Use of all reflective components may be required to reduce this problem, possibly via diffractive mirrors. Measurements were undertaken on samples to discover if introducing a diffraction grating to an optic's surface increased the mechanical loss. However, the grating was not seen to do this, and also did not increase the mechanical loss of an optical coating applied on top of its surface, which verified that diffractive optics are viable for use in future detectors.

Chapter 1

Gravitational Wave Detection

1.1 Introduction

It is over 90 years since the existence of gravitational radiation was first postulated by Albert Einstein's Theory of General Relativity [1]. His 1916 theory surmised that space time has some curvature caused by bodies with mass, and that any body moving in this regime would simply traverse space time on a path that was as straight as possible given the curvature – namely it would follow a trajectory along a geodesic of curved space time. Perturbations, or 'ripples', in this overall background curvature can be generated by localised changes in gravity.

Despite Einstein's belief in the integrity of his theory, he was sceptical of the likelihood that these 'gravitational waves' would actually ever be detected [2]. However, the prospect of uncovering new understanding of the physics behind some of the most violent astronomical events and relativistic physics in such extreme environments has proved tantalising for astrophysicists and experimental physicists. For the last 50 years

they have been endeavouring to rise to the challenge of achieving a direct detection of gravitational radiation.

The first astronomically observed evidence for the existence of gravitational waves resulted from close observation of the binary pulsar system PSR 1913+16 by Hulse and Taylor [3] over many years, which showed the orbital period was decreasing with time, with this change increasing quadratically with time. This was consistent with inspiralling of the pulsar. Crucially, when the rate of this inspiral was compared with that predicted to arise from gravitational radiation emission by general relativity, the astronomical observation had a fractional accuracy of better than 0.4% [4] [5]. The most recent measurements have improved this, with an uncertainty of only 0.21% [6]. The importance of this first experimental evidence for the existence of gravitational waves was recognised with a Nobel Prize in physics in 1993. More recent observations of a different double pulsar system, J0737-3039, have also produced inspiral rate timing measurements that agree with General Relativity's prediction to within 0.3% [7]. However, whilst such binary systems strongly imply the existence of waves, they do not directly observe the waves themselves.

Prior to Hulse and Taylor's discovery, research had started into methods to observe gravitational waves directly. Joseph Weber initiated the experimental search for gravitational waves by developing resonant bar detectors in the 1960's [8]. There was initial excitement when two independent bar detectors recorded coincident events in the late 1960's [9] indicating detection of passing gravitational waves. However, these detections were discounted soon afterwards [10] [11] and subsequent measurements by much more sensitive instruments yielded no similar detections.

These null results prompted renewed interest in developing methods of detection other than room temperature resonant bars and one such type of instrument is the Michelson

interferometer. In the 1960s, large scale interferometers had already been used in laser ranging and monitoring of seismic events [12] [13]. Currently interferometric gravitational wave detectors are some of the most sensitive displacement measurement instruments on earth, though a first confirmed detection of a gravitational wave has proven elusive. Research continues with vigour to rise to the experimental challenge of increasing the sensitivity of interferometric detectors to permit the first detection.

Direct detection of gravitational waves will allow a new form of astronomical observation, and is likely to enhance our understanding of bodies such as neutron stars, binary star systems and black holes, as well as giving insight into the gravitational collapse at the centre of supernovae. Gravitational waves from the very early universe may provide insight into inflation and the universe shortly after the Big Bang.

This chapter will discuss the nature of gravitational waves, the astronomical sources expected to produce them and the proposed detection methods. The current status of operational detectors will also be reviewed.

1.2 Properties and nature of Gravitational Waves

Perturbations in the curvature of space time are predicted to be produced by acceleration of mass. This situation is analogous to the emission of electromagnetic waves, which results from the acceleration of electric charges. Conservation of charge in electromagnetic theory precludes the existence of monopole radiation, and similarly, energy conservation (and hence, mass conservation) means no gravitational monopole radiation exists either. Furthermore, the conservation of momentum also forbids the existence of dipolar gravitational radiation. This differs from electromagnetism, as charges can have one of two signs; whereas only one sign of mass exists. Hence, gravitational waves are only produced when masses are accelerated non-axisymmetrically [2]. So the lowest order of radiation must be quadrupole.

For quadrupole radiation detectable on Earth from distant sources, the wave will comprise a superposition of two independent polarisations, + and x. The effect of these wave polarisations on a ring of free test mass particles is shown in Figure 1.1, where the wave is incident perpendicular to the plane containing the ring of masses.

Ripples in the curvature are sent out at the speed of light and these waves produce a time varying tidal strain in space.

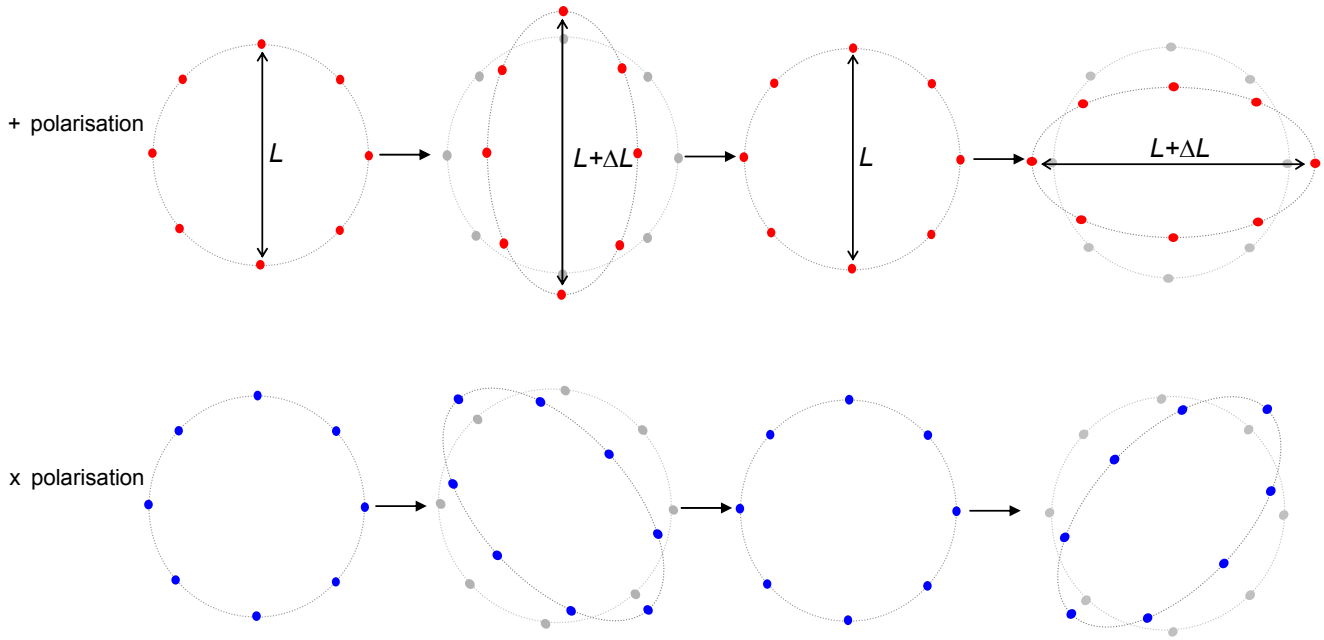

Figure 1.1 A loop of test mass particles, showing the effects of a gravitational wave which interacts with the loop at normal incidence.

The distance between two diametrically opposed masses in the ring will increase by an amount ΔL, whilst reducing by the same amount in the orthogonal direction.

The strain amplitude h of the gravitational wave is defined:

$$h = \frac{2\Delta L}{L} \tag{1.1}$$

Naively, it may seem a trivial task to construct a source of gravitational waves in the laboratory, therefore demonstrating their existence. However, as gravity is the weakest of the four fundamental forces of nature, the resulting wave would be of such diminutive magnitude that detection by any of the current or projected gravitational wave detectors would prove impossible. Indeed, this was considered by Saulson in 1994 [2] with an estimation of the amplitude of a wave produced from two 1 tonne masses held two metres apart and rotated at 1 kHz. The resulting wave amplitude is $h = 9 \times 10^{-39}$ at a distance of 1 wavelength from the source. As we will see later in this chapter, this is some 17 orders of magnitude lower than the best detectable wave amplitude using current instruments. Hence, we need to look to astronomical sources where the masses involved are exceedingly large.

1.3 Gravitational Wave Sources

Ground based detectors are limited by a number of noise sources which will be discussed later in this chapter, and analysis implies that the greatest sensitivity occurs in the frequency band of a few Hertz to a few thousand Hertz. Therefore it is worth considering the types of sources which produce radiation in this frequency band.

1.3.1 Burst Sources

Sources resulting in a sudden short timescale emission of gravitational radiation are known as burst sources, and the mechanisms for radiation emission are astronomical events such as supernovae or binary coalescence.

1.3.1.1 Supernovae

Supernovae are some of the most violent events in the Universe and were an early motivation for development of resonant bar detectors. Stars have a finite lifespan, and when this comes to an end the star can undergo several processes, which in some cases can result in the emission of a burst of gravitational waves.

When the supply of fusible elements within a star core is depleted the outward pressure supplied by fusion reactions in the core disappears and there is nothing to support the core structure. For low mass stars less than the "Chandrasekhar mass" of 1.4 solar masses [14], the core will undergo a catastrophic gravitational collapse until the degeneracy pressure of electrons halts the collapse; for larger mass stars the electron degeneracy pressure is not able to support the core and therefore collapse will continue until neutron degeneracy pressure halts it. This sudden stop causes a rebounding shock wave and an outward explosion of the outer stellar layers creating the brightest and most visible object in the universe. During this collapse electrons and protons are forced together to form neutrons and neutrinos. Stars with mass greater than 20 solar masses collapse to form black holes [15], since neutron degeneracy pressure is not sufficient to resist the large gravitational attraction resulting from these very large masses.

If the core collapses in a totally symmetrical manner then no waves will be produced; but if the core has significant angular momentum the collapse can occur asymmetrically and a burst of gravitational waves is emitted [16].

The gravitational wave strain amplitude from such supernovae was predicted by Schutz [17] to be:

$$h = 5\times10^{-22}\left[\frac{E}{10^{-3}M_{\Theta}c^{2}}\right]^{\frac{1}{2}}\left[\frac{\tau}{1\text{ms}}\right]^{-\frac{1}{2}}\left[\frac{1\text{kHz}}{f}\right]\left[\frac{15\text{Mpc}}{r}\right] \tag{1.2}$$

where E is the total energy emitted, M_{Θ} is the mass of the sun, f is the frequency of gravitational wave emission, τ is the time taken for the collapse, and r is the distance of the source from the detector. Schutz [17] predicted that even if only 1% of gravitational collapse events produced gravitational wave bursts of amplitude 10^{-21}, the event rate experienced in advanced interferometric detectors would be of the order of 1 per day.

However, more recent modelling of core collapse by Muller [18] suggests that the wave amplitude may be less than Schutz predicted.

1.3.1.2 Coalescing Compact Binaries

The majority of stars that exist occur in multiples orbiting a common centre of mass. When such a system contains two stars it is known as a binary star system. If the stars contained are large density bodies such as neutrons stars or black holes the binary system is referred to as a "compact binary".

Three such binary companion systems can exist:

1. Neutron star / Neutron star (NS/NS)
2. Neutron star / Black Hole (NS/BH)
3. Black Hole / Black Hole (BH/BH)

The system PSR1913+16 which resulted in the Nobel prize for Hulse and Taylor is an example of a NS/NS binary system. These systems inspiral with increasing orbital frequency, and the energy lost in this process is emitted as gravitational radiation. In the final few seconds prior to merging the stars emit waves at a frequency and amplitude that is expected to be detectable by ground based gravitational wave detectors.

Schutz [19] predicted the amplitude of waves emitted in this way to be:

$$h = 1\times10^{-23}\left[\frac{100\,\mathrm{Mpc}}{r}\right]\left[\frac{M_B}{1.2M_\Theta}\right]^{\frac{5}{3}}\left[\frac{f}{200\,\mathrm{Hz}}\right]^{\frac{2}{3}} \tag{1.3}$$

where $M_B = \frac{(M_1 M_2)^{\frac{3}{5}}}{(M_1+M_2)^{\frac{1}{5}}}$, with M_1 and M_2 the masses of the two binary companions, f is the frequency of gravitational wave emission and r is the distance of the detector from the source.

Observation of these sources will permit information on the populations of neutron stars in distant galaxies to be gathered.

1.3.2 Periodic Sources

1.3.2.1 Pulsars

Individual neutron stars can also emit gravitational waves if they spin non-axisymmetrically. Such stars have been observed through the radio emission of characteristic periodic pulses This gives rise to this naming of this class of astronomical object as 'Pulsars'.

Non-axisymmetric rotation can occur due to irregularities in the surface of the star, or from accretion of material from a companion star. The pulsar rotation spins down over time with emission of electromagnetic waves. There is the possibility of gravitational radiation contributing to the spin down. The ellipticity, ε, of the star is a measure of the deviation from perfect spherical symmetry, and from this the expected gravitational wave amplitude is [20]:

$$h \approx 6\times10^{-25}\left[\frac{f_{\text{rot}}}{500\,\text{Hz}}\right]^2\left[\frac{1\,\text{kpc}}{r}\right]\left[\frac{\varepsilon}{10^{-6}}\right] \tag{1.4}$$

where f_{rot} is the rotational frequency of the star and r is the distance of the detector from the source. Estimates of the crustal shear moduli and breaking strengths have predicted the ellipticity ε to have an upper limit of around 10^{-4} to 10^{-6} [20]. If the Crab Pulsar (PSR B0531+21) is taken as a candidate pulsar (with distance of 2 kpc,

expected emission frequency of 60 Hz, and ellipticity of 10^{-4}) the expected amplitude of gravitational wave emission $h \approx 4 \times 10^{-25}$ would be anticipated.

1.3.2.2 Low-Mass X-Ray Binaries

Neutron stars such as pulsars can also exist in binary systems with ordinary stars, and if the matter is pulled off the companion by the strong gravitational field of the compact neutron star the system is known as a low-mass X-ray binary. This process of accretion causes an increase of angular momentum of the neutron star, and the star can reach an instability point known as the Chandrasekhar-Friedman-Schutz point where the rotation becomes non-axisymmetric and gravitational radiation emission can occur. Such stars are known as Wagoner stars [21]. These sources are predicted to produce a strain amplitude of [21]:

$$h \approx 3 \times 10^{-27} \left[\frac{1\ \text{kHz}}{mf} \right] \left[\frac{l_\gamma}{10^{-8}\ \text{ergs cm}^{-2}\ \text{s}^{-1}} \right] \tag{1.5}$$

where l_γ is the time averaged X-ray flux, m is the mode number and f is the frequency of the gravitational wave.

1.3.3 Stochastic Background Radiation

One other source of gravitational waves which may be large enough to be detectable is the "stochastic background", which results from superposition of signals from a variety of different sources. Such background sources may include primordial gravitational waves originating from the Big Bang, from phase transitions in the early Universe, or from cosmic strings in the early Universe.

1.4 Experimental Gravitational Wave Detectors

Currently, there are two broad classes of ultra-sensitive gravitational wave detectors in use and under development. The first is the resonant bar detector, as initially conceived by Weber, and more recently large scale laser interferometers have been developed.

1.4.1 Ground Based Resonant Bar Detectors

Weber's original 1960s detectors [22] [23] were ground based devices which relied on the concept of the passing gravitational wave causing tidal strains on large cylindrical metal bars. The bars where chosen such that they had longitudinal resonances in the region of 1600 Hz where Weber expected a wide peak of gravitational radiation originating from stellar collapse. If such a wave was incident on a resonant bar the tidal strain exerted on it would cause the cylinder to vibrate. This vibration could then be measured using a piezoelectric crystal transducer and amplifier. Weber's detectors comprised large 1.5 ton, 66 cm diameter aluminium cylinders, and several were constructed to permit the correlation of any observed gravitational wave events.

Such coincidences began to occur in observed detector events in bars located in Maryland and California in 1968 [24], and several instances were observed in the subsequent 2 years [9] [25]. However, similar resonant bar detectors constructed by other groups failed to confirm these claimed detections, and subsequently more sensitive detectors have also not detected similar events. Therefore the early Weber detections were discounted [10] [26] [11].

However, bar detectors have continued to be developed, and currently there are several groups worldwide developing or running such detectors. These include a 2.27 tonne cryogenically cooled aluminium bar detector, Explorer, located at CERN in Switzerland [27] cooled to 2.6 K [28] and Nautilus in Italy [29] cooled to 0.1 K to reduce the effects of thermal noise (a phenomenon which affects interferometers too, and will

be discussed in detail in Chapter 2). In the Netherlands, a spherical bar detector, MiniGRAIL [30] [31], is also under development. This will also be cryogenically cooled to milli-Kelvin temperatures [32] to aid thermal noise performance. Other detectors include AURIGA (similar to Nautilus) in Italy [33].

Currently there have been many data taking runs undertaken with these detectors [34] [27] [35], with typical strain sensitivity of 10^{-19} - 10^{-20} for 1 ms gravitational wave bursts [27] [36].

Resonant bar detectors are however limited to detecting gravitational waves in at frequencies close to the bar resonance, so an extension of the concept of the bar detector has been proposed by Cerdonio [37] using dual bar detectors, one contained within another providing a gap which could be set up as a Fabry-Perot optical cavity for differential motion sensing. The outermost resonator would be resonant at a frequency two or three times less than the inner one. This permits the extending of the frequency band detectable and passage of a wave that has a frequency between that of the two resonators will cause an anti-phase excitation of the two resonators allowing enhancement of the observed signal. However, analysis of the noise sources of this system suggests that it may be difficult to achieve competitive sensitivities [38].

1.4.2 Laser Interferometry

Use of interferometry as a method for detecting gravitational waves was first proposed by Gertsenshtein and Pustovoit in 1962 [39] [2] and experimentally investigated by Forward in 1970s [40]. In its most basic form, a Michelson interferometer can be seen to be an ideal detector as seen in Figure 1.2.

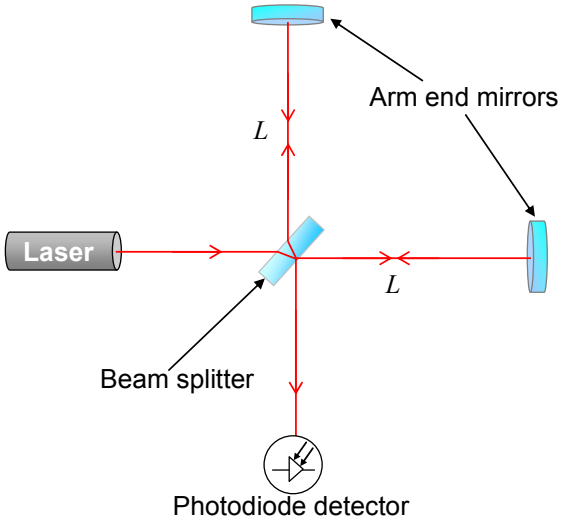

Figure 1.2 Schematic diagram of a basic Michelson interferometer

The interferometer, first conceived by Michelson and Morley [41], works by splitting the input laser beam into two components, each component then traversing an orthogonal arm of the interferometer, being reflected back along the path it came by the arm end mirrors. The returning light is recombined at the beam splitter and the resulting interference pattern is observed at the interferometer output by a photodiode detector. Passage of a gravitational wave will result in the interferometer undergoing a differential change in arm length, as shown in Figure 1.3. This process changes the interference conditions when the light from the two arms is recombined, allowing a signal to be recorded at the output of the interferometer. Interferometric gravitational wave detectors generally run with the interferometer output held ("locked"), close to a dark fringe, which minimises laser noise, whilst maximising the signal. This interferometer locking is achieved by applying a force on the mirrors proportional to the output signal, and this feedback is often taken as the output signal for analysis.

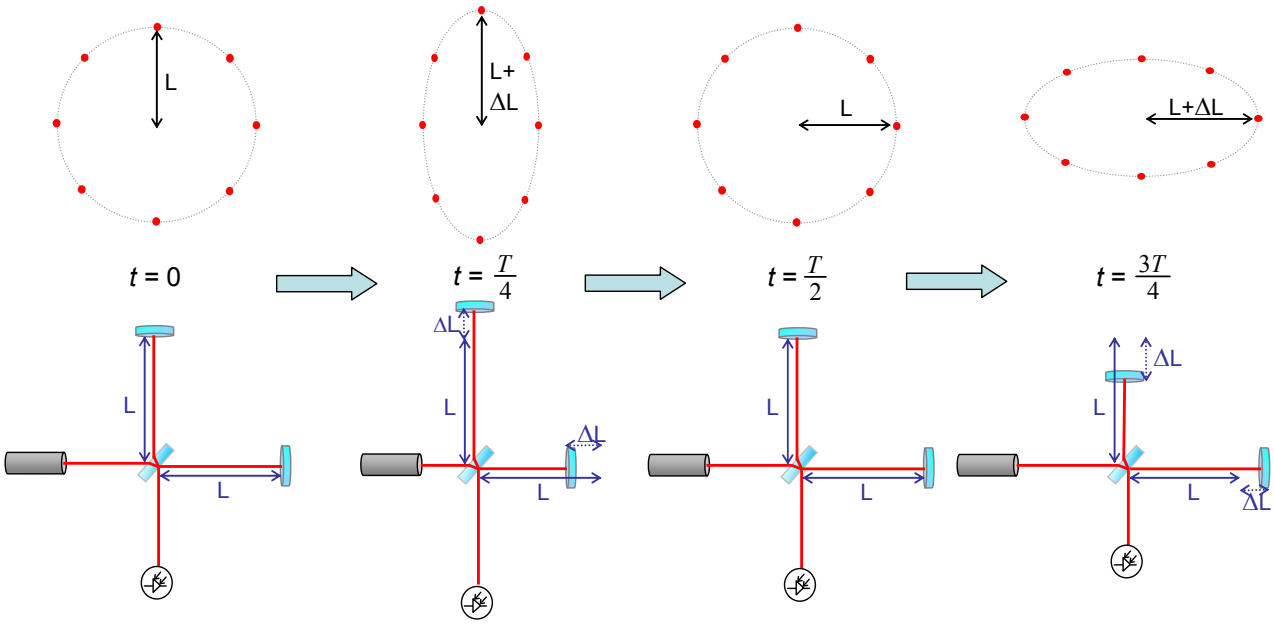

Figure 1.3 Effect on a ring of free test mass particles of the passage of a singularly polarised (h_+) gravitational wave of period T (travelling perpendicular to the plane containing the masses) (top) and a Michelson interferometer (bottom). If made free to move the interferometer's end mirrors act like the particles in the ring, and cause a detectable differential arm length change.

Choosing the appropriate arm length depends on the incoming wave frequency, as the maximum sensitivity of the interferometer is realised when the storage time of the light in the interferometer arms is half the period of the gravitational wave. In this situation the light in the interferometer takes one quarter of the wave period to travel from the beam splitter to the end mirrors, striking the end mirrors at a time where they are maximally displaced, as shown in Figure 1.3. For a wave of frequency 100 Hz, the required storage time is 5 x 10^{-3} s, meaning an optimal arm length is:

$$L = \frac{5 \times 10^{-3} c}{2} = 750\ \text{km} \tag{1.6}$$

This distance is clearly larger than is physically feasible to construct on earth due to the cost and size of infrastructure that would be required. Indeed, since the laser beam travels in a straight line, the curvature of the earth places a limit on the length the interferometer can be constructed. Therefore, different methods have to be employed to

provide a longer storage time for the light travelling within the interferometer arms. This can be achieved via delay line interferometry, or Fabry-Perot interferometry.

1.4.2.1 Delay Line Interferometry

Two delay line interferometer schemes are shown in Figure 1.4. The delay line utilises additional mirrors located near to the beam splitter, to permit an increased length beam path increasing the light storage time.

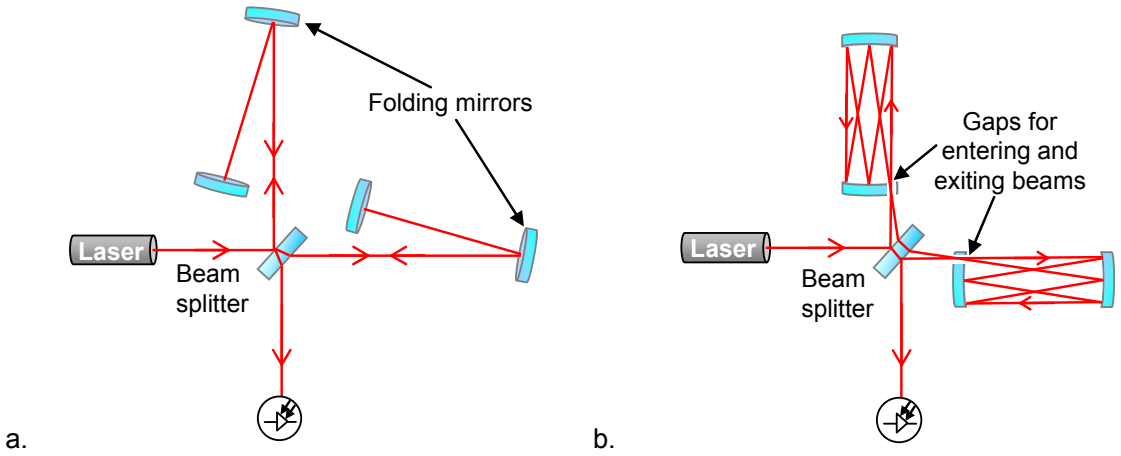

Figure 1.4 Delay line interferometers a. Delay line using folding mirrors b. Herriot delay line using input mirrors with small gaps for entering and exiting beams

The first scheme, shown in Figure 1.4a, uses folding mirrors at the end of the initial arm path to effectively double the storage time of the light in the arms. The second scheme is the Herriott delay line [42], and is shown in Figure 1.4b. This configuration uses two curved mirrors to give multiple transits between the pairs of mirrors. The innermost mirrors of the arms have small gaps in them to permit the light to enter and exit the arms.

1.4.2.2 Fabry-Perot Interferometry

Increased storage time and optical paths of interferometers can be achieved by utilising Fabry-Perot cavities in the interferometer arms. These cavities use a pair of mirrors, one of which is partially transmitting, and the other is highly reflective. These cavities

are then operated at resonance, with the energy stored in the arms being maximised by feedback to either the laser wavelength or the position of the end arm mirrors. Maximal energy is contained when the arm lengths are an integral number of half wavelengths.

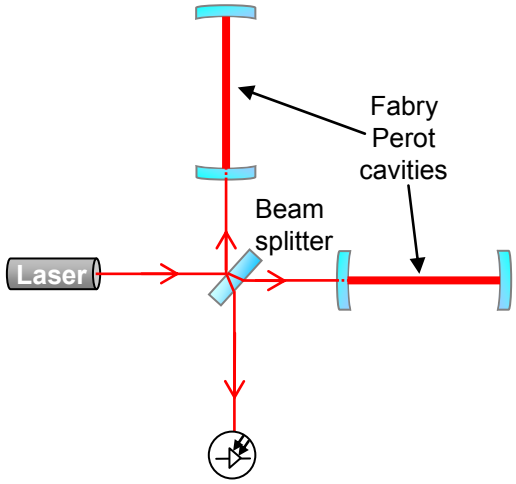

Figure 1.5 Interferometry using Fabry-Perot cavities in the interferometer arms

This technique is employed on several of the current interferometric gravitational wave detectors that will be discussed in section 1.6.

1.4.2.3 Power and Signal Recycling

Other optical techniques can be employed to further boost the output signal from interferometers. Such techniques include power recycling and signal recycling.

Power recycling [43] is a method of increasing the laser power circulating within the interferometer, without increasing the power of the laser itself. Increasing the power contained in the interferometer increases the observable signal. Since the interferometer is operated held close to a dark fringe, most of the light exits the interferometer toward the laser rather than the output port. Thus, power within the interferometer can be increased by reflecting this light back into the interferometer. This can be achieved by placing a partially reflective mirror at the interferometer input port to reflect light back into the instrument, as shown in Figure 1.6a.

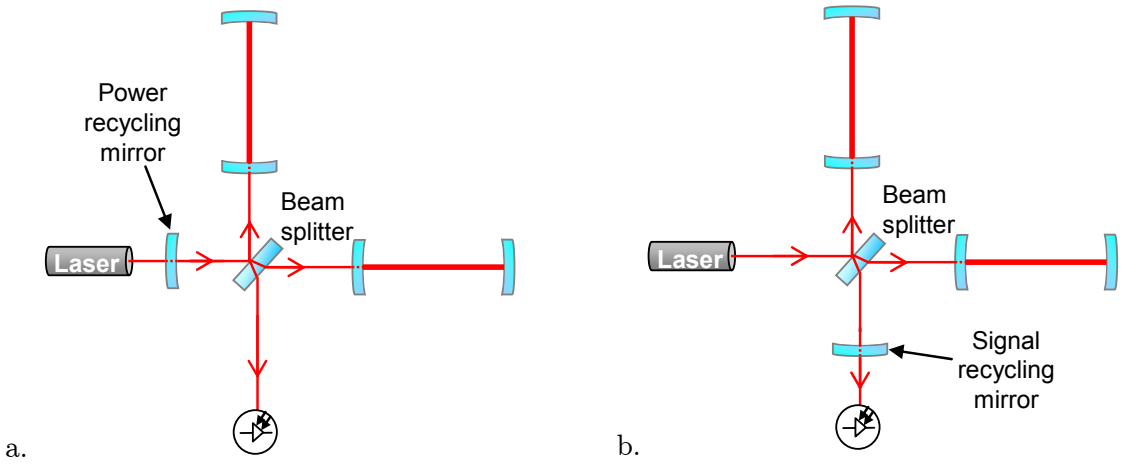

Figure 1.6a. Michelson interferometer with Fabry-Perot arm cavities and power recycling mirror at the input of the interferometer b. Michelson interferometer with Fabry-Perot arm cavities and signal recycling mirror at the output of the interferometer

This mirror and the interferometer act as a resonant cavity allowing an additional build up of power within the interferometer, allowing additional sensitivity to be gained.

Signal recycling operates in a similar manner, by reflecting output light back into the interferometer using a partly reflecting mirror. Since the interferometer is typically run in a state of destructive interference, any passage of a wave results in light produced at the output. Signal recycling forms a cavity between the interferometer and the signal recycling mirror similar to power recycling. Altering the position of this mirror allows tuning of the frequency at which the interferometer is most sensitive [44] [45].

1.5 Interferometric Detector Noise Sources

Bounds are placed on the sensitivity of gravitational wave detectors by a variety of noise sources, each of which contributes to the total noise over the band of frequencies where sources are hoped to be observed, and contribute different relative amounts at different frequencies. The following section will discuss the nature of these noise contributors and how to restrict their impact on detector sensitivity.

1.5.1 Quantum Noise – Photon Shot Noise

In order to detect a phase change in the output signal of an interferometer, and therefore detect a signal induced by passage of a gravitational wave, the interferometer must be held ('locked') at a particular interference condition, with any change in this condition giving an observed output signal. This condition, or 'interference fringe pattern' could be chosen at any point on the fringe, however it is desirable to choose a condition where any observed signal is maximised and noise minimised (namely a high signal to noise ratio is attained).

The greatest signal is achieved by locking the interferometer to a point half way up a fringe, where the fringe gradient is steepest and therefore the signal change is greatest for a given differential arm length change. Locking is achieved by actively feeding back to transducers which adjust the position of one of the test mass mirrors, using the changing interferometer output signal as observed by a photodiode. Analysis of this feedback signal, which contains the information on deviation of test mass position is therefore used to search for incoming gravitational wave signals.

However, the ideal condition for minimising the noise in this signal and achieving a maximal signal to noise ratio is at, or near to a dark fringe (where the output light is minimised and hence the noise is also minimised) [46].

Noise occurs due to statistical variations in the number of photons detected in a given time of observation. Assuming that the number of observed photons N in a time t follows Poisson counting statistics then the uncertainty in the number of photons will be $\sqrt{N}$. The photon shot noise sensitivity limit can be given by [47] [2]:

$$h_{\text{shot}}(f) \approx \frac{1}{L}\left(\frac{\lambda\hbar c}{2\pi P_{\text{in}}}\right)^{\frac{1}{2}} \quad \text{Hz}^{-\frac{1}{2}} \tag{1.7}$$

where λ is the laser light wavelength, c is the speed of light, $\hbar$ is the reduced Planck's constant ($\frac{h}{2\pi}$), L is the interferometer arm length, and P_{in} is the input laser power. For a simple Michelson interferometer arm length 4 km, the required input power to attain a strain sensitivity of 10^{-22}, with laser wavelength of 1 μm, is some 31 kW.

Achieving such power is a challenging experimental prospect with laser powers of several hundred watts currently being researched, however the effective input optical power can be significantly boosted by use of advanced techniques such as the Fabry-Perot arm cavities discussed in section 1.4.2.2 and power recycling described in section 1.4.2.3.

1.5.2 Quantum Noise – Radiation Pressure

Whilst shot noise can be successfully reduced by increasing the circulating laser power; another noise source known as '*radiation pressure noise*' is amplified by doing this. Radiation pressure can be considered to arise from fluctuations in the number of photons being reflected from the test mass mirrors. This reflection results in a force being applied to the test mass mirror that occurs since the photons impart momentum to the mirror, and if the number of photons striking the mirror fluctuates, so does the resulting force. The fluctuation can be considered to occur due to the statistical uncertainty in the way the beam splitter divides the input laser beam and therefore the statistical uncertainty in the number of photons in each arm of the interferometer [46]. However, a second more accurate explanation was given by Caves [48] in terms of the vacuum (zero-point) fluctuations in the electromagnetic field. Suppose some light enters the interferometer from the output port. If the light has the correct phase to increase

intensity in one arm it will decrease the intensity in the other arm, therefore giving anti-correlated variations in each arm. Whilst there is no actual source of light at the interferometer output, vacuum (zero-point) fluctuations from this direction cause such variations in the intensity in the arms, causing a fluctuating force on the mirrors. For a simple interferometer the radiation pressure noise can be expressed [2]:

$$h_{\mathrm{rp}}(f)=\frac{1}{mf^{2}L}\left(\frac{\hbar P_{\mathrm{in}}}{2\pi^{3}c\lambda}\right)^{\frac{1}{2}} \quad \mathrm{Hz}^{-\frac{1}{2}} \tag{1.8}$$

where P_{in} is the input laser power, m is the mass of the mirror, L is the interferometer arm length, c is the speed of light and λ is the wavelength of the laser light.

1.5.3 Standard Quantum Limit

Photon shot noise and radiation pressure noise are both related to the quantum nature of light, but their statistics are independent, and therefore we can express their effects as one single 'optical readout noise' given by the quadrature sum:

$$h_{\mathrm{o.r.n.}}(f)=\sqrt{h_{\mathrm{shot}}^{2}(f)+h_{\mathrm{rp}}^{2}(f)} \tag{1.9}$$

Given that the both components of this depend on the value of the input laser power P_{in} with opposite scaling, the optimum laser power to use, P_{opt} occurs when $h_{\mathrm{shot}}(f)=h_{\mathrm{rp}}(f)$ [2]. Equating expressions (1.7) and (1.8) gives:

$$P_{\mathrm{opt}}=\pi c\lambda mf^{2} \tag{1.10}$$

and in equation (1.9) this gives the '*Standard Quantum Limit*':

$$h_{\mathrm{SQL}}(f)=\frac{1}{\pi fL}\left(\frac{\hbar}{m}\right)^{\frac{1}{2}} \tag{1.11}$$

This sets a limit at to the minimum displacement that can be measured at a certain frequency using a simple interferometer.

It is possible to reach the standard quantum limit over small frequency band by "squeezing the vacuum field" [49] [50], and it is possible to reduce the observed noise below the standard quantum limit in this way, as postulated by Braginsky [51] [52].

1.5.4 Seismic Noise

Seismic noise results from ground vibrations in the vicinity, or far from the detector, which spuriously perturb the mirrors. This type of noise can originate from man made sources including vibrations from nearby traffic, railways or earthworks. Also, natural occurrences such as the effect of waves striking continental shelves also generate seismic noise in a detector. The specific seismic noise experienced in a detector depends on its location, and for seismically quiet locations on the earth's surface, seismic noise in all three directions at a frequency f can approximately be given by $\frac{10^{-7}}{f^2}\,\mathrm{m\,Hz^{-\frac{1}{2}}}$ [2]. If the disturbance to a test mass is to be less than $3\times10^{-20}\,\mathrm{m\,Hz^{-\frac{1}{2}}}$ at 30 Hz then the reduction in horizontal seismic noise required is greater than a factor of 10^9 [53].

Seismic isolation is therefore very important in reducing this noise source. Both vertical and horizontal motion must be attenuated as vertical motion can couple into horizontal motion and therefore interferometer noise. Horizontal isolation can be accomplished by hanging the mirror as a pendulum. The pendulum acts as a low pass filter, and the transfer function of a simple pendulum is given by [2]:

$$\frac{x_{\mathrm{mass}}}{x_{\mathrm{clamp}}} = \frac{{f_o}^2}{{f_o}^2 - f^2} \tag{1.12}$$

where x_{mass} is the displacement of the mass at the end of the pendulum, x_{clamp} is the displacement of the pendulum clamping point, f_o is the resonant frequency of the pendulum and f is the frequency of the ground motion. It can be seen that for ground motions with $f >> f_o$ the attenuation is approximately:

$$\frac{x_{\text{mass}}}{x_{\text{clamp}}} \approx \frac{{f_o}^2}{f^2} \tag{1.13}$$

At such frequencies the inertia of the mass means that the horizontal seismic motion transmitted to the mass is small in the time before the force changes direction.

For frequencies $f << f_o$ the transfer function approximates to:

$$\frac{x_{\text{mass}}}{x_{\text{clamp}}} = \frac{{f_o}^2}{{f_o}^2} \approx 1 \tag{1.14}$$

In this case the frequency is low enough that the pendulum acts like a rigid system, transferring all the clamp motion to the mass.

The transfer function for a 1 Hz pendulum is shown in Figure 1.7. The transfer function is bounded at the pendulum resonance f_o by damping from internal friction, and internal friction will be discussed in chapter 2.

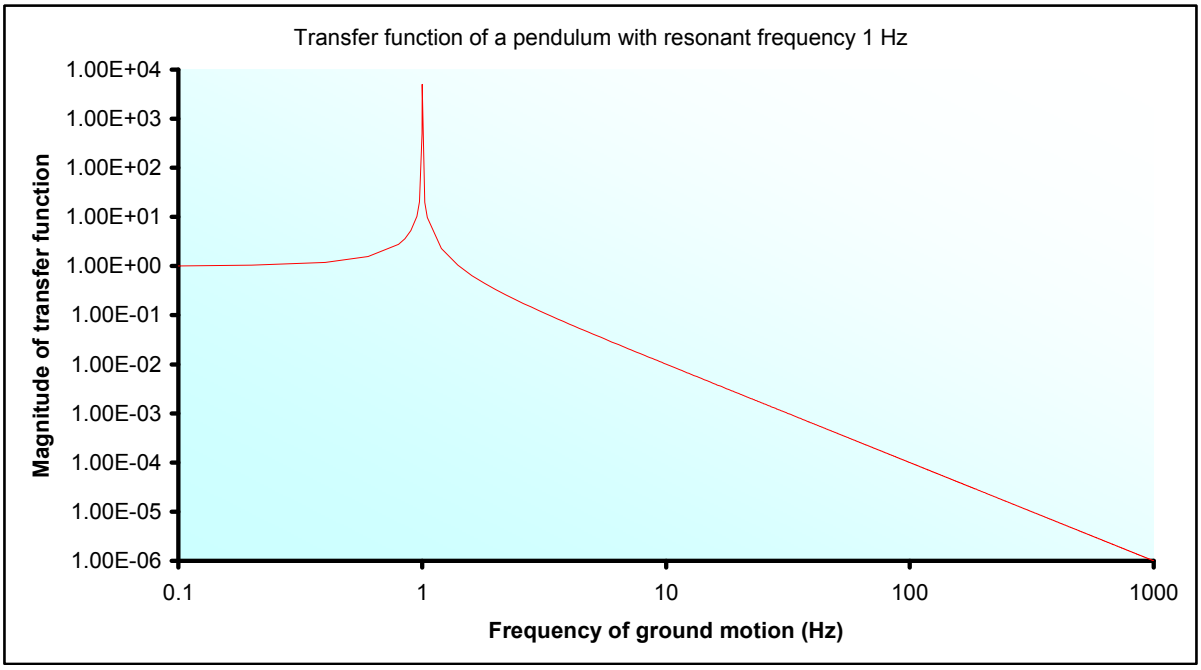

Figure 1.7 Transfer function of a 1 Hz pendulum

The attenuation that a pendulum provides well above its resonant frequency can be further boosted by using a multiple pendulum system, with the transfer function of a multiple pendulum system of N pendulums being given by [2]:

$$\frac{x_{\text{mass}}}{x_{\text{clamp}}} \approx \left(\frac{f_o^{\,2}}{f^2} \right)^N \tag{1.15}$$

Therefore to attenuate as much horizontal seismic motion as possible it is desirable to use multiple stage pendulums with low resonant frequencies to suspend gravitational wave detector mirrors.

Additional vertical isolation is required as some coupling of vertical motion into horizontal motion does occur (of the order of 10^{-3} [54]) due to the way the pendulum must hang under gravity. So a laser beam can be passed between two mirrors over several kilometres, the mirrors cannot be orientated parallel to the local vertical (which will be discussed in section 2.8.2.4 of the following chapter of this thesis) – this occurs

due to the curvature of the earth which causes the local verticals at two separated locations to be non-parallel. This results in coupling of vertical motion to horizontal motion. Vertical isolation can be achieved using cantilever springs to hang the pendulums from [55].

1.5.5 Gravity Gradient Noise

Random gravitational fluctuations in the vicinity of any ground based interferometric gravitational wave detector place limits on the sensitivity of detectors at low frequencies. This is known as gravity gradient noise [56] [57]. Fluctuations can occur due to changes in the distribution of matter in the proximity of the interferometer, and can also occur due to such instances as seismic waves in the ground near the test masses or vehicles passing close by. Seismic isolation cannot help in attenuating this source of noise.

This source of noise will limit the sensitivity of future gravitational wave detectors below around 10 - 15 Hz. A possible route to reduction of this type of noise is to build the detector underground where gravitational fluctuations are reduced, or alternatively build a detector in space where gravity gradients are minimal.

1.5.6 Thermal Noise

1.5.6.1 Brownian Thermal Noise

Thermal noise results from the thermally excited motion of the constituent atoms that make up the interferometer mirror suspensions. Equipartition of energy dictates that each degree of freedom of the atoms and molecules that make up the system has $^1/_2 k_B T$ of energy, where k_B is Boltzmann's constant, and T is the temperature. This random motion couples into excitation of resonant modes of the system, and this motion contributes to the displacement noise in the mirrors within the interferometer.

Thermal noise is one of the most important noise sources at low frequencies in current detectors, and research is focussed on reducing its effect. This thesis contains research on improving the thermal noise contribution of a number of components of the mirror suspensions, and as will be shown in detail in Chapter 2, the thermal noise can be reduced by use of low *mechanical loss* materials, and intelligent design to minimise its effects.

1.5.6.2 Thermorefractive Noise and Thermoelastic Noise

Bodies experience localised statistical temperature fluctuations throughout their volume, and this causes fluctuations in the refractive index of the material. This can affect both the mirror and beamsplitter substrates (of chosen materials that will be discussed in section 2.9) and mirror optical coatings (which will be discussed in Chapter 5). This fluctuation in the material properties (and hence the optical path length being changed) will result in a phase change in the light traversing or reflected from the beamsplitter and mirrors. This fluctuation in phase of the resulting signal is known as thermorefractive noise [58].

Braginsky showed in 2000 [58] that thermorefractive noise is a significant source of noise to be considered in advanced detectors that will seek very high sensitivities, and current gravitational wave detectors have thermorefractive noise that is typically of the order of 10^{-22} to 5×10^{-23} [59].

Thermoelastic noise is another form of noise that results from temperature fluctuations throughout a body. These variations in temperature result in mechanical displacement noise through the coefficient of thermal expansion of the material. Thermoelastic noise will be discussed further in Chapter 2.

1.5.7 Noise Spectra

A typical theoretical sensitivity curve is shown in Figure 1.8, showing the contributions of the various noise sources within an interferometric detector [60].

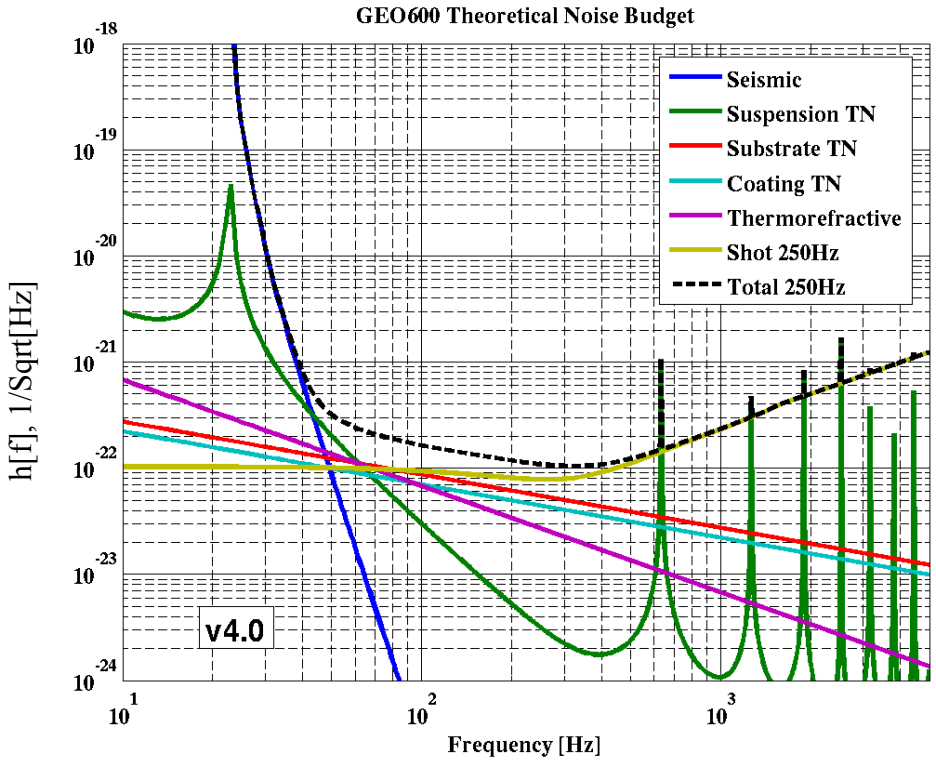

Figure 1.8 Theoretical sensitivity and noise sources for the GEO600 interferometric gravitational wave detector (described in the coming section), tuned to 250Hz, showing the contributions of the various noise sources. Noise sources marked "TN" are thermal noise sources, which will be discussed further in Chapter 2.

It can be seen that the best sensitivity can be achieved at mid-band frequencies, with seismic noise placing a steep limit at lower frequencies and photon shot noise reducing sensitivity at higher frequencies.

1.6 Operational Interferometric Detectors

Currently there are several ground based interferometric gravitational wave detectors operating around the world. The technology used in these instruments has been developed from early test prototypes which included a 3 m delay line prototype and a 30 m instrument at the Max-Planck-Institute for Astrophysics in Germany [61] [62], a

10 m arm length interferometer with Fabry-Perot arm cavities in Glasgow [63], and a 40 m prototype at Caltech [64].

1.6.1 LIGO Detector Network

The LIGO (Laser Interferometer Gravitational-wave Observatory) detector network comprises 3 detectors at two independent widely separated sites. Two interferometers sharing the same infrastructure (one of 4 km arm length, the other of 2 km arm length) are located in Hanford, Washington; and a third 4 km detector is located in Livingston, Louisiana (Figure 1.9).

Figure 1.9 LIGO 4km arm length detectors at Hanford, Washington (left) and Livingston, Louisiana (right). The Hanford instrument shares its infrastructure with a smaller with a 2km interferometer.

The LIGO instruments use Fabry-Perot arm cavities, with end test mass mirrors suspended on single wire pendulums. The LIGO mirror suspensions will be further discussed in Chapter 3.

The LIGO network has now undertaken 5 data taking science runs since 2002, with the most recent year long run being concluded in November 2007. These runs were undertaken in collaboration with the GEO600 detector, and the Japanese TAMA300 detector joined in the third and fourth runs, to permit the confirmation of any signal received via coincident detections. Results of the fourth and fifth science runs are now being analysed.

With each run the interferometers have had their sensitivities improved as noise sources have been identified, and during the 5th run the LIGO sensitivity reached its design goal over most of the frequency band, as shown in Figure 1.10 [65].

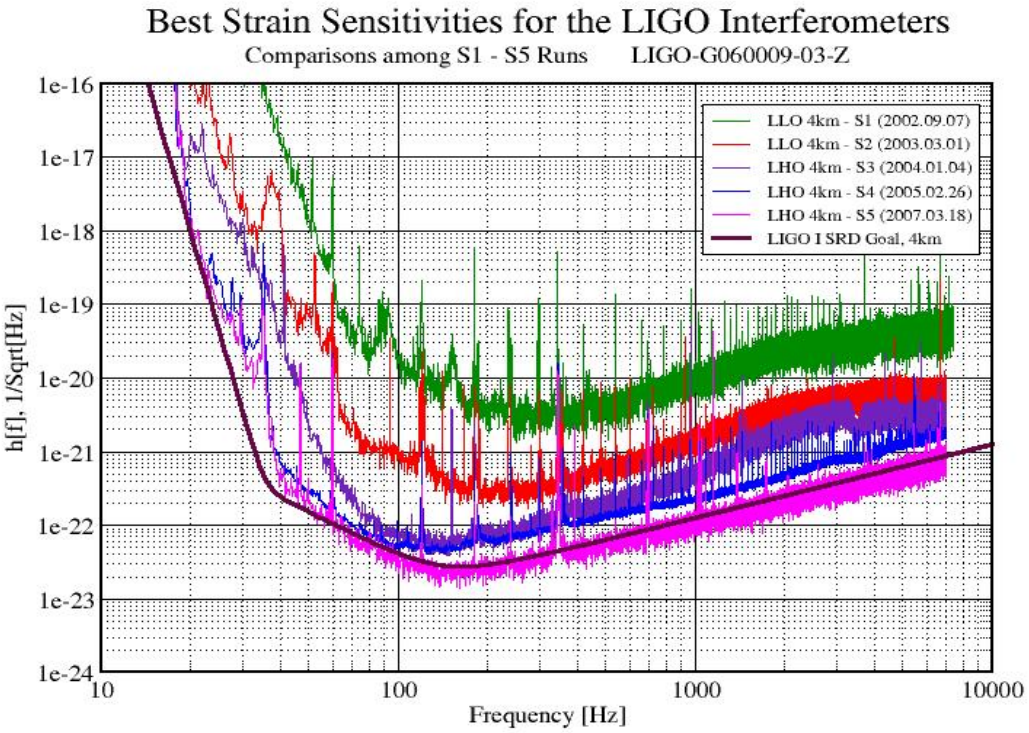

Figure 1.10 Strain sensitivities of LIGO detectors at Hanford (LHO) and Livingston (LLO) during the first 5 data taking runs

1.6.2 GEO600

The GEO600 detector [66] has been developed in a collaborative effort between the UK and German groups. The detector is located in Ruthe, near Hannover and uses 600 m long arms with the interferometer configured as a delay line giving an effective arm length of 1.2 km. GEO600 employs more advanced techniques like power and signal recycling to increase interferometer sensitivity. Advanced low mechanical loss silica suspensions have been employed to reduce the effects of thermal noise. This technology will be discussed in Chapter 3.

Figure 1.11 Aerial view of the GEO600 detector with 600 m long perpendicular arms, at Ruthe, Germany

GEO600 has also now completed 5 data taking runs in collaboration with the LIGO instruments [67], and similar to LIGO the sensitivity has progressively been improved as shown in Figure 1.12 [59].

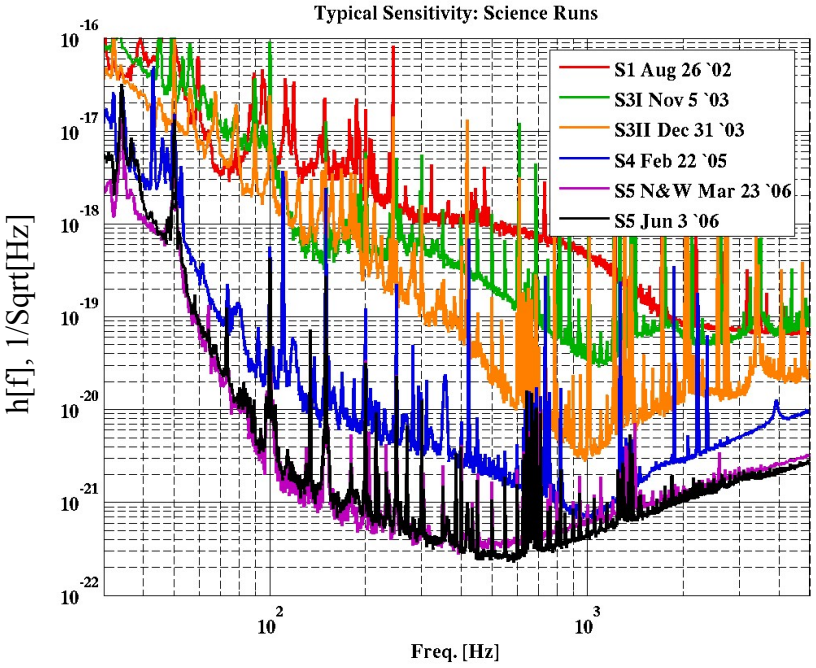

Figure 1.12 Strain sensitivities of GEO600 detector during the first 5 data taking runs

1.6.3 VIRGO

A more recent addition to the group of operational interferometers is the 3 km arm length European VIRGO detector located in Cascina, Italy [68] [69]. This instrument has been constructed as part of a joint collaboration between French and Italian groups. VIRGO is unique as it employs sophisticated 7 stage superattenuating pendulums to hang the test mass mirrors. This method aims to reduce the effects of seismic noise giving improved sensitivity down to 10 Hz [70].

Figure 1.13 VIRGO detector, Cascina, Italy

VIRGO has completed commissioning [71] and has undertaken one data taking run, collaborating with the bar detectors AURIGA, Explorer and Nautilus [34]. This also overlapped the fifth LIGO/GEO600 science run. The sensitivity during this science run is shown in Figure 1.14 [72].

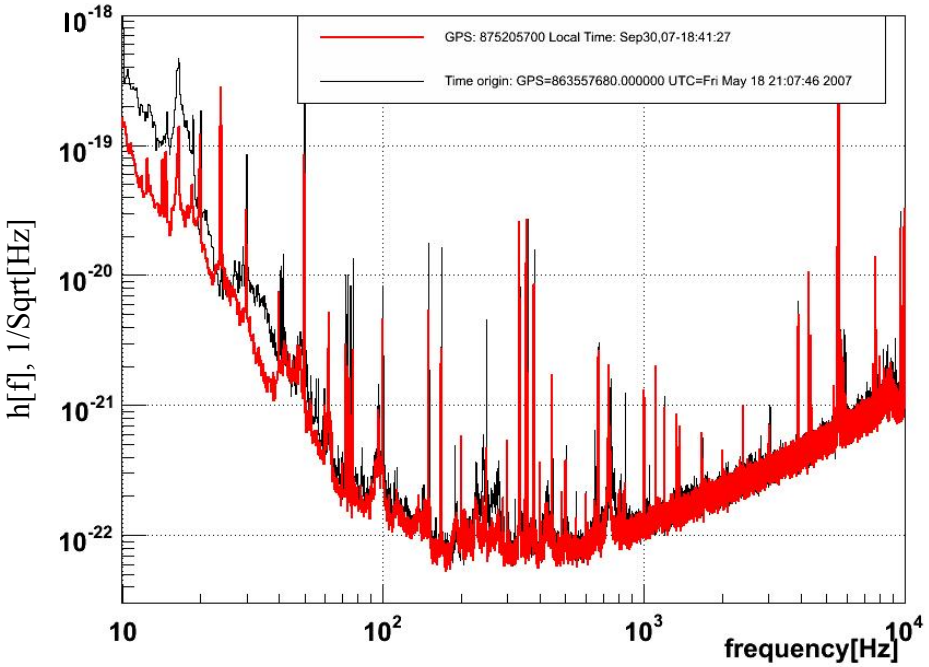

Figure 1.14 Sensitivity of VIRGO during the first data taking run, October 2007.

1.6.4 TAMA300

TAMA300 [73] [74] [75] is a Japanese detector with short 300 m arm length, operational in Tokyo. TAMA uses Fabry Perot arm cavities similar to LIGO and also employs power recycling. The aim of the TAMA project is to develop advanced techniques that may be employed in future detectors.

1.7 Second Generation interferometric gravitational wave detectors

With many of the current detectors running close to their design sensitivities, research is now focussed on upgrades to improve sensitivity. These improvements should lead to a factor of 10 - 15 enhancement in sensitivity and thus will increase the number of potentially detectable sources observable by the current instruments.

1.7.1 Enhanced and Advanced LIGO

With the LIGO detectors having now completed the fifth data taking science run, focus has moved to upgrades to the initial LIGO setup. These will take place in two stages, with the first upgrade called "Enhanced LIGO" now being undertaken. Changes that will be implemented in this upgrade will include increasing the laser power from 10 W to 35 W, which will give reduction in photon shot noise, and improved interferometer output sensing will be implemented together with reduction of noise from environment by placing all sensors in vacuum.

This enhancement is scheduled for completion by the end of 2008, and will provide an initial testbed for some of the advanced technology to be utilised in the future upgrade commencing in 2010 - "Advanced LIGO", a second generation detector network.

Advanced LIGO will extend the modifications implemented in Enhanced LIGO, aiming to reduce noise by a factor of 10 - 15 over the initial LIGO interferometers (increasing the number of detectable sources by more than 1000). A further increase of laser power to 180 W [76] will be implemented, as well as employment of signal recycling as used in GEO600.

Mirror and suspension thermal noise reduction will be achieved by advanced mirror suspension techniques pioneered in the GEO600 detector. Chapters 3 and 4 of this thesis detail research undertaken by the author in relation to suspensions for Advanced LIGO. Significant improvement is required in the seismic isolation of the mirror suspensions, with a reduction by over ten orders of magnitude to take advantage of reduced thermal noise [77].

1.7.2 GEO-HF

GEO600 will be used to maintain an "Astrowatch" vigil, remaining operational whilst the two 4 km LIGO instruments are upgraded to "Enhanced" status over the coming six months. The LIGO Hanford 2 km detector will also run in Astrowatch to complement GEO600 during the upgrade of the 4 km LIGO instruments.

Upgrading GEO600 to give a sensitivity similar to that envisaged for Advanced LIGO is not feasible using the current arm lengths, and increasing the arm lengths is also not possible. Therefore, future upgrading of GEO600 will look to focus on improving and tuning for optimal sensitivity at higher frequencies to complement Advanced LIGO, in what is known as the GEO-HF project [78].

Improvements that may be implemented include increased input laser power, use of squeezed light, and use of lower thermal noise optical mirror coatings [78], as will be discussed in Chapter 5.

1.7.3 Advanced VIRGO

VIRGO will also undergo a two stage upgrade process, similar to LIGO. The first upgrade is VIRGO+ and this will adopt increased laser power. This upgrade may also look to change the main test mass mirror suspensions to monolithic fused silica suspensions as used in GEO600 and envisaged for Advanced LIGO.

A second upgrade to "Advanced VIRGO" will follow afterwards, which will use monolithic suspensions, increased laser power, and lower thermal noise mirror coatings [79]. Advanced VIRGO aims to be operational on a similar timescale to Advanced LIGO [79].

1.8 Third Generation Interferometric Gravitational Wave Detectors

In the future even higher signal to noise ratios will be sought to allow more extensive determination of the astrophysical parameters associated with gravitational wave emission. However, further improvement of sensitivity will present even more experimentally challenging prospect.

Continued reduction of mirror thermal noise by improving material properties may prove impossible, and cryogenically cooled mirrors may be required to allow improvement in this area. Increasing laser powers will reduce shot noise, but this will lead to increased mirror heating, and thermal distortions which may prove difficult to control. Use of non-transmissive optical components may prove necessary, and chapter 6 of this thesis details work on the thermal noise that may occur from such components.

A design study into one such detector called the "Einstein Telescope" is being funded by the European EC 7th Framework Programme award [80]. This aims to investigate the reduction of relevant noise sources by at least another order of magnitude.

1.9 Space Based Detectors

Gravity gradient noise places limits on the sensitivities attainable at very low frequencies, ruling out the possibility of observing sources such as massive black hole mergers or creation, which for objects of mass 10^3 - 10^4 M_Θ will lie in the range of 10^{-4} to 10^{-1} Hz.

Flying an interferometer in space would allow escape from gravity gradient noise [81]. NASA/ESA are developing an interferometer system called LISA (Laser Interferometer Space Antenna) to do this [82] [83]. It will consist of 3 spacecraft located at the vertices of an equilateral triangle with side length 5 x 10^6 km. The spacecraft constellation will

fly in an orbit which would lag the Earth by approximately 20°, as shown in Figure 1.15a.

a. 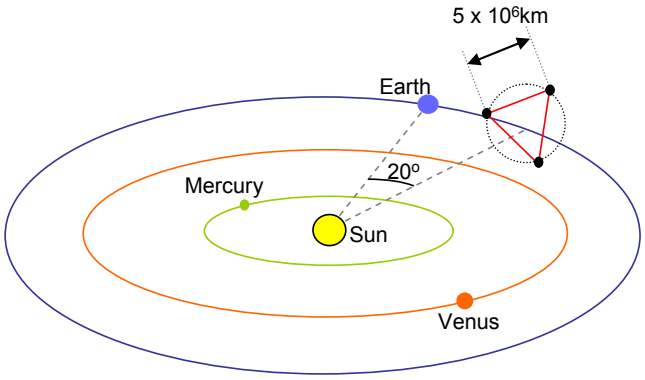

b. 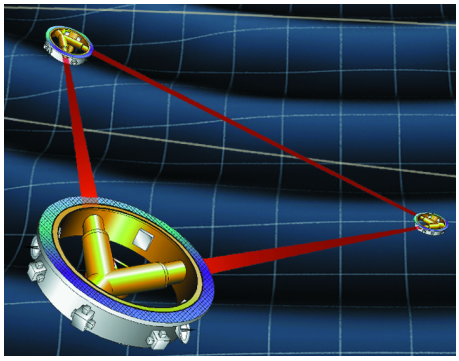

Figure 1.15a. Orbit of the three LISA spacecraft b. Artist's impression of the three LISA spacecraft

The spacecraft will each contain 2 freely floating test masses that will form the end mirrors of 3 interferometers of arm length 5 x 10^6 km.

Currently launch of a technology demonstrator mission "LISA Pathfinder" is scheduled for 2010, with launch of the full mission being envisaged for 2018.

1.10 Conclusions

A variety of gravitational wave detectors are now operational around the world, with both bar detectors and long baseline interferometric detectors having undertaken several data taking science runs. Currently no signals have been observed, but analysis of the most recently acquired data is still ongoing.

In order to guarantee the detection of gravitational wave signals, and open up the field of gravitational wave astronomy as a new way of looking at astronomical events, detectors of higher sensitivity are required. Suitably lowering of the various noise sources is however a significant experimental challenge. The remainder of this thesis focuses on the reduction of one aspect of the limiting noise – thermal noise, through monolithic suspension technology which will be discussed in Chapters 3 and 4, and

improved optical mirror coatings, detailed in Chapter 5. Chapter 6 will examine the thermal noise characteristics of non-transmissive optical components, which may be employed in third generation detectors to reduce the problems of thermal deformations of transmissive mirrors.

Chapter 2

Thermal Displacement Noise

2.1 Introduction

One area of current research to improve the sensitivity of gravitational wave detectors is the reduction of thermal displacement noise. Thermal noise is a by-product of atomic vibrations in the lattice structure of the mirror suspensions, and the mirrors themselves – the suspensions have many resonant modes of oscillation, and the mirrors have many rigid body resonant modes. It is within these resonant modes in which the thermal vibration energy can reside.

The resonant modes of the system can be modelled as classical harmonic oscillators, and hence the Equipartition Theorem decrees that each quadratic term, or *degree of freedom* that appears in the energy will have average energy of $^1/_2 k_B T$. When considering harmonic oscillators, both kinetic and potential energies contain such quadratic terms, and hence the energy for each mode will be $k_B T$. This is contained in thermal vibration energy of the atomic structure. In systems with multiple resonant modes, such as mirror suspensions, the energies for all modes will combine giving a net thermal motion of the front face of the mirror test masses. As will be shown, this

macroscopic motion of the mechanical system also leads to displacement noise at frequencies off resonance, and is therefore an important consideration over the entire range of detector frequencies. Its importance is paramount in the mid-band frequencies in the range 10 to 500 Hz, where it is currently a dominant noise source.

It may seem intuitive that reduction in thermal displacement noise can be achieved by simply reducing the thermal energy contained in the interferometer mirrors and suspensions via temperature reduction. This is indeed possible, and the principle of reducing the thermal energy in this way has already been implemented in cryogenic resonant bar detectors like MiniGRAIL [32] [31]. However, cryogenics need considerable additional infrastructure that may give a potential increase in coupling of environmental noise into the interferometer. Also, the high circulating laser powers (necessary to reduce photon shot noise) would result in deposition of thermal energy in the mirrors, making cooling them a more technically demanding proposition. Therefore, research is currently focussed on lessening mirror suspension thermal noise by clever design, and we will see that use of materials with a low *mechanical loss factor*, ϕ, is important for the reduction of thermal noise across the detection frequency band.

2.2 Brownian Motion

"Brownian" motion derives its name from the botanist Robert Brown. In 1827 Brown observed random motion of pollen grains suspended in water, and also observed this motion in trajectories of non-organic dust and mineral particles [84]. Brown could not provide a clear explanation for the observed motion, but did infer that he believed it was linked to the particles themselves. Hindsight reveals that Brown was close to discovering a link to thermal energy and temperature – and viewed samples that had been heated, but were subsequently quenched prior to observation. Mathematical models that describe this motion, developed later, are the same as those that can be

used to describe the atomic thermal motion in solid bodies, and therefore thermal noise is also often known as "Brownian" thermal noise.

True physical explanation of Brown's discovery was not forthcoming until Einstein used the molecular-kinetic theory of heat to predict the motion that Brown (and subsequently others) had observed, showing that random Brownian motion resulted from fluctuation in the number of collisions experienced by the pollen grains with the *thermally driven* water molecules [85] [86].

2.3 Einstein and Dissipation

Einstein's also realised that the random thermal driving force that caused Brownian motion would also exert a resistive drag on any particle that was moved through the liquid. This results in energy dissipation by the particle. This was an early demonstration of what was later to be formalised as the "Fluctuation-dissipation theorem" [87] [88]. It states that for any linear system in thermal equilibrium there is a relationship between the fluctuation in the system and the dissipation.

The theorem relates the power spectral density, $S_F(\omega)$, of the thermal driving force, to the real part of the mechanical impedance (the dissipation) of the system:

$$S_F(\omega) = \overline{F}^2_{\text{thermal}}(\omega) = 4k_B T\,\Re(Z(\omega)) \tag{2.1}$$

The mechanical impedance is defined:

$$Z = \frac{F}{v} \tag{2.2}$$

where v is the velocity response of the system resulting from an applied force F. The power spectral density of the displacement is:

$$S_x(\omega) = \overline{x^2}_{\text{thermal}}(\omega) = \frac{4k_B T}{\omega^2}\Re\left(\frac{1}{Z(\omega)}\right) \tag{2.3}$$

In the detector mirrors and suspensions, dissipation is seen as damping in the system. The fluctuation dissipation theorem is valuable in allowing us to relate the damping to the thermal driving force, and ultimately to the resulting displacement noise observed in a detector, and this will be demonstrated later in this chapter.

It is informative to first consider some of the forms of damping that can exist in a detector suspension.

2.4 Forms of Damping

Damping in suspensions can be classified into two forms – external and internal.

2.4.1 External Damping

- Gas damping results where impacts of gas molecules with the suspension elements give rise to viscous damping. The impacts, similar to Brownian motion result in a frictional dissipation.

- Thermal energy from the motion of the suspension elements can be dissipated as recoil energy into the structure that supports the suspension

- Dissipation can arise from friction at the points where the suspension are clamped

- Energy loss in eddy current or hysteresis damping

2.4.2 Internal Damping

With clever design and careful implementation, external damping sources can generally be lowered to a level which is no longer dominant, and hence internal damping becomes

the dominant means of dissipation. Internal friction is a result of the pendulum suspension materials not behaving elastically – namely they do not follow the ideal form of Hooke's law:

$$F = -kx \tag{2.4}$$

where x is the resulting displacement of the system to an applied force F, with spring constant k. This implicitly implies that the application of a force will generate an instantaneous displacement. Any true material will, however demonstrate *anelasticity*, namely a delay in response to the application of any external force.

One can imagine this if we model the system as an array of springs and a dashpot as shown in Figure 2.1.

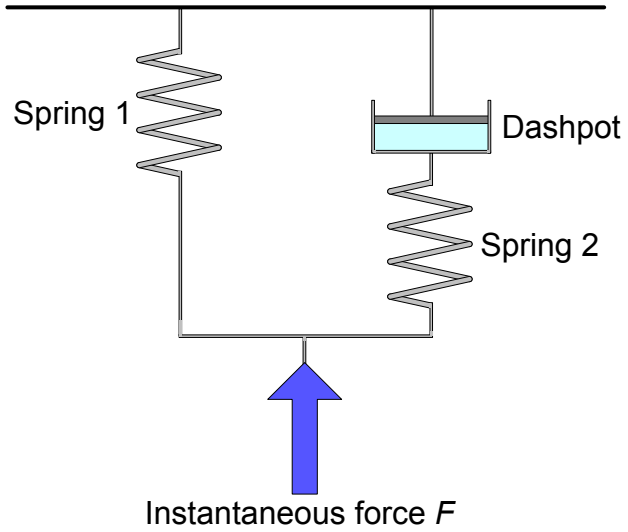

Figure 2.1 Simple representation of an anelastic material, with a single relaxation process.

If an instantaneous force F is applied, both springs will compress and the dashpot does not move. Over a certain period after the application of the force the second spring will relax moving the dashpot. In real materials this relaxation occurs due to the inability of the internal degrees of freedom to adjust instantaneously to a new state. The relaxation often follows the Arrhenius law with an exponential relaxation given by:

$$\tau_\tau = \tau_a e^{-\frac{\Delta E}{k_B T}} \tag{2.5}$$

where τ_τ is the characteristic relaxation time, ΔE is the potential energy barrier that needs to be traversed to move to the new state and τ_a is the characteristic time between barrier crossing attempts [2].

To model anelastic materials we must include the phase lag of the system response, and this can be achieved by using Hooke's law in complex form [89]:

$$F_{\text{spring}}(\omega) = -k(1 + i\phi(\omega))x \tag{2.6}$$

where $\phi(\omega)$ is the known as the *mechanical loss* of the material, and represents the phase angle in radians that the strain response lags behind the driving force. The mechanical loss can be considered as the degree of anelasticity of the spring, and is a very important property when considering thermal noise. For a thermal driving force $F_{\text{thermal}}(\omega)$ the differential equation of motion for a system with internal friction is:

$$m\ddot{x} = F_{\text{thermal}}(\omega) - k(1 + i\phi(\omega))x \tag{2.7}$$

Solutions take the form $x = x_o e^{i\omega t}$, meaning $\dot{x} = i\omega x$ and $\ddot{x} = -\omega^2 x$. Therefore it can be shown that:

$$i\omega m\dot{x} = F_{\text{thermal}}(\omega) + \frac{ik\dot{x}}{\omega}(1 + i\phi(\omega))$$

$$\Rightarrow \quad F_{\text{thermal}}(\omega) = i\omega m\dot{x} - \frac{ik\dot{x}}{\omega}(1 + i\phi(\omega))$$

$$\Rightarrow Z = \frac{F_{\text{thermal}}(\omega)}{\dot{x}} = i\omega m - \frac{ik}{\omega}(1 + i\phi(\omega)) = i\left(\omega m - \frac{k}{\omega}\right) + \frac{k\phi(\omega)}{\omega} \tag{2.8}$$

$$\frac{1}{Z} = \frac{k\omega\phi(\omega) - i\left(\omega^3 m - k\omega\right)}{\left(\omega^2 m - k\right)^2 + \left(k\phi(\omega)\right)^2} \tag{2.9}$$

The real part of this expression is:

$$\Re\left(\frac{1}{Z}\right) = \frac{k\omega\phi(\omega)}{\left(\omega^2 m - k\right)^2 + \left(k\phi(\omega)\right)^2} \tag{2.10}$$

which allows the fluctuation-dissipation theorem to be written:

$$S_x(\omega) = \overline{x^2}_{\text{thermal}}(\omega) = \frac{4k_B T}{\omega^2}\left(\frac{k\omega\phi(\omega)}{\left(\omega^2 m - k\right)^2 + \left(k\phi(\omega)\right)^2}\right) \tag{2.11}$$

with $k=\omega_o^2 m$. This leads to an expression for the root mean square thermal displacement:

$$x_{\text{rms}}(\omega) = \sqrt{\overline{x^2}_{\text{thermal}}(\omega)} = 2\sqrt{\frac{k_B T}{\omega m}\left(\frac{\omega_o^2\phi(\omega)}{\omega_o^4\phi^2(\omega) + \left(\omega_o^2 - \omega^2\right)^2}\right)} \tag{2.12}$$

It is clear that the mechanical loss factor $\phi(\omega)$ is very important in determining the displacement noise that will occur in a detector. However, direct measurement of displacement noise at arbitrary frequency is not easy as the magnitude of the noise is usually much smaller than any experimental noise floor, and therefore finding an experimental setup which has low enough noise is challenging. A less experimentally challenging method of determining the mechanical loss of a system is to measure the quality factor, Q, of resonances of the system.

The quality factor is defined [90]:

$$Q(\omega_o) = \frac{2\pi E_{\text{stored}}}{E_{\text{lost per cycle}}} \tag{2.13}$$

Q can also be usefully defined by [90]:

$$Q(\omega_o) = \frac{m\omega_o}{b} \tag{2.14}$$

where b is the damping coefficient of the system. This coefficient is the real (dissipative) part of the mechanical impedance, Z, which at resonant frequency is given by $\frac{k\phi(\omega_o)}{\omega_o}$ from equation (2.8). With $k=\omega_o^2 m$ it follows immediately that:

$$Q(\omega_o) = \frac{1}{\phi(\omega_o)} \tag{2.15}$$

This is important, as measurement of Q can be more readily achieved in a laboratory setting.

Equation (2.15) only describes the mechanical loss of a system at resonant frequencies of the system, and does not imply the behaviour of the mechanical loss off resonance, so therefore it is important to consider the form ϕ takes through the full frequency spectrum.

2.5 Mechanical Loss Factor ϕ

There are two possible forms that the mechanical loss factor can take – either frequency dependent or, frequency independent.

Frictional dissipation is commonly modelled by a velocity proportional damping force:

$$F_{\text{friction}} = -b\dot{x} \tag{2.16}$$

Damping in this manner is known as *viscous* damping.

The imaginary part of equation (2.6) is the dissipative part, and this can be expressed as:

$$\Rightarrow \Im\left(F_{\text{spring}}(\omega)\right) = -ik\phi(\omega)x = F_{\text{friction}} = -b\dot{x} \tag{2.17}$$

With $\dot{x} = i\omega x$, with and $A = \frac{b}{k}$ the mechanical loss can be seen to have a linear frequency dependence.

$$\phi(\omega) = A\omega \tag{2.18}$$

However, experimental evidence [91] suggests that this is not a realistic model for many materials, and that a frequency independent ("structural" damping) model is more often appropriate. In this model it is believed that each loss mechanism has its own resonant loss peak ("Debye peak") at a frequency that characterises the particular loss mechanism and anelastic relaxation process. These loss peaks have a spread of frequencies separated by several orders of magnitude. When examining frequencies far from the loss peaks, the mechanical loss can be considered as effectively constant over the frequency range [92]. The detection band for gravitational waves lies in one of these regions between peaks, as in regions between the peaks the lower loss results in lower thermal noise, permitting increased sensitivity. Losses displaying this frequency invariance have been reported in a variety of solids by Kimball [93].

2.6 Thermoelastic Noise

Another source of dissipation is thermoelastic dissipation, which does show frequency dependence. This dissipation occurs when temperature variations occur in an object give rise to a heat flow. It can affect both thin beam-like objects, as studied by Zener [94], and Nowick and Berry [95], such as the mirror suspension fibres, as well as the test mass mirrors themselves.

2.6.1 Thermoelastic Noise in Suspension Fibres

Consider a moving suspension wire or fibre. When this element bends back and forth one side will expand and the opposite side with compress. The expansion will result in cooling, whilst the consequence of compression is heating, governed by the material's thermal expansion coefficient, $\alpha = \frac{1}{l}\frac{dl}{dT}$. This results in a temperature gradient being introduced across the fibre, and the resulting heat flow that returns the material to thermal equilibrium is energy that is dissipated. This effect is thermoelastic dissipation.

Consider now a wire or fibre at rest. If local temperature variations cause one side of the wire or fibre to be heated or cooled then expansion or contraction will occur, causing bending in the wire. This results in a net displacement of the wire or fibre (which will deflect the test mass suspended on it) and is therefore a source of displacement noise within a detector – thermoelastic noise.

The thermoelastic loss attributable to this process can be expressed as [95] [94]:

$$\phi_{\text{thermoelastic}}(\omega) = \Delta \frac{\omega\tau}{1+\omega^2\tau^2} \tag{2.19}$$

with:

$$\Delta = \frac{Y\alpha^2 T}{\rho C} \tag{2.20}$$

For rectangular cross section wire:

$$\tau = \frac{1}{\pi^2}\frac{\rho C t}{\kappa} \tag{2.21}$$

For circular cross section wire:

$$\tau = \frac{1}{4.32\pi}\frac{\rho C d}{\kappa} \tag{2.22}$$

where Y is the Young's modulus of the material, T is its temperature, τ is the characteristic time for the heat to cross the wire, t is its thickness (if rectangular cross

section), d is the diameter (if circular cross section), C is the specific heat capacity of the material, κ is its thermal conductivity and ρ is its density.

Thermoelastic loss in wires and fibres will be further discussed in Chapter 3.

2.6.2 Thermoelastic Noise in Test Mass Mirrors

Statistical temperature variations throughout a body like a test mass can also result in thermoelastic dissipation – this is relevant for the crystalline materials sapphire and silicon, which are candidate materials for future detector suspensions (these materials will be discussed in section 2.9). Braginsky [96] derived the expression:

$$\bar{x}_{\text{thermoelastic}}(\omega) = \sqrt{\frac{8\alpha^2 \kappa k_B T^2 (1+\sigma)^2}{\sqrt{2\pi}\rho^2 C^2 r_o^3 \omega^2}} \tag{2.23}$$

for the displacement due to thermoelastic noise, where ρ is the material density, σ is Poisson's ratio, κ is the thermal conductivity, r_o is the radius at which the incident laser beam intensity has fallen to $\frac{1}{e}$ of its maximum value.

This is derived for an infinite sized test mass, and a correction factor has been determined for finite sized test masses by Liu and Thorne [97].

2.7 Noise Spectra as a Function of Mechanical Loss

Equation (2.12) shows that the level of thermal displacement noise of the system is dependent on the mechanical loss factor, and the thermal noise also depends on the frequency being considered.

2.7.1 Single Resonance Systems

There are three possible frequency cases that can be considered, when ω_o is the resonant frequency:

- $\omega << \omega_o$
- $\omega = \omega_o$
- $\omega >> \omega_o$

Consider equation (2.12) for the r.m.s. thermal displacement in a single resonance system with $\omega << \omega_o$:

$$x_{\text{rms}}(\omega) = 2\sqrt{\frac{k_B T}{\omega m}\left(\frac{{\omega_o}^2 \phi(\omega)}{{\omega_o}^4 \phi^2(\omega) + \left({\omega_o}^2 - \omega^2\right)^2}\right)}$$

$$\approx 2\sqrt{\frac{k_B T}{\omega m}\left(\frac{{\omega_o}^2 \phi(\omega)}{{\omega_o}^4 \phi^2(\omega) + {\omega_o}^4}\right)}$$

$$= 2\sqrt{\frac{k_B T}{\omega m}\left(\frac{{\omega_o}^2 \phi(\omega)}{{\omega_o}^4 \left(\phi^2(\omega) + 1\right)}\right)}$$

For very low mechanical loss materials $\phi(\omega) << 1$ this reduces to:

$$x_{\text{rms}}(\omega) \approx 2\sqrt{\frac{k_B T}{{\omega_o}^2 m}\left(\frac{\phi(\omega)}{\omega}\right)} \tag{2.24}$$

For $\omega >> \omega_o$:

$$x_{\text{rms}}(\omega) \approx 2\sqrt{\frac{k_B T}{\omega m}\left(\frac{{\omega_o}^2 \phi(\omega)}{{\omega_o}^4 \phi^2(\omega) + \omega^4}\right)} = 2\sqrt{\frac{k_B T}{m}\left(\frac{{\omega_o}^2 \phi(\omega)}{\omega {\omega_o}^4 \phi^2(\omega) + \omega^5}\right)}$$

which reduces for $\phi(\omega) << 1$ to:

$$x_{\text{rms}}(\omega) \approx 2\sqrt{\frac{k_B T}{m}\left(\frac{\omega_o{}^2 \phi(\omega)}{\omega^5}\right)} \tag{2.25}$$

It is therefore clear that to reduce off resonance thermal noise at frequencies both above and below resonance, we must reduce the mechanical loss of the system. Since energy in the system is conserved, and the equipartition theorem decrees that a harmonic system must have $k_B T$ of energy per mode, then if the loss is reduced off resonance (and hence the displacement noise is also reduced), more energy must be contained at resonance – namely the resonant motion will be increased.

Setting $\omega = \omega_o$ in equation (2.12):

$$x_{\text{rms}}(\omega) = 2\sqrt{\frac{k_B T}{\omega_o m}\left(\frac{\omega_o{}^2 \phi(\omega)}{\omega_o{}^4 \phi^2(\omega)}\right)} = 2\sqrt{\frac{k_B T}{m}\left(\frac{1}{\omega_o{}^3 \phi(\omega)}\right)}$$

Therefore, if the mechanical loss factor is reduced to a very low level of $\phi(\omega) << 1$ then it is clear that the motion on resonance is greatly increased.

These are significant results, as they reveal that reduction of the mechanical loss of the system changes the thermal energy distribution, with more of the energy contained in resonant motion of the system. Generally the frequencies of this motion are outwith the gravitational wave detection frequency band of 10 Hz to 500 Hz. Hence, a reduction in mechanical loss of the system will also yield a reduction in thermal displacement noise in the detection band – this noise reduction allows greater sensitivity.

Therefore, detector mirror suspensions use low loss or high Q (as shown by equation (2.15)) materials and suspension systems to achieve a reduction in noise.

2.7.2 Multi-Resonance Systems

Real mirror suspensions are not limited to having single resonances, and therefore the contribution from all the resonances must be considered. Assuming that the resonant frequencies lie above the band of detection, then equation (2.24) can be used in a generalised form for a system with n resonant modes:

$$x_{\text{rms}} \approx \sqrt{\sum_{i=1}^{n} \frac{4k_B T}{\alpha_i m \omega_i^{\,2}} \left(\frac{\phi_i(\omega)}{\omega} \right)} \tag{2.26}$$

where $\phi_i(\omega)$ is the mechanical loss associated with the ith mode, $\alpha_i m$ is the effective mass of the ith mode, with α_i as an empirical coefficient which characterises the mode coupling into the interferometer, which is dependent on the laser spot diameter [98].

This is an idealistic method however, as it assumes the masses have homogeneous mechanical loss distribution. Additionally, it assumes no correlation of resonant motion between different modes. These issues were addressed by Levin [99], who applied the fluctuation dissipation theorem directly to give the thermal displacement of the front face of a test mass as:

$$\bar{x}(f) = \sqrt{\frac{2k_B T}{\pi^2 f^2} \frac{W_{\text{Diss}}}{F_o^{\,2}}} \tag{2.27}$$

where W_{Diss} is the power dissipated when applying an oscillatory force, magnitude F_o on the front face of the test mass.

2.8 Mirror Suspension Modes

With the concept of minimising off resonance noise by containing as much energy as possible at resonance, it is worth studying the different types of resonant mode that can exist in a detector mirror suspension. Modes exist as both internal modes of the actual

test mass, and also modes of the suspension elements used to support the mass. The motion of the suspension elements can couple into motion of the mass which will contribute to the detector noise.

2.8.1 Internal Modes of the Test Mass

Internal modes of the test mass mirror occur when the centre of mass of the mirror remains stationary, but the mass oscillates in shape. It is intuitively clear that any change of shape that causes deformation of the front face of the test mass will lead to noise in the detector. Some modes therefore contribute more thermal noise than others, dependent on the internal mode shape.

Typical mode shapes of an Initial LIGO fused silica test mass are shown in figure and similar modes are observed in the test mass samples studied in Chapter 5.

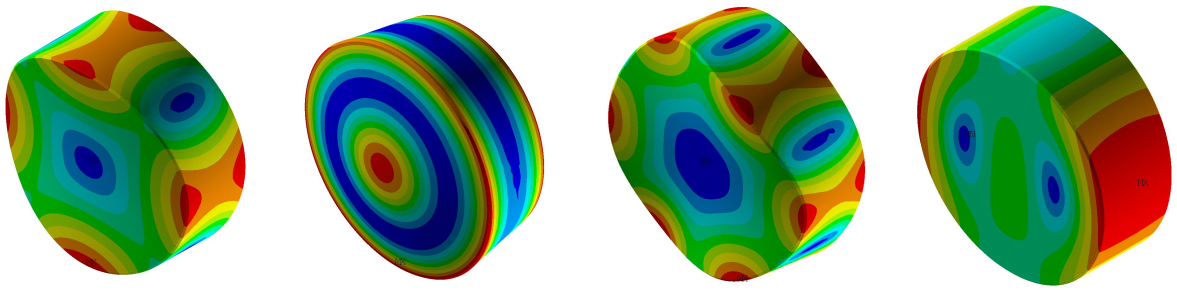

Figure 2.2 Typical Mode shapes of an Initial LIGO 10.7 kg test mass.

Actual frequencies of the resonances do not encroach into the detection frequency band, as they are typically > 10 kHz, though their off resonance noise contribution is still important.

2.8.2 Modes of Suspension Elements

2.8.2.1 Pendulum Modes

Whilst much is gained by the reduction of seismic noise by suspending the mirror as a pendulum, there are thermal noise considerations with this kind of suspension. The

longitudinal pendulum mode with motion along the axis of the interferometer arm will couple directly into the detector noise. Usually the mirror pendulums are designed such that this resonant frequency is below the detection band. Use of a pendulum also permits reduction of thermal noise as will now be demonstrated.

2.8.2.2 Mechanical Loss of a Pendulum Suspension

Consider an idealistic single pendulum, comprising a mass m suspended as a simple pendulum by suspension wire of length l from an infinitely rigid ideal clamping structure (namely, there are no external mechanisms of energy dissipation).

When laterally displaced, the pendulum experiences both a gravitational restoring force, and another provided by the elasticity of the tensioned suspension wire. For a simple pendulum, the restoring force is governed by Hooke's law, with spring constant [100]:

$$k_{\text{gravity}} = \frac{mg}{l} \tag{2.28}$$

The elastic spring constant for the wire is [89]:

$$k_{\text{wire}} = \frac{\sqrt{TYI}}{2l^2} \tag{2.29}$$

where T is the wire tension, Y is the Young's modulus of the wire material, and I is the second area moment of the suspending wire. This value is computed from:

$$I = \frac{\pi r^4}{4} \qquad \text{for circular cross section fibres}$$

$$I = \frac{ba^3}{12} \qquad \text{for rectangular cross section fibres}$$

where r is the fibre radius, a is the thickness of the fibre in the direction of bending, and b is the thickness in direction perpendicular to this.

These spring constants can then be used to calculate the mechanical loss in the pendulum. Returning to the definition of mechanical loss given by equation (2.13):

$$\phi(\omega) = \frac{E_{\text{lost per cycle}}}{2\pi E_{\text{stored}}}$$

The potential energy stored in the wire is:

$$E_{\text{stored in wire}} = \frac{1}{2} k_{\text{wire}} x^2 \tag{2.30}$$

Dissipation of energy in the form of internal friction will occur in the bending of the wire, resulting in the dissipation of some fraction α of the potential energy stored in the wire, meaning the energy lost per cycle is:

$$E_{\text{lost per cycle}} = \alpha \frac{1}{2} k_{\text{wire}} x^2 \tag{2.31}$$

The mechanical loss of the material of the suspension wire follows:

$$\phi_{\text{wire}}(\omega) = \frac{\frac{1}{2}\alpha k_{\text{wire}} x^2}{2\pi\left(\frac{1}{2} k_{\text{wire}} x^2\right)} = \frac{\alpha}{2\pi} \tag{2.32}$$

The gravitational field is conservative, so no dissipation of the gravitational energy occurs, meaning the energy stored is given by:

$$E_{\text{stored}} = E_{\text{stored in wire}} + E_{\text{stored in gravitational field}} = \frac{1}{2} k_{\text{wire}} x^2 + \frac{1}{2} k_{\text{gravity}} x^2$$

The mechanical loss of this complete pendulum system is then:

$$\phi_{\text{pendulum}}(\omega) = \frac{\frac{1}{2}\alpha k_{\text{wire}} x^2}{2\pi\left(\frac{1}{2}\left(k_{\text{wire}} + k_{\text{gravity}}\right)x^2\right)} = \phi_{\text{wire}}(\omega)\frac{k_{\text{wire}}}{k_{\text{wire}} + k_{\text{gravity}}}$$

Clearly $k_{\text{wire}} < k_{\text{wire}} + k_{\text{gravity}}$ and therefore it can be seen that the mechanical loss of the pendulum is less than that of the material of the supporting suspension wire, demonstrating an advantage of using pendulums to support mirrors in gravitational wave detectors.

Typically, the suspension wires are very thin, meaning the value $k_{\text{wire}} << k_{\text{gravity}}$. Taking this, we can express the mechanical loss of the pendulum more simply as:

$$\phi_{\text{pendulum}}(\omega) \approx \phi_{\text{wire}}(\omega)\frac{k_{\text{wire}}}{k_{\text{gravity}}} \tag{2.33}$$

The ratio of gravitational and wire spring constants is known as the pendulum *dilution factor, D*, and with the aid of equations (2.28) and (2.29) can be expressed:

$$\frac{1}{D} \approx \frac{k_{\text{wire}}}{k_{\text{gravity}}} = \frac{\frac{\sqrt{TYI}}{2l^2}}{\frac{mg}{l}} = \frac{\sqrt{TYI}}{2mgl} \tag{2.34}$$

The dilution factor can be considered as the factor by which the mechanical loss of the pendulum is reduced over the mechanical loss of the wire. Care must be exercised when considering dilution in pendulums with more than one suspension fibre, like those used in mirror suspensions. Use of n identical wires will result in bending, and therefore dissipation, in all wires. Therefore, dilution must be multiplied by the number of wires. Furthermore, dilution also depends on the pendulum mode considered. Double wire suspensions will have one pendulum mode where bending occurs at the top of the wires only, and one pendulum mode where bending happens at both the top and bottom of the wires, as shown in Figure 2.3. In this case the number of dissipative points in the wire is doubled. Therefore a general expression for the dilution factor is:

$$\frac{1}{D} \approx \frac{\beta n \sqrt{TYI}}{2mgl} \tag{2.35}$$

where n is the number of wires, and β takes the value of unity if the wires bend only at the top, and the value 2 if they bend both top and bottom.

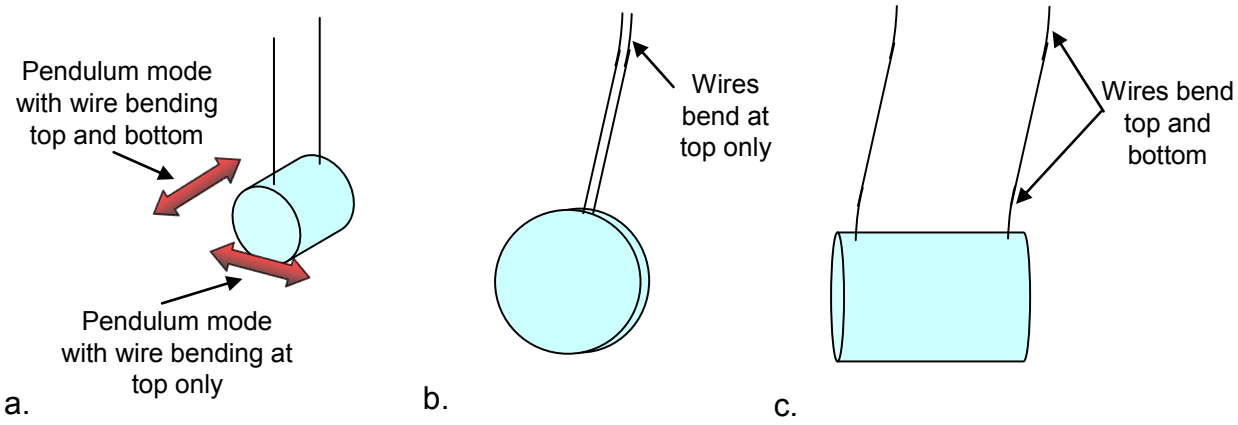

Figure 2.3 a. Pendulum modes for 2 wire pendulum b. Bending occurring at top only c. Bending occurring both top and bottom

Clearly, as we have seen, if the mechanical loss at the pendulum resonant frequency has been reduced from that of the wire material by dilution, then less thermal energy is contained off resonance meaning that there is less off resonance thermal noise. Therefore, the use of a pendulum is advantageous for both seismic and thermal noise reasons.

2.8.2.3 Violin Modes

The thin suspending wires that hold the mirror also have transverse modes of vibration. The test mass experiences a very small recoil due to this motion. These modes are universally known as "violin modes". If we imagine the motion of the mass resulting from these modes as very small then the violin modes can be approximately modelled as transverse modes on a vibrating string clamped at both ends. It can therefore be shown that the frequency of the nth harmonic violin mode is then [100]:

$$f_n = \frac{n}{2L}\sqrt{\frac{T}{\mu}} \tag{2.36}$$

where L is the length of the suspension wire, T is the tension in the wire, μ is the wire's mass per unit length. It is clear therefore that the frequency of the violin modes can be altered by changing the length of the wire suspension, or by changing the tension in the wire (namely changing the suspended mass when considering a mirror suspension). Additionally, varying the length or tension can also change the separation in frequencies between harmonics, which can be seen when considering the rate of change of frequency with respect to mode number:

$$\frac{\partial f_n}{\partial n} = \frac{1}{2L}\sqrt{\frac{T}{\mu}} \tag{2.37}$$

Shorter suspensions will therefore have greater frequency separation between adjacent modes.

It can be shown that [101]:

$$\phi_{\text{violin}}(\omega) = 2\phi_{\text{pendulum}}(\omega) \tag{2.38}$$

Since the mechanical loss of the suspension wires or fibres is very low, the thermal motion due to the violin modes is concentrated in narrow regions around the resonant violin mode frequencies, meaning that only those resonant frequencies significantly contribute to the thermal noise. These can be filtered out of data using notch filtering, since they have very narrow peaks in the frequency spectrum.

2.8.2.4 Bounce, Pitch, Yaw and Roll Modes

Other modes that exist in a mirror suspension include the vertical bounce mode, pitch, yaw and roll modes of the test mass, and these are schematically illustrated in Figure 2.4.

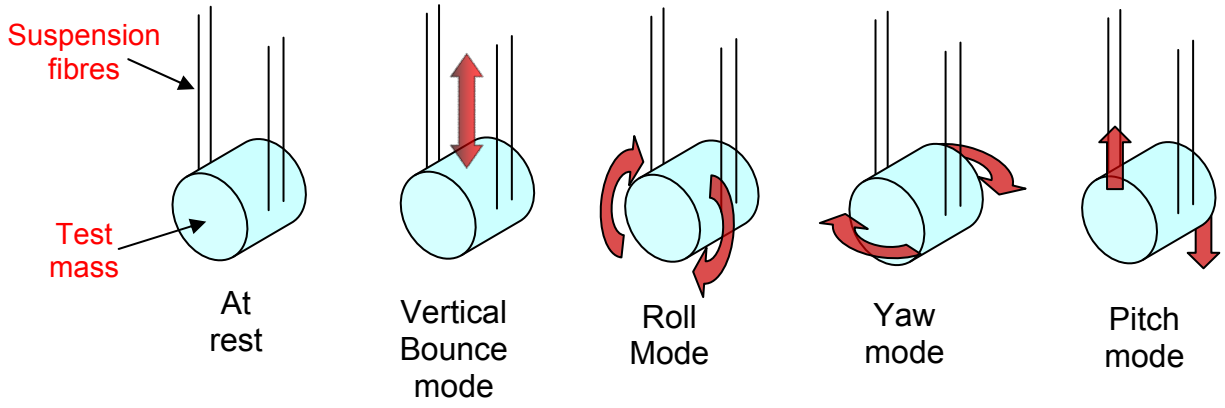

Figure 2.4 Bounce, roll, yaw and pitch modes of a test mass suspension

Keeping the laser beam as close to the centre of the mass as possible will minimise the noise contribution from the pitch and yaw modes. Design of suspension is important to keep the vertical bounce frequency in a certain frequency band, as energy can couple into horizontal motion which will then be a noise source. This coupling can occur if the interferometer arms are long enough such that the test mass does not hang parallel to the beam splitter or inner test mass of the Fabry Perot cavity due to the curvature of the earth. This occurs as the test masses have to be orientated parallel to each other so that the laser beam is returned along the path it came. However, this is not parallel to the local gravitational acceleration, and therefore coupling into arm length change from the bounce results as shown in Figure 2.5.

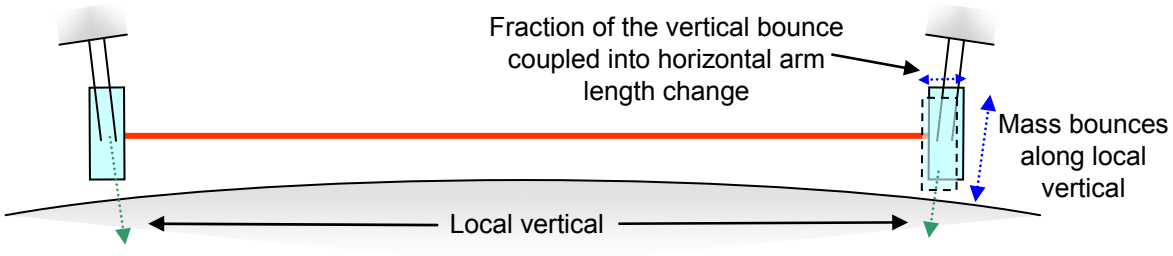

Figure 2.5 Vertical bounce mode coupling into arm length change (and hence displacement thermal noise) of a long interferometer arm.

Suspension bounce frequencies will be discussed further in Chapter 3. Pitch, roll and yaw modes are damped to reduce their resonant motion via coils acting on magnets attached to the test mass as in LIGO [102] or via control of the uppermost mass in the main test mass suspension of GEO600 [67].

2.9 Low Loss Suspension Materials

Currently, all first generation interferometric gravitational wave detectors use fused silica as mirror substrate material, with GEO600 using this material for the suspension fibres also. Fused silica combines suitable optical properties [103] with ultra low mechanical losses, and is therefore an appropriate suspension material.

2.9.1 Empirical Models of Mechanical Loss of Fused Silica

Recent studies by Penn et al have shown that many of the previously measured mechanical loss values for fused silica can be seen to fit a semi-empirical model [104], and that this could potentially be used to predict the mechanical loss of any given silica sample.

In this model the mechanical loss is made up from the sum of several components comprising internal friction from the substrate material, dissipation at the material surface and material thermoelastic loss.

By this method, the mechanical loss of fused silica can be represented:

$$\phi\left(f, \frac{S}{V}\right) = C_1 \frac{S}{V} + C_2 f^{C_3} + C_4 \phi_{\text{th}} \tag{2.39}$$

where $C_2 f^{C_3}$ represents the mechanical loss of the substrate ("bulk loss"), $C_1 \frac{S}{V}$ represents the contribution of the material surface ("surface loss"), and $C_4 \phi_{\text{th}}$ represents the contribution of thermoelastic damping.

Work is ongoing to refine this model and some measurements of certain types of fused silica have shown mechanical loss values lower than Penn's model currently predicts [105] [106].

The research detailed in this thesis is focussed on suspensions constructed from fused silica, although detectors may employ other materials when they reach their third generation.

2.9.2 Other Suitable Materials

2.9.2.1 Sapphire

Fused silica is not the only candidate material for use in gravitational wave detectors. Studies of various materials have identified sapphire as another low mechanical loss material [107] [108] [105]. Sapphire has the additional benefit that it is more thermally conductive than fused silica, which would permit sapphire mirrors to support a higher incident laser power before thermal deformation of the mirror becomes large enough to contribute significant excess noise from scatter.

However, it has been noted that thermoelastic noise may be more dominant than thermal noise for sapphire, and for this reason, fused silica continues to be the material used in detector mirror suspensions.

2.9.2.2 Silicon

Future detectors may choose to manage the level of thermal noise by cooling the mirror suspensions to cryogenic levels. Care must be exercised when considering what materials are suitable for cryogenic use, due to changing material properties over the temperature range. Fused silica is not suitable as a cryogenic suspension material as it exhibits a broad peak in mechanical loss at around 40 K [109] [110].

Sapphire does not exhibit this loss peak [111], so is more suitable for cryogenic use, however it only exhibits significant performance gains at temperatures below 30 K [112]. With transmissive interferometer optical configurations absorption of the laser light by both the reflective mirror coatings and the sapphire substrate itself results in heating that would make cooling to sub-30K difficult to achieve.

However, interferometers containing no transmissive components are possible. Such topologies can be attained by use of diffractive coupling mirrors [113]. These topologies permit the use of opaque suspension materials. Studies have shown that silicon has many valuable properties that give advantages over sapphire. Measurements by Reid et al [114] [105] [115], have shown that mechanical loss decreases with temperature for silicon, meaning a reduction in thermal noise. Additionally, silicon has nulls in its thermal expansion coefficient at 18 K and 120 K, implying that thermoelastic noise is reduced to zero at these temperatures. Silicon has been seen to exhibit loss peaks at 13 K and 115 K. These peaks are not well understood, and it is unknown whether they are linked to the nearby nulls in thermal expansion coefficient. If the peaks can be reduced or moved to different temperatures, use of silicon in a cryogenic detector running at 18 K or 120 K is a potentially viable method of attaining improved sensitivities for cryogenic gravitational wave detectors.

2.10 Conclusions

Thermal noise reduction is one of the biggest challenges facing the next generation of gravitational wave detectors. It has been shown that the fluctuation dissipation theorem can be used to relate the thermal displacement motion to the mechanical loss factor of a system. We have seen that reduction of mechanical loss factors for the materials used in detector suspensions is a viable method by which off resonance thermal noise can be reduced.

Measurement of the mechanical loss of a system has been shown to be attainable by measurement of the quality factor of the system's resonances. Dilution of mechanical loss of pendulum suspension has been demonstrated as an effective method of reduction of the thermal noise associated with a pendulum suspension.

Finally, material choices for current and future detectors have been considered, with demonstration of the desirability of using fused silica for current interferometric detectors. The remainder of this thesis will study aspects of fused silica suspensions for second and third generation gravitational wave detectors, with the aim of reduction of thermal noise in both the suspensions and the mirrors themselves.

Chapter 3

Characterisation of mirror suspension fibres

3.1 Introduction

With the first generation interferometric gravitational wave detectors having recently completed their fifth data taking run at, or close to, their design sensitivities [116] [67] [117], research is now focussed on implementing further increases to sensitivity. Improvements such as "Enhanced LIGO" [118] will extend the capabilities of the first generation detectors, with large scale upgrades taking them into their second generation following thereafter. One such upgrade will be "Advanced LIGO". An area of focus for sensitivity improvement in Advanced LIGO is reduction in thermal noise by improvement of the interferometer mirror suspensions [54] [55]. This chapter details research carried out on characterising suspension elements proposed for use in the Advanced LIGO test mass mirror suspensions.

The first generation detectors have utilised different approaches in suspending the interferometer end mirrors. It is therefore useful to first consider the suspension techniques employed in two of the current gravitational detectors together with their advantages and drawbacks.

3.2 First Generation Detector Suspensions

3.2.1 Initial LIGO Mirror Suspensions

The three initial LIGO interferometers use a comparatively simple single mass stage with a 10.7 kg fused silica mass in a sling suspension using a loop of 310 μm diameter steel piano wire to give a single pendulum, as shown in Figure 3.1 [119].

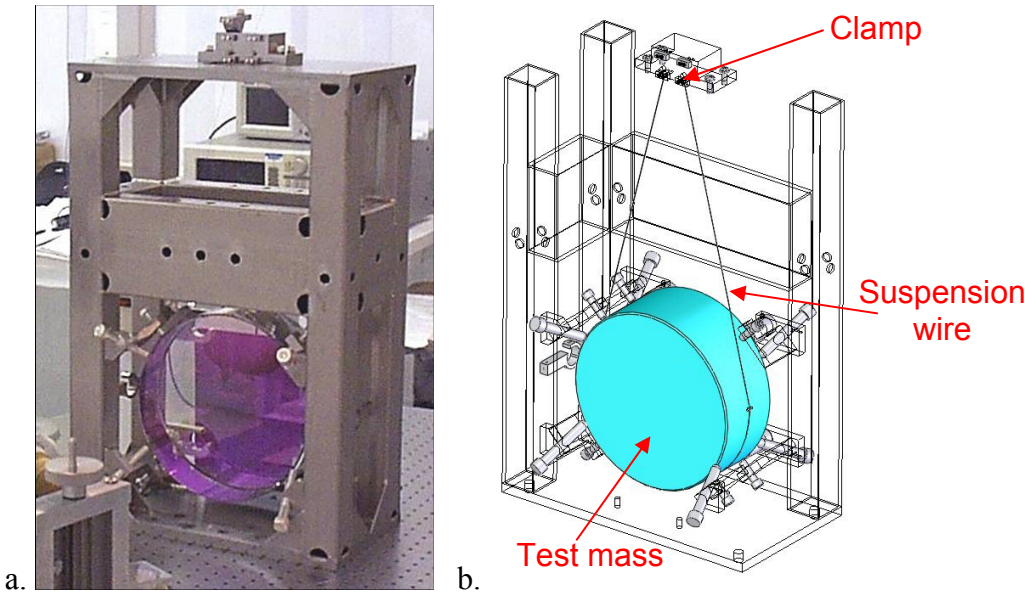

Figure 3.1 a. Initial LIGO test mass suspension and frame b. Cutaway drawing showing suspension wire loop and clamp

Control of the suspension is gained by use of magnets attached to the rear face of the mass, with coils acting on them.

This type of suspension experiences a relatively high mechanical loss due to the use of steel wire as a suspension material – the typical mechanical loss has been seen to be of the order of 10^{-4} [120] compared to 10^{-6} and below for the fused silica of the mass [91] [121]. Additionally, the Young's modulus of steel (200 GPa) is nearly triple that of fused silica (72 GPa) meaning that the dilution factor of steel suspensions is a factor of $\sqrt{3}$ less than silica suspensions, from equation (2.35) (with all variables apart from Young's modulus held constant). Another source of dissipation in this type of

suspension results from frictional damping that occurs at clamps and break off points – these being the points in the suspension loop where the wire loses contact with the mass.

3.2.2 GEO600 Mirror Suspensions

The UK-German GEO600 detector operates with an arm length of 600 m, with delay line interferometry employed allowing effective arm length of 1.2 km. This is smaller than the 4 km arms of the LIGO interferometers meaning that advanced techniques are required to ensure GEO600 can attain a similar level of sensitivity to LIGO.

One area where sensitivity gains are made in GEO600 is through the advanced mirror suspension technology that has been employed. GEO600 uses a triple stage pendulum. Two stages of cantilever blade springs are used – one to support the triple suspension, and a second within the top mass, providing additional vertical isolation to the lower two masses. This is important as vertical motion can couple into horizontal motion of the test mass as was shown in section 2.8.2.4.

The lower two masses are both fused silica. Thermal noise is reduced by utilising fused silica fibres of 280 μm diameter to hang the lower test mass – these have lower mechanical loss than the steel wires of LIGO [122], and lower Young's Modulus, allowing improvement of the dilution factor of the longitudinal pendulum mode of suspension, and also reducing the mechanical loss of other suspension modes (such as violin modes). Wire break offs are also eliminated from the lower test mass. The fibres are welded to fused silica "ears" which are silicate bonded to flats on the sides of the masses [54] [123], forming a quasi-monolithic lower stage.

a. 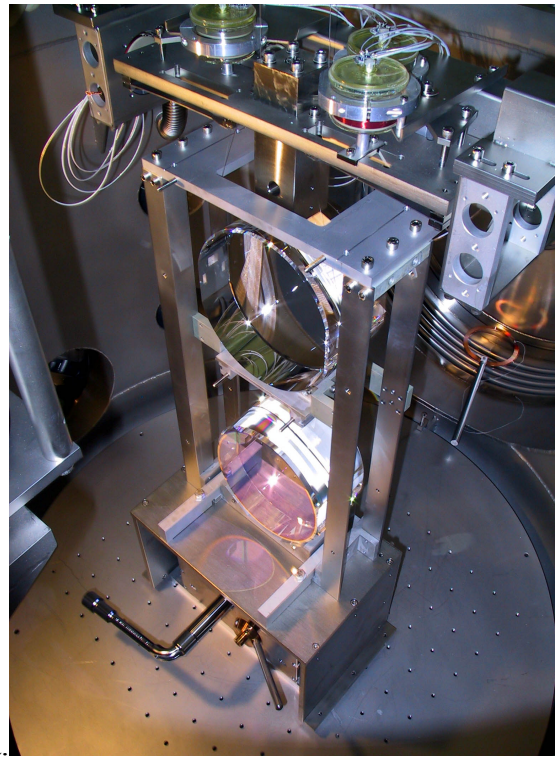 b. 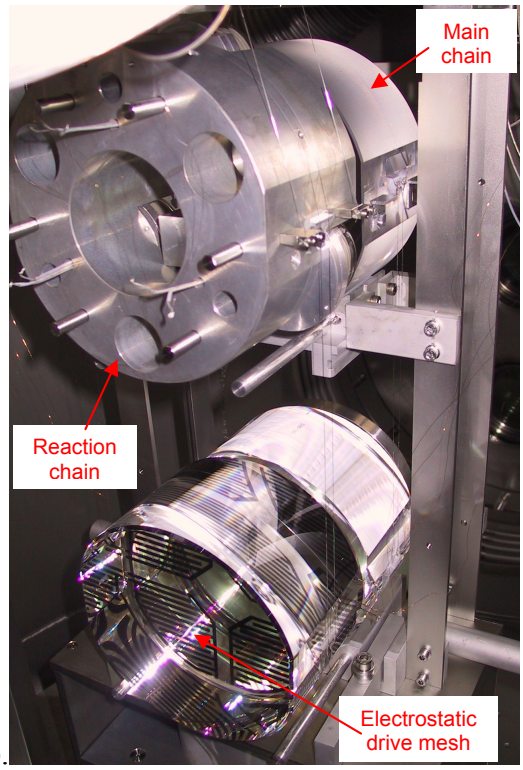

Figure 3.2a. GEO600 test mass triple suspension b. GEO600 reaction chain, showing electrostatic drive

a. 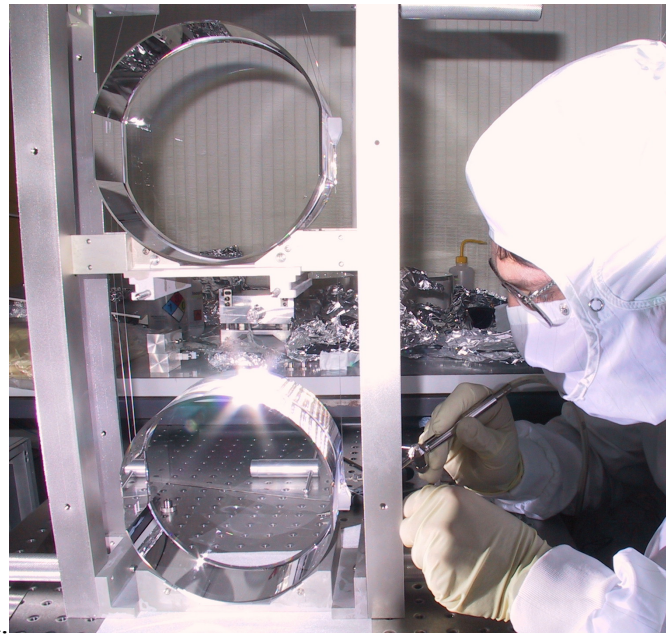 b. 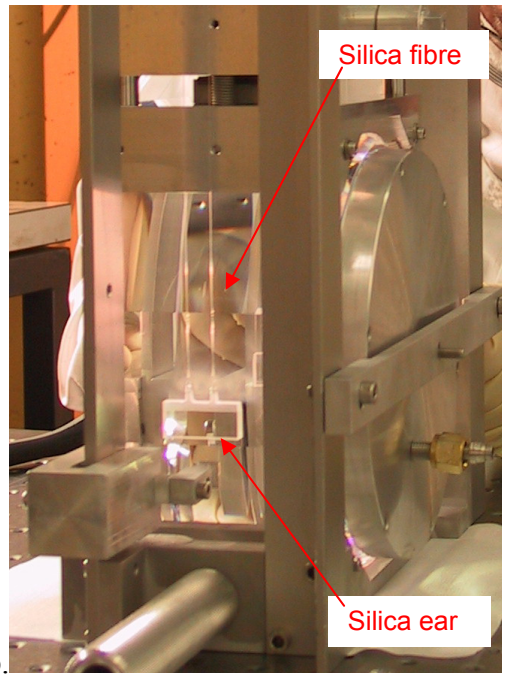

Figure 3.3a. GEO600 monolithic stage under construction b. Fused silica ears and fibres on GEO600 test mass.

Pitch and yaw of the test mass is controlled ("local" control) by application of feedback to the uppermost of the 3 masses, with the lower pendulum stages helping to filter out any electrical noise introduced in this process. Additionally, the test mass is positioned relative to the other mirrors in the interferometer ("globally" controlled) by use of a "reaction chain" of masses held behind the main suspension, as shown in Figure 3.2b. This control is achieved electrostatically via electrodes on the faces of the lowermost reaction mass, with the force acting on the rear of the test mass [67].

These methods of control avoid using magnets recessed into the rear of the mass as in LIGO, and remove any direct contact between higher mechanical loss materials (that the magnets and attaching adhesive are made from) and the GEO600 test mass. This again should aid the thermal noise performance.

3.3 Suspension Design Requirements for Advanced LIGO

Advanced LIGO aims to significantly increase sensitivity over the frequency band from 10 Hz and above. At higher frequencies (greater than around 100 Hz) the dominant noise source is photon shot noise [124]. In the 10 Hz to 100 Hz frequency band suspension thermal noise becomes an important consideration, and to reduce noise in this band Advanced LIGO will employ an extension of the GEO600 quasi-monolithic suspensions.

Requirements governing the Advanced LIGO suspension design are [125] [126] [55]:

- Vertical bounce mode of the suspension to be less than 12 Hz
- Lowest violin mode frequency to be greater than 400 Hz, and this combined with the 12 Hz bounce mode requirement maximises the detection band in which no resonances occur

- Horizontal thermal noise has a specified requirement of $10^{-19}\,\mathrm{m}/\sqrt{\mathrm{Hz}}$ at 10 Hz

The Advanced LIGO mirror suspensions will use a quadruple pendulum with four individual masses hung from cantilever blade springs. The upper two masses will be 22 kg metal masses, and also contain blade springs for further isolation.

The baseline design of the final silica stage as shown in Figure 3.4 comprises two 40 kg masses, the lower test mass suspended by rectangular cross section fused silica "ribbon" fibres welded to individual ears. The ends of the ribbons have a "neck" region where the ribbon tapers up in dimension to a larger cross section block which permits the ribbon to be reliably welded to the ears. The ears are bonded to the sides of the mass, in a similar manner to the GEO600 suspensions. A fallback solution of using circular fibres as in GEO600 is also possible for the Advanced LIGO suspension, using 400 μm diameter fibres.

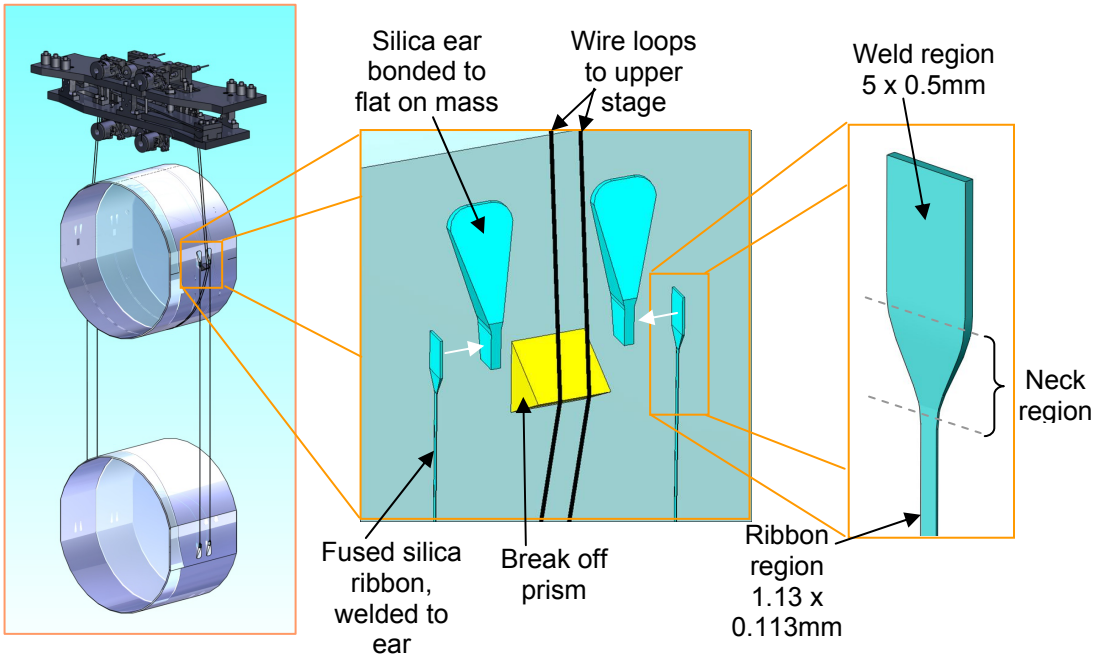

Figure 3.4 Advanced LIGO monolithic suspension (left, showing one of the two metal masses and the fused silica lower stage). Insets show detail of the ears and ribbon fibres.

Global control will again be achieved by use of a reaction chain suspension held behind the main test mass chain (not shown in Figure 3.4 for clarity), with local control achieved through feedback applied to the uppermost 40 kg mass.

Use of a quadruple pendulum will help to further attenuate vertical seismic motion over the triple pendulum system of GEO600, and permit reduction of noise that is input into the system from the feedback for orientation control on the upper mass [55].

The choice of rectangular cross section ribbons was deliberate as this geometry appeared to have a number of potential advantages over the circular GEO600 fibres. The cross section was chosen to be 1.13 x 0.113 mm based on the forecast breaking stress achievable at the time of choice [127], with the ratio of width to thickness chosen at 10:1 for ease of manufacture [128] [129] [130].

The advantages cited for employing such ribbons will now be discussed. Chapter 3 and 4 of this thesis will re-examine the properties and resulting mechanical loss of the rectangular ribbons and circular fibres using the characterisation equipment presented in this chapter together with finite element modelling of ribbons that will be detailed in chapter 4.

3.4 Ribbon Suspension Fibres

Use of rectangular cross section ribbons instead of circular fibres appeared to offer several potential reductions in suspension mechanical loss.

Intuitively, use of ribbon geometry will permit the pendulum to be more compliant to motion along the axis of the incoming laser beam. With the ribbons orientated as shown in Figure 3.4 more energy can be stored in the non-dissipative gravitational field in the pendulum mode. With the thickness of dissipative silica reduced, the pendulum dilution

will increase, as governed by equation (2.35). Comparison of the ratio of the theoretical dilution factors of these ribbons and fibres yields:

$$\frac{D_{\text{fibre}}}{D_{\text{ribbon}}} = \frac{\frac{\beta n\sqrt{TYI_{\text{ribbon}}}}{2mgl}}{\frac{\beta n\sqrt{TYI_{\text{fibre}}}}{2mgl}} = \sqrt{\frac{I_{\text{ribbon}}}{I_{\text{fibre}}}} = \sqrt{\frac{ba^3}{3\pi r^4}} \tag{3.1}$$

Consider a ribbon with cross sectional dimensions 1.130 mm x 0.113 mm. This has cross sectional area of 0.128 mm^2 – a circular fibre would require the same cross section to achieve an equal breaking strength, so therefore would require a radius of 202 μm. Using these values the ratio of dilution $\frac{D_{\text{fibre}}}{D_{\text{ribbon}}} = 0.325$. This means that the theoretical mechanical loss of a pendulum held with ribbons is 3.07 times lower than that of a similar fibre pendulum.

This is, however, a simplified interpretation of the effects of dilution and assumes that the ribbon or fibre has constant dimensions along its entire length. Actual ribbons and fibres in real suspensions have tapered neck sections, meaning the thickness in the bending region is likely to be larger so therefore the actual dilution experienced will be different – in the light of this, dilution will be considered more rigorously in Chapter 4.

Reduction of the thickness of the material experiencing the flexing pushes up the frequency at which the maximum thermoelastic loss occurs, allowing the noise to be reduced in the 10 Hz to 100 Hz region. This was another important reason for choosing ribbons. A comparison of thermoelastic loss as a function of frequency is shown in Figure 3.5.

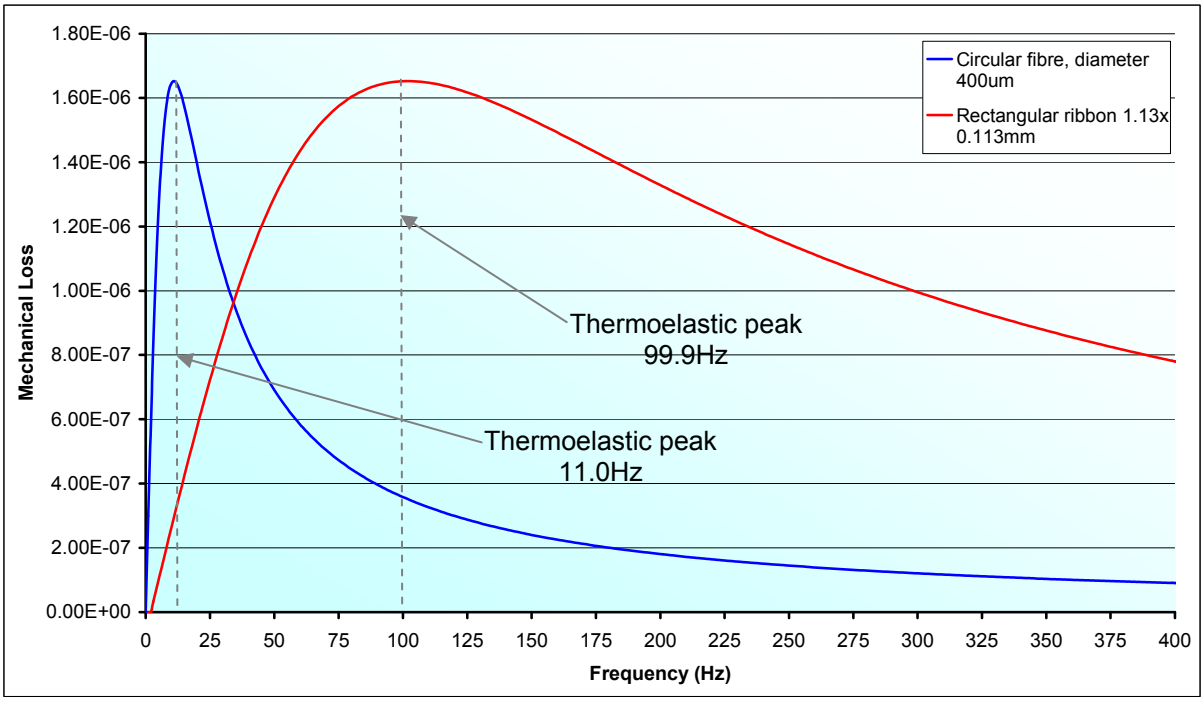

Figure 3.5 Frequency dependence of thermoelastic loss in ribbon and fibre, showing different locations of the thermoelastic peak.

It can be seen that circular fibres have a sharp peak at 11.0 Hz, whereas the equivalent ribbon's peak is an order of magnitude higher in frequency, and further from the 10 Hz region.

However, subsequently another thermoelastic effect has been discovered. It was noted by Cagnoli and Willems [131] that Young's modulus, Y, is also a function of temperature. For a simple case where there is no static stress in the ribbon (i.e. there is no suspended mass), changes in Young's modulus with temperature do not result in displacement of the ribbon. However, when a static stress σ_o is applied, then there is a length change dl, and strain $\frac{dl}{l}$ resulting from Y. Hence, any change in Young's modulus, dY, due to a temperature change dT will result in a change in dl. The fractional change in Y, is:

$$X = \frac{dY}{Y} \tag{3.2}$$

Therefore, the fractional change per unit temperature is:

$$X_{\text{per unit T}} = \frac{dY}{Y}\frac{1}{dT} \tag{3.3}$$

Hence a parameter β can be introduced:

$$\beta = \frac{1}{Y}\frac{dY}{dT} \tag{3.4}$$

this being the "thermal elastic" coefficient – the fractional change in Y per unit temperature.

The change per unit length, per unit temperature in dl due to the change in Y is therefore:

$$\alpha' = \beta\frac{dl}{l} \tag{3.5}$$

Applying the definition of Young's modulus Y, it is immediate that:

$$\alpha' = \sigma_o\frac{\beta}{Y} \tag{3.6}$$

This parameter is the fractional change in length, per unit length, per unit temperature, and is therefore directly analogous to the thermal expansion coefficient, α.

In the definition of thermoelastic loss:

$$\phi_{\text{th}} = \Delta\frac{\omega\tau}{1+(\omega\tau)^2} \tag{3.7}$$

With:

$$\Delta = \frac{Y\alpha^2 T}{\rho C} \tag{3.8}$$

Since the thermal elastic coefficient acts in a similar way to the thermal expansion coefficient, an effective thermal expansion governed by $\alpha_{\text{effective}}$ where:

$$\alpha_{\text{effective}} = \alpha - \alpha' = \alpha - \sigma_o \frac{\beta}{Y} \tag{3.9}$$

Hence, the true thermoelastic loss experienced in a loaded ribbon is:

$$\phi_{\text{th}} = \frac{\omega\tau}{1+(\omega\tau)^2} \frac{YT}{\rho C} \left(\alpha - \sigma_o \frac{\beta}{Y} \right)^2 \tag{3.10}$$

For many materials the value of β is negative, and this would be seen to increase the level of thermoelastic loss experienced if a large positive (tensile) stress is experienced by the material. However, fused silica has a β value which is positive, meaning that thermoelastic loss can be reduced by application of an appropriate static stress, and nulled entirely where $\alpha = \alpha'$, namely when:

$$\sigma_o = \frac{\alpha Y}{\beta} \tag{3.11}$$

Thermoelastic loss as a function of static stress at 10 Hz is shown in Figure 3.6.

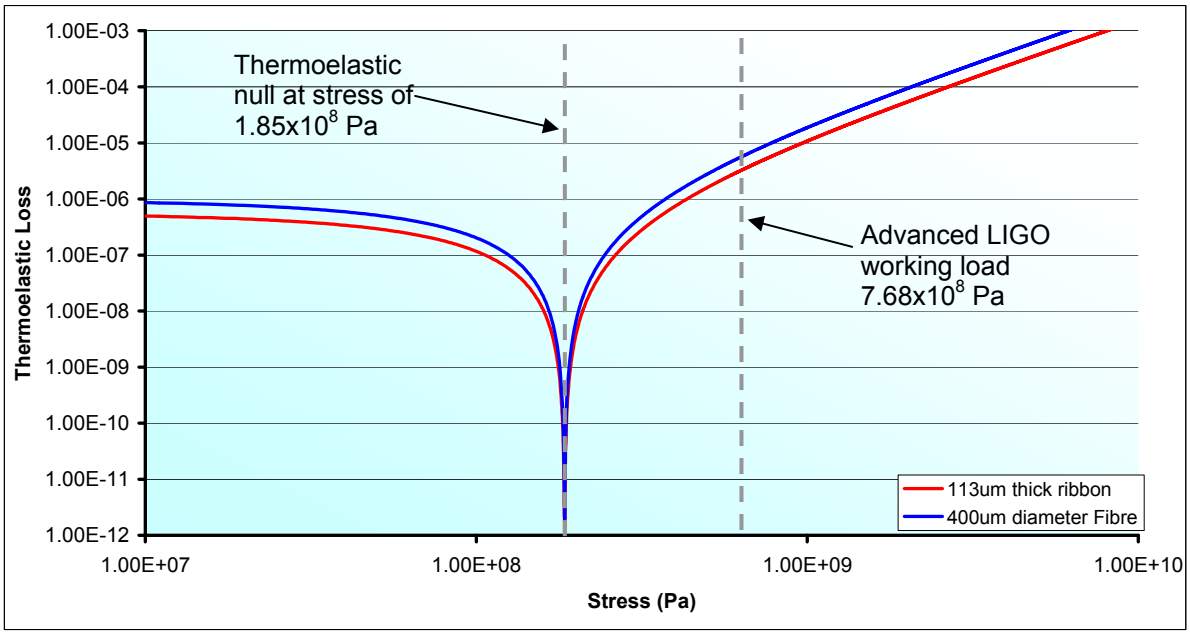

Figure 3.6 Thermoelastic noise at 10 Hz, when nonlinear effects are taken into account

In Advanced LIGO, changing the static stress in the ribbons can only be achieved by altering their cross sectional area. Using equation (3.11) the area required to null the thermoelastic loss is:

$$A_{\text{null}} = \frac{F\beta}{\alpha Y} \tag{3.12}$$

where F is the tension in a single ribbon fibre. The required stress to null the thermoelastic loss in a single fibre (1.85×10^8 Pa) is much lower than the static working load of Advanced LIGO:

$$\frac{mg}{A} = \frac{10 \times 9.81}{1.130 \times 10^{-3} \times 0.113 \times 10^{-3}} = 7.68 \times 10^8 \text{ Pa} \tag{3.13}$$

Therefore to null the thermoelastic loss in Advanced LIGO would require a ribbon 2.30 mm x 0.23 mm, which would reduce the theoretical pendulum dilution factor from 2048 to 458.

Additionally, this would also adversely affect the vertical bounce frequency of the final stage, pushing it from 6.23 Hz to 12.68 Hz, which therefore encroaches into the crucial 10 - 100 Hz region.

In the light of the discovery that thermoelastic loss can be reduced, the baseline ribbon design required more detailed re-evaluation. Also, analysis of real ribbons with their changing cross section was necessary to give a more realistic estimate of the anticipated thermal noise performance prior to full installation in the operating detectors. Fabrication and characterisation of Advanced LIGO ribbons is detailed in the remainder of this chapter.

3.5 CO_2 Laser Production of Ribbon Fibres

Circular fibres for GEO600 were produced using a hydrogen-oxygen flame to heat and melt a silica rod, with a thin 280 μm fibre being pulled from this softened silica melt [132]. The pull was accomplished using the semi-automated machine shown in Figure 3.7a. The silica rod is clamped between two pulling arms and its centre heated strongly to melting point by four gas flame nozzles (Figure 3.7b). Gas to the burner is then cut and the fibre is pulled quickly from the melt by the pulling arms, which move apart with equal speed.

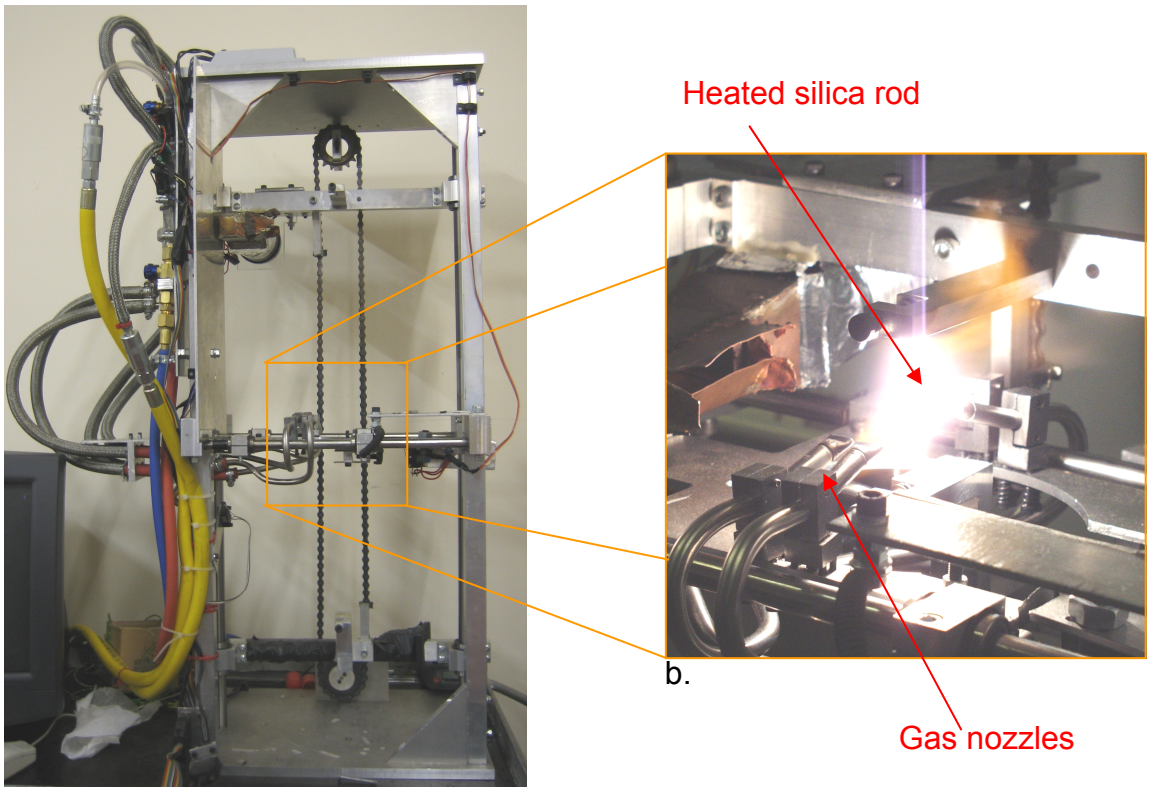

Figure 3.7a. Flame pulling machine, as used to produced fibres for GEO600 mirror suspensions b. Flame heating of silica

There are several aspects to this type of manufacture which are not ideal. Flame pulling allows only limited control of the shape of the fibres produced as the heating is stopped just prior to the fibre being pulled – this means that the fibre has to be pulled rapidly from the melt before the silica has time to cool enough to solidify again. Only minimal shape control during the pulling phase of the process is therefore possible and length repeatability was within 5 mm [133]. This is particularly true in the neck region of the fibre – this type of pulling does not permit fine control of either neck shape or length.

Because the control was limited in this manner many fibres had to be produced, and their properties characterised, with the best matching fibres selected for use in the detector suspensions.

Additionally, heating by flame provides the risk of contamination being introduced onto the fibre surface, either from dirt from the burners, or from absorbed water which is

produced in the hydrogen/oxygen combustion. Such contamination risks causing micro-cracks on the surface of the silica, which can potentially compromise the strength [134] [135].

Ribbon production for Advanced LIGO has therefore been approached in a different manner, with heating by CO_2 gas laser, delivering infra-red radiation at wavelength of 10.6 μm. This offers several advantages over the flame technology:

1. Heating is applied throughout the pull process rather than only at the start, allowing more control of the ribbon shape at any time during the pull.

2. Heating can be applied in a quantifiable and controlled manner.

3. The risk of contamination of the surface of the ribbon is reduced as the heating is produced by IR radiation, removing the risk of pollution from water produced in the flame process.

4. Increased reproducibility of ribbons with identical heating and pull for successive ribbons, using automated machine.

These advantages have been encapsulated in a laser pulling machine constructed in Glasgow.

3.5.1 CO_2 Laser Pulling Machine

The machine is based around a 120 W CO_2 laser, producing 10.6 μm wavelength radiation for heating the silica.

The machine uses a metre tall double leadscrew tower, on which 2 carriages run, as shown in Figure 3.8a. Each carriage is driven independently by a DC servo motor with brake and reduction gearbox. The fused silica slide to be pulled is clamped between

both carriages. The laser beam is dithered horizontally to provide even heating across the slide, using a gold mirror galvanometer. Instead of running in opposite directions as the flame pulling setup did, the carriages run in the same direction. This is necessary as the laser beam heating area is only around 5 mm in diameter, meaning that it does not heat the entire volume of material that will be required to complete the pull at once. Instead, the machine employs a "feed-pull' method where the upper carriage pulls the ribbon from the molten material, and the lower carriage slowly moving upwards to feed additional fresh material into the path of the beam for heating. The flame machine did not require this, as the volume of material heated was much greater, and sufficient for the whole pull - therefore no heating of additional material during the pull process was required to successfully fabricate a ribbon or fibre.

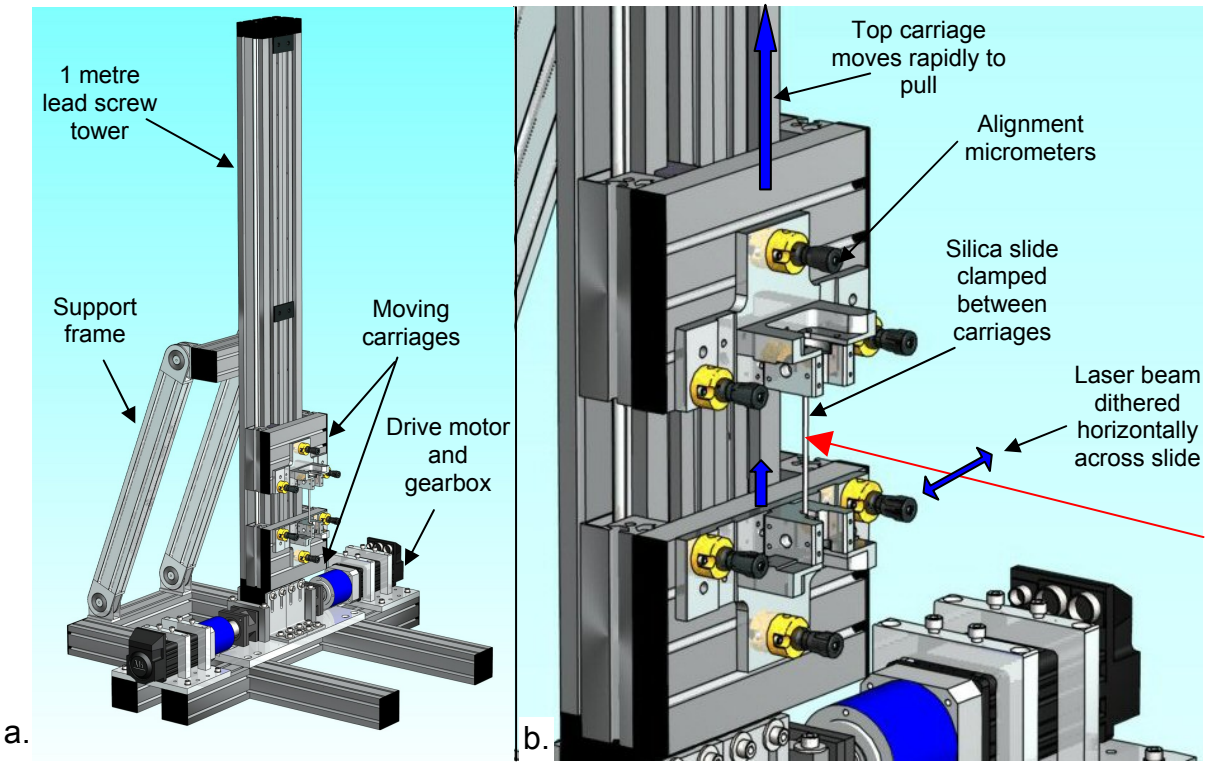

Figure 3.8a. Drawing of CO_2 laser pulling machine b. Close up of laser beam delivery point and motorised carriage arrangement.

Position sensing of the carriage locations is achieved by a linear position encoder running on the rear of the carriage. Protection against carriages running into the ends of the leadscrew unit or running together is provided by microswitches that are monitored by the computer control program.

The laser requires safety precautions since the infra-red beam is invisible, powerful and highly coherent. Therefore, the optics bench is protected with a motorised carbon beam dump. Between this and the laser, there is a Brewster window which picks off a small fraction of the laser power for monitoring and active feedback control of the stability of the laser power.

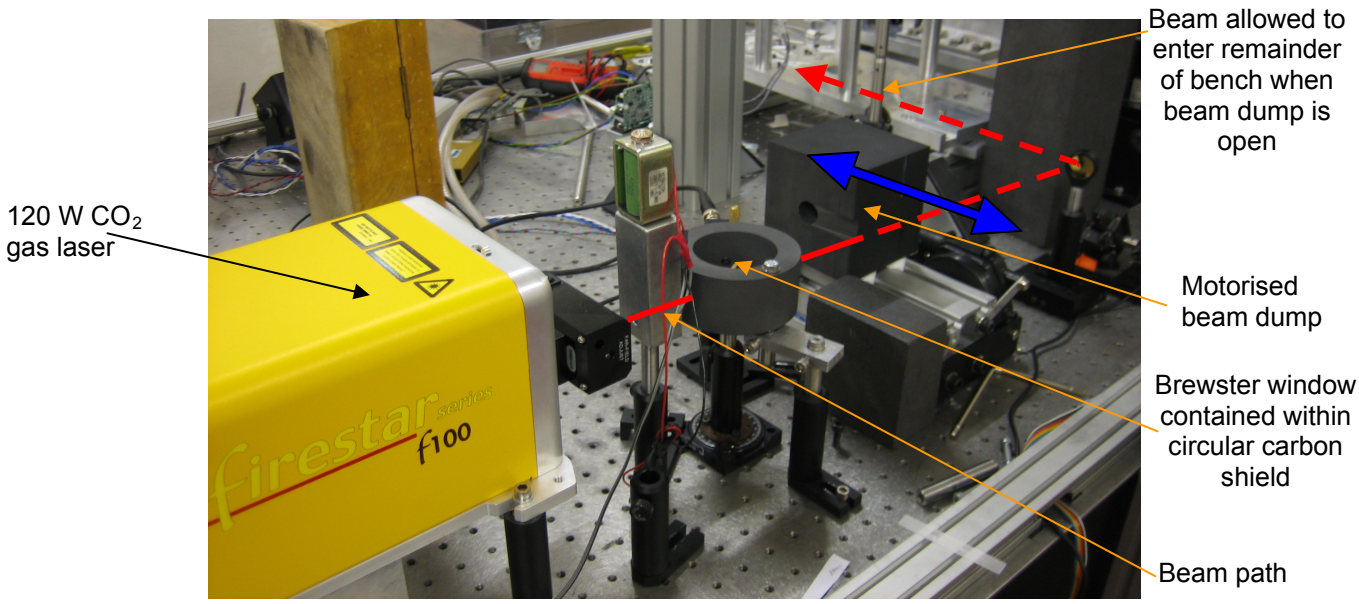

Figure 3.9 Laser bench showing motorised beam dump and power monitoring

3.5.2 Pulling Machine Control

The pulling machine is controlled via an automatic National Instruments LabVIEW control program, written by the author, with feedback control for laser stabilisation by Dr. Mark Barton also incorporated.

The control program employs a 'state machine' structure which is detailed together with the program code in Appendix A. A schematic of the program process is shown in Figure 3.10.

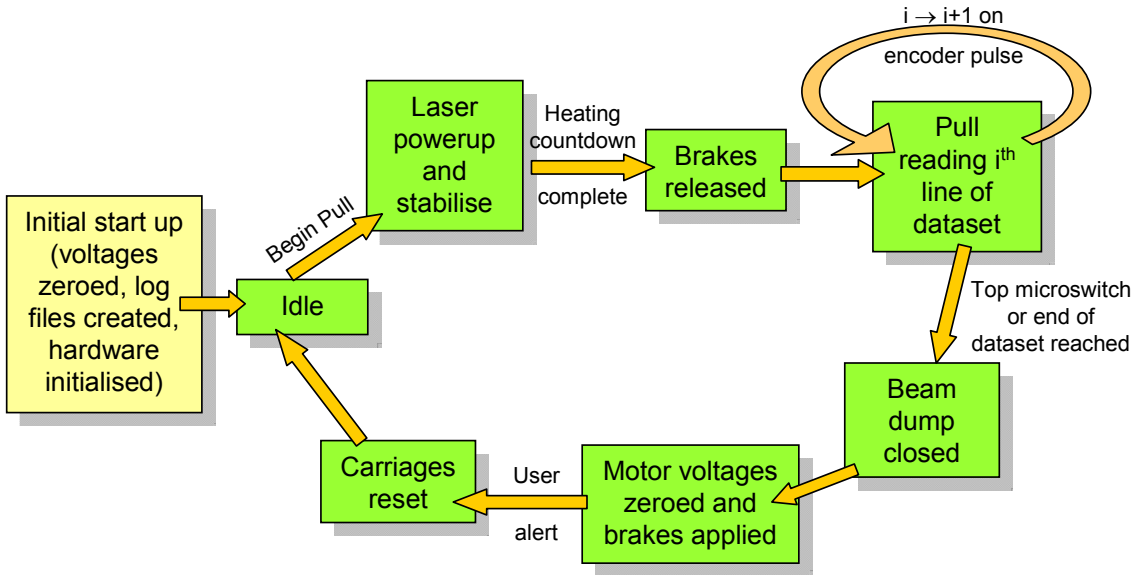

Figure 3.10 Schematic diagram of laser pulling machine control program.

The control program steps involved in a pull are as follows:

- When the program is initially started several initiation steps are taken. All voltages to motors are zeroed (to ensure program begins without risk of voltages being applied to the motors). Laser stabilisation log files are setup automatically (to record the requested and achieved output laser power), and the voltage output hardware is enabled.

- The program will then sit in an idle state, awaiting command to begin the pull. Whilst idle, a pre-written voltage dataset can be selected, and the user specified desired "Time to wait before pull" input – this is the time for which the silica slide is heated from its initial room temperature to melting before the pulling commences.

- When "Begin Pull" is selected the program will begin monitoring the status of the motorised beam dump. During this period the laser is powered up and allowed to stabilise using the stabilisation aspect. When the user is satisfied with the laser stability, the motorised beam dump is opened. The user defined "heating time" is then counted down. During this countdown the laser beam is free to circulate around the optics bench and heat the silica slide.

- On completion of the countdown the motor brakes are released.

- The pull will then commence, with the program reading the first line of the voltage dataset file, and applying the voltages to the respective motors. Each increment of the linear position encoder initiates the reading of the next line of the voltage dataset file.

- The pull will end when either the last line of the dataset file has been read, or the top carriage triggers the microswitch at the top of the leadscrew tower (this ensures that if a dataset that is of incorrect length is used there is no risk of the carriage overrunning.

- The beam dump is then closed (at this point the laser can either be powered down manually by the user, or left running to maintain a stable power for another pull).

- The motor voltages are zeroed and the brakes applied to lock the carriages in their end positions.

- The user is then issued with an alert that the pull has been completed. At this point the ribbon clamps are formed into a cartridge which is then removed from

the pulling machine, and taken for characterisation (as will be discussed in section 3.6).

- The carriages are then reset to their starting positions by user command, with the lower carriage being run back down the leadscrew tower first, and the upper then being run down afterwards, and being stopped by a microswitch on the lower carriage.

- The program will then return to the idle state awaiting command to pull again. At this point the user can continue with the same voltage dataset file and waiting time, or select alternatives.

A typical voltage dataset for a ribbon neck is shown in Appendix A, section A.4. The ability to supply such voltage profiles to dictate the shapes of the resulting ribbons gives the machine much greater capability of producing the required shaped ribbons for Advanced LIGO.

3.6 Ribbon Characterisation

Once fabricated, ribbons undergo a range of tests to ensure their properties meet those required for Advanced LIGO. The tests include measurement of the thick and thin cross sectional dimensions of the ribbon ("dimensional characterisation" / "profiling"); an overload strength test of the ribbon with a 12.5 kg load; measurement of the vertical bounce frequency of a loaded ribbon. The order of the procedures is shown in Figure 3.11.

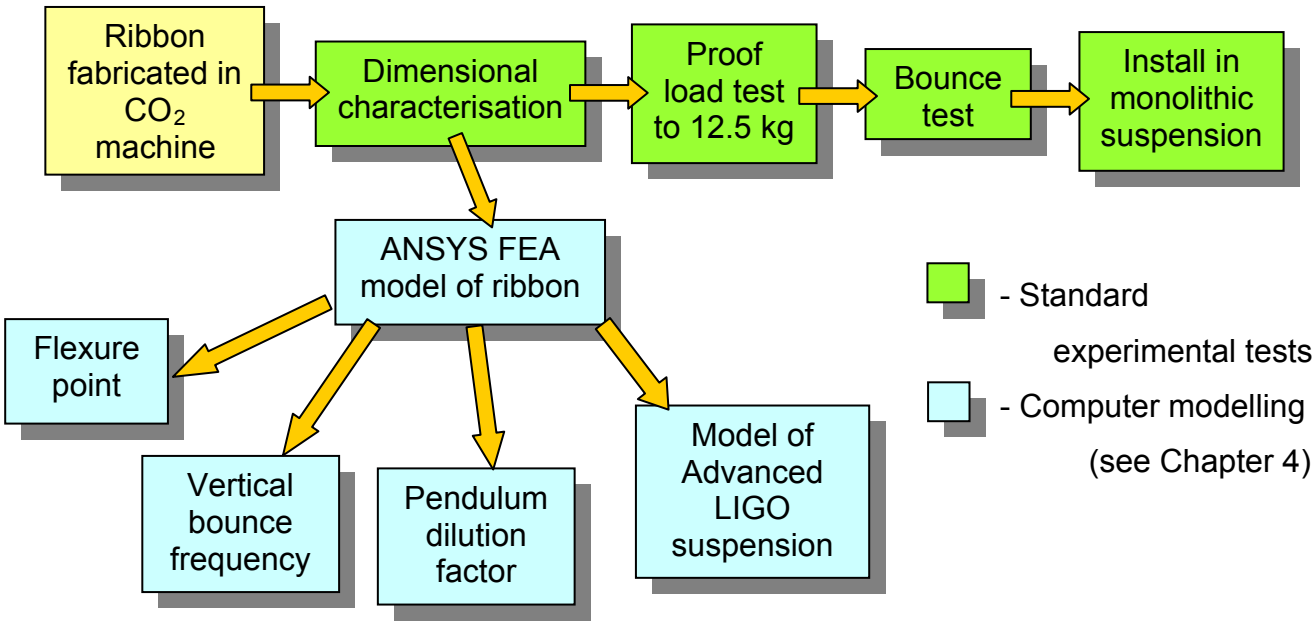

Figure 3.11 Characterisation procedures for Advanced LIGO ribbons.

Additional analysis was done on Finite Element Analysis (FEA) models of the ribbons, using the FEA program ANSYS, and this work will be explored in depth in Chapter 4.

3.6.1 Dimensional Characterisation of Laser Pulled Fibres

Knowledge of the cross sectional dimensions of the ribbons, together with detailed profiles of the neck regions was important for initial development of ribbons, and will be required as a check that ribbons installed in detector suspensions have accurately matched bending points and therefore correctly positioning the ears on the masses [136]. The dimensional characterisation, or "profiling" measurements also provide data to construct a finite element (FE) model of the ribbon in ANSYS. This allowed checking of bounce frequencies, calculation of the ribbon flexure points, the dilution factor of a pendulum constructed with such a ribbon and ultimately the total mechanical loss of ribbons to be evaluated.

The profiling measurements are required to be non-contact, as any contact risks introducing cracks into the ribbon surface, compromising its strength.

3.6.1.1 Characterising Fibres for GEO600

The dimensions of the fibres produced for GEO600 suspension were measured using a monochrome CCTV camera attached to a microscope. The fibre was then observed on a TV screen. The fibre diameter was obtained by measuring the size of the image on the TV screen. Primarily, checking and matching was achieved in GEO600 by comparison of vertical bounce frequencies. It was later discovered that the bending points of the fibres used were in a different location in the fibre from what had been expected [137] [138] [139].

It was clear that whilst this method had proved adequate for dimensional measurements on fibres used in GEO600, it was limited in its ability to provide accurate measurements for many reasons. In particular:

- Positioning along the length of the ribbon was not easy or accurately quantified by this system, meaning significant error in the position at which the ribbon dimension was measured

- Image quality - sharpness were not always consistent and reproducible introducing reading errors into the measurement

- Process of taking measurements along the length of a full fibre was very time consuming and labour intensive

- It was also not possible to obtain any accurate quantified neck shape data for the fibres, and this became apparent when the positions of the flexure points of the fibres installed GEO600 were found to be different than anticipated

Therefore, for Advanced LIGO more stringent profiling was seen as necessary, allowing accurate measurement of the ribbon shapes along their full length, permitting realistic

prediction of their performance when installed in the final detector suspension. A profiling machine was built by the author to meet this requirement.

3.6.1.2 Preliminary Concepts

Several concepts were evaluated to discover the best methods for performing dimensional measurements on ribbons.

3.6.1.3 Scanner

The first concept was optical scanning of the ribbon. Tests were conducted using a standard PC flatbed scanner as an imaging device. The ribbon was held in a metal frame ("cartridge") just above the glass window of the scanner. This used two lengths of angle section to brace between the pulling machine slide clamps, allowing these to be removed from the pulling machine complete with the pulled ribbon as one single unit. This setup permitted the ribbon to be kept lightly tensioned, and eased handling. The cartridge also protected the ribbon and did not allow it to contact the surface of the scanner. This setup allowed the full ribbon to imaged at once, quickly using one pass of the scanner. A typical scan of a very early development ribbon neck is shown in Figure 3.13.

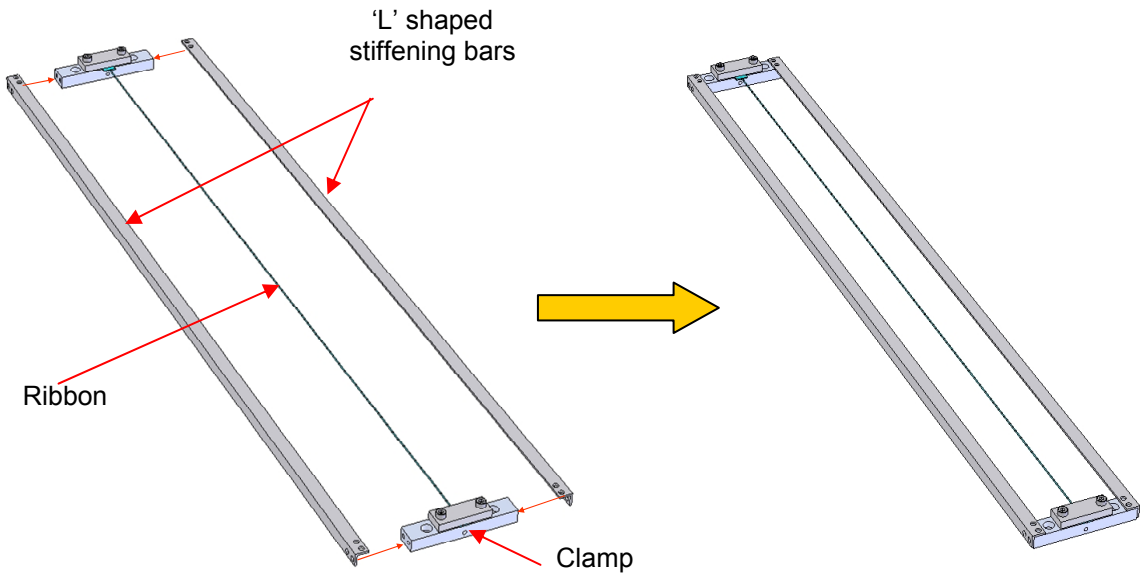

Figure 3.12 Construction of early prototype ribbon cartridge.The ribbon was pulled on the pulling machine in the clamps shown, and the L-shaped stiffening bars were attached to the clamps in-situ. The complete rigid cartridge was then removed from the pulling machine as a single unit.

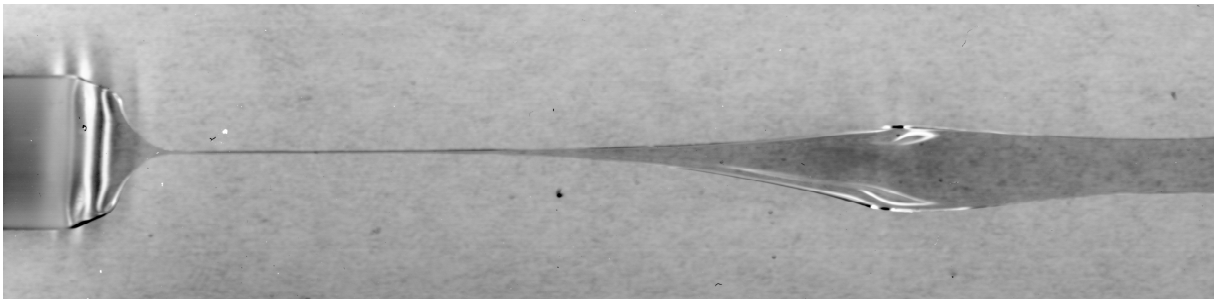

Figure 3.13 Image of early laser pulled ribbon neck section made using flatbed scanner. Ribbon shows very thin section after the initial neck, which was due to initial pulling problems with laser machine

A LabVIEW program was written to make an edge detection measurement on the image. This measured in from the image edges, and from the pixel count the dimension of the ribbon could be calculated. Figure 3.14 shows the image with this measurement being undertaken.

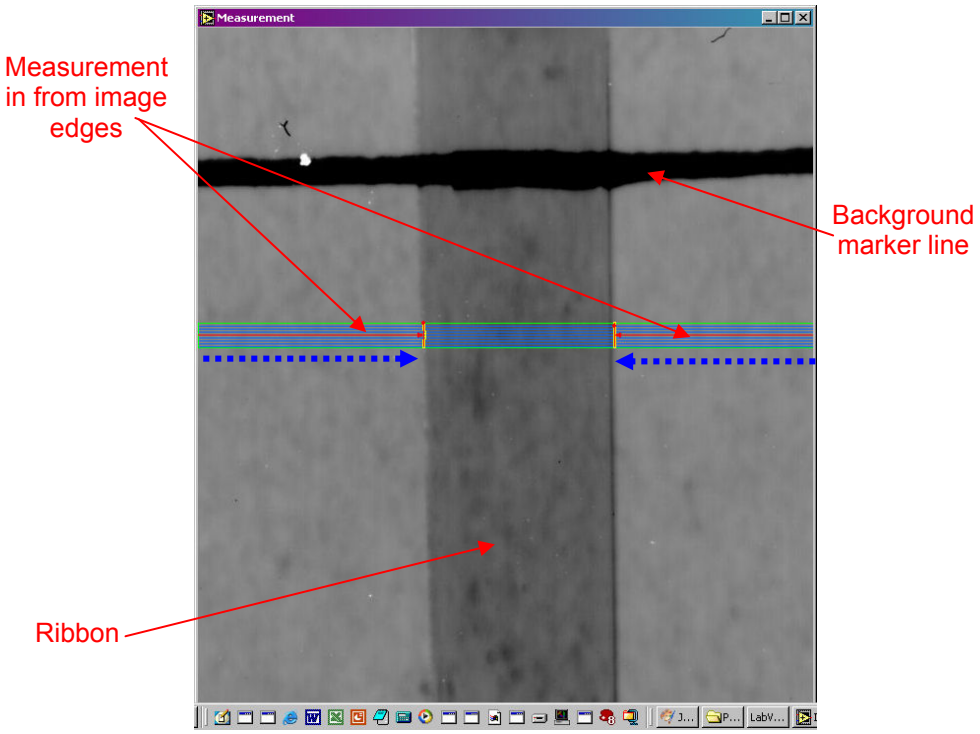

Figure 3.14 Measurement by LabVIEW edge detection program

This scanning technique had several distinct drawbacks, the most important of which is the resolution that could be obtained. Initially a scanner with 300 x 300 dpi resolution, which provided a maximum resolution of 85 μm per pixel was used. Latterly a higher resolution scanner of 3200 x 1600 dpi was used, yielding a theoretical maximum resolution of 8 μm per pixel. This would be satisfactory for the larger ribbon dimension, but too coarse for the thin dimension, as this would leave an 8% uncertainty in a measurement of a 100 μm thick ribbon.

Additionally, this assumes a perfect focus, which was found to be difficult to obtain – this would add an additional error onto the measurement. By its construction, the scanner's optimal focus position is on the glass bed; but the ribbon could not be allowed to touch this (as this would risk damage to the ribbon surface), instead being held around 1 cm above the scanner bed in the metal cartridge frame which also offered

protection. Holding the ribbon horizontally on the scanner bed also meant that gravity would cause it to sag toward the scanner bed, meaning that the focus would be fractionally different along the ribbon length.

Furthermore, image file size using the higher resolution scanner was large enough that post-processing a full ribbon image could not be efficiently achieved, due to the amount of PC memory required to view large high resolution images. This meant significant post-processing would be required to divide the image up into manageable sized chunks.

3.6.1.4 Imaging by Web-camera – 1st Prototype

In order to address some of the issues that arose when imaging using the flatbed scanner, an alternative imaging system was devised by the author.

This used a Firewire webcamera, which is supplied on a 5 cm square circuit board, as shown in Figure 3.15. The camera used was Unibrain Fire-i Digital Board Camera [140] with CCD sensor resolution of 640 x 480 pixels. This camera was chosen due to the small dimensions of the circuit board allowing for easy mounting. Other cameras that were examined were considerably bulkier [141].

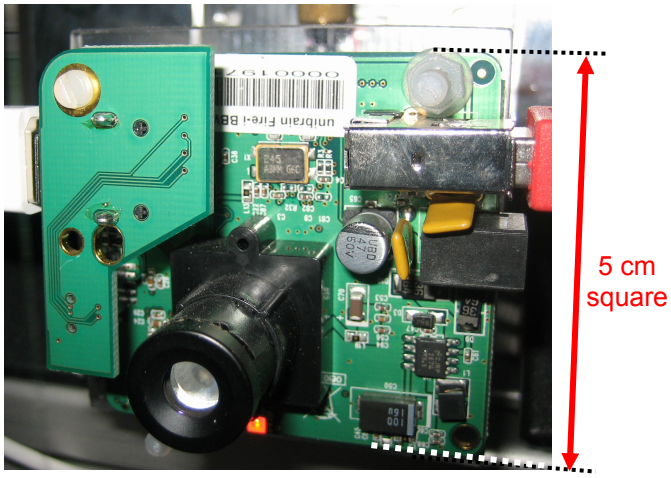

Figure 3.15 Firewire web camera used for imaging

The camera was mounted on a motorised leadscrew unit to allow it to travel along the length of the ribbon, as shown in Figure 3.16. The ribbon was held in the same cartridge as used with the scanner, and this was clamped on a second tower. Focus adjustability was provided by mounting the camera on a linear translation stage. It was also mounted on a tilt base to allow any twisting along the length of the ribbon to be accommodated.

Use of the motorised carriage system was analogous to the mobility provided by the flatbed scanner's imaging head, although it was found that the carriage had to be halted in order to take an image. This proved advantageous however, as it permitted the focus to be checked and adjusted if necessary.

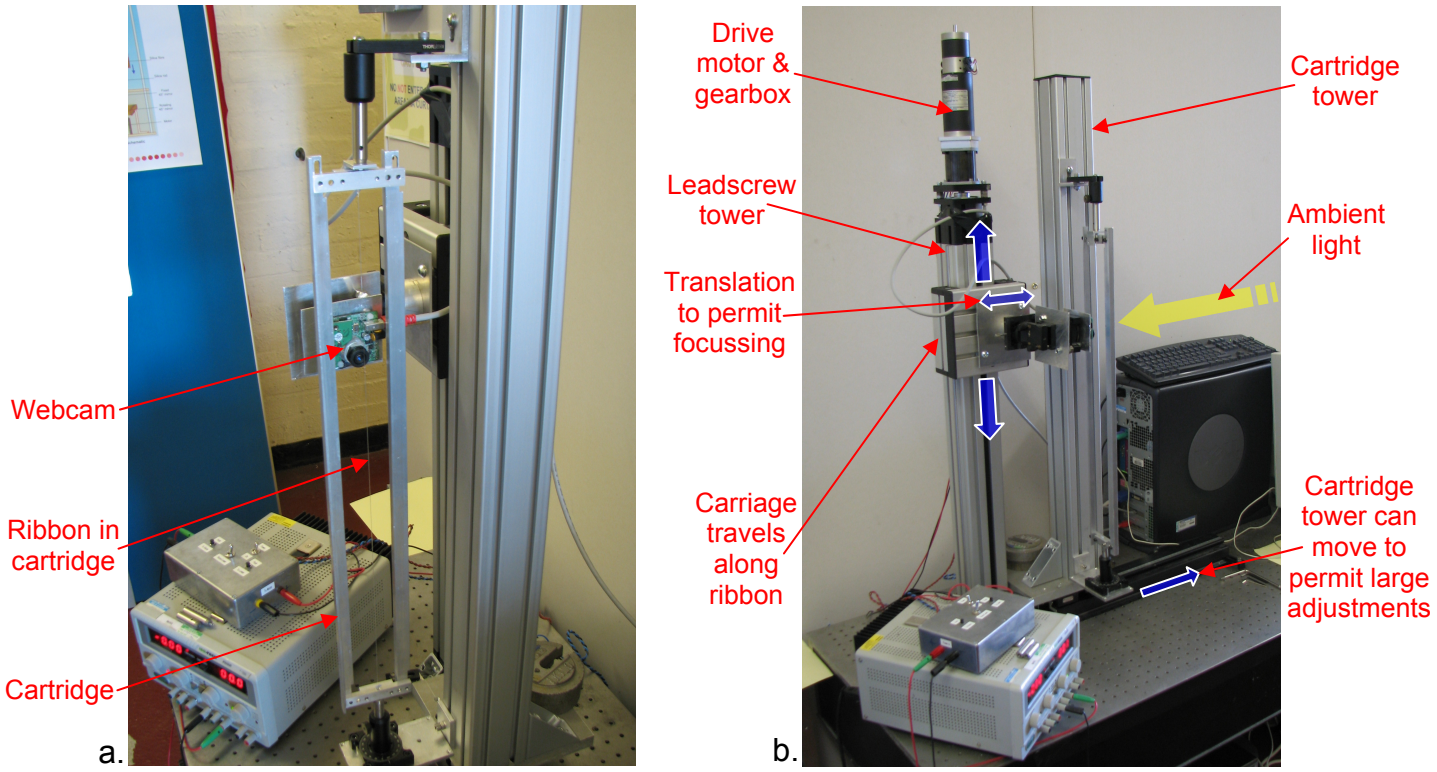

Figure 3.16 Proof-of-concept web-camera based dimensional characterisation setup. a. view of camera and ribbon cartridge b. Complete setup from different angle showing mobility of imaging head.

Different sizes of ribbons could be accommodated by different focal length lenses and suitable ribbon/lens and lens/CCD distances. This also permitted appropriate

resolutions to be obtained easily by choice of lenses, with greater magnification for thinner/smaller ribbons.

Initially the ambient lighting in the room was found to provide adequate image contrast, as shown in Figure 3.16b, although later a variety of lighting sources were tested, as the ambient light tended to vary, affecting the image contrast. These included a fluorescent tube and LEDs. It was found that consistently good quality images could be obtained when using high intensity 4 W 'Lumiled' LEDs [142].

This machine was found to be capable of obtaining clear images at a higher resolution than the scanner, with resolution dependent on the magnification from the different lenses. A typical image and measurement obtained using this system is shown in Figure 3.17.

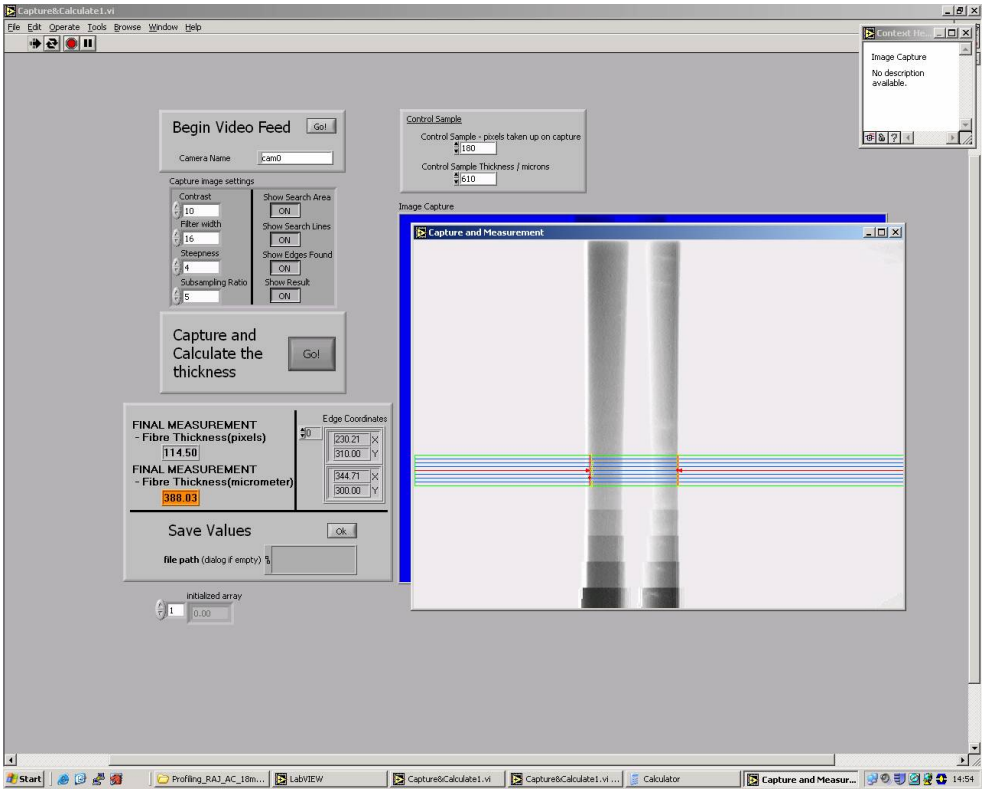

Figure 3.17 LabVIEW imaging and measurement showing ribbon as imaged by firewire web-cam. The contrast change visible toward the bottom of the image was later attributed to a lens misalignment.

It was decided to proceed with an improved machine design of this type, capable of measuring both dimensions of ribbon simultaneously.

3.6.1.5 Imaging by Web-camera – 2nd Prototype - Dual Camera System

It was ultimately desirable to be able to measure both thick and thin dimensions at once. However, with the first single camera prototype, the ribbon would need to be rotated through 90° and lens magnification changed for each measurement; or the ribbon would first have to have one of its dimensions measured, and then have the process repeated for the second dimension. It was clear that the former would be labour intensive, and the latter would risk that the width and thickness were not accurately related to each other.

It was therefore decided to mount two independent cameras orthogonally, with Lumileds providing the background lighting source. This revised setup is shown in Figure 3.18.

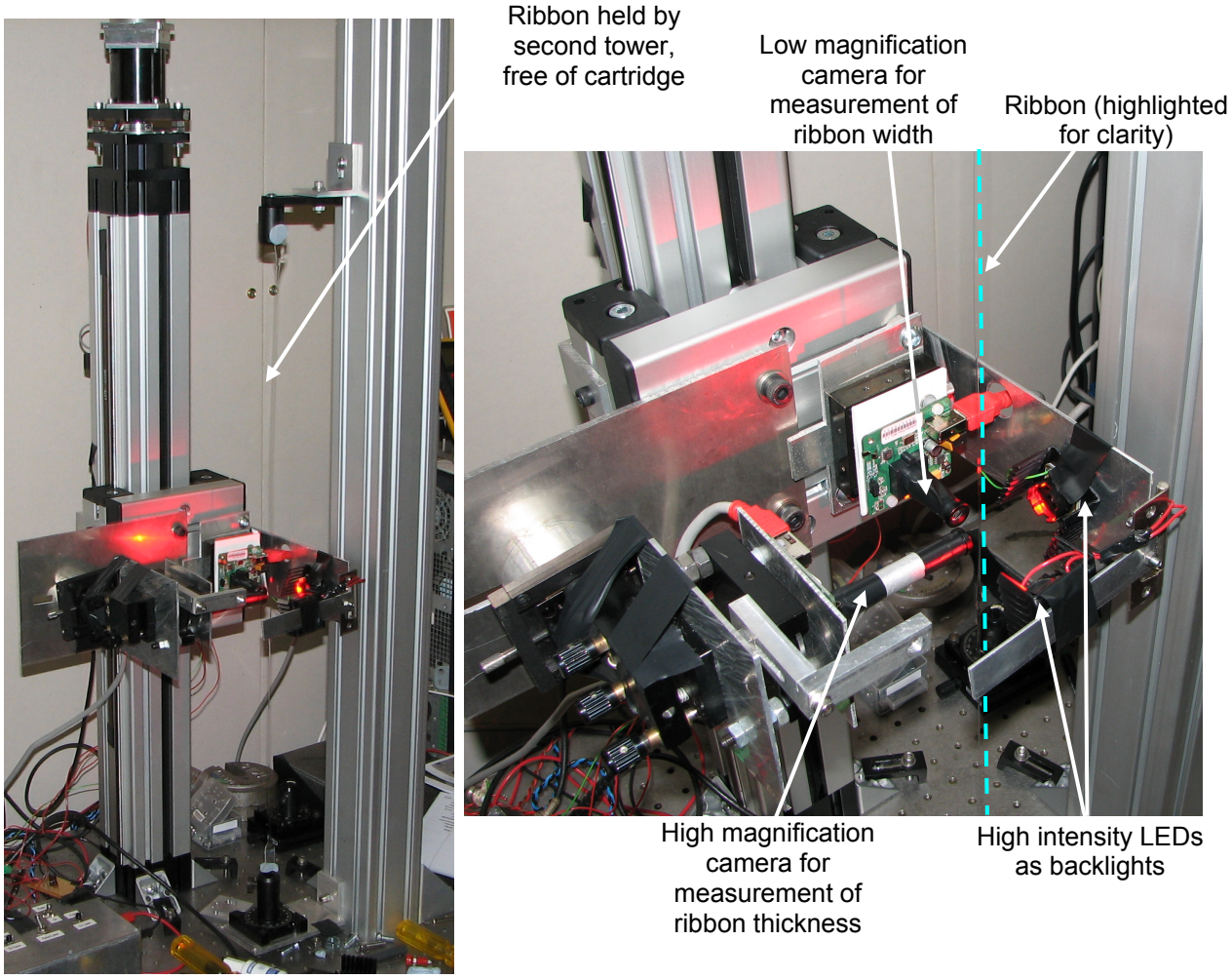

Figure 3.18 Profiler under development, showing initial test upgrade to use dual cameras. Ribbon was not contained in the cartridge for these tests, as the cartridge design precluded the use of both cameras simultaneously

The low magnification camera was mounted on the bed of the carriage, and the higher magnification camera perpendicular to this. The LED backlights were mounted on the carriage too, with one hinged to allow access to the ribbon. The ribbon was held from a second tower. The travel along the ribbon was measured using a linear position encoder mounted to the rear of the carriage.

Testing of this setup showed that a two camera system worked efficiently permitting simultaneous measurements of ribbon width and thickness using a revised LabVIEW program.

Some problems were encountered with this setup, the most notable being that twists in the ribbon often led to difficulty in focussing the high magnification camera. This was due to the small depth of field this camera had. Also, holding the ribbon freely (without the light tensioning supplied by the cartridge) from the second tower meant that it was susceptible to violin mode vibrations, making measurement difficult since the ribbon moved on screen.

These issues were addressed in the final version of the machine, updated to a configuration that would ultimately be suitable for duplicate installation at detector sites.

3.6.1.6 Profiler Final Development

Use of two perpendicular webcams prohibited use of the ribbon cartridge shown in Figure 3.12, since the stiffening bars would obscure the ribbon in one of the directions. Therefore a revised clamp cartridge was designed to interface with both the pulling machine and the profiler. This revised cartridge is shown in Figure 3.19.

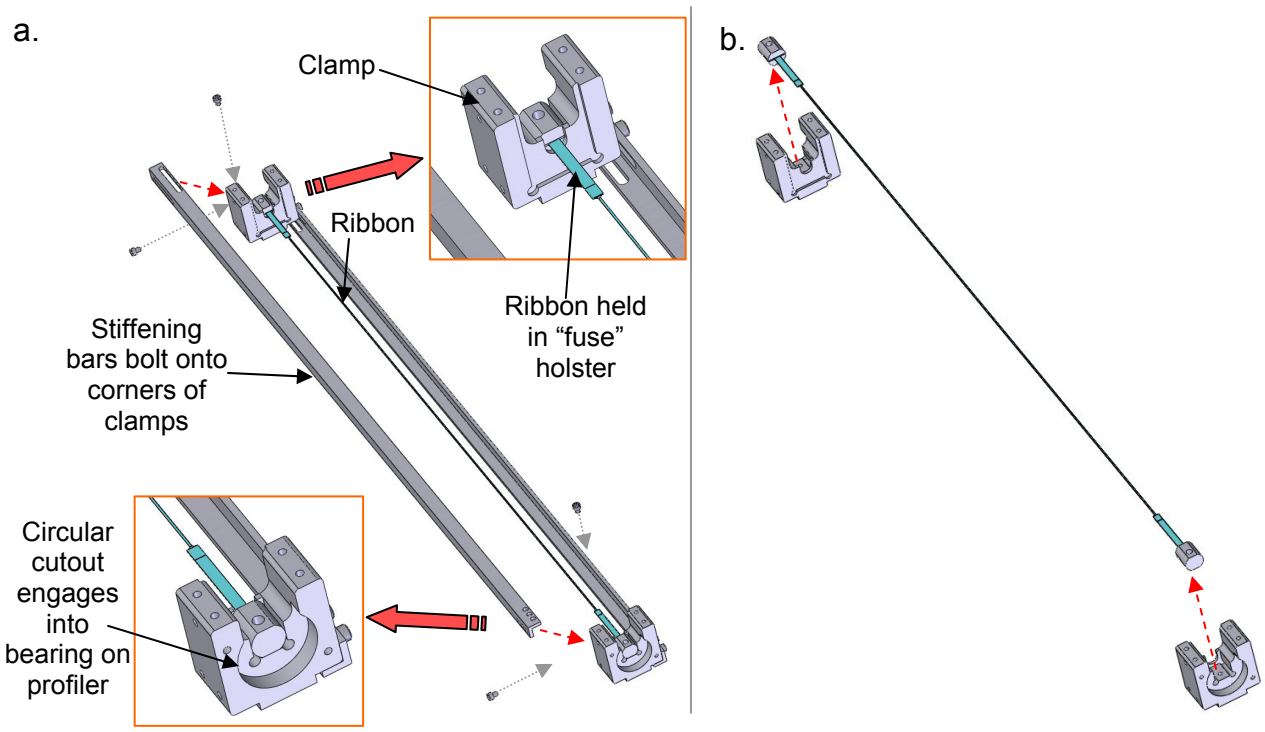

Figure 3.19 a. Construction of revised ribbon cartridge, showing the ribbon held in "fuse" holsters, and stiffening bars relocated to the corners of the revised clamps. b. Ribbon removal from the clamps to allow proof and bounce testing after profiling.

The cartridge had the stiffening bars relocated to the corners of square block clamps. The ribbon is held in two small clamps ("fuse ends") which are used in all parts of the pulling and characterisation process (pull, profile, bounce and proof tests). The ribbon is attached with Araldite 2012 epoxy resin adhesive into slots in these, and this assembly locates into the clamps for pulling and profiling. The clamps also have circular cutouts in their bases which locate into loose clamps on the profiler.

The final profiling setup is shown in Figure 3.20. The profiler cartridge locates into a loose clamp at the base, and at the top a circular bearing is then moved down to locate into the cut-out in the cartridge. The lower clamp contains a rotational stage which allows the complete cartridge to be rotated by small angles when the profiler measurement is being undertaken. This allows compensation for twists in the ribbon along its length. Use of the cartridge allows the ribbon to be kept in light tension, reducing the tendency for large violin mode vibrations.

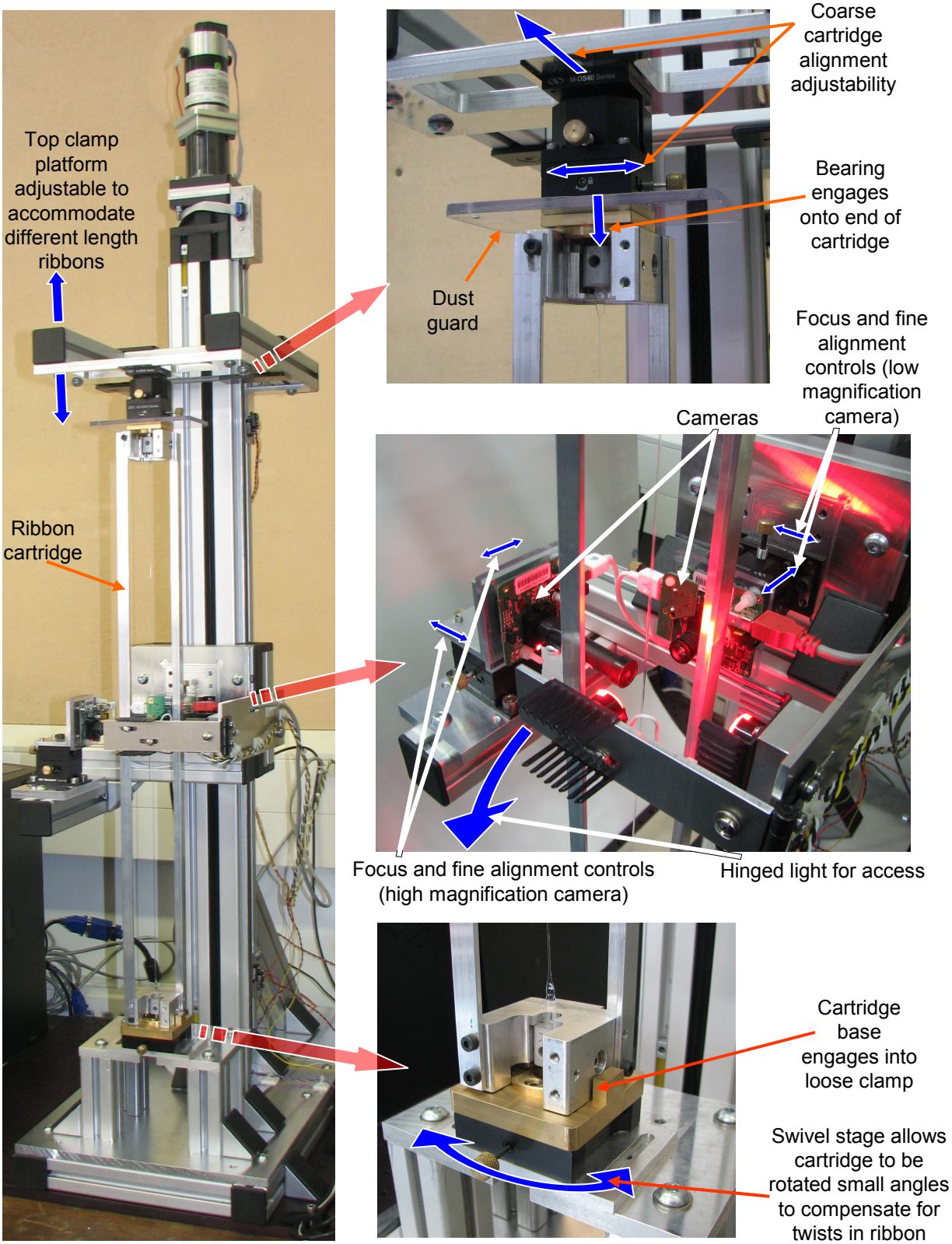

Figure 3.20 Finalised ribbon profiling machine, showing cartridge with ribbon installed in top and bottom loose clamp holders, which have coarse alignment and rotation adjustability built in. Fine adjustment and focus is achieved with the cameras as is shown.

The clamping fixtures at the top and bottom also had adjustability built in to allow coarse positioning of the cartridge relative to the cameras. Fine positioning and focus of the cameras was accomplished using translation stages mounted to the cameras themselves.

Additional depth of field was also gained on the high magnification camera by reducing the aperture size to approximately 0.75 mm, giving f-number of $\frac{f}{10.7}$. Further reduction of the aperture resulted in excess noise which would have interfered with the software edge detection.

A revised LabVIEW program (see Appendix B for the final program code) was written to ease the use of the machine, with two modes of operation. The first mode is used for the neck regions where an edge detection measurement is taken on every row of pixels of the image. These measurements are then automatically joined with any overlap taken into account, and give both the width and thickness together with a dimensioned shape profile of the ribbon. This mode of operation enables very high resolution scans of the ribbon necks to be achieved, and these were subsequently used in the FEA modelling which will be detailed in the next chapter.

Along the central thin section of the ribbon measurements are not required at this resolution (indeed this would provide too much data to process), so measurements are taken at user defined intervals along the ribbon length, typically every 5 to 10 mm. These are averaged over a user defined number of pixels, typically ~20.

A duplicate of this machine has recently been installed at the LIGO test facility at M.I.T. Boston in readiness for the thermal noise quad suspension prototype which will be constructed in late summer 2008, and pictures of this setup are shown in Appendix C.

3.6.1.7 Machine Capabilities and Testing

The resolutions attained by the two cameras (and used in the measurements in the remainder of this chapter) were 9.61 μm for the low magnification (ribbon width) measurement, and 1.62 μm for the high magnification (ribbon thickness) measurement.

In order to test the repeatability of the system, several tests were undertaken. The first comprised simply repeating the measurement at a given point on a test ribbon, without adjusting the focus between repetitions. The second test added refocusing of the system between each repetition. Both measurements are shown in Table 3.1.

	Repeatability test 1 – no refocus between repetitions		Repeatability test 2 – with refocus between repetitions	
	Measured Ribbon width (um)	Measured Ribbon thickness (um)	Measured Ribbon width (um)	Measured Ribbon thickness (um)
	1067	181	1067	181
	1068	181	1066	175
	1067	180	1062	178
	1066	181	1064	181
	1067	181	1067	179
	1071	180	1068	180
	1068	180	1065	179
	1069	181	1067	178
	1067	180	1070	179
	1068	181	1071	181
Average	1067.8	180.6	1066.7	179.1
Standard error	1.4	0.5	2.7	1.9
% error	0.13%	0.28%	0.25%	1.06%

Table 3.1 Repeatability tests of profiler measurement system – test 1 repeated the measurement with no change made to a good focus, test 2 refocussed the image for each repetition.

It can be seen that the spread in measured values due to the measurement itself (test 1) is small, being less than 0.3% (small motions of the ribbon will mean that each observed image will be slightly different, resulting in this small spread of measurements). When refocusing was undertaken the spread of measurements increased. This was expected as determining if the image is at best focus relies on an amount of user discretion.

However, the level of error is still suitably low, and would only result in a negligible cumulative error in any cross sectional area calculation.

Repeatability was also tested by repeating the measurement over the full length of the ribbon neck and a small part of the thin section (to cover both types of measurement undertaken by the program). These measurements for ribbon width and thickness are shown in Figure 3.21 and Figure 3.22 respectively.

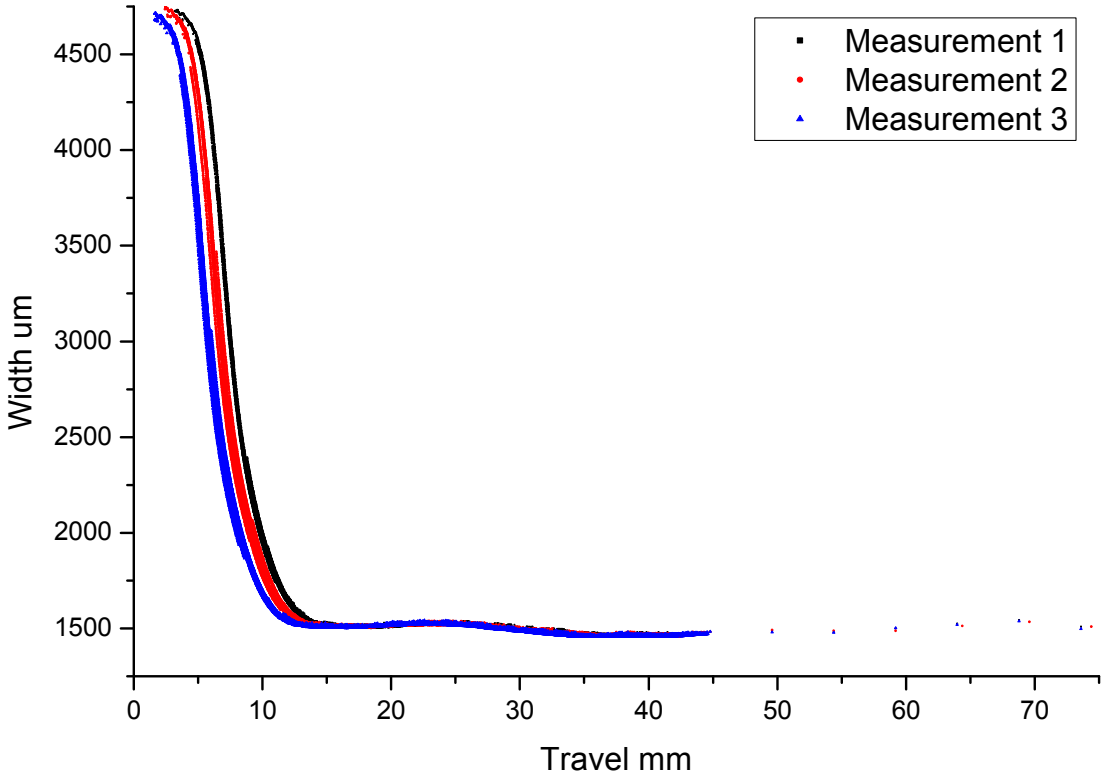

Figure 3.21 Repeatability of width of test ribbon neck and segment of thin section

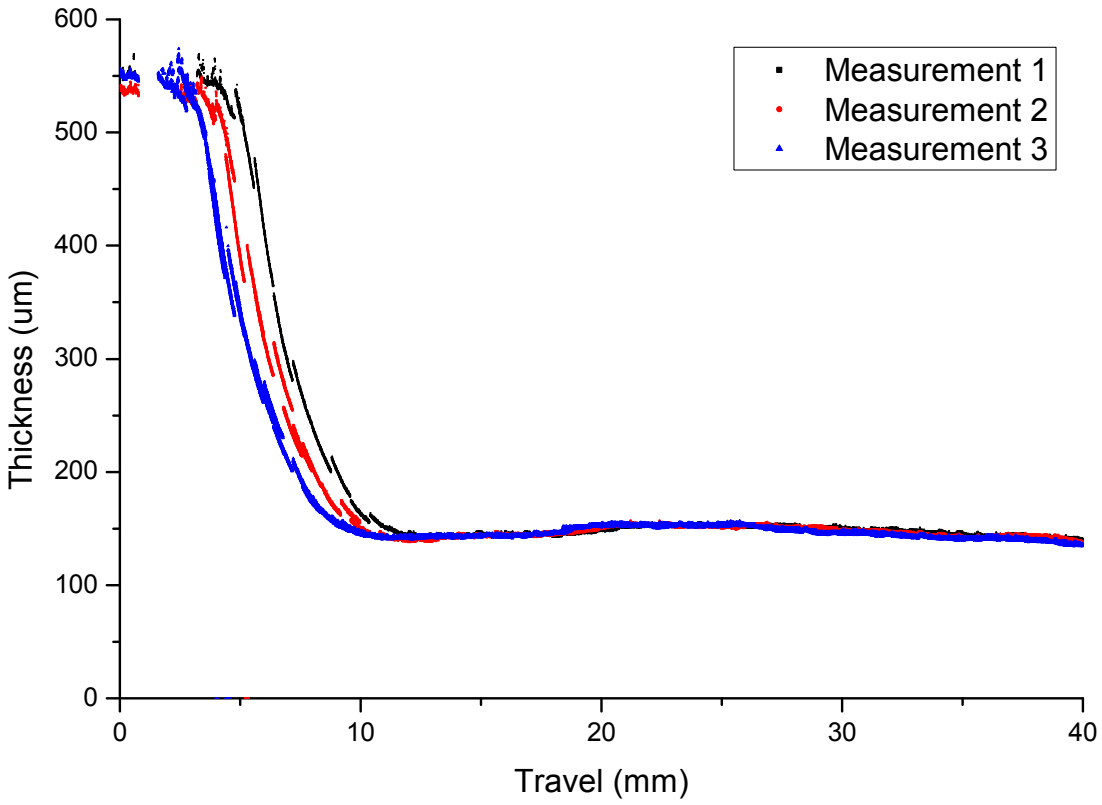

Figure 3.22 Repeatability of thickness of test ribbon neck and segment of thin section

Both width and thickness show an offset between repeated measurements – this is due to slightly different starting positions for the cameras relative to the ribbons – this was deliberate to add clarity. Some variation is also seen, most notably in the thickness measurement – this is due to the resolution of the linear encoder being more coarse than was desirable meaning that the precision of the position of the cameras along the length of the ribbon had up to 0.4 mm error. This issue will be addressed in the machines to be installed at the LIGO sites by fitting higher resolution rotational encoders to the drive motor itself, which take advantage of the 50:1 reduction gearbox to increase the actual resolution also. The measurements undertaken in the remainder of this chapter did not utilise this as its installation was not completed by the time measurements were required to feed back into the pulling machine development.

3.6.2 Proof Load Testing of Laser Pulled Ribbons

The second stage of characterising a ribbon checks that it will support the required load prior to installation in a detector suspension. This helps remove weak ribbons from the system prior to the expenditure of effort welding them into a full suspension.

A simple "proof load" test was therefore constructed to permit controlled hanging of 10 kg, or 12.5 kg masses. The machine is shown in Figure 3.23.

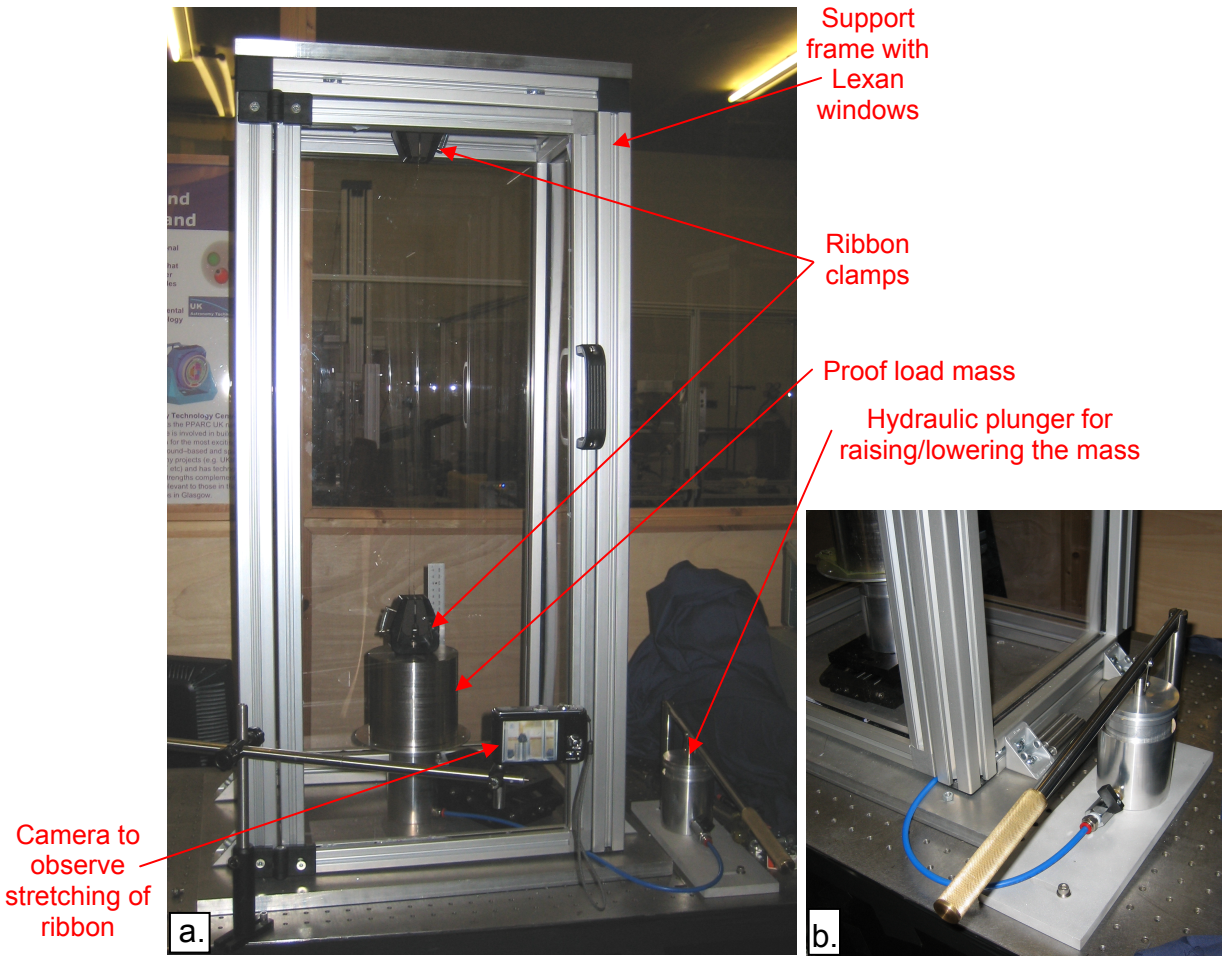

Figure 3.23 a. Proof test machine b. Close up of hydraulic mass lifter

The test is conducted in a support frame with Lexan windows and hinged door, so that the user is protected against silica shards should the ribbon break during the process. The ribbon is clamped between the top of the frame and the mass. The weight of the

mass is gently transferred onto the ribbon by means of a hydraulic plunger. This permitted controlled lowering of the mass, with the mass itself pushing the plunger down slowly when released – the plunger then being lowered further by hand to let the mass hang freely on the ribbon alone.

Stretching of the ribbon during this process was monitored by observing the position of the top edge of the mass relative to a ruler, and also photographed by a camera.

3.6.3 Vertical Bounce Frequency of Laser Pulled ribbons

3.6.3.1 Experimental Bounce Testing

The final characterisation test is a vertical bounce frequency measurement. The ribbon's width and thickness will not be entirely constant along its length meaning only an approximate bounce frequency could be calculated from an averaged ribbon width/thickness value. Therefore, to ensure the frequency is known accurately, a measurement will be performed on each ribbon before installation into a suspension.

The apparatus for this measurement is shown in Figure 3.24.

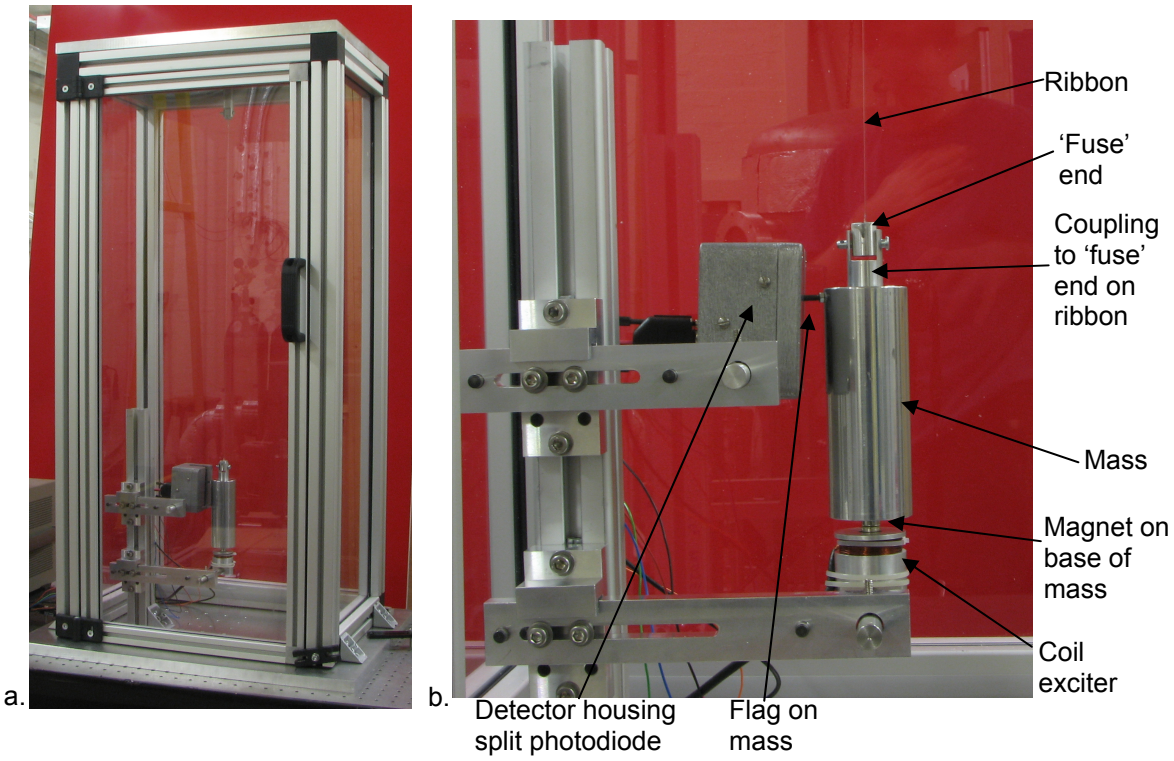

Figure 3.24 a. Ribbon bounce tester b. Close up of mass, detector and exciter

The ribbon is hung similar to the proof test in a lexan box with a universal joint used at the top attachment to ensure that the ribbon hangs freely under gravity. A small 1.1 kg mass is used and the measured bounce frequency is then scaled by the mass, to give the bounce frequency in a 10 kg load mirror suspension situation. The mass has a small bar extending from its side acting as a flag to a split photodiode detector which senses the motion of the bouncing mass. The mode is excited by use of a coil acting on a magnet attached to the bottom of the mass. The coil is driven over a range of frequencies until it coincides with the bounce frequency, where large displacement is then observed via the photodiode detector.

3.6.3.2 Calibration

Theoretical bounce frequencies assume that the supporting structure and clamping is completely stiff and rigid, and therefore makes no contribution to the vertical frequency. In reality, no support structure is totally stiff, and therefore the structure

will contribute to a difference in the observed frequency from that predicted by theory. It is necessary to calibrate this out to allow the true bounce frequency of the ribbon to be determined, and compared to the Advanced LIGO requirement.

A circular constant cross section steel suspension wire of 193 μm diameter was tested to calibrate the machine. This was chosen as it was easily compared to theory – ribbons do not have a perfectly rectangular cross section (corners round off due to surface tension and if the CO_2 laser beam is dithered incorrectly the ribbon can thin across the centre of a cross section), meaning their cross sectional area was not easily compared to a theoretical rectangular ribbon. The wire was initially held in rigid pin vice clamps, with the universal joint and actual fuse end clamps and Araldited "fuse end" attachments introduced individually. The resulting measured frequencies are shown in Table 3.2.

Configuration	Theoretical Bounce frequency (Hz)	Measured Bounce frequency (Hz)
1. Using rigid pin vice clamps	16.3	15.9 ± 0.1
2. Including universal joint	16.3	15.8 ± 0.1
3. Including universal joint, fuse ends and glue (wire shortened by 10 mm)	16.5	16.1 ± 0.1

Table 3.2 Bounce testing of steel suspension wire

These measurements showed that the structure and clamping resulted in a smaller bounce frequency measurement than would be expected from theory – this is since the clamping components aren't completely rigid. The observed difference for the third measurement of 2.5% was taken as the calibration, with this taken into account for subsequent bounce frequency measurements.

3.7 Characterisation of Typical Advanced LIGO Suspension Ribbons

Three individual ribbons were used for analysis in the characterisation equipment. The first was of a larger cross sectional area than that chosen for Advanced LIGO, as an example of a ribbon that would have a wide safety margin in terms of strength. The second ribbon had a closer cross section to that envisaged, and the third contained the shortest neck that it had been possible to pull.

3.7.1 Profiling

Dimension measurements obtained on the profiler are shown in Figure 3.25 and Figure 3.26.

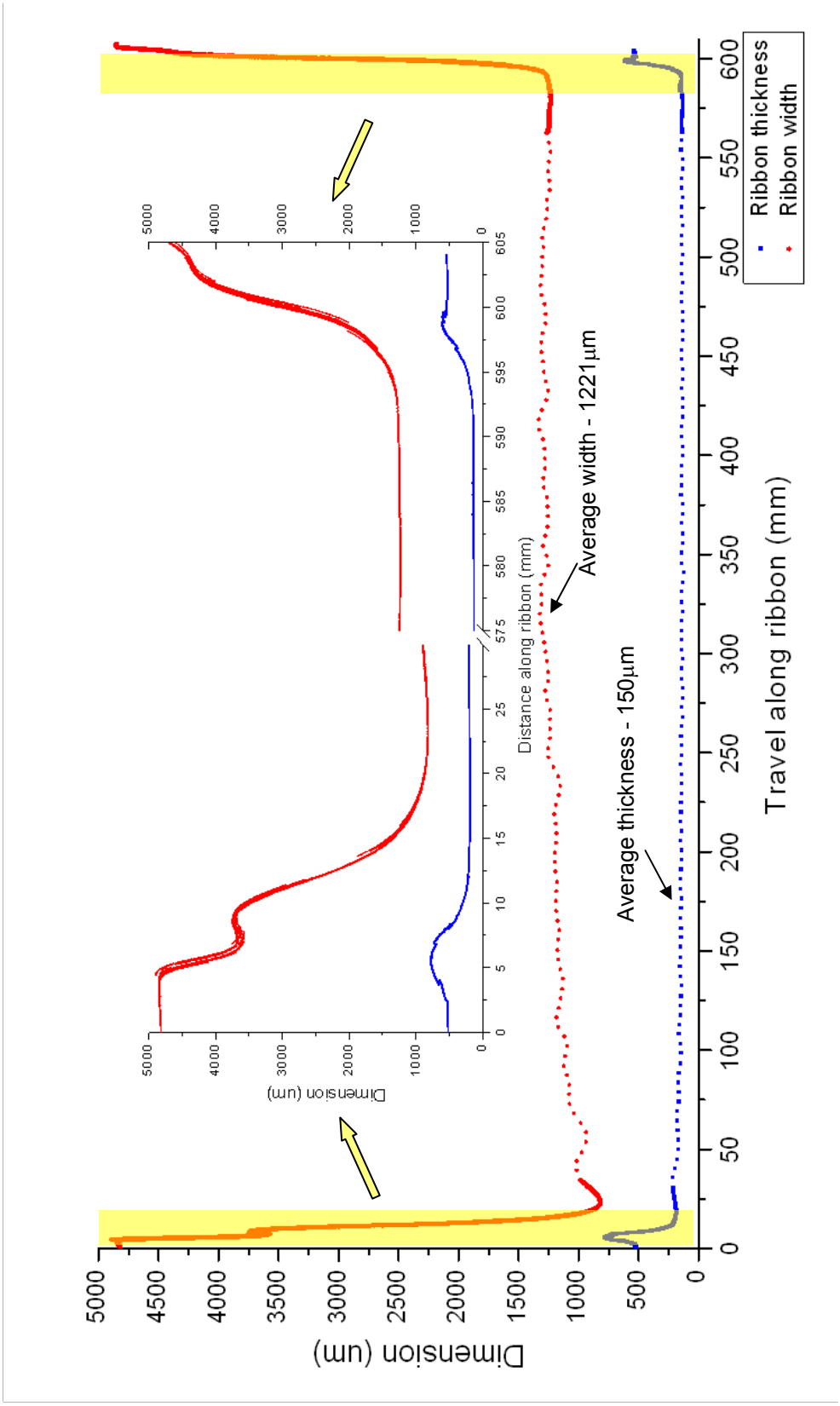

Figure 3.25 Ribbon profile of oversize Advanced LIGO ribbon. Average dimensions do not include the neck regions.

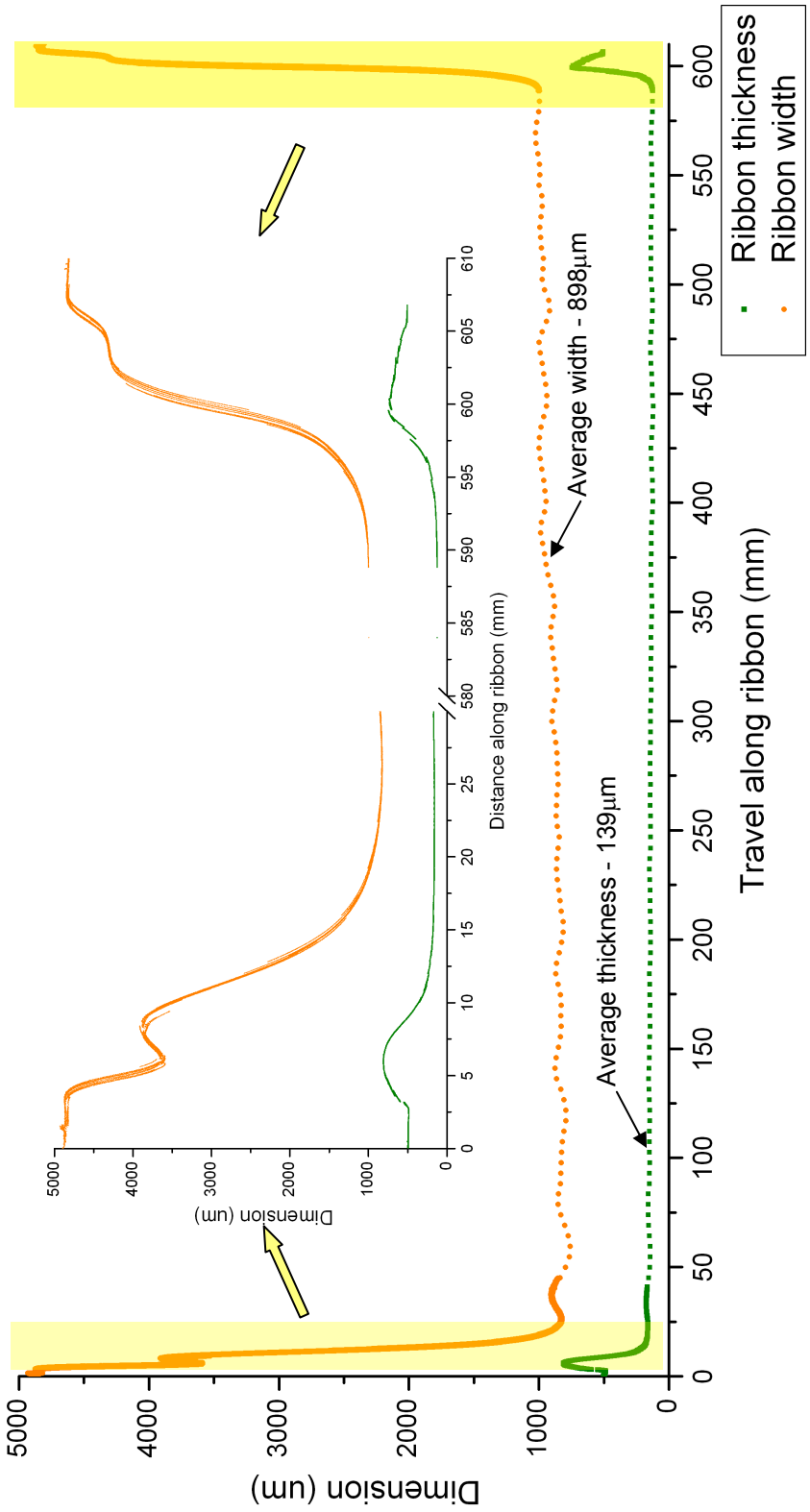

Figure 3.26 Ribbon profile of Advanced LIGO ribbon with approximately correct cross section. Average dimensions do not include the neck regions.

It can be seen that both ribbons show a number of variations in thickness along their length. Both exhibit a thin section at the end of the first neck, and this was an artefact of the pulling and heating process, which would require a refined pulling dataset to correct, and research into removing this is currently ongoing.

All the necks showed a bulging in the thickness and a corresponding reduction in width – this was a result of the initial heating to melt the silica slide – surface tension tending to pull the rectangular ribbon more circular. This is an indication that the slide was heated for a little too long before the pull commenced.

The second ribbon also shows significant deviation from the desired 0.113 mm x 1.13 mm dimensions – this was deemed to have arisen from variations in heating during the pull (as laser power stabilisation had yet to be implemented) and also the slight overheating that resulted in the tendency to pull the rectangular ribbon more circular would also result in a thicker ribbon with lower width, as seen here.

The third ribbon characterised was only a neck section as a demonstration of the shortest that had been neck pulled, and the profile of this neck is shown in Figure 3.27.

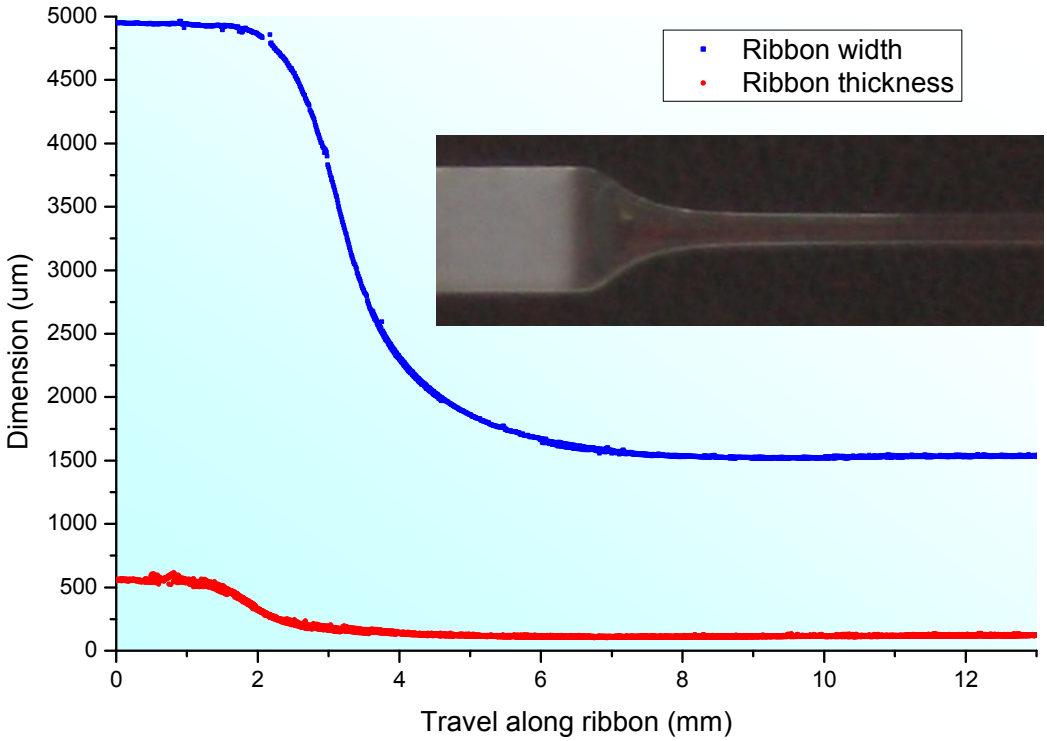

Figure 3.27 Neck profile of the shortest neck achieved.. Inset shows photograph of the actual ribbon width.

This neck shows no bulging and necks down to the thin ribbon quickly. This seems the most desirable neck as its short length will mean that less bending is likely to occur in the neck and therefore alter the dilution factor.

3.7.2 Proof Load Testing

Both oversize and accurate cross sectioned ribbons were also proof load tested to 12.5 kg and were seen to successfully hold this load for several minutes before the load was removed. Stretch was seen to be between 6 – 8 mm, as expected from theory. The mass hanging on a ribbon is shown in Figure 3.28.

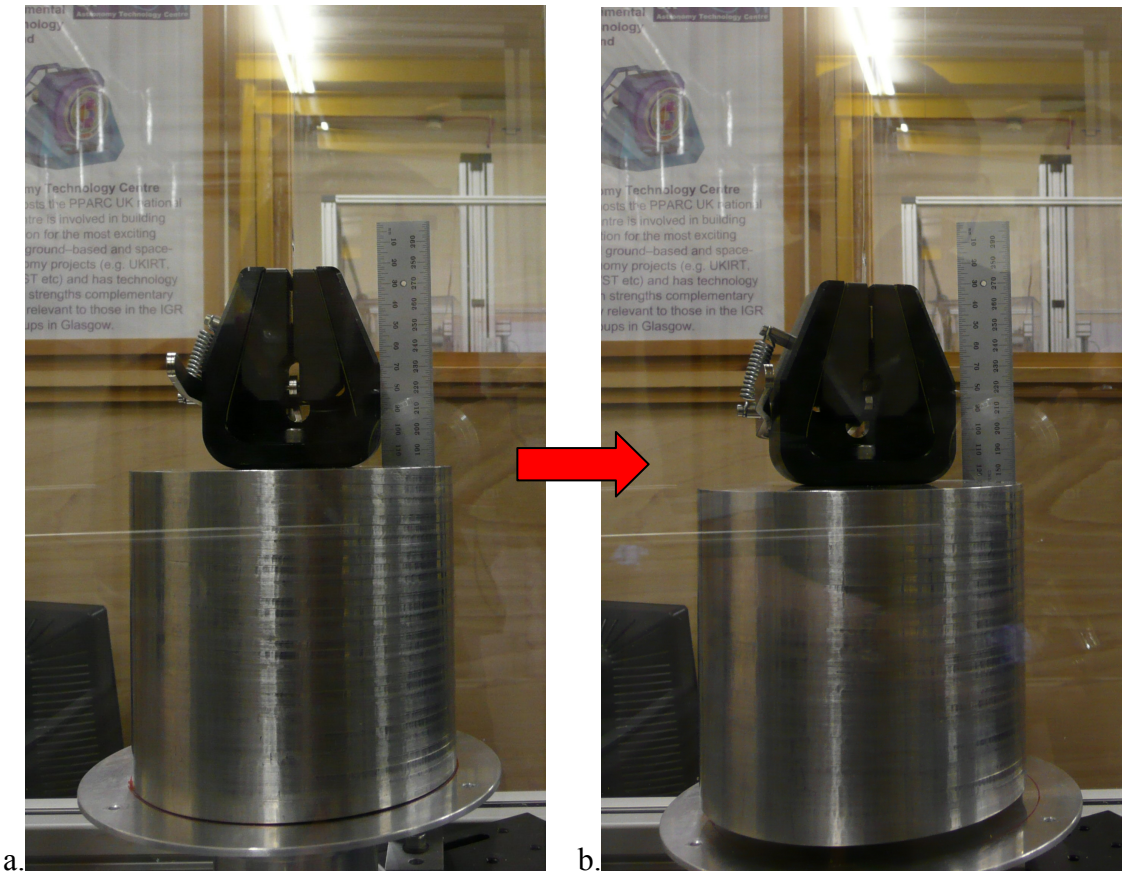

Figure 3.28a 12.5 kg mass in proof tester. b. mass hanging on loaded ribbon showing stretch of ribbon (mass is seen hanging lower than in the first picture due to stretching)

3.7.3 Bounce Frequencies

The measured bounce frequencies for the ribbons are shown in Table 3.3.

Ribbon	Theoretical bounce frequency (Hz), using average cross sectional area	Measured Bounce frequency (Hz)	Measured bounce frequency after calibration correction (Hz)	Predicted bounce frequency hanging 10 kg	Predicted Advanced LIGO bounce frequency
Oversize	22.9	21.7	22.2	7.4	10.5
Correct	18.9	17.3	17.7	5.9	8.3

Table 3.3 Vertical bounce frequency measurements for Advanced LIGO ribbons

The measured frequencies were scaled by the calibration, and then by the mass to arrive at the anticipated bounce frequency using 10 kg. In order to calculate the

predicted Advanced LIGO bounce frequency, this must then be multiplied by a factor of $\sqrt{2}$ to compensate for the fact that the upper mass in the detector suspension will be free to move also (whereas the bounce test here are with the ribbons attached to a rigid structure) [55] [143].

It is clear that the predicted bounce frequencies both lie below the required level of 12 Hz, and hence both ribbons would meet the design requirements for Advanced LIGO. The correctly cross sectioned ribbon has a lower frequency, and this is more desirable as the bounce frequency is held further from the detection band (10 Hz and above).

3.8 Conclusions

Currently more research and development into shaping ribbons correctly is ongoing, and it is clear from the results of the shortest neck characterised that good neck shapes with no bulging or deformation can be made using that additional control permitted by the laser pulling machine and its LabVIEW control program.

This chapter has also shown the development of the profiler, proof and bounce test machines. The profiler is capable of characterising the dimensions of the ribbons with high resolution and the resulting dimensional data permits valuable feedback to refine the pulling process and future fabrication tolerances.

The data was also useful for construction of FEA models of the ribbons which allowed the re-analysis of thermal noise.

Chapter 4

FE Analysis of Advanced LIGO pendulum suspensions

In order to accurately predict the dynamics and thermal noise performance of fused silica suspensions fabricated by CO_2 laser pulling, methods were developed to take ribbon dimension data from the profiler machine, and import it into the finite element analysis program ANSYS. This would allow finite element models of the ribbons, and ultimately the full mirror suspensions using such ribbon technology to be simulated. Two critical factors that were to be quantified using these simulations were the bending points of the ribbons, and pendulum suspension dilution factors, the analysis of which will be detailed in this chapter. These results were combined with a re-evaluation of the thermoelastic loss in ribbons to give a re-appraisal of ribbons compared to circular fibres.

This work was carried out in parallel to that undertaken by Rahul Kumar [144], whose focus was on modelling circular cross section fibres, with the author conducting analysis of the rectangular ribbons detailed in this chapter. Work on tapered fibres at the end of this chapter was carried out in conjunction with Dr. Alastair Heptonstall.

4.1 FEA Modelling Techniques in ANSYS

The finite element analysis program ANSYS uses numerical analysis to evaluate the dynamics (such as displacement, stress, energy) of a mechanical system under chosen constraint and/or load conditions. As will be discussed in Section 4.1.1, the system is physically modelled in ANSYS by use of keypoints, lines, areas and volumes. These entities are then laced with a lattice of points (nodes) in a process known as "meshing". These nodes define both the geometry of the model and its properties under any given constraints or loads.

"Elements" are formed from units of these nodes, and the partial differential equations that define properties such as displacement of the nodes are solved by ANSYS (by approximating to ordinary differential equations) to predict the performance of the system under given constraints or loads.

4.1.1 Creating Masses and Ribbons in ANSYS

Figure 4.1 shows the method for creating a model of a simple solid block in ANSYS. Points at vertices of the solid being modelled are created in the Cartesian plane – these are "keypoints". These points are joined by lines to form a 'wireframe' of the solid, which in turn creates areas and volumes that make up the solid. Meshing this solid produces a 3-dimensional array of nodes. 'Solid' elements are formed from nodes at the vertices of cubes or tetrahedra - for example 8 nodes at the vertices of a cube would define that cube as a single finite element such as that shown Figure 4.1. Accuracy can be gained by use of additional nodes between element vertices – this permits the solution of the analysis to show more representative deformation of the element shape.

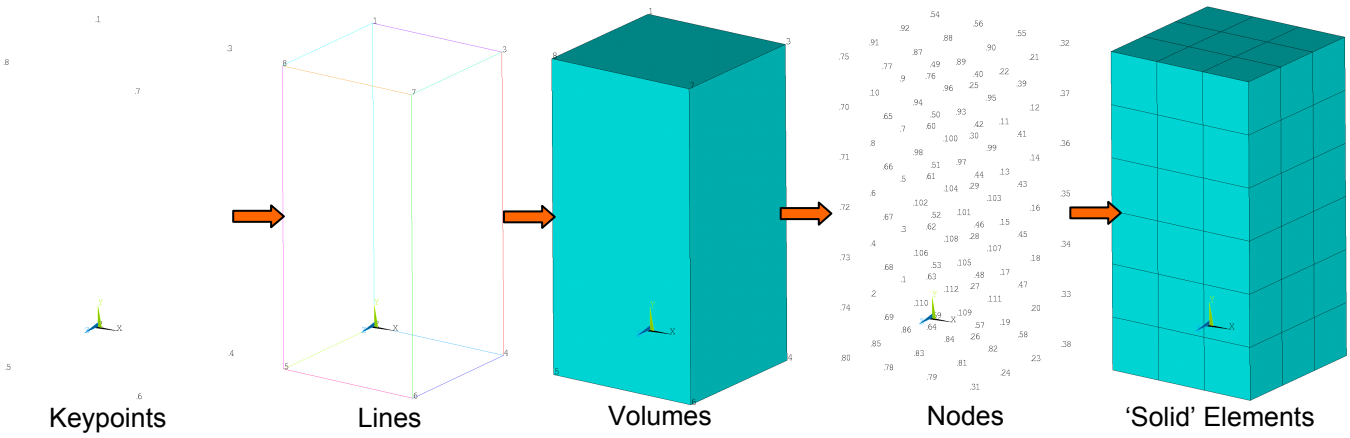

Figure 4.1 Steps taken in building a solid element model in ANSYS. Keypoints define vertices of the block, lines joining keypoints define the edges allowing a volume to be created. Nodes mesh this volume, with (in this case) each node being located at the vertex of an element.

The process of constructing entities that use solid elements can be speeded by creation of the solid that is required in a CAD program such as Solidworks [145]. ANSYS permits such solids to be imported, and this method was used to create the masses used in the pendulum models that will be discussed in this chapter. Once imported, the solids are meshed to give the finite element model.

This method can also be used to construct and mesh the ribbons/fibres. However, in order to define accurately the shapes of the necks and variation along the lengths, a great many nodes are required, which can result in very long computation times when solving the models. In some cases the number of equations that ANSYS would be required to solve was too memory intensive for a solution to be derived by a typical desktop PC.

Therefore, a different type of meshing was employed making the models far more efficient - this method of using "beam" elements is shown in Figure 4.2. Keypoints run along the central axis of the ribbon/fibre, and are joined by lines. Nodes are then generated along the lines only, without any additional nodes forming the body of the ribbon.

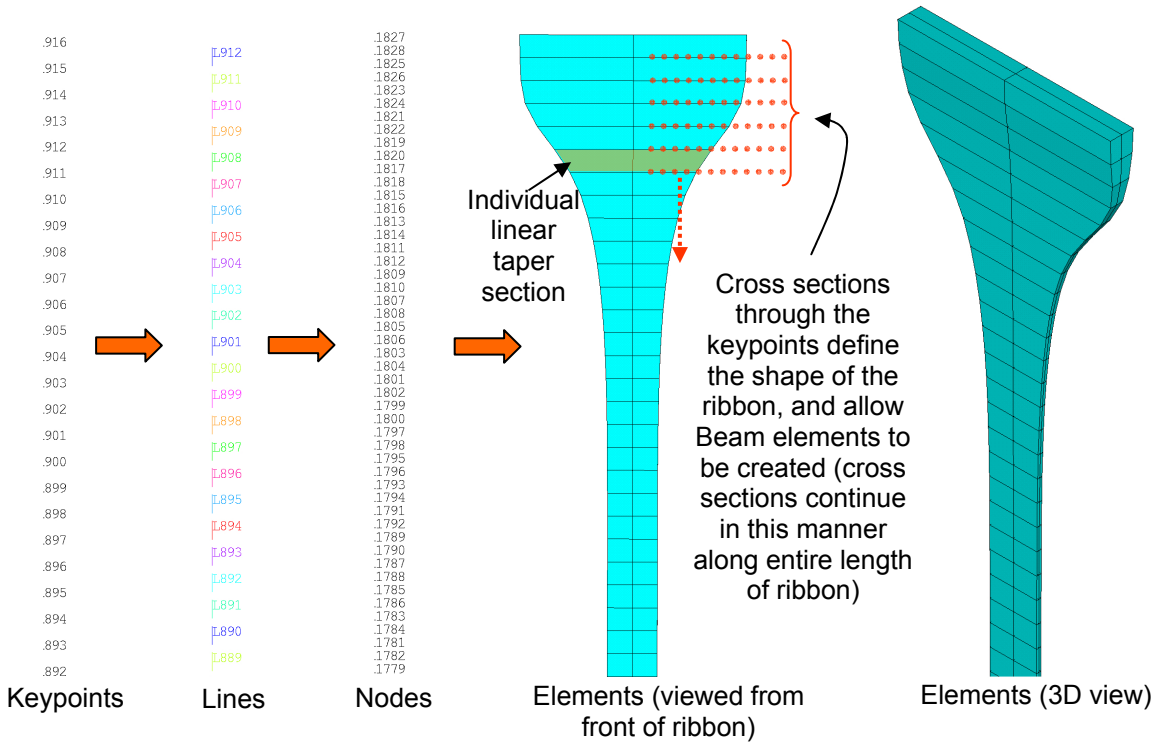

Figure 4.2 Steps used in building a beam element ribbon in ANSYS. Keypoints are defined along the ribbon length, these being linked by lines. Meshing these lines gives an array of nodes along the ribbon length, and cross sections are defined to give the ribbon its shape.

Instead, cross sections are defined centred at the keypoints. It is these sections that define the element shapes. If the cross section at one keypoint is different to that of an adjacent keypoint, a linear taper is created. By choosing a suitable resolution of keypoints, these linear tapers will approximate the real curved profiles (such as the ribbon/fibre necks).

This removes the need for a large number of nodes to define the volume of the ribbon, and hence the solving time is significantly reduced. This method can be used as the cross section through a bending beam is always perpendicular to the tangent along the axis at that point. This means that only the positions of the points along the central axis need to be explicitly defined.

Because of this, beam elements do not model shear stresses. However, the analysis undertaken in this chapter is concerned with the bending of the ribbon, and beam

elements are specifically designed to accurately model bending. Checks were undertaken for a bending beam model to ensure that the energies and stresses measured in beam element models and the resulting energies were seen to come within 2% of each other, despite the solid element version containing shear. Since bending in the ribbons/fibres would be of this type, it was concluded that the shear stresses and resulting strain energies are insignificant compared to the energy contained in bending.

4.1.2 Importing Ribbon Dimension Data into ANSYS

Initially models were simple enough that ribbons could be constructed individually for each model. However, constructing more complicated ribbons, in particular neck profiles that used real ribbon data from the dimensional characterisation machine, was found to be very difficult due to the large number of individual cross sections required to define the ribbon dimensions (in excess of 200).

ANSYS builds models using command line code that executes the procedures required to construct the FEA model. By reverse engineering the command line code for producing a simple ribbon in ANSYS, it was possible to isolate the required commands that define the cross sections of the beam elements. From this a program was written by the author in LabVIEW to generate the appropriate ANSYS command line code to produce a model using dimensional data from the profiler to define the beam element cross sections. This therefore allowed a real ribbon to be profiled and inserted into ANSYS, giving an accurate FEA representation of a real ribbon shape. The LabVIEW program is detailed in Appendix D.

A resulting ANSYS model for a ribbon, compared to the actual real ribbon and its profile, is shown in Figure 4.3. After characterising the ribbon, the results refined to use smaller number of points to reduce the number of sections required for the ANSYS

model. The LabVIEW program then converts the data into the appropriate command line code to generate the ribbon profile in ANSYS.

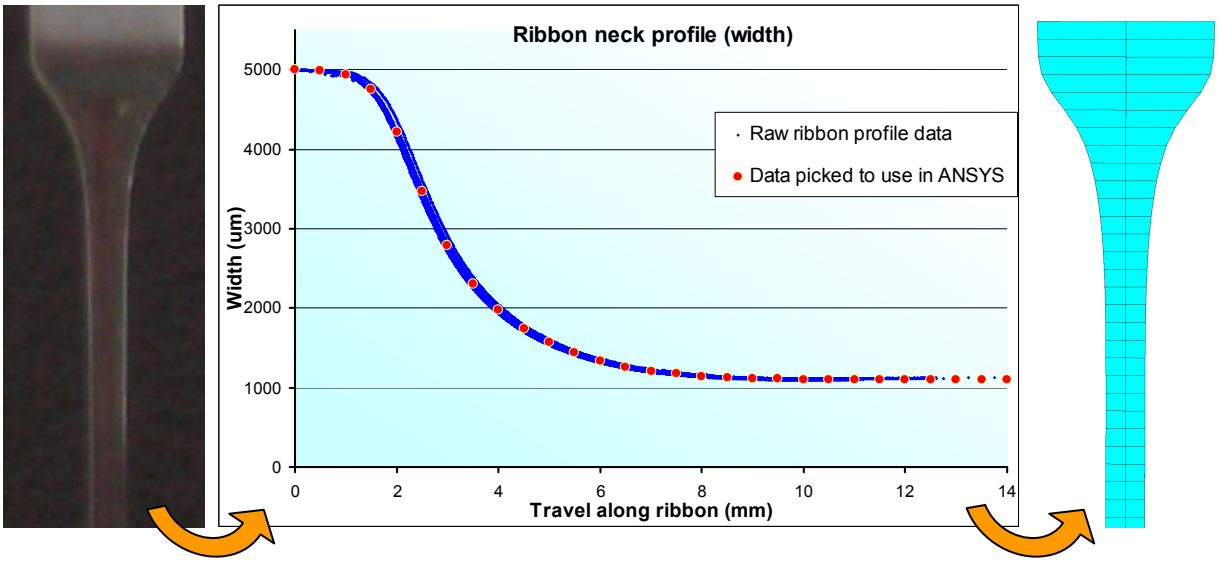

Figure 4.3 Schematic showing process of producing a neck model of a real ribbon.. Ribbon (left) is characterised in the profiler giving data shown in blue curve (only width data shown for clarity). Red data points are those chosen to create cross sections in ANSYS. Image on right shows the resulting ribbon model in ANSYS.

4.1.3 Extracting the Bending Point

Once a ribbon/fibre model is constructed in ANSYS there are several parameters that can be investigated. An important consideration for the Advanced LIGO suspensions is the position of the 'bending', or 'dynamic flexure' point of the ribbons used to suspend the test masses [138]. The bending point is defined by extrapolating a straight line back along the pendulum back from the mass. The point at which this straight line meets the vertical through the point of suspension is the bending point, as shown in Figure 4.4. The top of the ribbon is constrained in displacement and rotation, with the cross section at this point always normal to the attachment surface. All models were constrained in this manner, except the model studied in section 4.4.4 (boundary conditions for this model are discussed on p145).

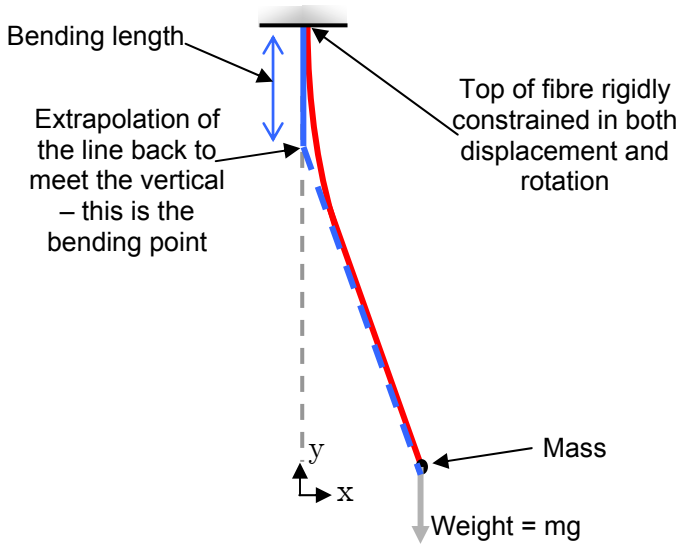

Figure 4.4 Schematic showing bending length and bending points of a pendulum fibre.

Knowledge of the precise location of the bending point is important for the dynamics of the suspension, and the chosen length between bending points of 600 mm also gives the desired bounce and violin modes with suitably dimensioned ribbons. The bending points of the ribbon are chosen to be 1 mm above the plane through the centre of mass of the test mass in Advanced LIGO - this is important for stability of the masses when hanging as pendulums [136]. This in turn influences the position at which the ears are bonded to the masses.

The bending point is calculated in ANSYS by considering a simple 'static' analysis of the ribbon/fibre in question. The static analysis first applies the load and constraint conditions to evaluate the static displacement and stresses in the system. To calculate the bending point the mass is applied and the end of the ribbon/fibre displaced horizontally by 3 cm to induce bending. The resulting bending of the ribbon/fibre will take the general form shown in Figure 4.5a, with the bending confined at the top of the ribbon/fibre and the rest of the ribbon/fibre lying on a straight line. This permits the bending point of the ribbon/fibre to be calculated by evaluation of the equation of the straight line through two nodes chosen along the straight section of the ribbon/fibre.

These are chosen such that they have a reasonable separation and are far from the upper bend in the ribbon/fibre. Typically the lowermost node and the node at the centre of the ribbon/fibre were chosen. The point where the line through these nodes intersects the vertical is the bending point.

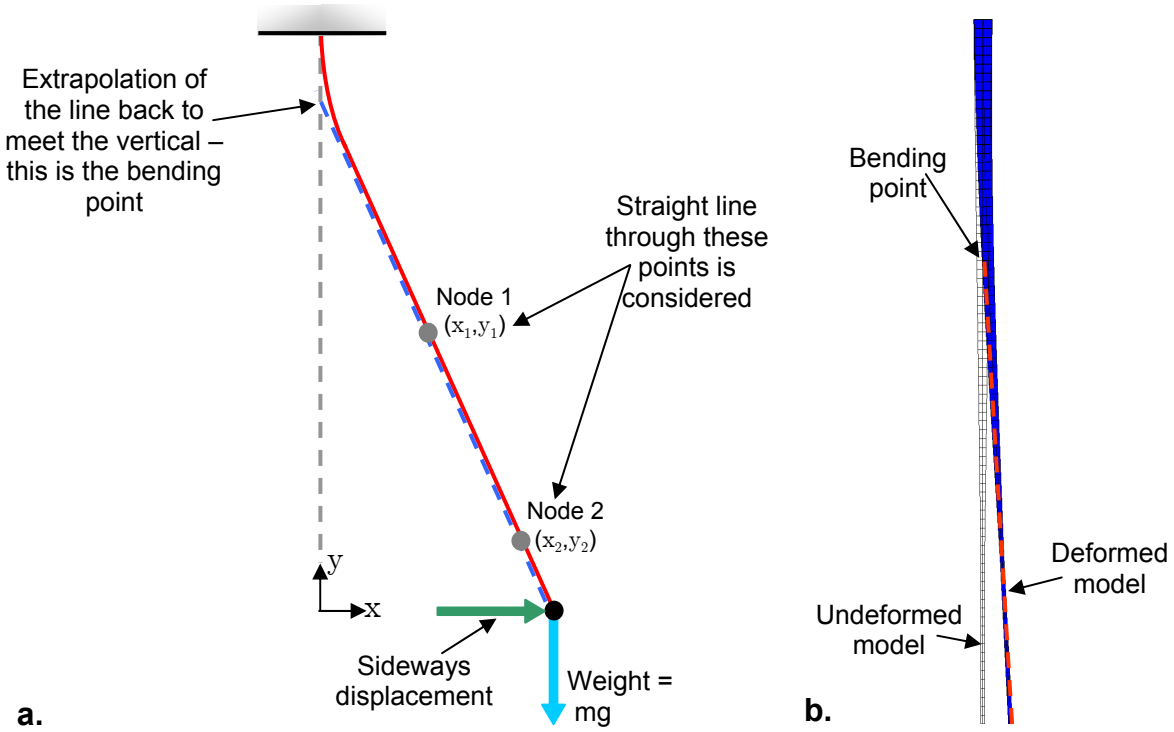

Figure 4.5a. Schematic diagram of pendulum bending (in red) and method of extracting the bending point b. Example of bending in a 15mm long taper neck in ANSYS

4.2 Calculating the dilution factor

High dilution factors were one of the main reasons for choosing rectangular cross section ribbons for use in Advanced LIGO, with high dilution giving a reduction in the mechanical loss of the pendulum suspension. ANSYS can be used to calculate the dilution factor of the pendulum system, as introduced in section 2.8.2.2. Recall the definition of dilution from equation (2.34):

$$D \approx \frac{k_{\text{gravity}}}{k_{\text{wire}}}$$

Additionally, from equation (2.30) the energy stored in the suspending wire (or ribbon/fibre) of a pendulum is:

$$E_{\text{stored in wire}} = \frac{1}{2} k_{\text{wire}} x^2$$

Similarly, the energy stored in the gravitational field is:

$$E_{\text{stored in gravitational field}} = \frac{1}{2} k_{\text{gravity}} x^2$$

Rearranging these it is immediate that:

$$D \approx \frac{k_{\text{gravity}}}{k_{\text{wire}}} = \frac{\frac{2E_{\text{stored in gravitational field}}}{x^2}}{\frac{2E_{\text{stored in wire}}}{x^2}} = \frac{E_{\text{stored in gravitational field}}}{E_{\text{stored in wire}}} \tag{4.1}$$

Extracting these energies from a modal analysis in ANSYS is comparatively simple. The energy stored in the gravitational field is simply the gravitational potential energy, $E_{\text{gravitational potential}} = mg\Delta y$. Since this energy is conserved, it is equal to the kinetic energy of the pendulum at its lowest point (namely the maximum kinetic energy of the pendulum).

Energy stored in the wire results from the additional potential energy gained in bending of the wire (primarily at the top as discussed in section 4.1.3). This manifests itself as bending strain in the wire, and therefore as bending strain energy along the length over which bending occurs.

These energies can be extracted in ANSYS by way of running a static analysis followed by a 'modal' analysis. The resonant modes of the system are extracted within the modal analysis, with the constraints and loading from the static analysis also applied. The modal analysis also permits calculation of strain energies contained in each element

for a given resonant mode, as well as the total maximum kinetic energy contained in the resonant motion of the system. From this the strain energy in the elements that experience bending can be calculated, and the pendulum dilution evaluated. Since bending will occur all along the ribbon/fibre length (albeit only a very small amount occurring along the majority of the ribbon/fibre length, and most occurring in the first few multiples of the bending length) the dilution calculation considered the strain energy in the full ribbon/fibre length.

4.2.1 Verifying the Technique

A simple model was constructed to use as a direct comparison of this technique against theoretical values calculated using equation (2.35). The model used is illustrated in Figure 4.6, and comprised a 600 mm long ribbon, of cross section 1.1 x 0.11 mm, suspending a 10 kg solid mass. A circular fibre with the same cross sectional area, and radius 200 μm was modelled by R. Kumar. 10 kg was chosen as this mimicked the loading that the ribbon will experience in Advanced LIGO. A large element density of 10000 elements was chosen to ensure that the solution was well converged (checks of convergence follow in section 4.2.2).

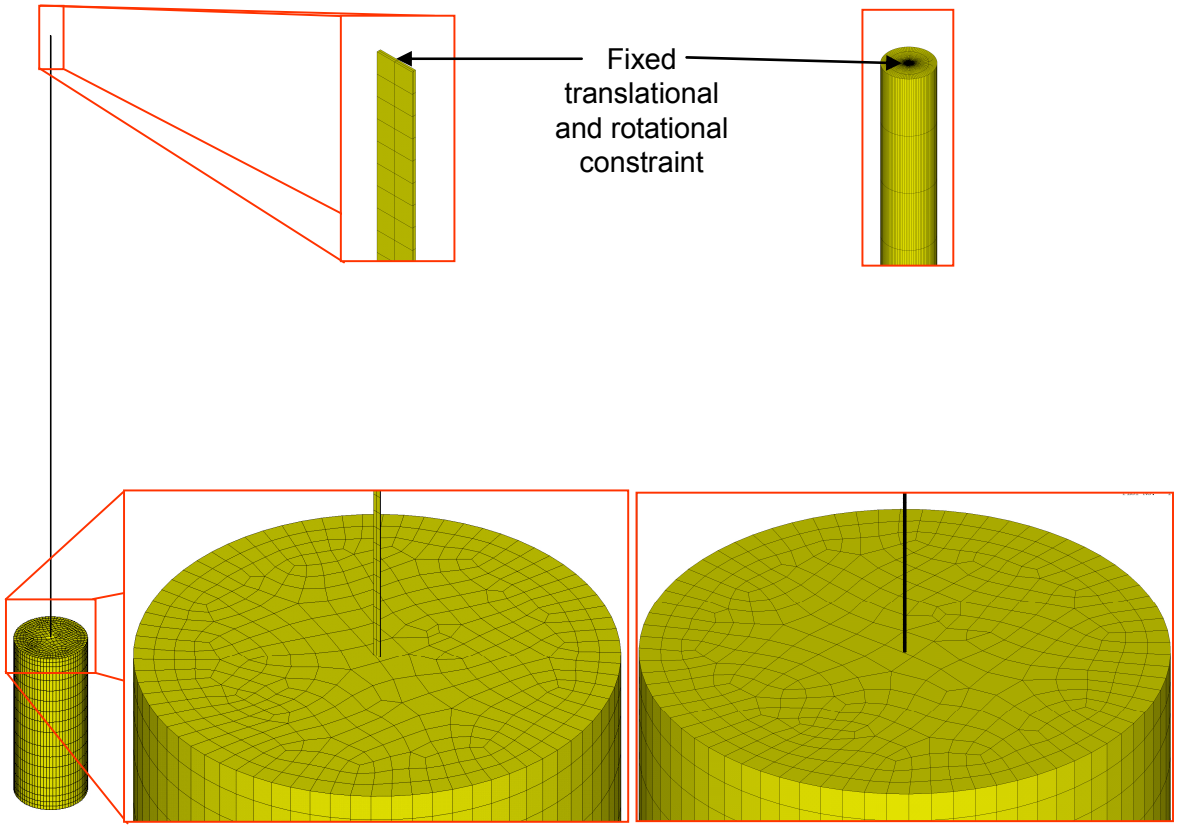

Figure 4.6 Single ribbon FEA ANSYS model, suspending mass of 10kg, with ideal ribbon containing no end necks. Insets to the right show the equivalent circular fibre as modelled by R. Kumar

The longitudinal pendulum mode was considered for the ribbon models – this is the mode in which the ribbon bending occurs in the thinner of the dimensions, as shown in Figure 4.7.

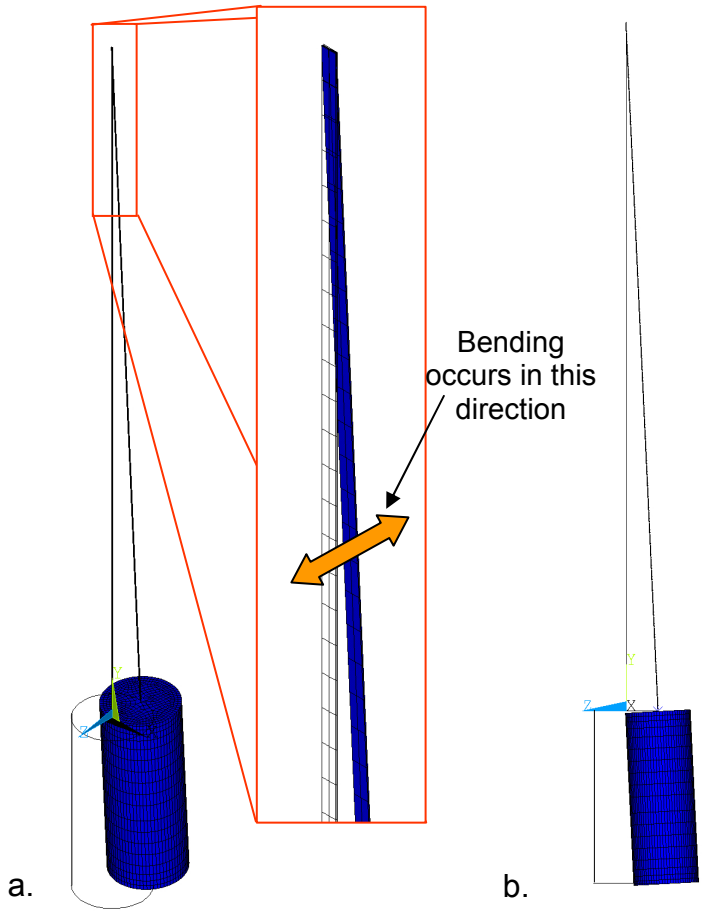

Figure 4.7 a. Longitudinal pendulum mode considered in the ribbon pendulum analysis, showing bending occurring in thin dimension. Wireframe shows pendulum equilibrium position b. Side view of longitudinal pendulum mode.

The theoretical dilution value is calculated taking the pendulum length as the length from the clamping point to the centre of the suspended mass - this accounts for the theoretical value's simplistic assumption that the mass is all contained at a point located at the end of the ribbon. The dilution results are shown in Table 4.1.

Case	Theoretical dilution value (for 600 mm long ribbon)	Theorerical dilution value (for 600 mm long ribbon, plus length to centre of suspended mass)	Dilution from ANSYS (using strain energy in bending at top)	Dilution from ANSYS (using total strain energy in ribbon)
Rectangular ribbon	4096	4511	4484	4478
Circular fibre	1250	1405	1399	1396

Table 4.1 Dilution results for simple single ribbon/fibre holding 10 kg, showing

Two dilution values were calculated in ANSYS – the first with only the energy in the bending at the top considered; the second using the total strain energy contained in the ribbon. It was seen that both values calculated using ANSYS come very close to the theoretical value, with less than 1% difference when considering the pendulum length as the ribbon length plus the distance to the centre of the mass. Results of similar accuracy were attained for the circular fibre case.

The large difference seen in dilution between ribbon and fibre can be explained by the strain energy distribution in the top of the ribbon/fibre, as shown in Figure 4.8. The top of the circular fibre can be seen to contain significantly more strain energy than the equivalent ribbon. This is because the ribbon is thinner and therefore more compliant to bending. The bending point was calculated to occur 0.46 mm from the top of the ribbon; whereas the bending point of the circular fibre occurs 0.96 mm from its top. This also confirms that the bending occurs for a greater length down the circular fibre compared to the ribbon.

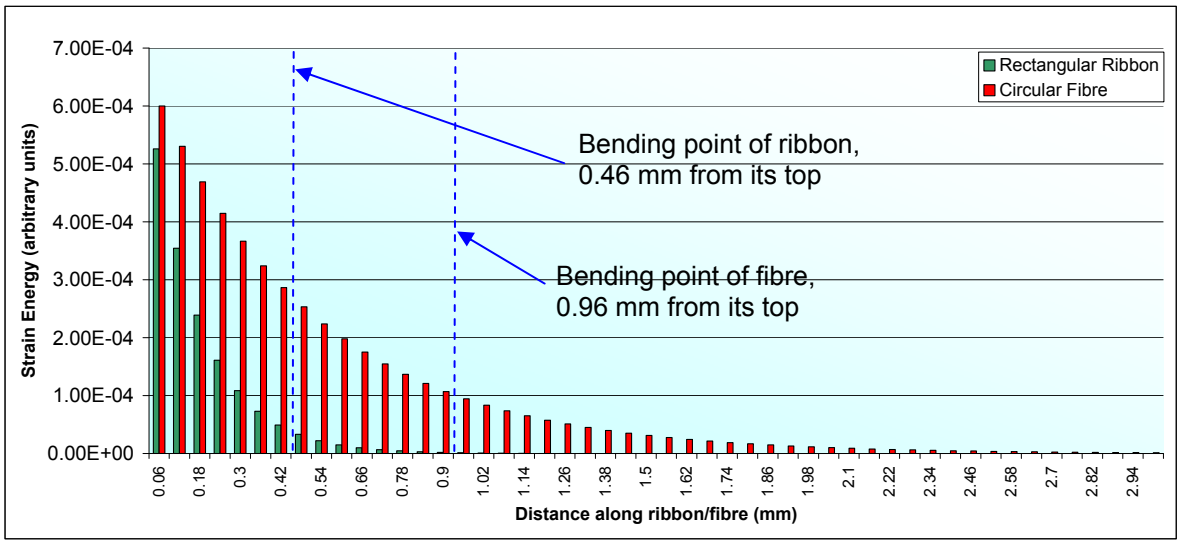

Figure 4.8 Strain energy distribution for top 3 mm of ribbon and fibre with no necks

No significant energy is seen along length of either the ribbon or fibre, and this is consistent with there being no significant bending occurring in this region

The difference between the two values calculated in ANSYS can be accounted for in a small amount of bending that occurs at the point where the ribbon/fibre joins to the mass (namely the bottom end of the ribbon/fibre). This can be seen in the strain energy distribution as shown in Figure 4.9.

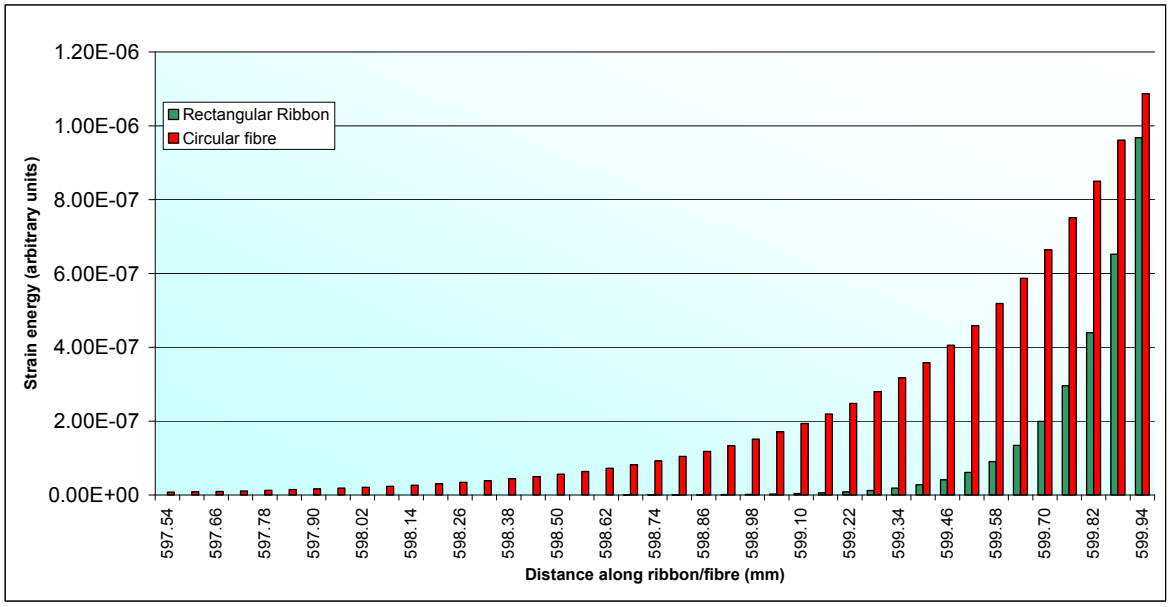

Figure 4.9 Strain energy distribution for bottom 3 mm of ribbon and fibre with no necks

It can be seen that bending occurs in a similar manner to that at the top of the ribbon/fibre. This bending occurs due to the inertia of the mass during the swinging of the pendulum. When the pendulum reaches the end of the swing, it will pitch slightly due to its inertia, as shown in Figure 4.10.

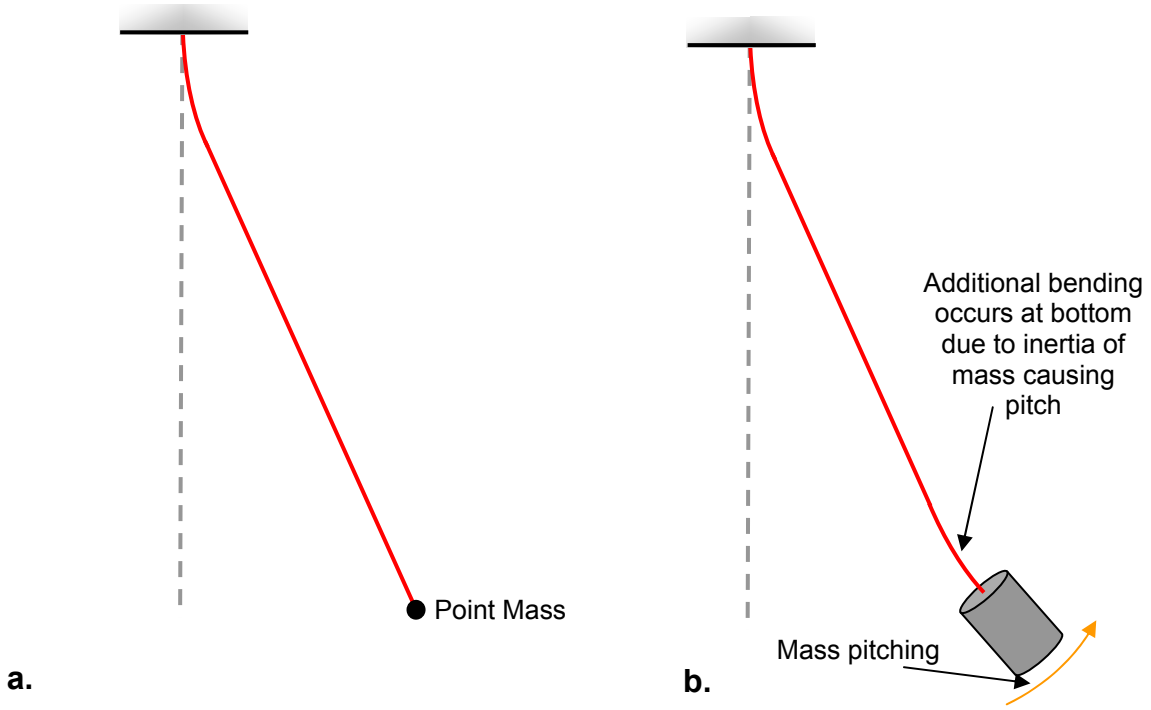

Figure 4.10 a. Theoretical system b. System as modelled in ANSYS, showing additional bending (exaggerated for clarity) and pitching of the finite sized mass.

However, the amount of strain energy that occurs due in this bend is around 600 times less than that occurring at the top. Therefore, inclusion of this strain energy in the dilution calculation will have little significant effect – as demonstrated in Table 4.1. However, this energy should be included as the effect is real – it is simply not accounted for in the theoretical calculation.

4.2.2 Checking Solution Convergence

The number of elements used in this first simple model was relatively large, and in order to check whether this was necessary the models were re-constructed using many

fewer elements, to see which element density was required to ensure accurately converged solutions.

Dilution values were sought from models with 2, 4, 6, 8, 10, 25, 50, 100, 250 elements. Models using masses with beam elements and models using solid element mass were considered (since it was envisaged that more complex masses would not be able to be constructed from simple beam elements).

The resulting convergence of the dilution solutions are shown in Figure 4.11 and Figure 4.12.

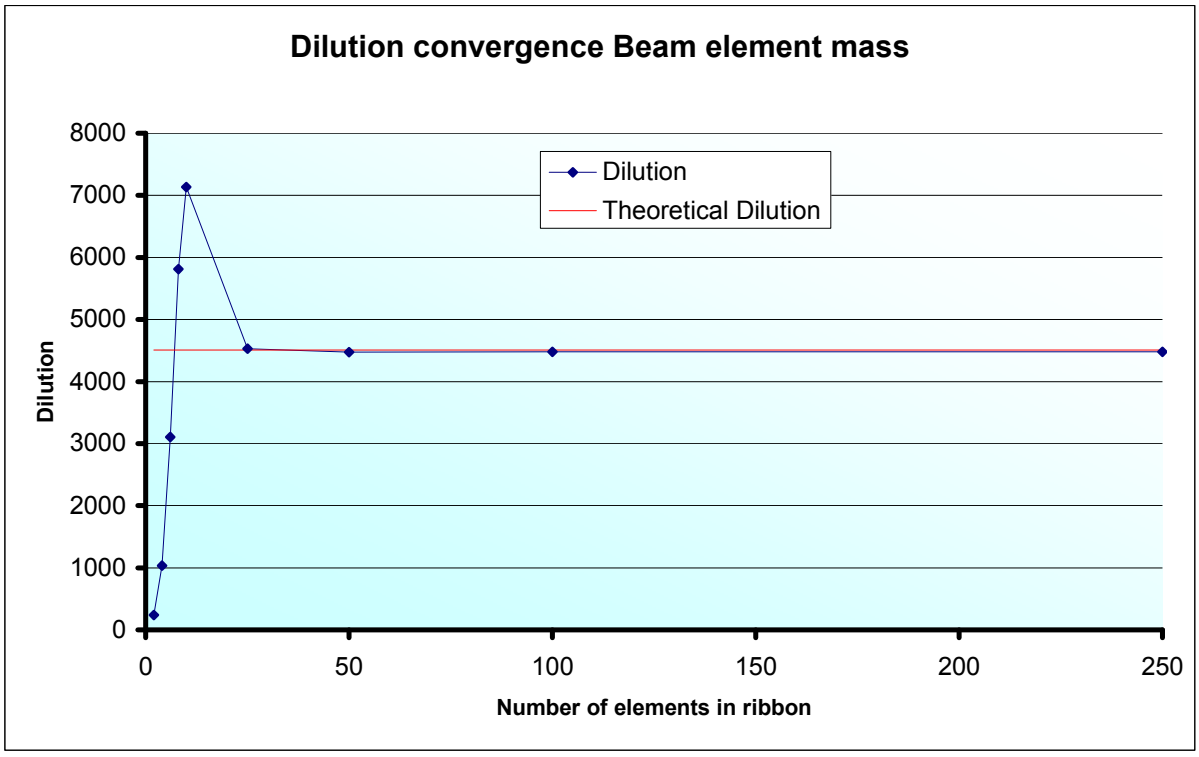

Figure 4.11 Convergence of dilution using a 10 kg mass constructed from beam elements

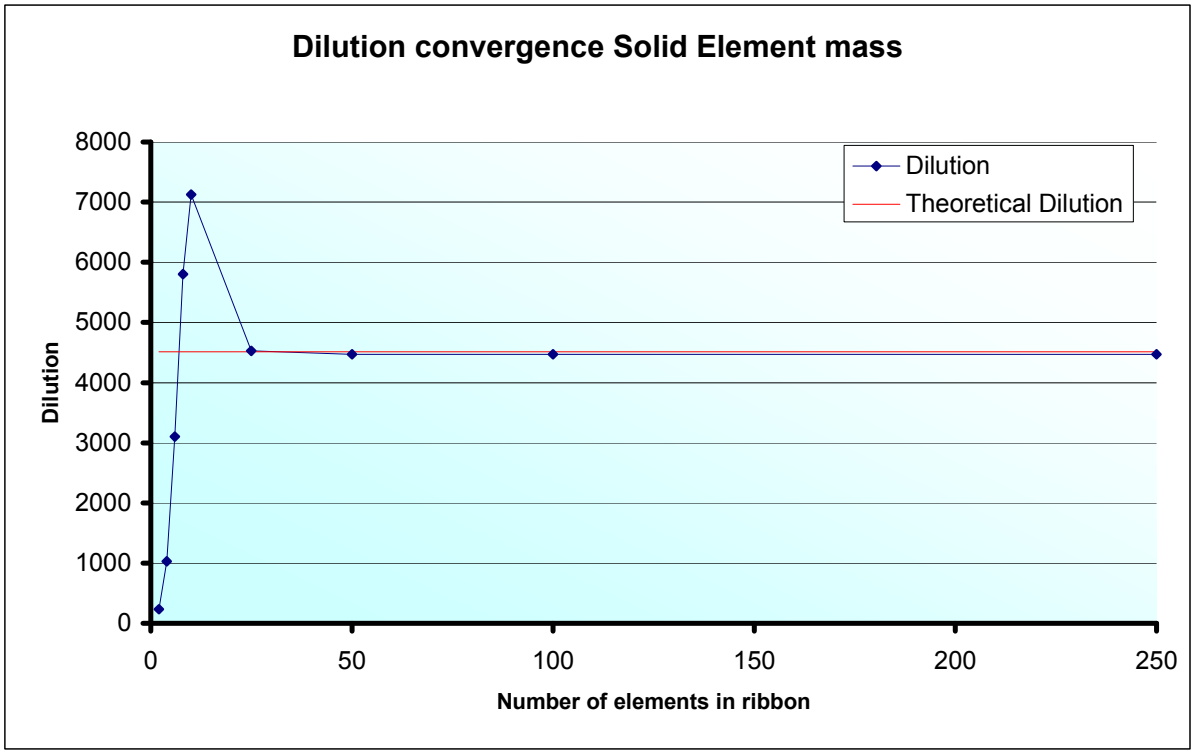

Figure 4.12 Convergence of dilution using a 10 kg mass constructed from solid elements

Both solutions were seen to be well converged to within 1% of the theoretical value once they were made up of 50 elements or greater, corresponding to an element every 12 mm along the ribbon or fibre. This convergence is the result of the strain energy in the bending converging – the kinetic energy was seen to converge much sooner. This is understandable as the kinetic energy relied primarily on the mass, and this was not changed between models.

For all subsequent models the element density for both rectangular ribbon and circular fibre models was standardised to one element every 0.5 mm for the first and last 3 cm of ribbon/fibre (equivalent to one node every 0.25 mm since additional nodes are located at the midpoints of beam elements), and one element every 5 mm in the centre of the ribbon/fibre (equivalent to one node every 2.5 mm). This was chosen to give a good resolution in the neck areas to allow different shaped necks to be applied to the ribbons/fibres with an acceptable resolution of elements to define the given neck. The

central region of the ribbon/fibre did not require such a resolution, so a node every 2.5 mm was deemed satisfactory. A model using this element density was also tested and found to be well converged to the same solution.

4.3 Single Ribbon/Fibre Models

4.3.1 Single Ribbon/Fibre with No Neck

The most trivial case of a single ribbon/fibre supporting a 10 kg mass was addressed in testing of the methods in section 4.2.1, and shown to agree closely to theoretical calculations.

4.3.2 Single Ribbon/Fibre with Linear Taper Neck of 7.5mm Length

In real detector suspensions the ribbons and fibres cannot be accurately portrayed by a simple model with no representation of the ribbon/fibre neck, as bending occurs in or around the neck region. Therefore this region is important to consider when evaluating pendulum dilution, as will be shown.

A typically short ribbon neck was chosen for analysis, being of length 7.5 mm (the shortest pulled ribbon neck had been around 7 mm, such as the profile shown in Figure 4.3). Two versions of this were studied, as shown in Figure 4.13 – the first with starting dimensions 8.4 mm x 0.84 mm, and the second with starting dimensions 5 mm x 0.5 mm. The former had exactly equivalent cross section to the circular fibre modelled by R. Kumar (Figure 4.13c). The 5 mm x 0.5 mm ribbon matched the actual start dimensions that are currently proposed for fabricating the ribbons for Advanced LIGO. The circular fibre was chosen to be of starting dimensions that would be suitable for use in Advanced LIGO – such a fibre would typically be pulled from a 3 mm diameter rod [146], necking down to a 0.4 mm diameter fibre.

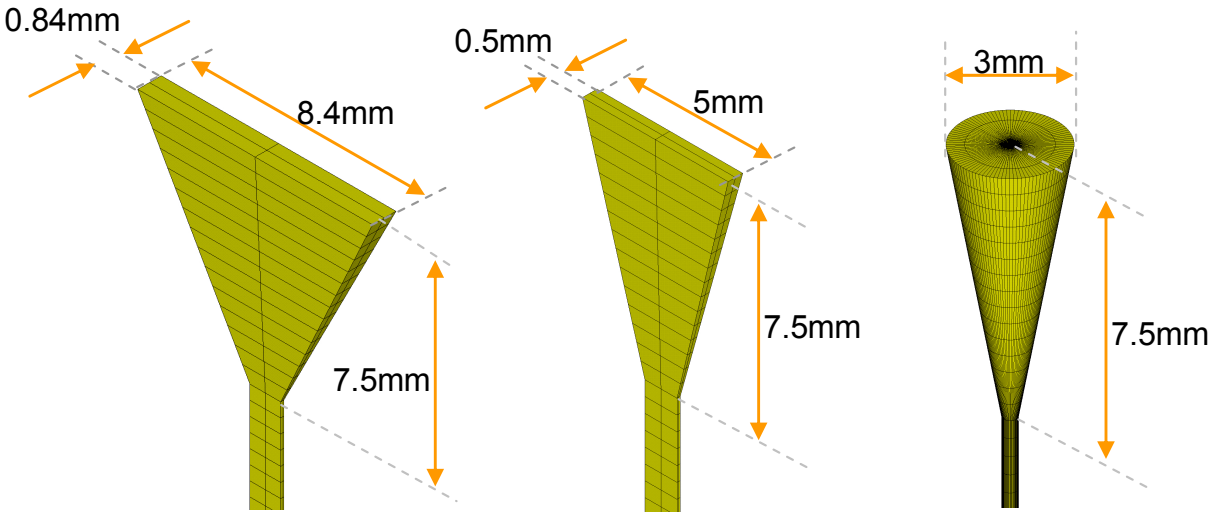

Figure 4.13 a. Linear taper neck used in FE models, with cross sectional area identical to circular fibre. b. Linear taper neck with actual start dimension of 5 x 0.5 mm. c. Comparison circular fibre, as modelled by R. Kumar. b. and c. have identical cross sectional area throughout.

The remainder of the model was identical to that studied in section 4.2.1. The resulting dilution factors and bending points are shown in Table 4.2.

Circular fibre				Rectangular Ribbon			
Case	Bending point (distance from neck start)	Theoretical Dilution (using bending thickness)	ANSYS Dilution	Case	Bending point (distance from neck start)	Theoretical Dilution (using bending thickness)	ANSYS Dilution
7.5 mm Linear taper neck	8.02 mm	1405	**872**	7.5 mm neck, 8.4 x 0.84 mm	5.82 mm	721	**720**
				7.5 mm neck, 5 x 0.5 mm	3.77 mm	588	**590**

Table 4.2 Dilution factors for 7.5 mm taper necked fibres and ribbons

It is clear that addition of necks to both ribbon and fibre reduces the resulting dilution over that observed in the simple no-necked case. More notably, it can be seen that for both ribbons the dilution is actually lower than that observed for the equivalent circular fibre. Theoretical dilution factors were also calculated for comparison, with the second area moment of the ribbon/fibre cross sectional dimensions at the bending point used in the calculation. As demonstrated in Table 4.2 the theoretical dilution and the

dilution derived from ANSYS agree closely, whilst the theoretical dilution for the circular fibre is the same as for the non-necked case studied in section 4.2.1.

Explanation for these phenomena is forthcoming when the stress distribution (Figure 4.14) and strain energy distribution within the neck region are analysed.

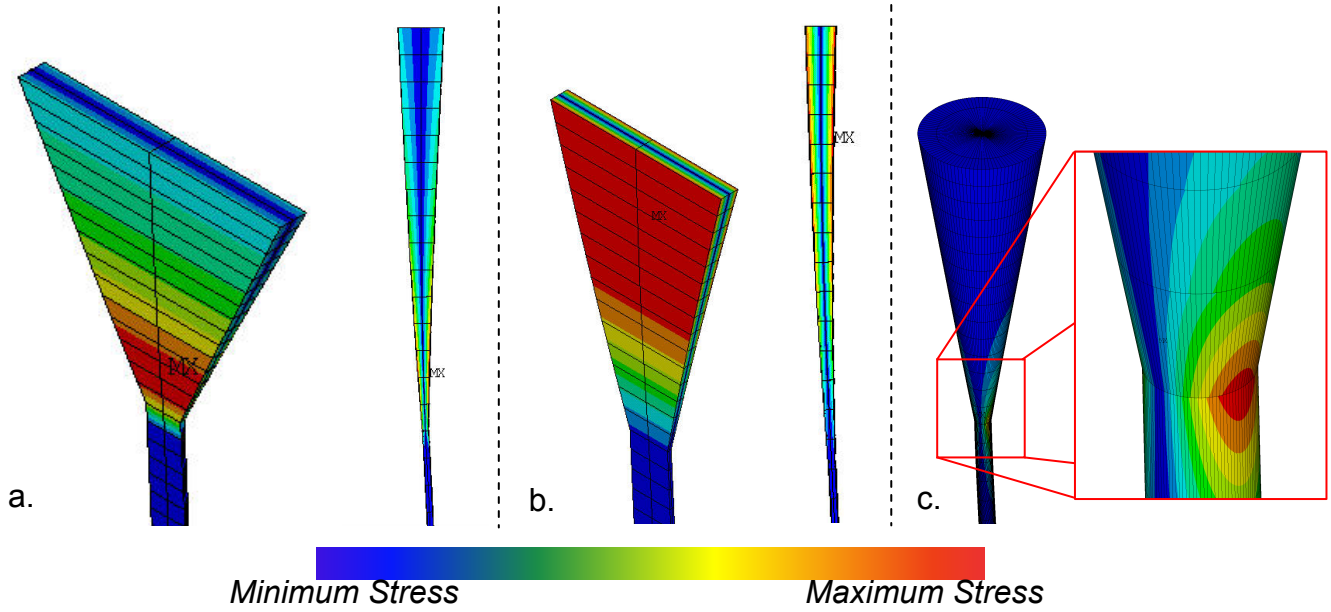

Figure 4.14 a. Stress distribution in 8.4 x 0.84 mm start dimension ribbon neck showing 3D and side views. MX denotes the position of maximum stress b. Stress distribution in 5 x 0.5 mm start dimension ribbon neck showing 3D and side views c. Stress distribution in circular fibre. Inset shows that the stress is more localised at the end of the neck

It is evident that the points of maximum stress occur in different positions for ribbons and circular fibres. In the case of the circular fibre, the maximum stress occurs at the end of the neck. For the ribbon of equivalent cross sectional area, the maximum stress occurs above this point, and this is indicative of the majority of the bending occurring within the neck region. This happens because the fibre is more resistant to bending within the neck, as the start and end diameters are greater than the start and end thicknesses of the ribbon of equivalent cross sectional area.

These observations are re-enforced by the observed strain energy distribution as shown in Figure 4.15. The circular fibre experiences the most bending outwith the neck, and

therefore has the most bending strain energy contained beyond the end of the neck. By contrast, both ribbon cases demonstrate significantly more bending strain energy in the neck region, and therefore the total strain energy due to bending is greater in the ribbons, with the 5 x 0.5 mm ribbon displaying the most bending strain energy, and consequently the lowest pendulum dilution.

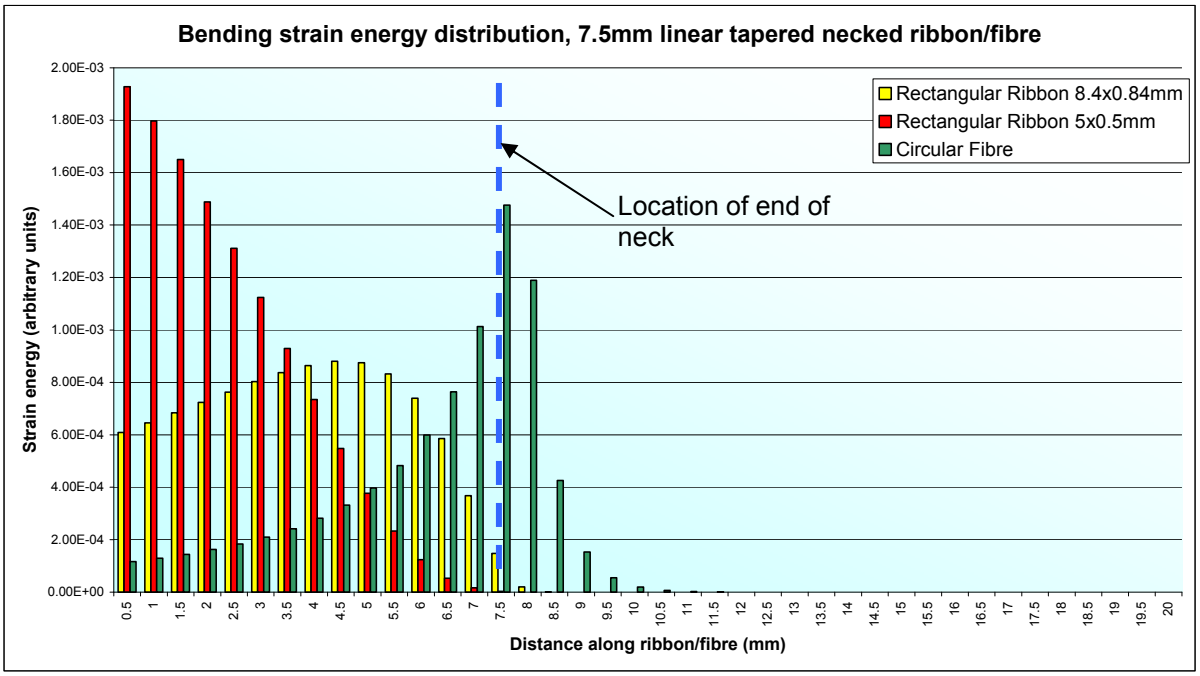

Figure 4.15 Bending strain energy discribution in 7.5 mm linear taper necks

It was therefore clear that necked ribbons and fibres required additional investigation. Given that the chosen neck length of 7.5 mm was seen to be around the shortest produced in real life, analysis of a neck double the length was undertaken to investigate the impact that this longer neck would have on dilution.

4.3.3 Single Ribbon/Fibre with Linear Taper Neck of 15 mm Length

The 15 mm linear taper necks modelled in ANSYS are shown in Figure 4.16, using the same element density as before. Again, the pendulum model was identical to the simple case in section 4.2.1, with the only change being the addition of the necks to the ribbon/fibre.

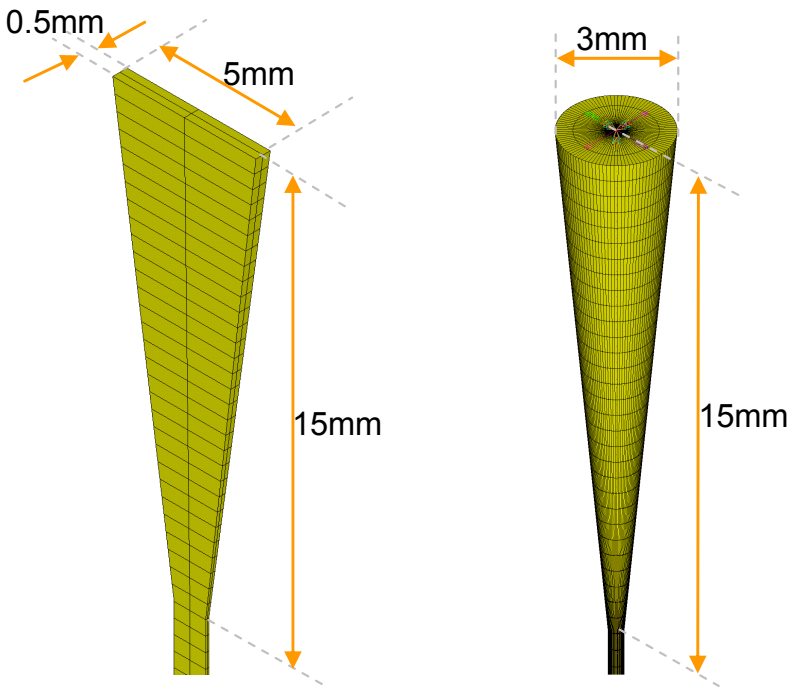

Figure 4.16 a. Linear tapered ribbon neck of 15mm b. Comparison neck as modelled by R. Kumar

The resulting dilution factors and bending points are shown in Table 4.3.

	Circular fibre			Rectangular Ribbon		
Case	Bending point (distance from neck start)	Theoretical Dilution (using bending thickness)	ANSYS Dilution	Bending point (distance from neck start)	Theoretical Dilution (using bending thickness)	ANSYS Dilution
15 mm linear taper neck	13.47 mm	453	**401**	4.89 mm	390	**381**

Table 4.3 Dilution factors for 15 mm taper necked fibres and ribbons

Again, it was observed that the circular fibre had a higher dilution than the ribbon. Plotting the stress distribution (Figure 4.17) shows that the ribbon experiences the most stress at the very start of the neck. The fibre shows that its maximum stress is still located at the end of the taper neck section, although a greater amount of stress is visible within the neck section as compared to the 7.5 mm necked model (Figure 4.14c.).

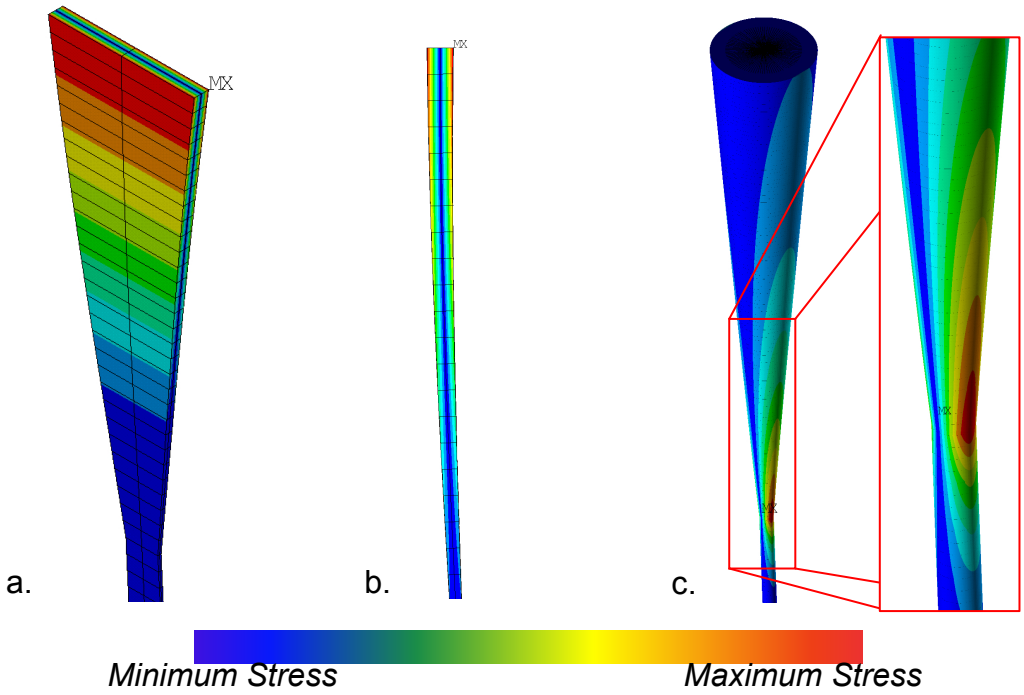

Figure 4.17 a. Stress concentration in 15 mm long linear taper ribbon neck. b. Ribbon viewed from side, showing stress concentration through its thickness. c. Comparison circular fibre, showing a more localised stress concentration, with maximum located at the end of the neck section.

The bending strain energy distribution (Figure 4.18) confirms that the longer necked fibres experience more bending in the fibre neck; whilst all the bending strain energy of the ribbon is contained within the neck. The total strain energy due to bending in the ribbon case is slightly greater resulting in the slightly lower observed dilution. The amount of strain energy contained in the circular fibre is also increased over the 7.5 mm necked case, due to increased bending occurring within the neck (evidenced from the bending point of 13.47 mm, which lies within the 15 mm neck).

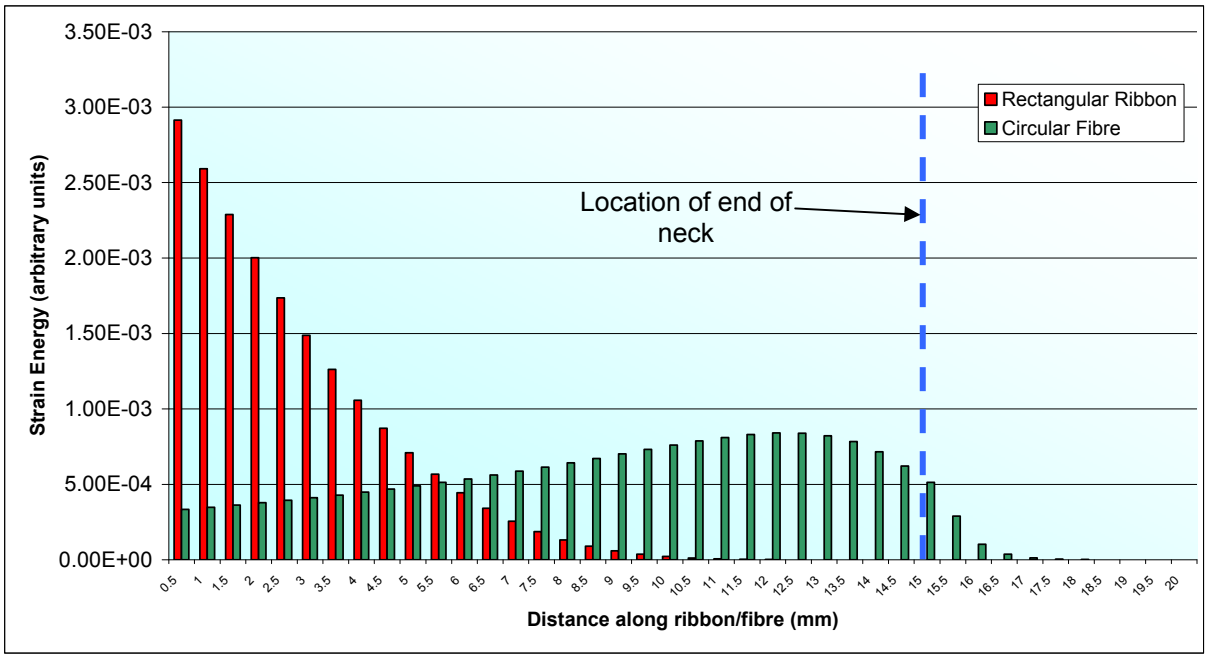

Figure 4.18 Bending strain energy discribution in 15 mm linear taper necks

4.3.4 Discussion

A summary of the dilution values determined for the simple no-neck and the linear taper necked ribbons/fibres are shown in Table 4.4.

	Circular fibre		Rectangular Ribbon	
Case	ANSYS	Theory (using bending thickness)	ANSYS	Theory (using bending thickness)
No Neck	1396	1405	4478	4511
7.5 mm Linear taper neck	872	1405	590	588
15 mm Linear taper neck	401	1130	381	390

Table 4.4 Summary of dilution factors for non-necked and taper necked ribbons and fibres

For both the necked cases studied, the dilution factor for the ribbon was actually lower than that for the corresponding fibre – a result which was not anticipated given the fact that for a no-necked model the ribbon gave far superior dilution. Additionally, Willems [147] had demonstrated that simple necked circular fibres showed a decrease of

around a factor of 2 from the no necked cases – the results shown here concur with this. The ribbons here were seen to undergo a much greater decrease in dilution than the equivalent fibres.

It was clear from the analysis of the stress and strain energy distributions that the reason for this is that for the simple non-necked case the ribbon is much more compliant to bending (as it is almost four times thinner than the fibre diameter). However, when necks are introduced this additional compliance actually penalises the performance of the ribbon, as it experiences much greater bending within the neck region, allowing more bending strain energy to reside there. In contrast, the circular fibre's greater diameter counters this effect by increasing the stiffness through the neck and reducing the bending that occurs there. Thus, the strain energy that resides in the neck is reduced.

An important question that immediately arises from this analysis is "for what neck length do ribbons have a superior dilution to the fibre?". This was addressed in the following section.

4.3.5 Dilution as a Function of Taper Length

Further models were constructed to evaluate the dilution for 2.5, 5, 10, 12.5 mm long linear taper necks. Additionally, for the ribbon case 0.5 mm and 1 mm long neck cases were studied to give a better indication of the trend near the ideal no-necked case. This was analysed for the cases where the ribbon had equal cross sectional area to the fibre (with ribbon neck starting dimensions 8.4 x 0.84 mm), and the more realistic case where the starting dimensions were 5 x 0.5 mm. The results are shown in Figure 4.19 and Figure 4.20 respectively.

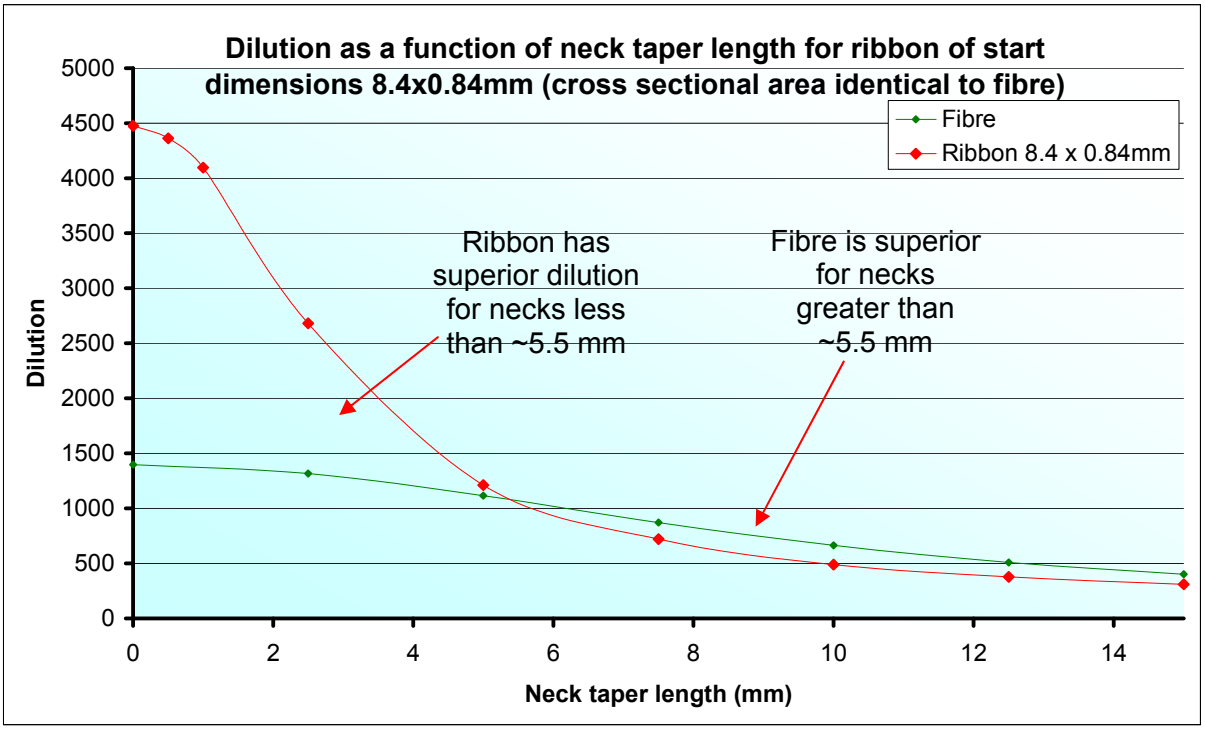

Figure 4.19 Graph showing dilution as a function of linear taper neck length for both ribbon and fibre, where cross sectional areas are identical through the taper.

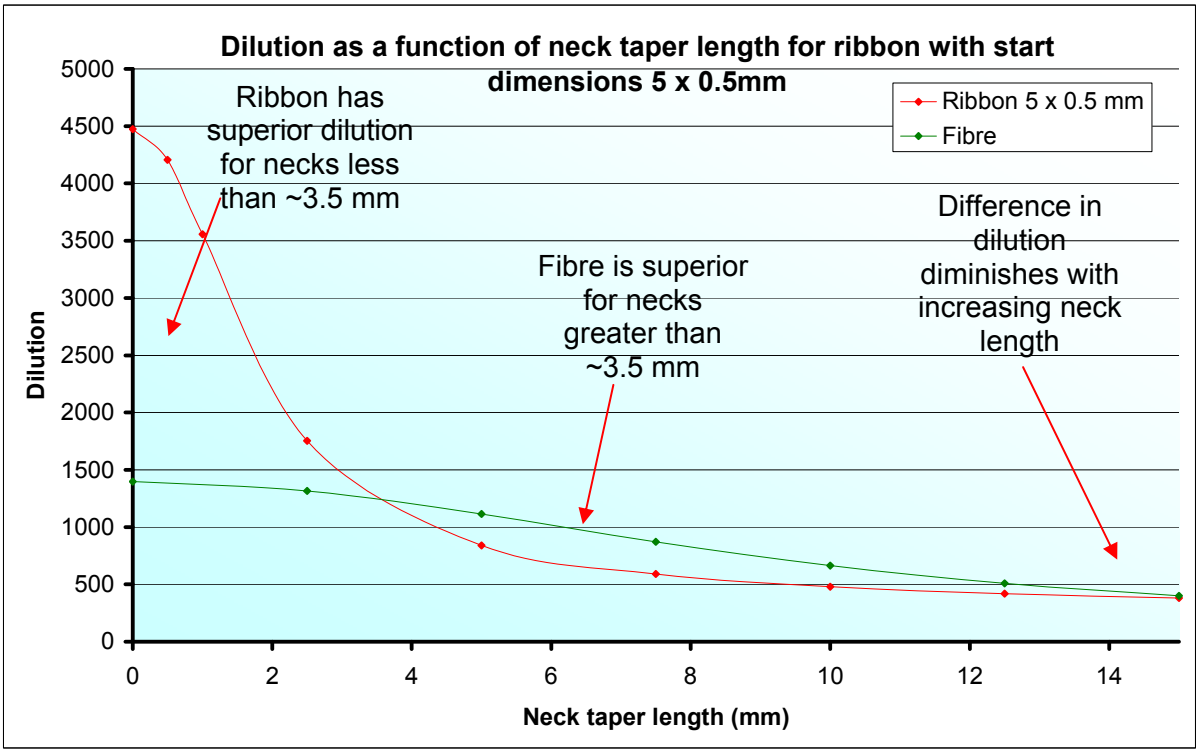

Figure 4.20 Graph showing dilution as a function of linear taper neck length for both ribbon and fibre where the start dimension of the ribbon is taken as the real life 5 x 0.5 mm.

These results show that the ribbon dilution falls sharply as the neck length increases from zero, and falls below that of the equivalent fibre for necks longer that approximately 5.5 mm in the first case and 3.5 mm in the second case. By contrast, the dilution of the fibre falls close to linearly throughout the range studied. As the necks become much longer the difference between the ribbon and fibre becomes less pronounced, as in both cases bending occurs mostly in the neck region.

This result is significant as it shows that while ribbons only have a superior dilution when necks are small. If the ribbons currently proposed for use in Advanced LIGO have necks that are too long, they will likely have inferior noise performance to the equivalent fibre. This is a result of an increased amount of bending strain energy being contained in the ribbons since the bending points are further up the necks that the equivalent fibres.

Since the geometry of the necks clearly has significant influence on the expected level of dilution, the final set of models investigated a more realistic Advanced LIGO suspension scenario, bringing in the real experimental ribbon profiles presented in section 3.7.1.

4.4 Advanced LIGO Models

Real suspensions are more complicated than the simple single ribbon/fibre models examined so far. Therefore the models were extended to use 4 fibres, using the correct Advanced LIGO masses, and ultimately including accurate finite element models of the ears on the sides of the test masses onto which the ribbons/fibres are welded (for detail of ears and suspension see Figure 3.4).

4.4.1 No Necks, Simple Ears

The first batch of 4 ribbon/fibre models were used to again confirm that the modelling technique performed as expected, the most simple case possible was analysed, with no

necked ribbons/fibres and the mass ears represented by simple blocks, as shown in Figure 4.21.

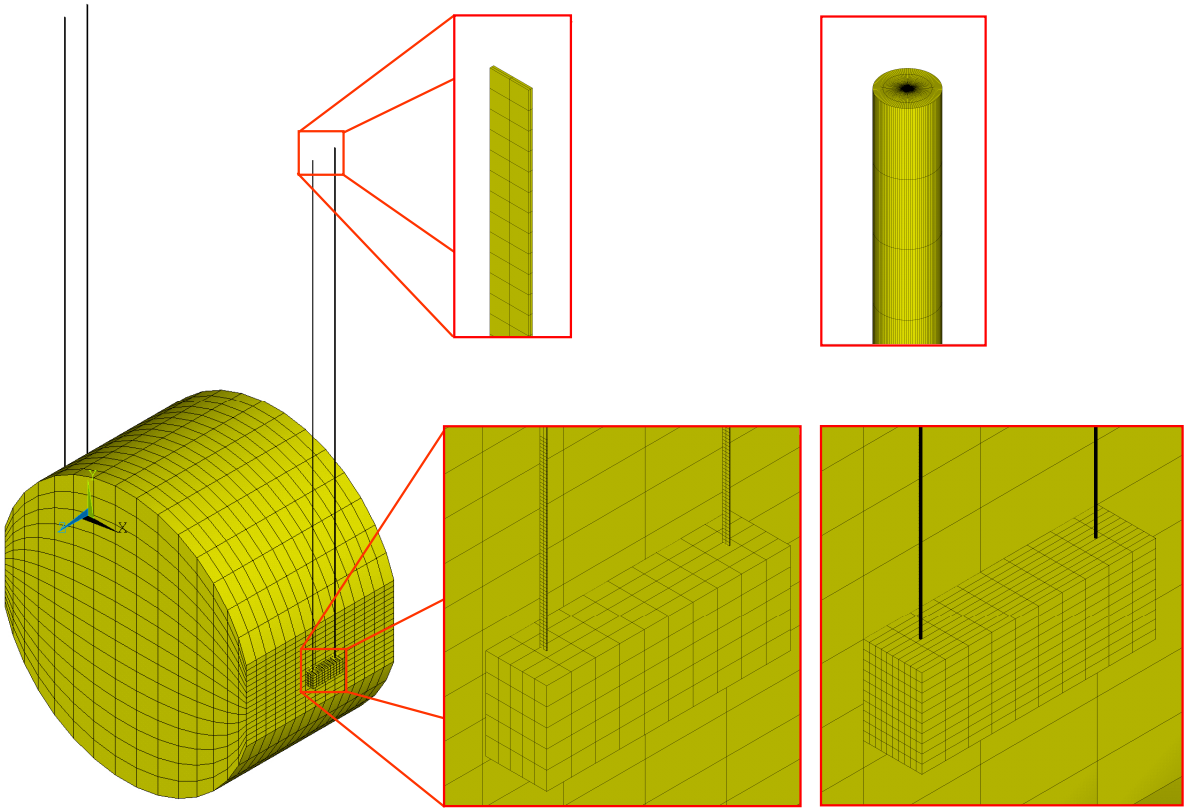

Figure 4.21 Simple model of Advanced LIGO suspensions, using simplified ears, and ideal no-necked ribbons/fibres.

The longitudinal pendulum mode was considered, since this couples directly into the horizontal displacement thermal noise in the interferometer, and this is shown in Figure 4.22.

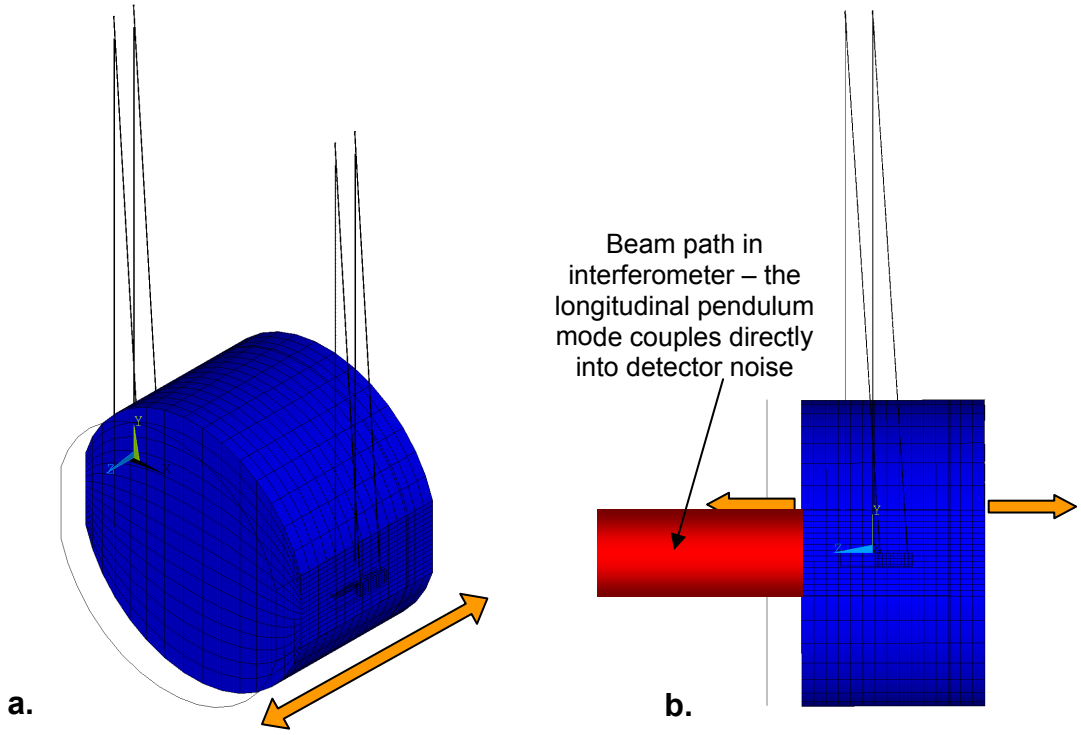

Figure 4.22 a. 3D view of longitudinal pendulum mode for Advanced LIGO b. side view of longitudinal pendulum mode showing mass ramaining horizontal due to its inertia

Two dilution numbers were extracted for this model, one using the total strain energy contained, the other using only that contained in the bending of the ribbons. The results are shown in Table 4.5.

Theoretical dilution (including bending top and bottom)	Dilution as calculated in ANSYS using total strain energy	Dilution as calculated in ANSYS using strain energy in bending
2048	1927	2040

Table 4.5 Dilution comparison for Advanced LIGO longitudinal pendulum mode

The theoretical values differ from that of the single fibre models studied as bending occurs both at the top and the bottom of the ribbon (halving the dilution) due to the inertia of the moving mass against pitch. The dilution is also further reduced as the length to the centre of mass is 60 cm. The single ribbon/fibre models used a 60 cm fibre with an additional 7.5 cm to the centre of the mass, as discussed in section 4.2.1.

Additional strain energy is contained in the ears at the join point for the ribbons and the join point to the mass, this being due to the 40 kg load mass. This is seen when the total strain energy in the model is considered to calculate the dilution. This additional energy is not an accurate bending strain energy (since the ears were simple representations) so was not considered for dilution calculations. When only the bending strain energy is used in the ANSYS calculation, the calculated dilution deviates from the theoretical value by 0.4%.

It was therefore seen that these results tie up closely with the theoretical values, and the dilution values extracted from the remaining Advanced LIGO models considered the strain energy in the ribbons due to bending only.

4.4.2 Linear Tapered Necks

The second pair of Advanced LIGO models considered used the same 7.5 mm and 15 mm linear taper necks as considered in sections 4.3.2 and 4.3.3. These models are shown in Figure 4.23 and Figure 4.24 respectively. The 7.5 mm long tapered neck with starting dimensions 8.4 x 0.84 mm (from section 4.3.2) was not considered, as these starting dimensions were not representative of those that are currently envisaged for the Advanced LIGO ribbons.

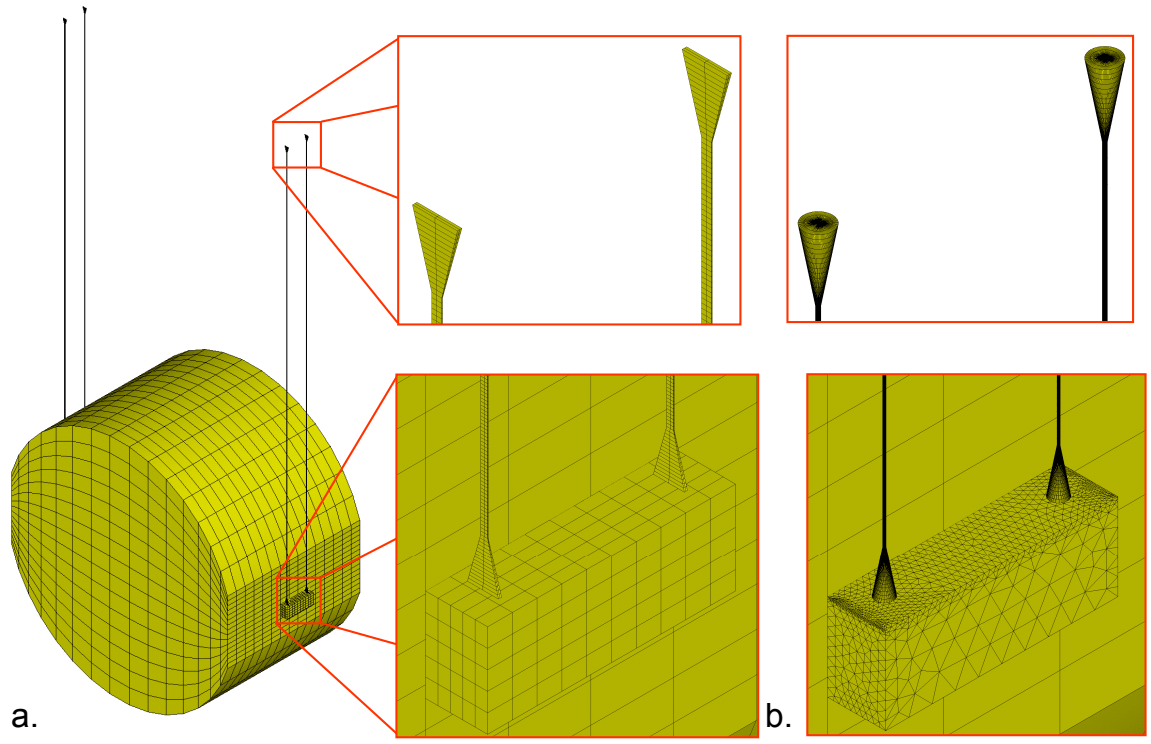

Figure 4.23 a. Advanced LIGO model with 7.5 mm linear taper necks b. equivalent circular fibre model

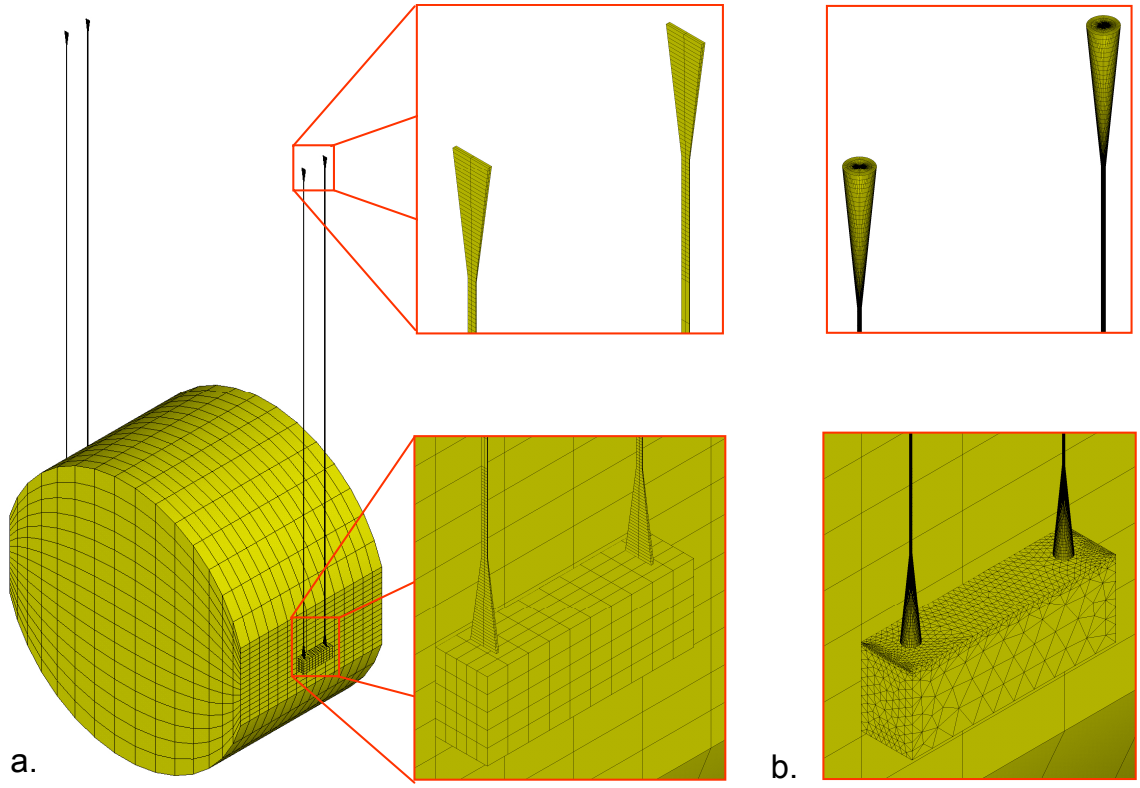

Figure 4.24 a. Advanced LIGO model with 15 mm linear taper necks b. equivalent circular fibre model

The resulting dilution values, calculated by considering the strain energy in the ribbons/fibres only, are shown in Table 4.6.

Case	Theoretical Dilution (using bending thickness)	Dilution from ANSYS
Rectangular Ribbon, 7.5 mm long neck	262	273
Circular Fibre, 7.5 mm long neck	625	396
Rectangular Ribbon, 15 mm long neck	174	174
Circular Fibre, 15 mm long neck	226	185

Table 4.6 Dilution values for linear tapered neck ribbons and fibres.

It is clear once again that the ribbons show lower dilution than the equivalent circular fibres, similar to the trend that was seen in sections 4.3.2 and 4.3.3. Also, the theoretical dilution values for the ribbons again come close to that predicted by theory when the width and thickness at the bending point is utilised in the calculation.

The circular fibres with 7.5 mm long necks again have the bending point occurring beyond the neck, with some neck bending causing the reduction in dilution as compared to the theoretical value. For the longer 15 mm neck much more bending occurs in the neck causing a greater reduction in dilution to a value comparable with the 15 mm necked ribbon. This again follows the same trend that was demonstrated in sections 4.3.2 and 4.3.3.

Bending strain energy distributions for the 7.5 mm neck and 15 mm necked ribbons/fibres are shown in Figure 4.25 and Figure 4.26 respectively.

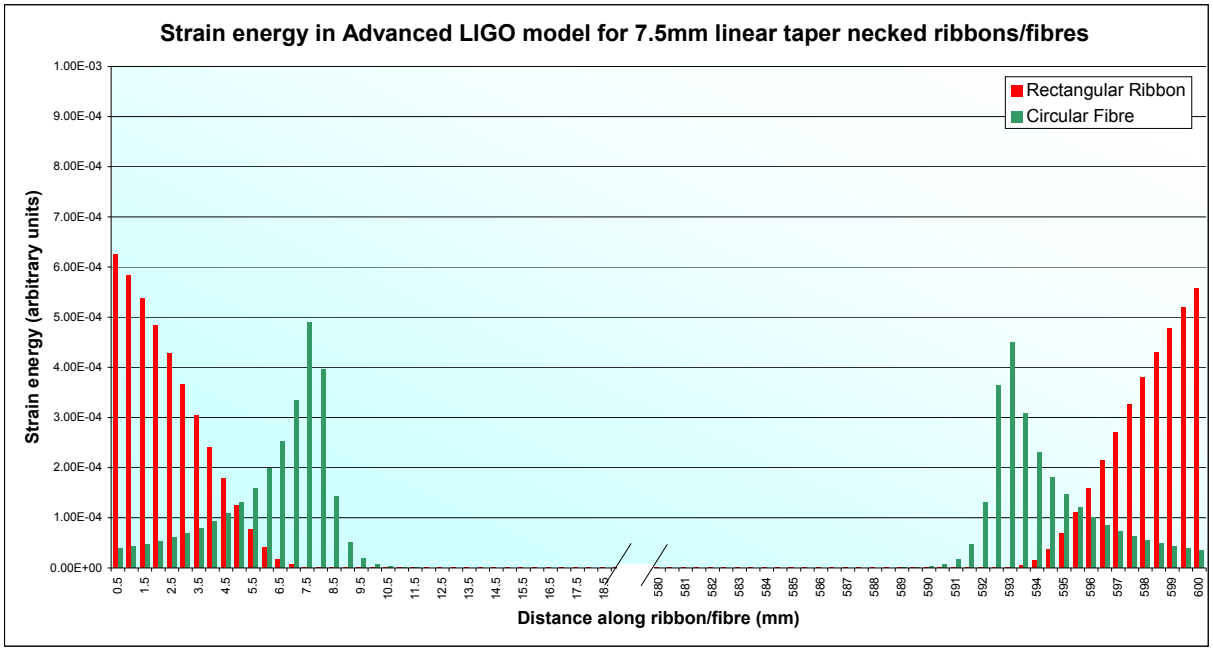

Figure 4.25 Strain energy distribution for a single ribbon/fibre in Advanced LIGO 4 ribbon/fibre model, with ribbon/fibre having 7.5 mm long linear tapered necks.

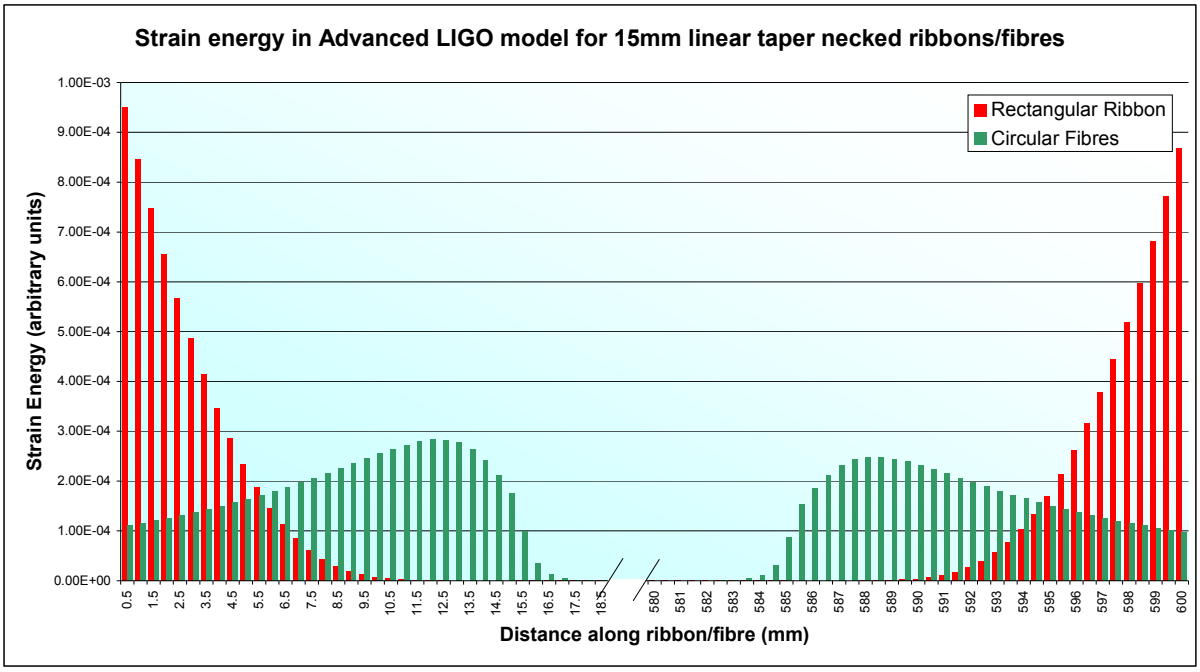

Figure 4.26 Strain energy distribution for a single ribbon/fibre in Advanced LIGO 4 ribbon/fibre model, with ribbon/fibre having 15 mm long linear tapered necks.

These strain energy distributions show similar structure for each neck as those for the single fibre models (Figure 4.15 and Figure 4.18) as would be expected since the mass loading is the same, and therefore the bending will also occur in the same manner.

It is therefore apparent that the effects of the necks also cause significant reduction in the dilution factor of the proposed Advanced LIGO suspensions.

4.4.3 Real Necks

Real ribbon necks have a more complex profile, as demonstrated in Chapter 3. In order to gauge the performance of a suspension using real ribbons, the profile data was imported into ANSYS using the LabVIEW program described in section 4.1.2. The resulting ANSYS models are shown in Figure 4.27.

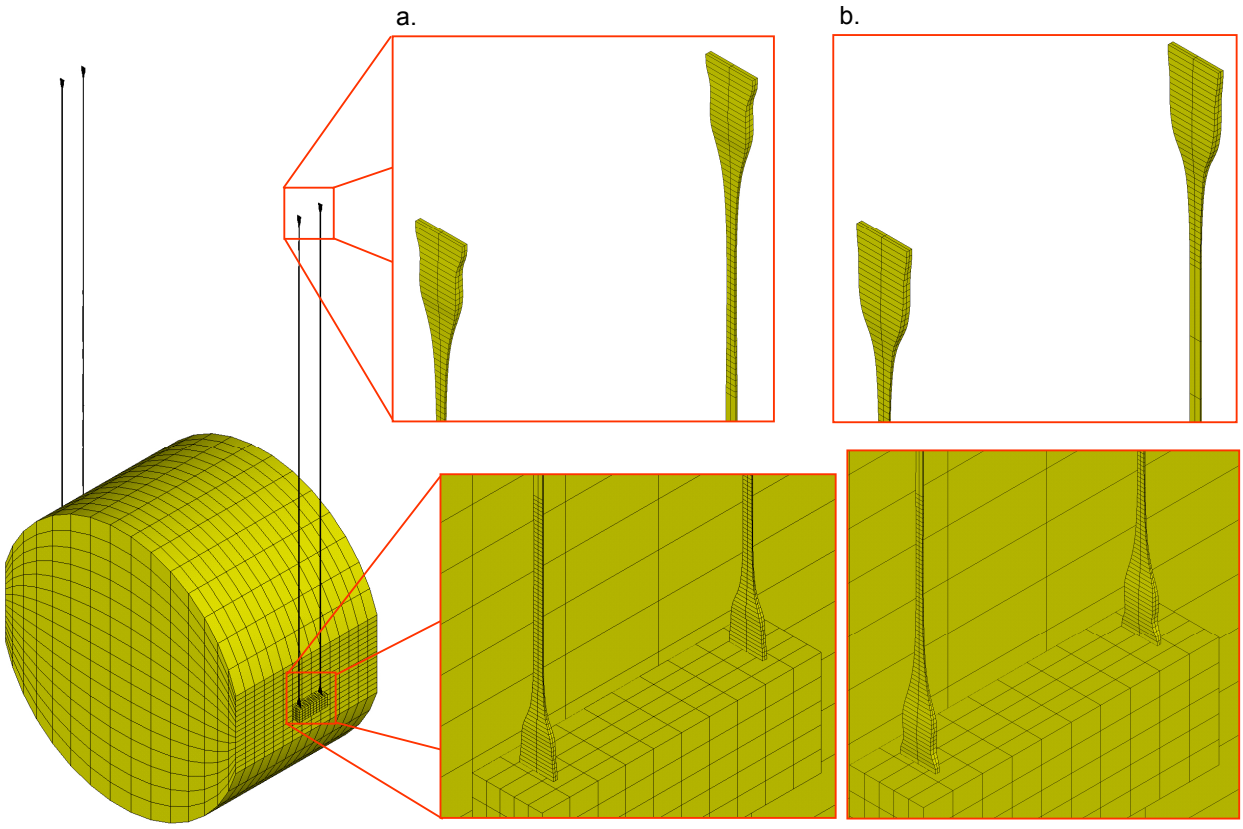

Figure 4.27 Advanced LIGO models using real ribbon profiles. a. shows the oversized ribbon, b. shows the thinner ribbon

Dilution values and energy distributions are shown in Table 4.7 and Figure 4.28 respectively.

Case	Dilution from ANSYS
Ribbon - oversize	146
Ribbon – correct	135

Table 4.7 Dilution values for real ribbons characterised in Chapter 3

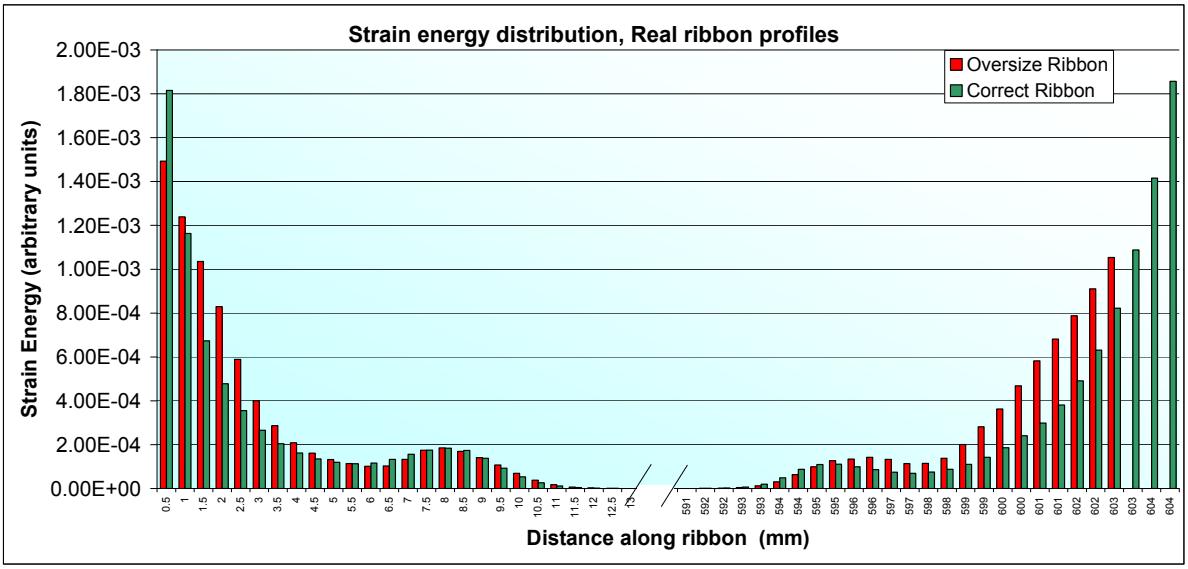

Figure 4.28 Strain energy distributions for the real ribbons characterised in Chapter 3

Again, dilution values can be seen to be lower than for an ideal non-necked ribbon, and the relatively long necks resulted in most of the bending strain energy being contained in the thicker neck region. This gave the lowest dilution values observed, and is therefore less desirable from a thermal noise point of view in Advanced LIGO suspensions.

The best neck profile (as profiled in section 3.7.1) was therefore modelled as shown in Figure 4.29.

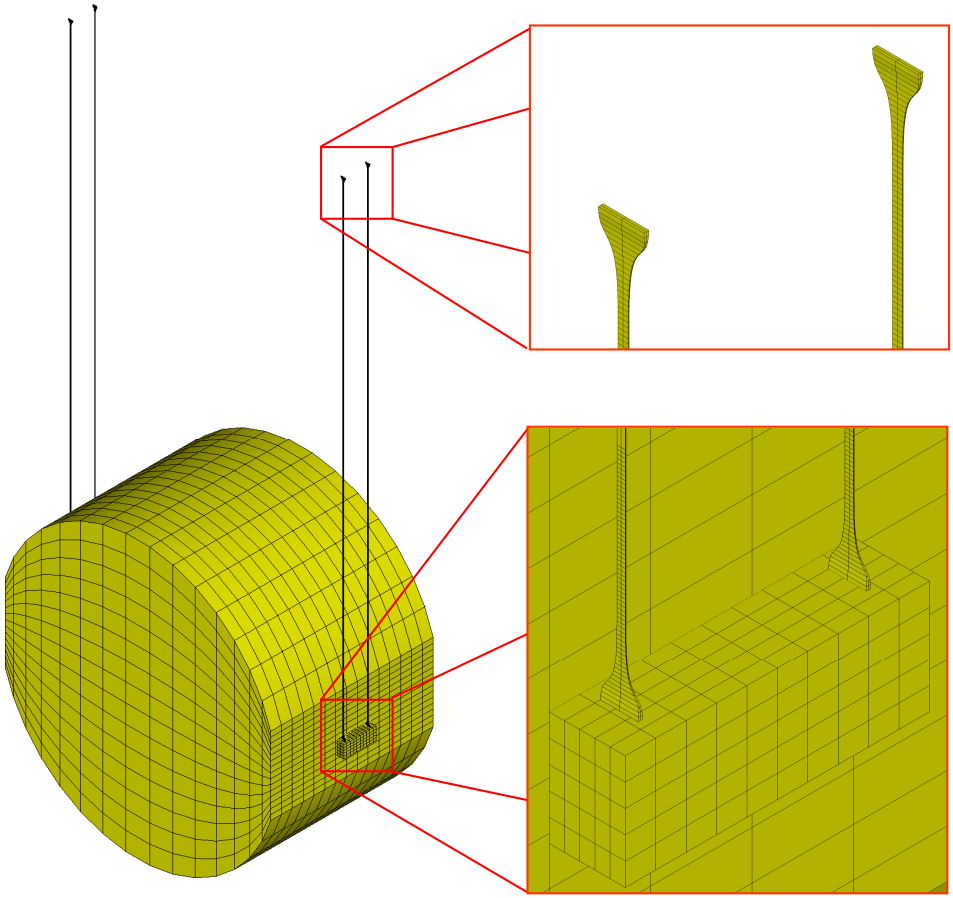

Figure 4.29 Advanced LIGO model for real short neck characterised in section 3.7.1, (see Figure 3.27).

The observed dilution was higher at 493, which was a result of the shortened neck (consistent with the results from section 4.3.5) and the resulting reduction in strain energy. The strain energy distribution also shows this, with strain energy occurring over a lesser neck length, as shown in Figure 4.30.

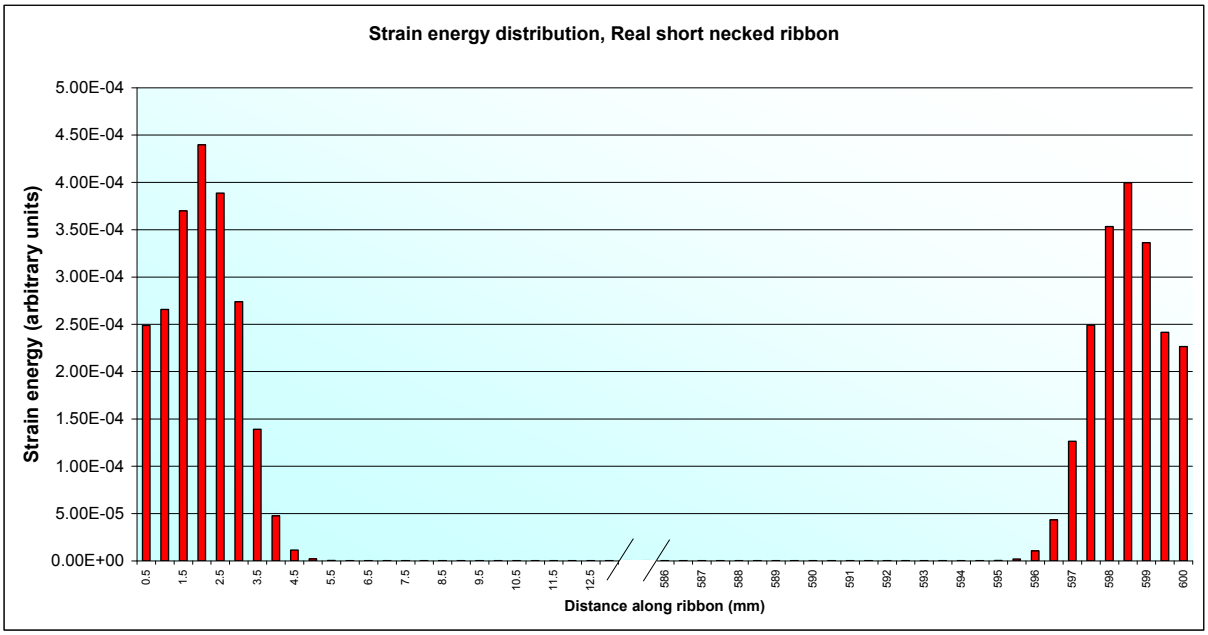

Figure 4.30 Strain energy distribution for Advanced LIGO model for real short neck characterised in section 3.7.1, (see Figure 3.27).

4.4.4 Real Necks, Real Ears

The final 4 ribbon model studied looked at the effect of adding accurate models of the ears proposed for use in Advanced LIGO. The upper intermediate mass was included, to allow the ears that join to the top of the ribbons to be modelled. Figure 4.31 shows the resulting FE model.

In this model, the upper mass was constrained in displacement and rotation at its four uppermost vertices to allow the ears and that tops of the fibres to bend freely as in a real detector suspension.

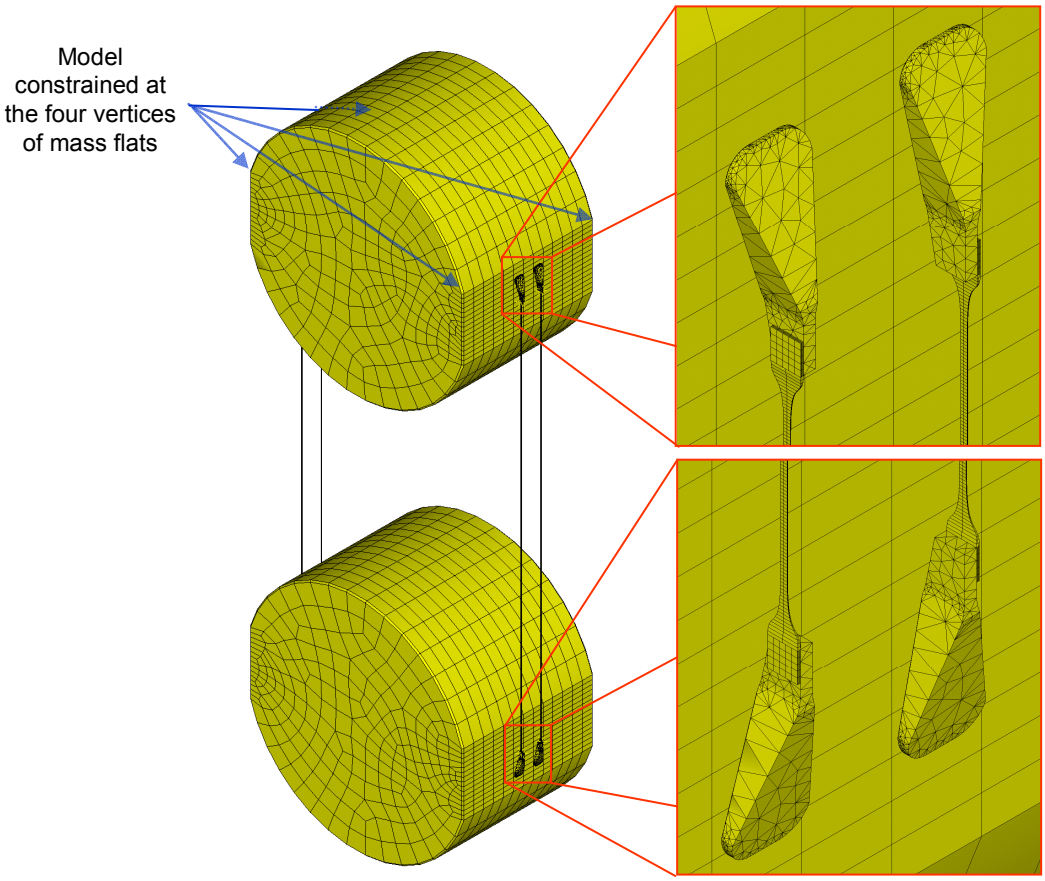

Figure 4.31 Advanced LIGO model using accurate models of the real ears, and also the best ribbon neck profile obtained from the data from section 3.7.1.

The dilution was considered in this case with the inclusion of the strain energy contained in the ears. The resulting values are shown in Table 4.8.

ANSYS (strain energy in ribbons and ears)	ANSYS (previous model with stiff ears)	Theory (no neck, ideally stiff ears)
277	493	2048

Table 4.8 Comparison of dilution when bending strain energy in ears is introduced.

Introducing the energy contained in the ears can be seen to cause another decrease in the pendulum dilution. Close observation of a modal animation showed that the weld region of the ear experienced a small amount of bending indicating that some strain energy would be residing in the ears also.

4.4.5 Discussion

A summary of all the dilution values for the 4 ribbon Advanced LIGO suspensions considered is shown in Table 4.9.

Ribbon model	Dilution from ANSYS
Ideal case, no necks (section 4.4.1)	2040
7.5 mm linear taper necked ribbons (section 4.4.2)	396
15 mm linear taper necked ribbons (section 4.4.2)	174
Real ribbon - oversized (section 4.4.3)	146
Real ribbon – thinner ribbon (section 4.4.3)	135
Real ribbon – short neck (section 4.4.3)	493
Real ribbon – short neck + ears (section 4.4.4)	277

Table 4.9 Summary of ribbon dilution factors for Advanced LIGO models

It is clear once again that the introduction of ribbon and fibre necks reduced the dilution value observed in the pendulum, and this was expected after the results of sections 4.3.2 to 4.3.5. However, it is notable that both the real ribbons and real fibres give the lowest dilution factors, underlining that neck shape and length are very important, and production of such necks is not a trivial undertaking.

4.5 Improving Thermal Noise Performance

4.5.1 Tapered Fibres

Since high dilution factors were originally cited as a reason for use of ribbon geometries, the discovery that the ribbon necks significantly reduced the dilution prompted a re-evaluation of the noise sources in the ribbons and fibres. In particular, the nulling of thermoelastic noise as detailed in section 3.4 had been demonstrated to yield potential reductions in mechanical loss by Cagnoli and Willems [131] in 2002, but was discovered

after the ribbon choice had been made for Advanced LIGO. In this paper, it is shown that the nulling of thermoelastic loss for ribbons can be achieved by use of a 0.2 x 2.0 mm cross section ribbon. However, nulling can also be achieved with circular fibres, and since these are simple to manufacture, their dynamics were analysed here, as a possible alternative to the current baseline ribbons.

In order to achieve a minimisation of the thermoelastic loss, the bending of the fibre top and bottom must occur in a region where it is 805 μm diameter (from Equation (3.12)). Therefore a fibre was proposed [148] which would have thicker ends to permit bending to occur in an 805 μm diameter region, and this is shown in Figure 4.32a. A transition to 400 μm diameter is required as this ensures that the vertical bounce frequency of the loaded fibre is below the 12 Hz Advanced LIGO requirement.

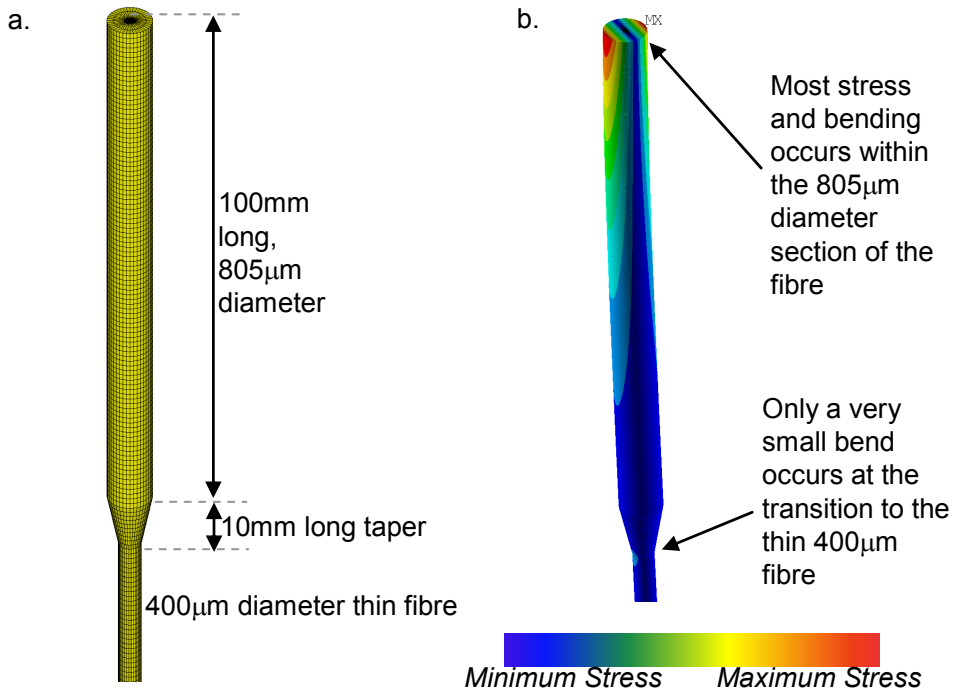

Figure 4.32a. Tapered fibre ANSYS model b.Stress in bending of tapered fibre showing bending contained in thicker 805 μm diameter section of fibre

The FEA model of this fibre preformed as expected, with almost all of the bending occurring in the thicker 805 μm diameter region, with only a small additional bend at the transition to thinner 400 μm. The strain energy distribution is shown in Figure 4.33.

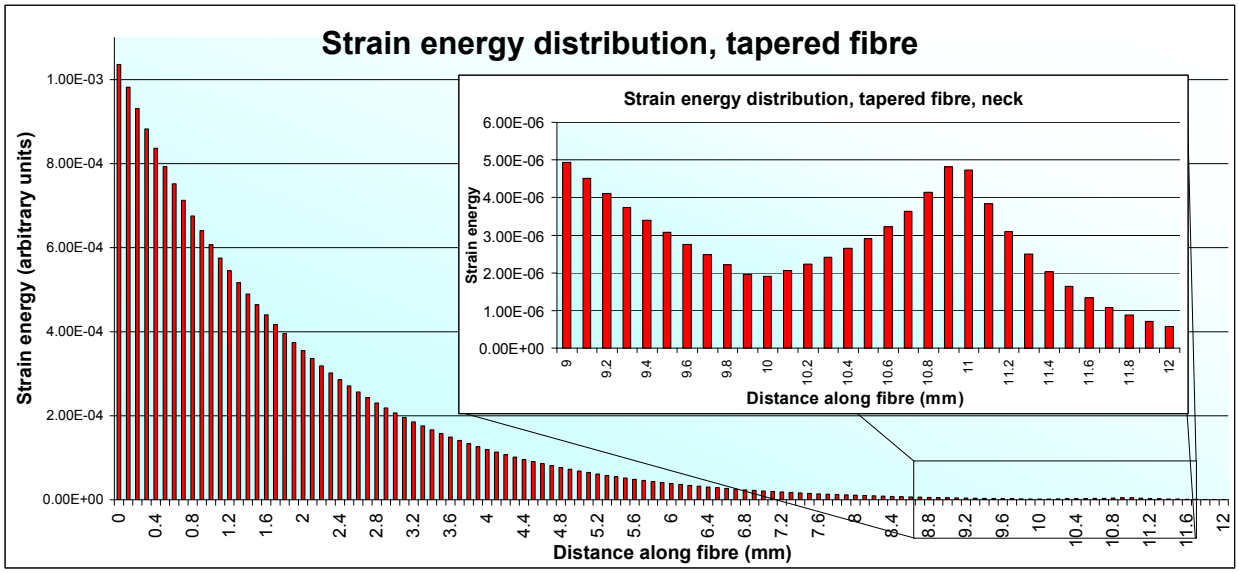

Figure 4.33 Strain energy distribution for tapered fibre. Inset shows the small peak in strain energy observed due to a small additional bend occurring at the transition to 400 μm diameter

The energy distribution shows that only a small fraction (0.27%) of the total strain energy is contained at the 805 μm to 400 μm transition, and therefore would be insignificantly detrimental to the expected dilution. This was confirmed from a single fibre model with a 10 kg mass, which yielded a dilution value of 371, with the theoretical dilution of 360.

4.5.2 Tapered Fibre with Ear Representation

In order to represent a tapered fibre welded to an ear, the model was extended as shown in Figure 4.34a. The end of an "ear" was represented by a circular section, 3 mm diameter, with a 1 mm long taper section representing the weld of the fibre to the ear. This basic representation of the end of an ear was used as using a circular rod as this is

a more likely welding scenario if circular fibres were used (this is the method that was used in the GEO600 suspensions). 3 mm diameter was chosen as the 2 mm thickness of the ears used in the model of the full suspension (section 4.4.4) resulted in a significant amount of bending in the ears.

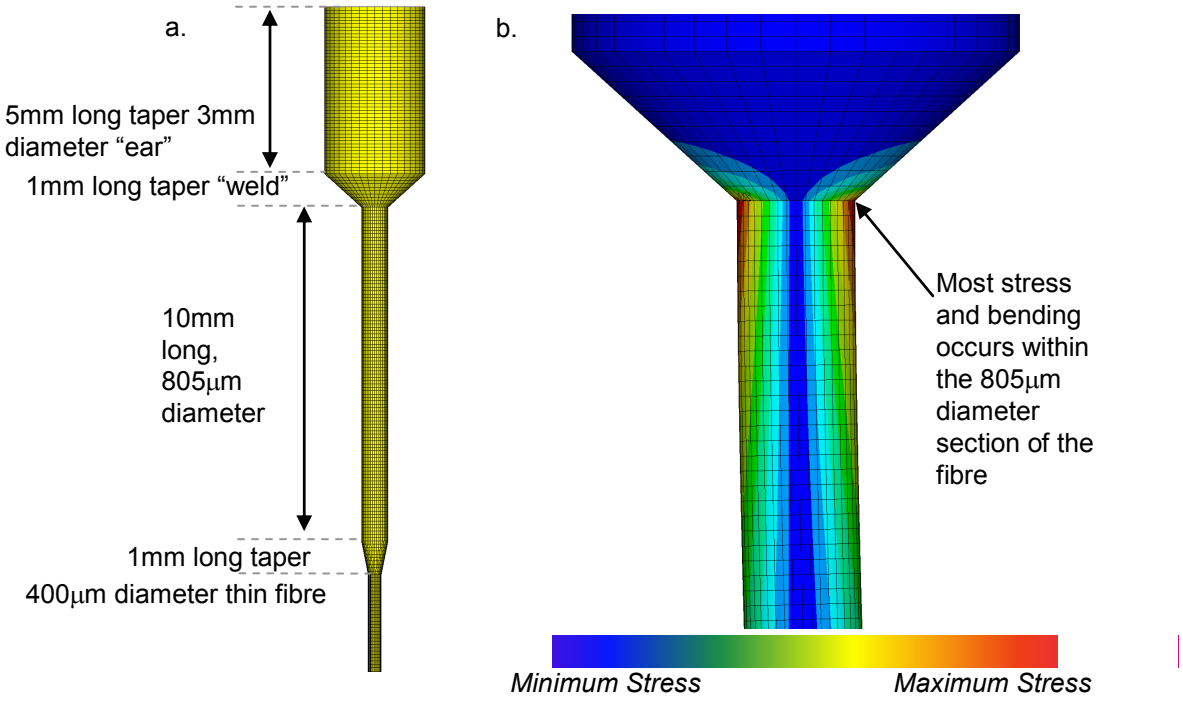

Figure 4.34a. Tapered fibre model with ear representation b. Some stress occurs in the weld region.

Figure 4.34b shows that some bending stress is pushed into the weld taper region, and the strain energy distribution (Figure 4.35) also shows that 6.2% of the total strain energy is contained in the weld section.

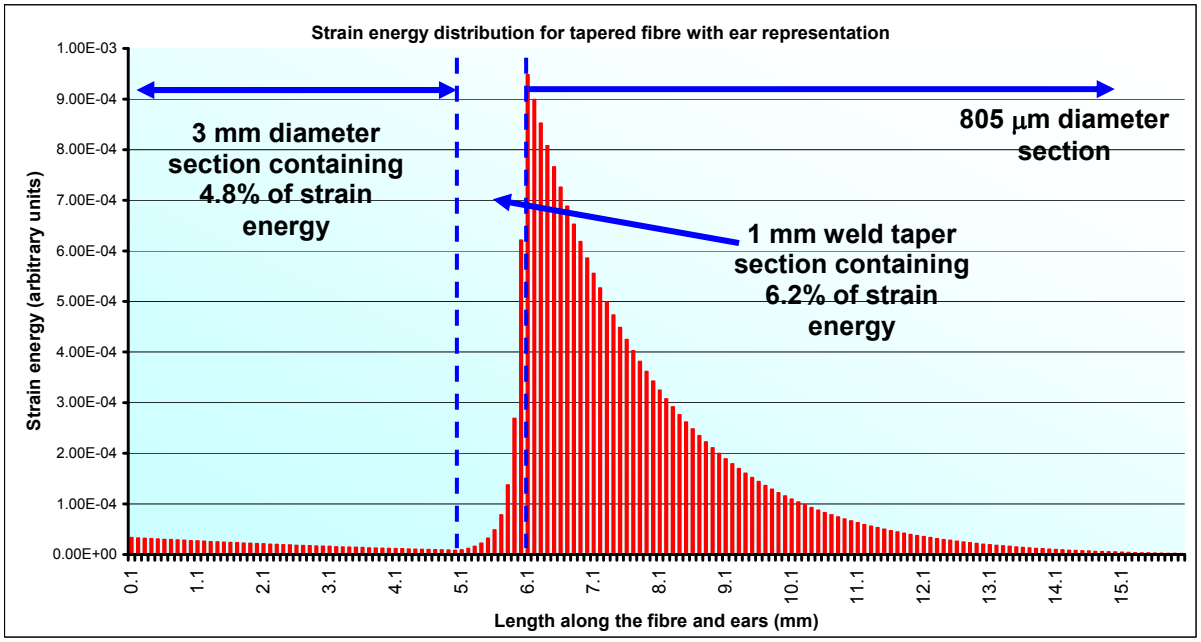

Figure 4.35 Strain energy distribution for tapered fibre and ear representation.

Dilution was 360 for this fibre (for a single fibre with a 10 kg mass model with bending only at the top), but since the weld may possibly have a greater mechanical loss than the fibre itself, it is desirable to have the weld further away from the bending region in order that less energy is stored here. Therefore welding a fibre in this manner is unlikely to be used in an Advanced LIGO scenario [148].

Instead, welding a thicker 3 mm section at the end of the tapered fibre is more feasible as this would move the weld away from the region of maximal bending. In order to analyse the strain energy in a fibre with a 3 mm section tapering to an 805 μm diameter section and then down to 400 μm, a real fibre was produced to model in ANSYS.

4.5.3 Real Tapered Fibre

The fibre that was produced, the profile and its resulting ANSYS model is shown in Figure 4.36.

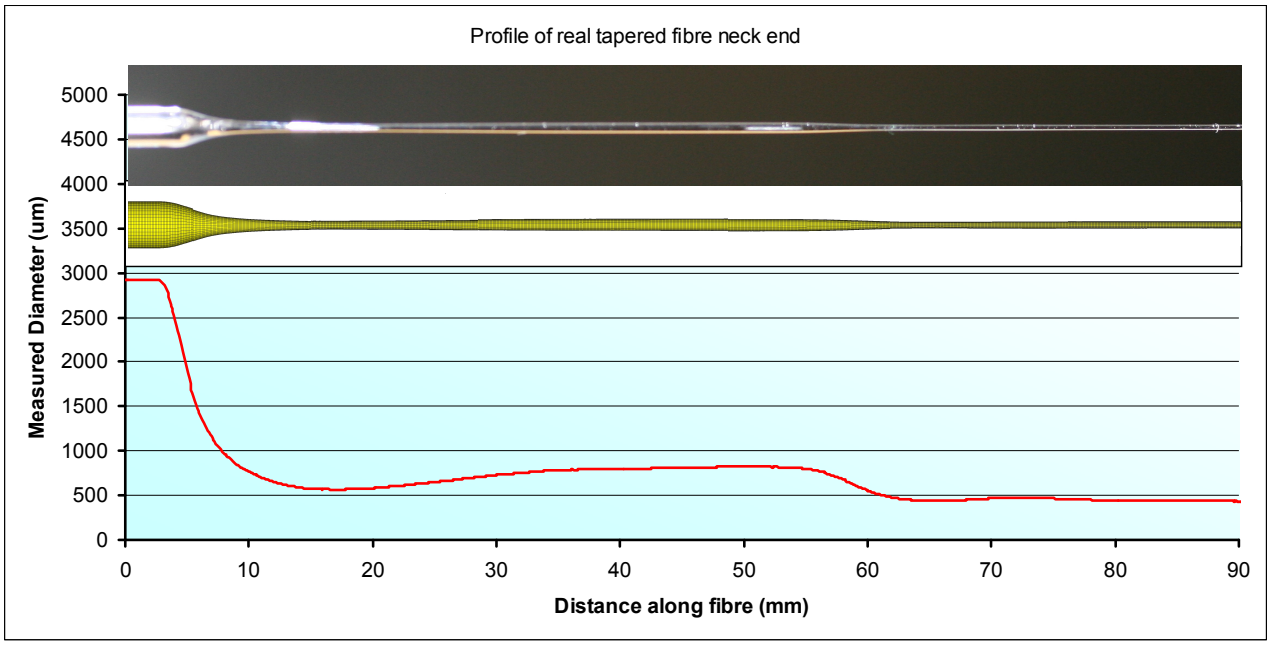

Figure 4.36 Real tapered fibre (top), ANSYS model (centre) and profile (plotted).

During the pull the fibre necked down lower than was desired at first, with the section required to be 805 μm dropping as low as 550 μm. The dilution resulting for this fibre was 385 (for a single fibre with a 10 kg mass model) and 160 in an Advanced LIGO scenario.

The strain energy distribution for the first 20 mm of the fibre is shown in Figure 4.37.

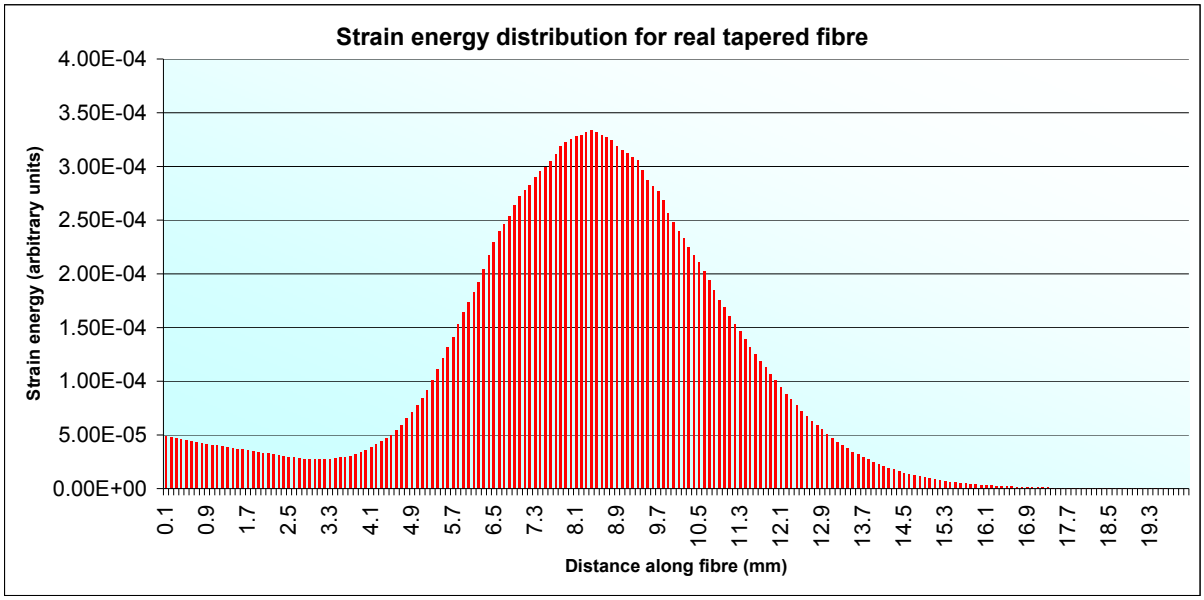

Figure 4.37 Strain energy distribution for real tapered fibre

It is clear that the bending occurs mostly at the end of the transition between the 3 mm starting diameter and the 805 μm diameter section. Insignificant energy was contained further down the fibre.

4.6 Evaluation of all Mechanical Loss Mechanisms in Real Ribbons/Fibres

Tapered fibres clearly give lower dilution values than ideal ribbons. However, the mechanical loss of a suspension constructed with such a fibre would also depend on the level of thermoelastic loss in the bending region and the surface loss of the fibre. Thermoelastic loss in particular is an important consideration as the aim of the tapered fibre was to minimise this. Surface loss is also important as the surface to volume ratio for these fibres is high when compared to the test mass itself. A method of calculating the mechanical loss for real fibres was therefore developed in order to give a clear indication of the factors that contribute to the thermal noise resulting from the fibre.

In order to evaluate the mechanical loss of such a fibre, with appropriate comparisons to ribbons, a Maple [149] program was written by Dr. Alastair Heptonstall together with the author, to use the ribbon or fibre profiled dimensions together with ANSYS

modelling strain energy results to calculate the total mechanical loss in the ribbon or fibre.

The mechanical loss in a uniform fibre can be represented:

$$\phi_{\text{fibre material}} = \phi_{\text{surface contribution}} + \phi_{\text{bulk contribution}} + \phi_{\text{thermoelastic contribution}} \tag{4.2}$$

where $\phi_{\text{surface contribution}}$ is the mechanical loss due to the ribbon/fibre surface, $\phi_{\text{bulk contribution}}$ is the mechanical loss of the material making up the ribbon/fibre and $\phi_{\text{thermoelastic contribution}}$ is the thermoelastic loss of the ribbon/fibre.

The surface loss can be modelled as shown by Gretarsson [150] and Heptonstall [151] as:

$$\phi_{\text{surface contribution}} = \mu h \phi_s \frac{S}{V} \tag{4.3}$$

where μ is a coefficient dependent on the ribbon or fibre geometry, $h\phi_s$ is the product of the mechanical loss of the material surface, ϕ_s , and the depth, h, over which surface loss mechanisms are believed to occur. $h\phi_s$ was taken from Gretarsson as $6.15\text{x}10^{-12}$ m [150]. $\frac{S}{V}$ is the ratio of surface area to volume. For ribbons of width x and thickness y the surface contribution is [150]:

$$\phi_{\text{surface contribution ribbon}} = \frac{3+a}{1+a} h\phi_s \frac{2(x+y)}{xy} \tag{4.4}$$

where a is the ratio of width to thickness. For circular fibres diameter d the surface contribution is [150]:

$$\phi_{\text{surface contribution fibre}} = \frac{8.53 h\phi_s}{d} \tag{4.5}$$

The thermoelastic loss is calculated using equation (3.10):

$$\phi_{\text{thermoelastic}} = \frac{\omega\tau}{1+(\omega\tau)^2}\frac{YT}{\rho C}\left(\alpha - \sigma_o \frac{\beta}{Y}\right)^2$$

This calculation was then performed for segments of the fibre all along its length. So, the mechanical loss of the ith section of a circular fibre is:

$$\phi_i = \frac{8.53h\phi_s}{d_i} + \frac{\omega\tau_i}{1+(\omega\tau_i)^2}\frac{YT}{\rho C}\left(\alpha - \sigma_i \frac{\beta}{Y}\right)^2 + \phi_{\text{bulk contribution}} \quad (4.6)$$

where d_i is the diameter of the fibre in the ith section, τ_i is the characteristic heat flow time over the diameter d_i , and σ_{i} is the static stress in the ith section. The bulk loss was taken to be 4.1 x 10^{-10} [152].

In order to calculate the loss in this manner, the fibre is approximated as shown in Figure 4.38, with each element in the ANSYS model of the fibre being approximated to an average constant diameter. The diameters are then used to calculate the mechanical loss contribution, ϕ_i, of each element using equation (4.6). The highest data resolution that ANSYS could solve was chosen, with one element every 0.1 mm along the fibre length to give the most accurate resulting loss values.

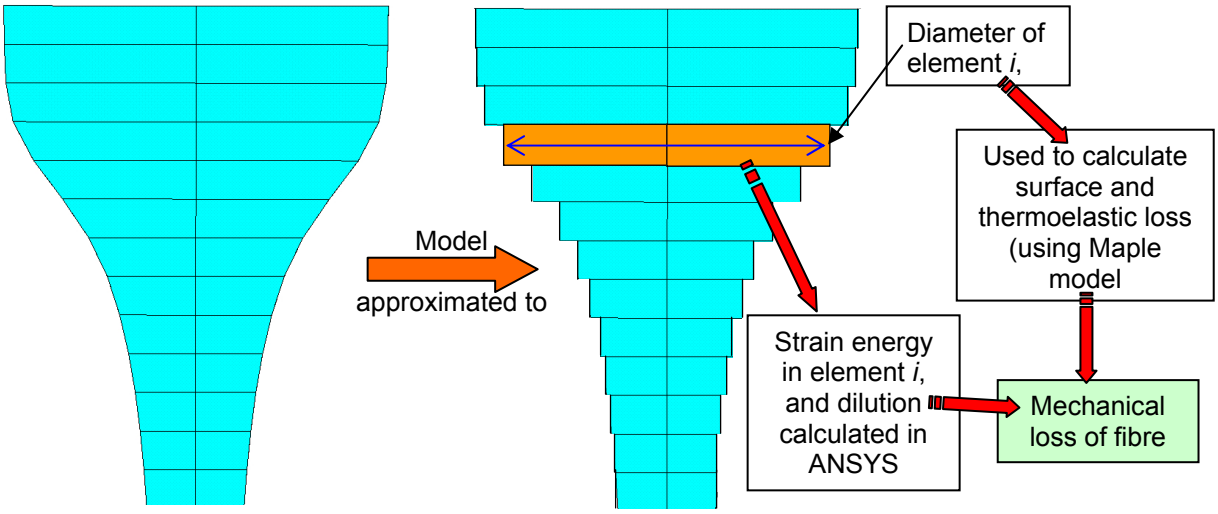

Figure 4.38 Schematic ANSYS model of fibre (side view of fibre), showing approximation of elements to constant diameter sections

To obtain the true mechanical loss these losses are scaled by the bending strain energy contained within the section (obtained from the ANSYS strain energy distributions), summed and multiplied by the dilution factor D to arrive at the total loss of the fibre in a suspension:

$$\phi_{\text{total}} = \frac{1}{D}\left(\frac{E_1}{E_{\text{total}}}\phi_1 + \frac{E_2}{E_{\text{total}}}\phi_2 + \ldots + \frac{E_n}{E_{\text{total}}}\phi_n\right) \tag{4.7}$$

The distribution of mechanical loss along the tapered fibre is shown in Figure 4.39, shown with the surface and thermoelastic components calculated separately, then scaled by the bending strain energy distribution.

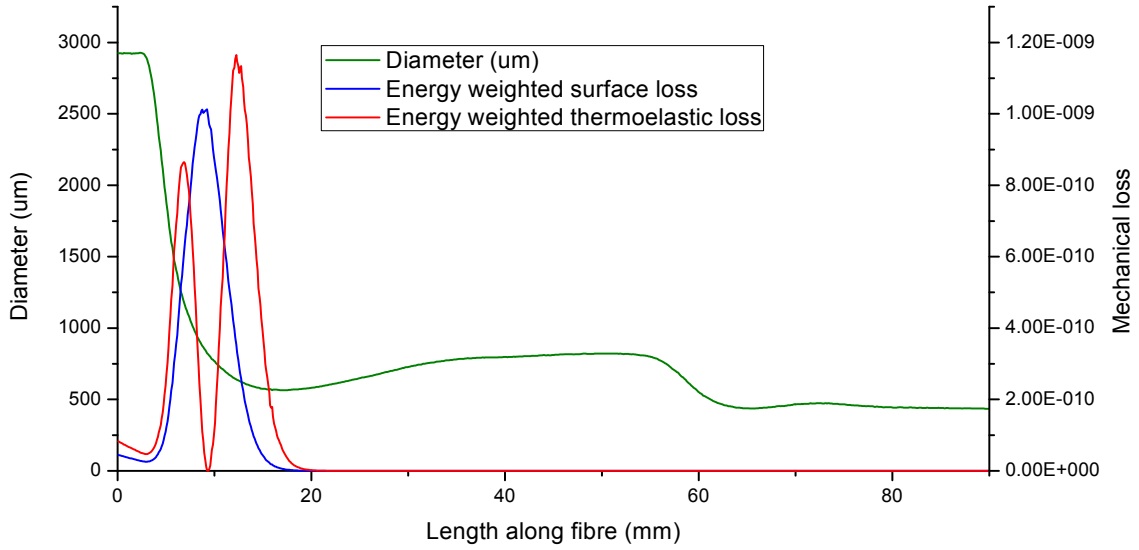

Figure 4.39 Mechanical loss contribution of surface and thermoelastic loss for real circular tapered fibre

The losses are weighted by the ANSYS bending strain energy distribution (Figure 4.37) to give the actual weighted loss contribution. The form of the surface loss is the same as the strain energy distribution, whilst the thermoelastic loss drops to zero at the point where the diameter of the fibre passes through the 805 μm – this being the diameter required to null thermoelastic loss. Bulk loss is not shown on this graph as its contribution was negligible by comparison.

The total loss ϕ_{total} was then calculated over a range of frequencies to show the mechanical loss of the ribbon/fibre at the low frequency end of the detection band. This was done for three ribbons/fibres:

1. "Baseline" ribbon – 1.13 x 0.113 mm ideal ribbon with no necks

2. "Real" ribbon with short neck as studied in section 4.4.3.

3. "Real" tapered cylindrical fibre as studied in section 4.5.3.

The resulting mechanical loss spectra from 0 to 30 Hz are shown in Figure 4.40.

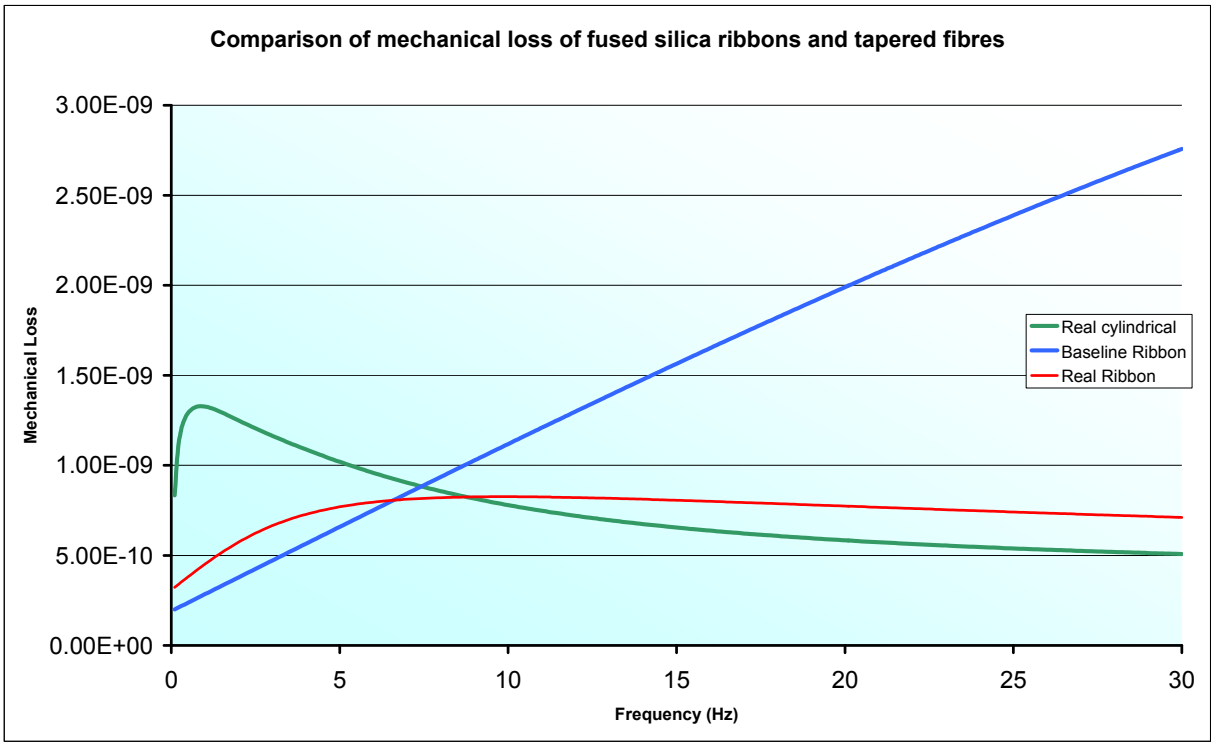

Figure 4.40 Mechanical loss spectra of real ribbon, real tapered fibre and baseline ribbon

It is clear that both the real ribbon and real tapered fibre have lower loss than the baseline ribbon at frequencies greater that around 8 Hz. The baseline ribbon experiences a peak in loss at 99 Hz (as was shown in Figure 3.5) due to the thermoelastic contribution. By contrast the peak frequency for the real ribbon is much lower (at around 10 Hz) and the real tapered fibre peak is lower still, at around 1 Hz. This lowering of the peak frequency results from the bending occurring in a thicker region of the ribbon or fibre. Pushing this peak thermoelastic frequency below 10 Hz is desirable as below this frequency the dominant noise source is seismic noise and therefore suspension thermal noise is less important in this region.

The thermoelastic loss is also reduced when bending occurs in the thicker region as the cross sectional dimensions are closer to those required to null the thermoelastic loss, and despite the lower dilution, the total mechanical loss is still reduced.

This is encouraging for improving the suspension thermal noise, as real ribbons or fibres have lower mechanical loss than the baseline requirement for Advanced LIGO, as was discussed in section 3.3. The proposed tapered fibre has the lowest mechanical loss of the three and is also likely to be the most straightforward to manufacture from a practical point of view. Indeed, in the light of the re-evaluation of the mechanical loss and dilution of such ribbons and fibres, a proposal has now been tabled for changing the Advanced LIGO suspension system to use tapered fibres [153].

4.7 Conclusions

The characterisation of ribbons and fibres using FEA modelling has given a clear indication that the necks on both rectangular ribbons and circular fibres reduce the resulting pendulum dilution factors. The high dilution of the ideal non-necked ribbon drops more rapidly that an equivalent circular fibre as the length of the neck is increased, since the bending occurs further up the ribbon. Only very short necks give an improvement over the equivalent circular fibre.

However, study of the different sources of mechanical loss in the ribbons and fibres revealed than minimising the thermoelastic loss can give greater total mechanical loss reductions than can be achieved solely through high dilution. It was seen that whilst the necked ribbons experience poorer dilution, the thermoelastic loss is significantly reduced where bending occurs in thicker parts of the ribbon which are nearer to the thickness where thermoelastic loss can be nulled.

The best mechanical loss performance in the 10 Hz region was observed in the tapered circular fibres, providing an alternative to the more difficult to manufacture ribbon geometry. Indeed, changing to such fibres has now been proposed as an improvement to the original Advanced LIGO baseline design, and if such a change is implemented it could permit additional gains in noise performance in the 10 Hz detection region.

Chapter 5

Test Mass Mirror Coatings

5.1 Test Mass Mirror Coatings

In order to obtain a mirror from a fused silica test mass, the surface must have a coating which is highly reflective to the 1064 nm wavelength laser light typically used in detectors [154]. It is possible to achieve this by applying thin layers of a pair of dielectric materials to the surface. Coatings in all the current first generation interferometric gravitational wave detectors use alternate layers of low refractive index silica, SiO_2, and high refractive index tantalum pentoxide ("tantala"), Ta_2O_5 with typically 30 such layers being used. Each coating layer is $\lambda/4$ in optical thickness, and physical thickness $h = \frac{\lambda}{4n}$, where n is the refractive index of the material and λ is the laser wavelength.

Whilst the fused silica used for the mirror substrate has been demonstrated as having very low mechanical loss [155] [156] [157] [104], the optical coating has been seen to introduce an additional source of mechanical dissipation [158] [159] [160] [161] and hence detector thermal noise. The capability of producing ultra low loss mirror suspension systems as shown in previous chapters means that thermal noise associated

with the mirror coating is likely to be a dominating noise source for advanced gravitational wave detectors beyond Advanced LIGO at midband frequencies (typically between 50 Hz and 500 Hz).

An area of great interest in current research is therefore understanding and reducing the mechanical loss of these coatings, in order to maximise midrange sensitivity. Investigations are focussed on possible reductions in loss obtained by doping the high refractive index tantala with materials like silica SiO_2, and titania TiO_2. Such samples have previously been seen to offer potential reductions in the mechanical loss of coatings [154]. Samples doped in this manner are the subject of study of this chapter, and the measurements were taken jointly with Peter Murray [162].

5.2 Measuring Mechanical Loss of Test Mass Samples

As previously explored in Chapter 2, the mechanical loss of a system or sample can be determined by measuring the quality factor, $Q(\omega_o)$, of resonant modes ω_o of the system where $Q(\omega_o) = \frac{1}{\phi(\omega_o)}$.

Measurement of the quality factor can be achieved by observation of the decay of an excited internal resonant mode of the test mass sample. The mode will exhibit damped harmonic motion, and therefore the amplitude of the envelope of the decay of the resonant motion can be represented by:

$$A(t) = A_o e^{-\frac{\omega_o t}{2Q(\omega_o)}} \tag{5.1}$$

for resonant mode frequency $f_o = \frac{\omega_o}{2\pi}$ and initial amplitude A_o at time $t = 0$ [90]. This exponential amplitude decay of resonant motion over time is often referred to as a "ringdown envelope", or "ringdown". By recording $A(t)$ during the ringdown it is possible

to use an exponential fit to determine the coefficient, $\frac{\omega_o}{2Q(\omega_o)}$, and hence the quality factor for a given resonant mode. Alternatively, it can be advantageous to rearrange equation (5.1) giving:

$$\log(A(t)) = -\frac{\omega_o}{2Q}t + \log(A_o) \tag{5.2}$$

Thus, from this linear expression, the quality factor Q value can be evaluated from the gradient of a logarithmic plot of $A(t)$ data where:

$$\frac{1}{\phi(\omega_o)} = Q(\omega_o) = \frac{\omega_o}{2 \times \text{gradient}} \tag{5.3}$$

All measurements carried out in this chapter were calculated using these methods, and are expressed in terms of mechanical loss, $\phi(\omega_o)$.

5.3 Experimental Measurement of the Mechanical Loss of a Mirror Coating

5.3.1 Samples

To measure the mechanical loss of the coating, small cylindrical test mass samples of silica are used, typically of dimensions 76.2 mm (3") diameter by 25.4 mm (1") thick. For this experiment three such silica samples of these dimensions were used with 30 alternating layers of silica and tantala ion beam sputtered on the masses, by the Australian science agency CSIRO (Commonwealth Scientific and Industrial Research Organisation) [163]. The samples were then annealed at 500°C for 24 hours, to help ensure there were minimal oxygen deficiencies in the coating structure.

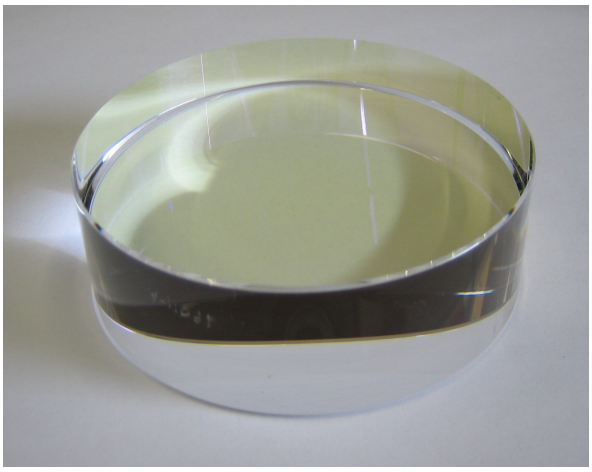

Figure 5.1 Coated test mass sample, with coating on top face.

Each mass had a different level of doping material contained in the high refractive index tantala layer. The composition of the three samples tested was as shown in Table 5.1, with details supplied by CSIRO [164] [165].

Coating sample	High index layer composition
1	35% Titania (TiO_2), 65% Silica (SiO_2)
2	85% Tantala (Ta_2O_5), 15% Titania (TiO_2)
3	65% Tantala (Ta_2O_5), 35% Silica (SiO_2)

Table 5.1 Composition of high index layers of three CSIRO coated samples.

The first sample was chosen to allow the investigation of the use of a doped titania high index layer coating with a low amount of this material used. The second sample was nominally identical to a sample previously tested which showed a reduction in mechanical loss over an undoped coating [154]. However, this previously investigated sample was made by a different coating vendor - Laboratoire des Materiaux Avances (LMA), France [166]. The CSIRO sample was therefore used to compare nominally identical coatings from different vendors. The third sample was chosen to investigate reduction of loss of the tantala layers by doping with silica which is known to have lower loss than tantala [167] [162].

No uncoated control mass was supplied, so one which was annealed to the closest temperature of 450°C was used instead, this being annealed in a batch by LMA.

5.3.2 Experimental Mechanical Loss Measurement Setup

The measurement system was based on the type used previously by Rowan [107], Sneddon [108], Murray [162], but with improvements to increase the flexibility and accuracy of the measurements undertaken.

5.3.2.1 Test Mass Suspension

The test mass samples must have freedom to move in accordance with their resonant motion. Any external sources of resistance to resonant motion will introduce excess damping to the system, meaning the measured losses will be higher than the actual loss of the sample alone. Additionally, the mass sample must be very well isolated from its surroundings to ensure that the energy is contained in the excited resonant mode, and minimal energy is lost to mechanisms other than internal friction. For these reasons, pendulum suspensions are again employed to provide isolation. The mass is held by a single loop of silk thread - this suspension material can allow low mechanical losses to be measured, as shown by Braginsky [168]. Loss of energy to the swinging pendulum modes of this suspension is minimal due to the large separation in frequency of the internal modes of the sample (typically 20 kHz and above) and the modes of the pendulum (typically around 1 Hz). Loss of energy to violin modes is minimised by use of short suspensions, and the suspension length is also varied to alter the potential for energy to couple into violin modes.

The silk loops around the centre of the barrel of the test mass, and is clamped by a metal clamping block, as shown in Figure 5.2. Energy loss at the clamp was minimised by hollowing out the faces of the clamp to ensure that clamping did not occur higher up between clamp surfaces, which would introduce the risk of the thread rubbing within

the clamp. This would also occur if the clamping block and clamp bar had lower faces at different heights - guide prongs ensure that these faces are flush.

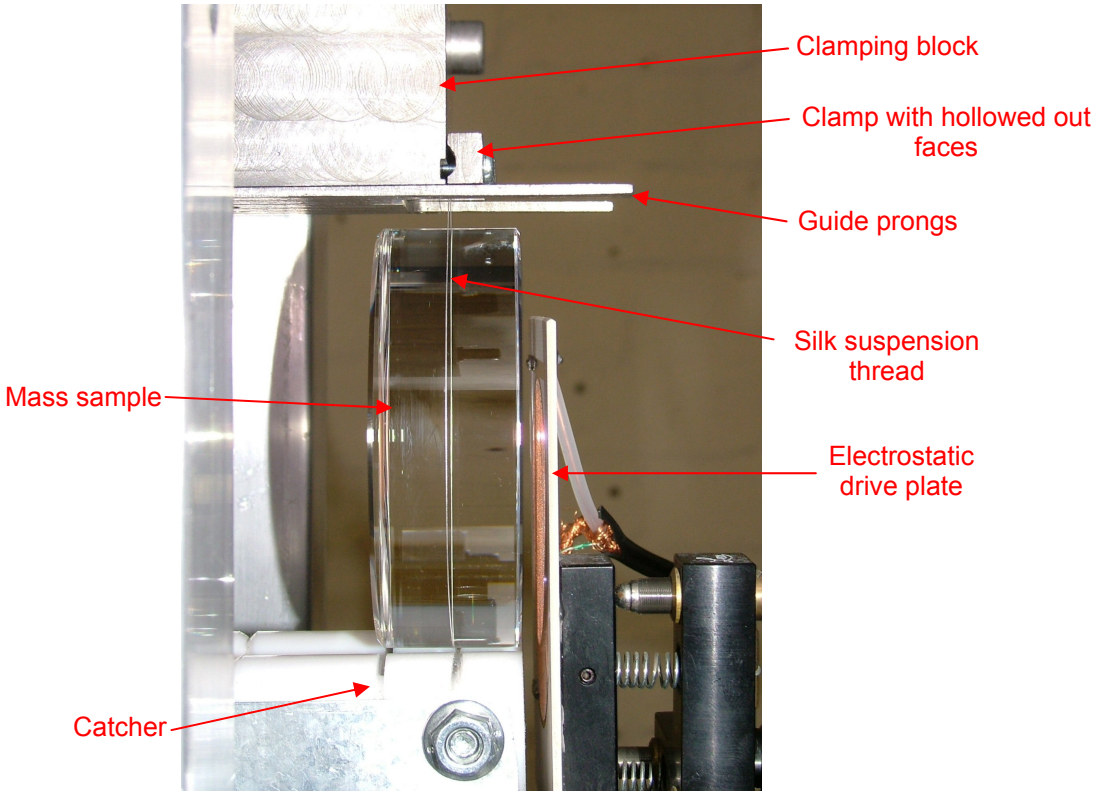

Figure 5.2 Side view of test mass sling suspension, showing clamping block, clamp with hollowed faces, mass, drive plate and catcher.

The sample's resonant modes are excited electrostatically by means of an actuator drive plate as shown in Figure 5.2. This plate is held 1 - 2 mm behind the rear face of the test mass. A DC voltage of 750 V is applied to this to polarise the material, together with an AC voltage of up to 1500 V peak to peak at frequency equal to that of the resonant mode being examined, which provides the driving force to the polarised material.

The sample, clamping structure and drive plate are placed in a vacuum tank which is pumped out to a pressure of approximately 10^{-6} to 10^{-7} millibars which ensures that the

resonant motion of the mass is not dominated by gas damping [89] at the level of loss measured here.

5.3.2.2 Detection System

Resonant motion of the front face of the mass is sensed using a small Michelson interferometer. The interferometer read-out system is detailed in Figure 5.3. One arm (the "internal" arm) of the interferometer is formed by reflecting laser light from the front surface of the test mass. The second ("external") arm is folded, with 3 mirrors attached to two types of actuator – one piezoelectric transducer, and two small loudspeakers. These actuators act to compensate for large amplitude low frequency motion (with displacement > 1 wavelength) of the test mass. The actuators are controlled by a low frequency feedback system driving the piezo, and via an additional low pass filter to the loudspeakers. This system adjusts the mirror's position, and hence the external arm length, to cancel out internal arm length changes caused by the low frequency pendulum motion. Multiple actuators were found necessary to compensate for large motions of thin disc samples whose measurements will be detailed in Chapter 6. The interferometer locks half way up an interference fringe, so that changes in arm length could give both positive and negative feedback signals to the actuators.

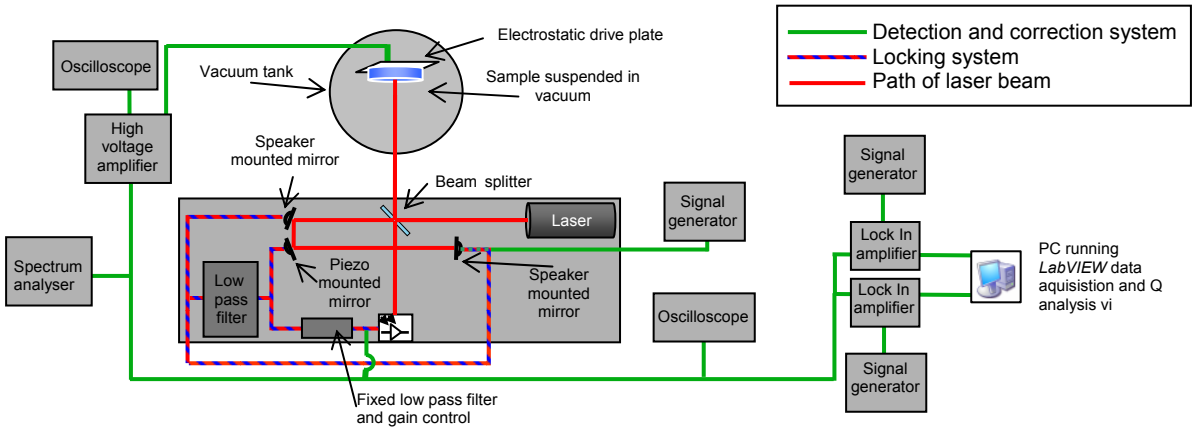

Figure 5.3 Experimental setup for measurement of mechanical loss of test mass samples.

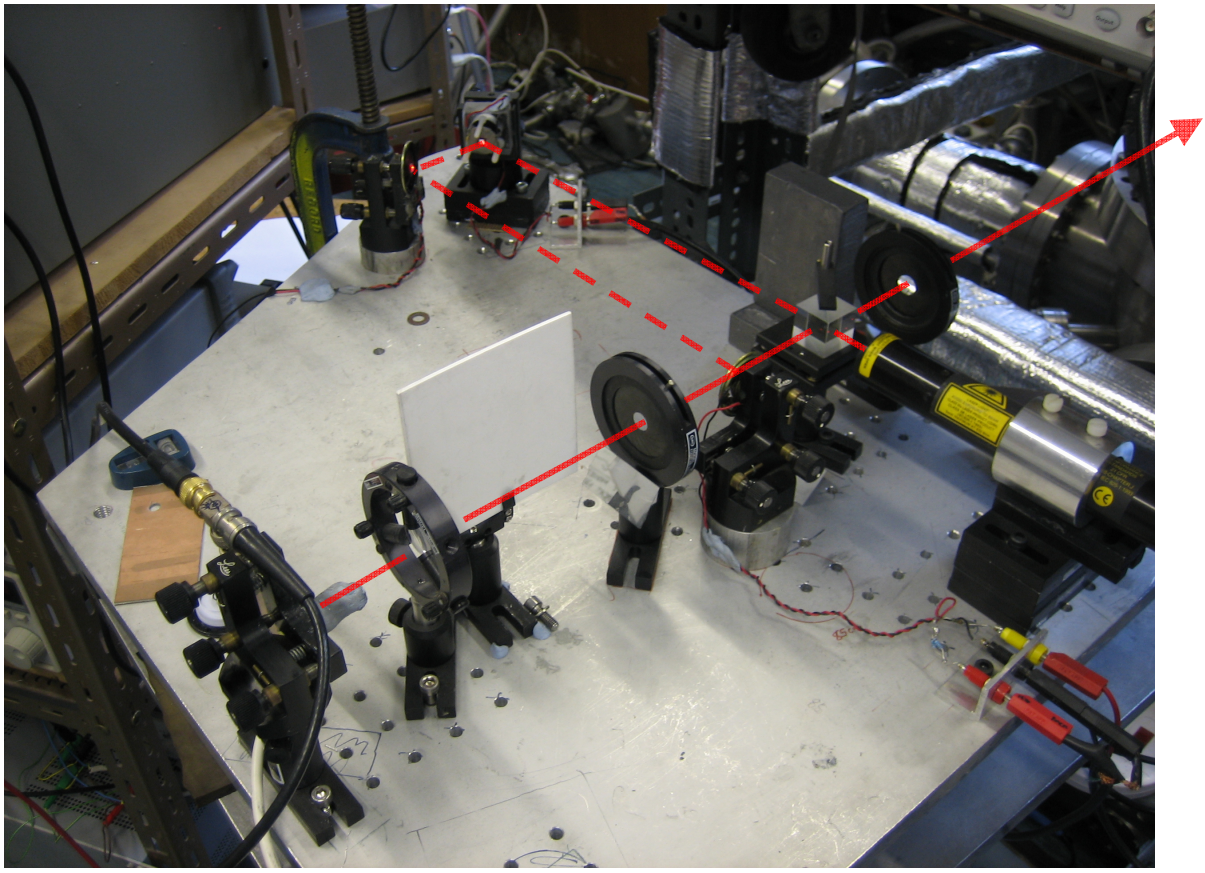

Figure 5.4 Photo of interferometer showing the beam paths around the optical bench of the interferometer. Beam exiting to the right incidents the front face of the test mass within the vacuum tank.

Figure 5.5 shows the typical recorded ringdown data, and shows the ringdown envelope of the decay which is used in the calculation of the quality factor Q of the resonance.

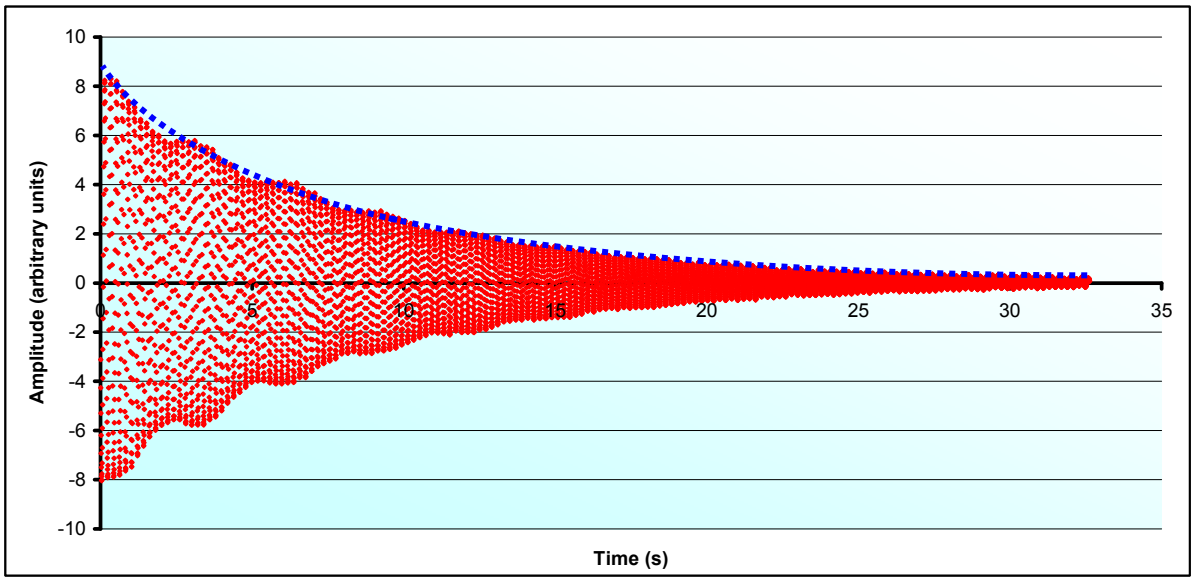

Figure 5.5 Plot showing raw ringdown data (red), and the exponential ringdown envelope from which the Q-factor of the resonance is calculated. The data shows a sinusoidal variation in amplitude, of the type that is discussed below.

Initial testing of the interferometer displayed several problems that led to the recording of inaccurate and erratic data. These problems included:

- Fluctuation of laser power – since the photodiode detector measures light intensity any variation in laser power will result in a variation in the intensity observed at the photodiode
- Long period drift of the interferometer from the state of maximal interference fringe amplitude. This deterioration in lock can occur for several reasons – thermal expansion/contraction of the optical bench and its components could cause deterioration of the alignment of beams due to expansion or contraction of the optical mounts for the actuators. Also, if the mass should move slightly in its suspension the beam alignment can be changed. It was observed that a mass pitch or yaw angle of around 0.05° was enough to cause a fringe amplitude drop that knocked the interferometer out of a locked state.

As well as causing loss of lock, both of these occurrences can result in fluctuations in the output fringe amplitude. This introduces variations into the amplitude of the recorded signal. Since the amplitude of the resonant oscillation of the sample is the quantity being observed, it is clear that any large variation in the fringe amplitude over the time span of the measurement will result in an incorrect exponential decay envelope being recorded.

The laser intensity was monitored using a pick off beam splitter and second photodiode. A typical resulting intensity profile from switch on (at time = 0) is shown in Figure 5.6. This shows that laser power builds rapidly to a peak when switched on, then decays with an oscillation in amplitude. This oscillation exhibited a steadily increasing period until dropping into a more steady state at around 10000 seconds ($2\ ^{3}/_{4}$ hours) after cold switch on. This phenomenon seemed intrinsic to this particular laser model, as two identical model lasers[1] were tested and found to perform similarly. For times longer than 10000 s the laser was more stable, but still exhibited some larger fluctuations in amplitude, and ring downs recorded when the laser was acting in this manner also contained similar fluctuations.

[1] Melles Griot 25-LHP-691-230, class 3B He-Ne laser, 633nm.

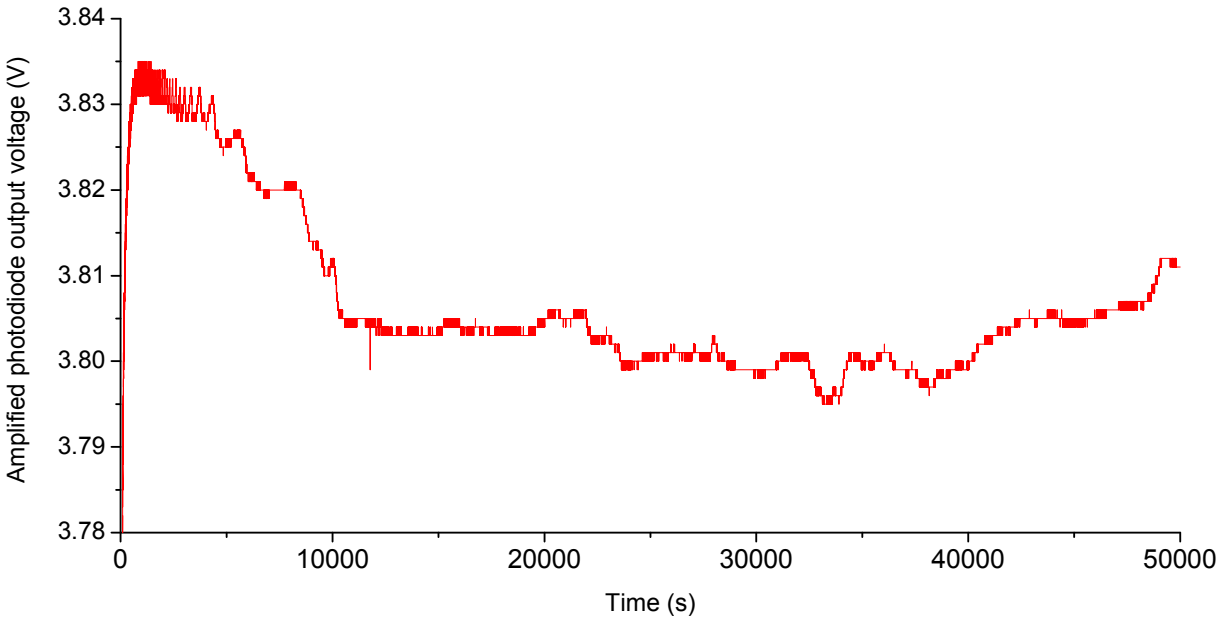

Figure 5.6 Laser intensity variation as a function of time for He-Ne laser used in interferometric loss measurements

This intensity change was observable in the ring down data as shown in Figure 5.7. The periodic beat of the intensity change showed a clear correlation with amplitude beating of the exponential ringdown envelope of a mass sample recorded at the same time, as shown in Figure 5.7.

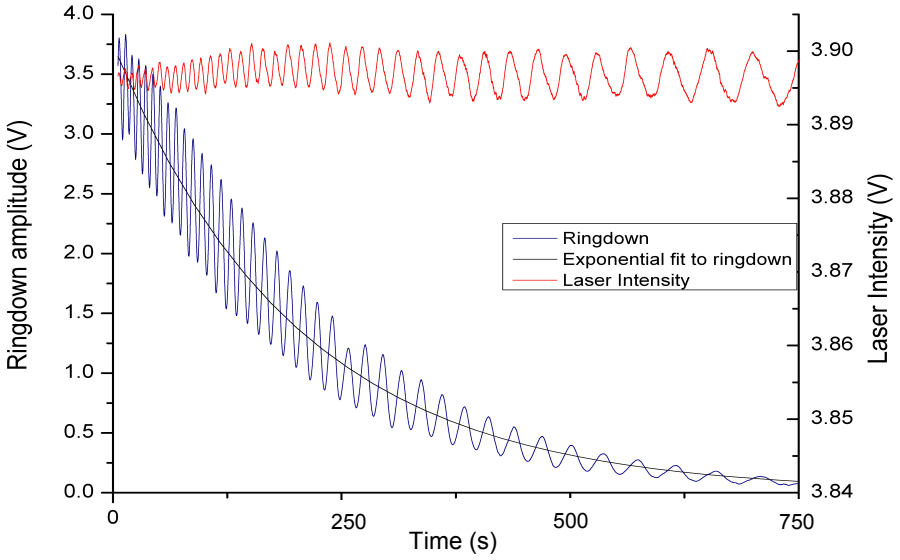

Figure 5.7 Variation in amplitude of a recorder ringdown as compared to the variation in intensity of laser power over the same period of 750 seconds.

It was clear that some form of compensation would be required to ensure that the most accurate exponential fit to the ringdown envelope could be attained.

5.3.2.3 Interferometer Signal Correction Apparatus

There was no way of directly stabilising the laser output for the simple He-Ne laser used – recovering the true ringdown envelope required an alternative method. Since the amplitude of the light in both interferometer arms is affected by any laser intensity change, the external arm can be used to correct for the discrepancies introduced into the ring down. One of the loudspeakers is used to inject a constant amplitude 10 kHz signal into the interferometer. This frequency was chosen as it was well outside the range of the low frequency feedback, but below that of the typical resonant modes of the sample. If the laser intensity and optical alignment remained constant, then the amplitude of the 10 kHz peak seen at the output of the interferometer must also be constant. Any variation due to laser intensity or change in alignment will be echoed in both the 10 kHz signal, and the ringdown itself, and hence normalising the ringdown

envelope amplitude with the amplitude of the 10 kHz signal restores the true ringdown envelope. The additional recorded 10 kHz signal ideally requires an additional lock-in amplifier (Figure 5.3) to beat the signal down to 5 Hz for ease of recording similar to the ring down.

Use of real test mass samples to check the ability of this system was not desirable, as the mechanical loss of the silica samples is of course the subject of the measurement, so not known accurately. Testing was therefore carried out using an additional loudspeaker mounted mirror attached in place of the sample. This was driven using a LabVIEW program (see Appendix E for program code) at 18 kHz with a predetermined exponential decay envelope, to mimic the decay of a resonance in a test mass sample. The 18 kHz signal was chosen as the highest frequency that can could reliably be output from the speaker, and is close in frequency to typical modes of test mass samples (20 kHz and above).

A mock ring down generated in this way and recorded using the interferometer is shown in Figure 5.8.

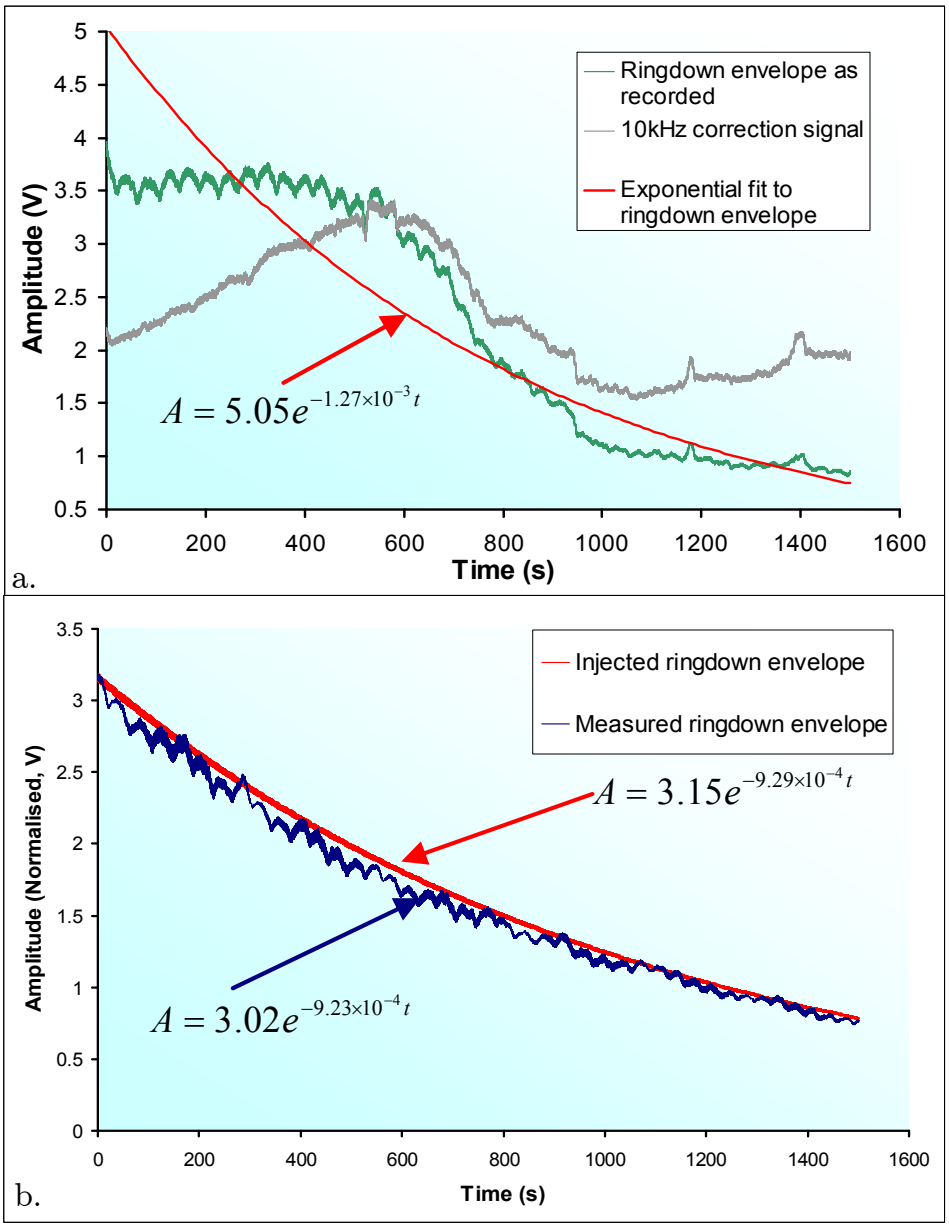

Figure 5.8 Recording and correcting of a ringdown envelope. a. Recorded ringdown envelope showing fluctuation in both ring down (green) and the recording of the constant amplitude 10kHz signal (grey). b. Ringdown envelope after normalisation by 10 kHz signal (black) is a much closer fit to the injected signal (red). The fit line for the black data is not shown for clarity.

The exponential fit to the ringdown envelope as recorded in Figure 5.8a is clearly poor, with larger fluctuation evident. After normalisation by the 10 kHz correction signal the recorded ringdown envelope has recovered its exponential form. The difference in the exponential coefficients is less than 1%, meaning the error introduced into the measured

Q by the exponential fitting is small. This coefficient is used to calculate the mechanical loss from equation (5.1), and therefore the correction system can be seen to have reduced the error in the measured mechanical loss.

Some typical datasets from real ringdowns showing fluctuations and capability of recovery by the correction signal are shown in Figure 5.9 and Figure 5.10.

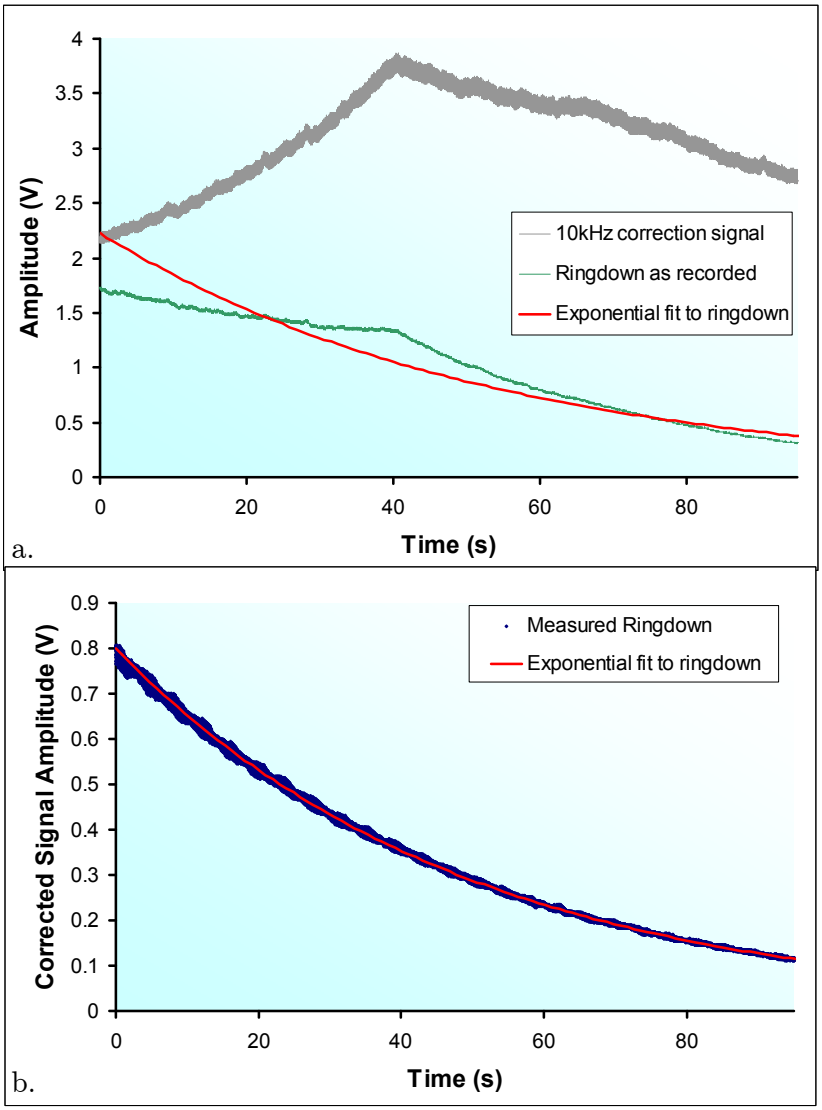

Figure 5.9a. Typical poor dataset showing a fluctuation and peak in the ringdown envelope after 40s, likely caused by a varying alignment in the interferometer. b. The corrected data shows near perfect exponential form.

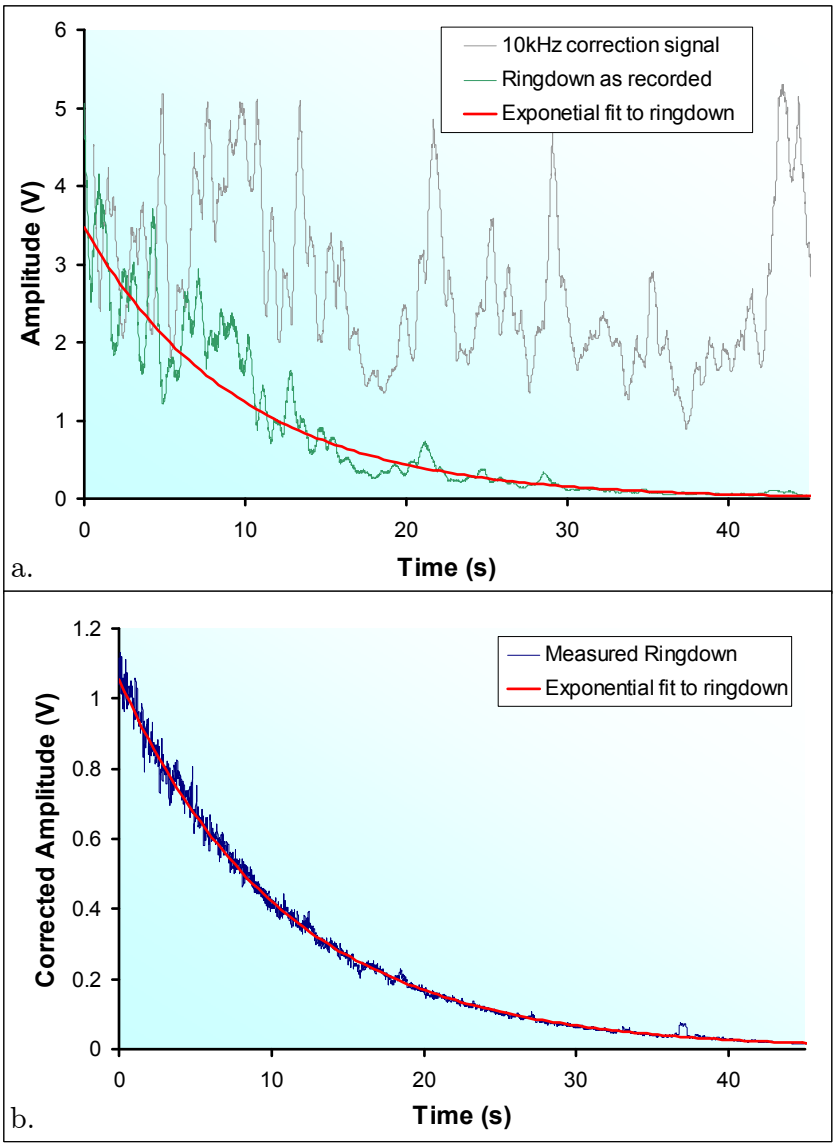

Figure 5.10a. Very poor dataset from a ringdown taken when significant vibration in laboratory. b. After correction, the corrected dataset is still very usable.

5.3.2.4 Data acquisition

The ringdown dataset was acquired using a LabVIEW data acquisition program written by the author, which allowed file structure of dataset files to be created automatically, plotted the pre- and post-correction of the measured data for the current ring down, and also calculated the mechanical loss automatically on ringdown completion. Code for this program is detailed in Appendix F.

5.3.3 Calculation of Coating Loss

The total measured mechanical loss of a coated test mass sample can be expressed as:

$$\phi(\omega_o)_{\text{Mass Sample}} = \phi(\omega_o)_{\text{Substrate}} + \phi(\omega_o)_{\text{Coating}} \tag{5.4}$$

where $\phi(\omega_o)_{\text{Substrate}}$ is the intrinsic mechanical loss associated with the substrate, and $\phi(\omega_o)_{\text{Coating}}$ is the any additional mechanical loss introduced by the coating on the front face. From equation (2.13) mechanical loss can be defined:

$$\phi(\omega_o) = \frac{E_{\text{Dissipated}}}{2\pi\, E_{\text{Stored}}}$$

Therefore equation (5.4) can be expressed:

$$\phi(\omega_o)_{\text{Mass Sample}} = \frac{E_{\text{Dissipated}_{\text{Substrate}}} + E_{\text{Dissipated}_{\text{Coating}}}}{2\pi\, E_{\text{Stored}_{\text{Substrate and coating}}}} \tag{5.5}$$

Also, the components of equation (5.4) can be expressed:

$$\phi(\omega_o)_{\text{Substrate}} = \frac{E_{\text{Dissipated}_{\text{Substrate}}}}{2\pi\, E_{\text{Stored}_{\text{Substrate}}}} \tag{5.6}$$

$$\phi(\omega_o)_{\text{Coating}} = \frac{E_{\text{Dissipated}_{\text{Coating}}}}{2\pi\, E_{\text{Stored}_{\text{coating}}}} \tag{5.7}$$

So equation (5.5) can be re-expressed as:

$$\phi(\omega_o)_{\text{Mass Sample}} = \frac{E_{\text{Stored}_{\text{Substrate}}}}{E_{\text{Stored}_{\text{Substrate and coating}}}} \phi(\omega_o)_{\text{Substrate}} + \frac{E_{\text{Stored}_{\text{Coating}}}}{E_{\text{Stored}_{\text{Substrate and coating}}}} \phi(\omega_o)_{\text{Coating}} \tag{5.8}$$

Since the coatings on the test mass samples are very thin compared to the thickness of the substrate, the energy stored in the coating is very small, and therefore:

$$E_{\text{Stored}_{\text{Substrate}}} \approx E_{\text{Stored}_{\text{Substrate and Coating}}} \tag{5.9}$$

Hence:

$$\phi(\omega_o)_{\text{Mass Sample}} = \phi(\omega_o)_{\text{Substrate}} + \frac{E_{\text{Stored}_{\text{Coating}}}}{E_{\text{Stored}_{\text{Substrate}}}} \phi(\omega_o)_{\text{Coating}} \tag{5.10}$$

which yields:

$$\phi(\omega_o)_{\text{Coating}} = \frac{E_{\text{Stored}_{\text{Substrate}}}}{E_{\text{Stored}_{\text{coating}}}} \left(\phi(\omega_o)_{\text{Mass Sample}} - \phi(\omega_o)_{\text{Substrate}}\right) \tag{5.11}$$

$\phi(\omega_o)_{\text{Masss Sample}}$ is obtained from the measured mechanical loss of the coated test mass sample, and $\phi(\omega_o)_{\text{Substrate}}$ from measurements of an identical uncoated sample. $\frac{E_{\text{Stored}_{\text{Substrate}}}}{E_{\text{Stored}_{\text{coating}}}}$ is the ratio of the total elastic energy in both substrate and coating to the elastic energy contained in the coating itself. This factor is dependant on the particular resonant mode in question, and therefore must be calculated for each mode that has been measured.

The coating loss can be subdivided into further components – namely a thermoelastic loss contribution and a contribution due to Brownian thermal noise:

$$\phi(\omega_o)_{\text{Coating}} = \phi(\omega_o)_{\text{Coating}_{\text{Thermoelastic}}} + \phi(\omega_o)_{\text{Coating}_{\text{Brownian}}} \tag{5.12}$$

The coating loss can be further expressed as [169] [161]:

$$\phi(\omega_o)_{\text{Coating}} = \phi(\omega_o)_{\text{residual}} + \frac{E_{\text{Coating}_{\text{Volume change}}}}{E_{\text{Coating}_{\text{Total}}}} \phi(\omega_o)_{\text{Thermoelastic}} \tag{5.13}$$

where $\phi(\omega_o)_{\text{residual}}$ is the level of loss associated with Brownian thermal noise and $\phi(\omega_o)_{\text{Thermoelastic}}$ is the loss associated with thermoelastic noise in the coating, which

occurs as the coating layers and substrate mass have different thermal and mechanical properties. $E_{\text{Coating}_{\text{Volume change}}}$ is the energy associated with the change in volume of the coating that occurs due to resonant motion. With no volume change there will be no thermoelastic loss, however this does not occur and thermoelastic loss is believed to contribute to the overall loss [169]. This ratio was calculated for each resonant mode by D. Crooks [159]. The ratio of energy stored in the coating to that stored in the substrate, used in equation (5.11) can be calculated using ANSYS finite element modelling of the test mass sample and its coating.

The residual loss is important to consider as it shows the intrinsic Brownian thermal noise component of the mechanical loss of the coating. Analysis of this is hoped to identify the mechanisms for dissipation within the coating layer, and therefore find methods to reduce the dissipation.

5.3.4 Extracting Energy Ratios from ANSYS

The energy ratio can be calculated in ANSYS by modelling the coated test mass sample as shown in Figure 5.11.

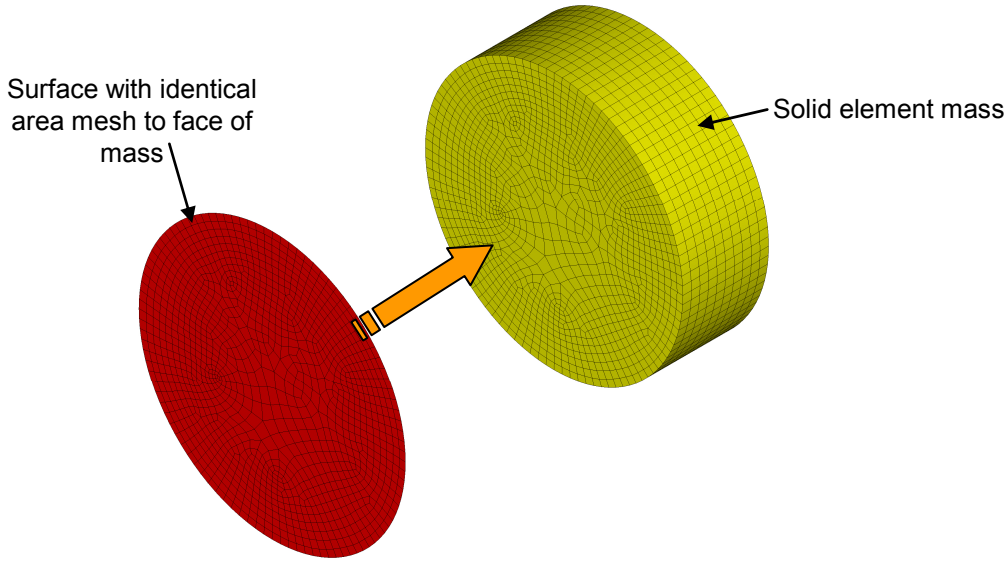

Figure 5.11 Application of a coating surface to a FEA model of the test mass sample in ANSYS.

The mass is modelled in solid elements and the mesh on one face is copied to form a second surface which represents the coating. This is given the appropriate thickness and the energy contained within the coating can thus be evaluated using ANSYS for each individual resonant mode of the sample.

The coating is treated as one composite material, with composite material properties used to represent the coating in ANSYS [159].

5.3.5 Composite Material Properties

The effective Young's modulus, Y_{eff} [170], Poisson's ratio, ν_{eff} [170] and density ρ_{eff} [161] for a composite material are calculated using:

$$Y_{eff} = \frac{Y_H h_H + Y_L h_L}{h_H + h_L} \tag{5.14}$$

$$\nu_{eff} = \frac{h_H \nu_H Y_H \left(1-\nu_H{}^2\right) + h_L \nu_L Y_L \left(1-\nu_L{}^2\right)}{h_H Y_H \left(1-\nu_H{}^2\right) + h_L Y_L \left(1-\nu_L{}^2\right)} \tag{5.15}$$

$$\rho_{eff} = \frac{\rho_H h_H + \rho_L h_L}{h_H + h_L} \tag{5.16}$$

where Y_L, h_L, ν_L, ρ_L are the Young's modulus, thickness, Poisson's ratio and density of the low refractive index material; and Y_H, h_H, ν_H, ρ_H are the Young's modulus, thickness, Poisson's ratio and density of the high refractive index material.

For the individual doped high refractive index layers of the coating, composite material properties must also be calculated. The composition is specified in a fraction t of material, and the composite material properties for the high index doped layers are calculated by [170] :

$$Y_H = \frac{Y_1 Y_2}{Y_1 t_2 + Y_2 t_1} \tag{5.17}$$

$$\nu_H = \frac{t_1 \nu_1 Y_1 \left(1-\nu_1^{\,2}\right) + t_2 \nu_2 Y_2 \left(1-\nu_2^{\,2}\right)}{t_1 Y_1 \left(1-\nu_1^{\,2}\right) + t_2 Y_2 \left(1-\nu_2^{\,2}\right)} \tag{5.18}$$

$$\rho_H = \frac{\rho_1 t_1 + \rho_2 t_2}{t_1 + t_2} \tag{5.19}$$

The properties of the coating component materials are shown in Table 5.2.

Material	Young's modulus, Y (GPa)	Poisson's ratio, ν	Density, ρ (kgm^{-3})
Silica (SiO_2)	72	0.17	2202
Tantala (Ta_2O_5)	140	0.23	6850
Titania (TiO_2)	290	0.28	4260

Table 5.2 Properties of individual constituent materials of the coating samples

The calculated composite material properties for the high refractive index layers are shown in Table 5.3.

Coating	Young's modulus, Y_H (GPa)	Poisson's ratio, ν_H	Density, ρ_H (kgm^{-3})
35% Titania (TiO_2), 65% Silica (SiO_2)	98	0.24	2921
85% Tantala (Ta_2O_5), 15% Titania (TiO_2)	152	0.24	6462
65% Tantala (Ta_2O_5), 35% Silica (SiO_2)	105	0.22	5223

Table 5.3 Composite material properties of high refractive index layers of doped coatings

Thicknesses of the coating layers are shown in Table 5.4, and were obtained from CSIRO [171].

Coating	Thickness of high index layer h_H (nm)	Thickness of low index layer h_L (nm)	Total thickness of 30 layer coating (μm)
35% Titania (TiO_2), 65% Silica (SiO_2) / Silica	191	129	4.80
85% Tantala (Ta_2O_5), 15% Titania (TiO_2) / Silica	127	187	4.70
65% Tantala (Ta_2O_5), 35% Silica (SiO_2) / Silica	145	174	4.78

Table 5.4 Thicknesses of the individual high and low index layers, and of complete coating

Use of equations (5.14)…(5.19) yielded the final composite material properties for the full 30 layer coatings, shown in Table 5.5. These values were used in the ANSYS models when extracting elastic energy ratios.

Coating	Young's modulus, Y_{eff} (GPa)	Poisson's ratio, ν_{eff}	Density, ρ_{eff} (kgm^{-3})
35% Titania (TiO_2), 65% Silica (SiO_2) / Silica	87	0.21	2631
85% Tantala (Ta_2O_5), 15% Titania (TiO_2) / Silica	104	0.21	3922
65% Tantala (Ta_2O_5), 35% Silica (SiO_2) / Silica	87	0.19	3572

Table 5.5 Effective material properties of 30 layer doped coatings.

5.3.6 Mode Shapes and Frequencies

ANSYS was also used to determine which modes are suitable for measurement, and to find the mode frequencies. This was done using an unconstrained modal analysis, and the measured modes of the samples tested are shown in Figure 5.12.

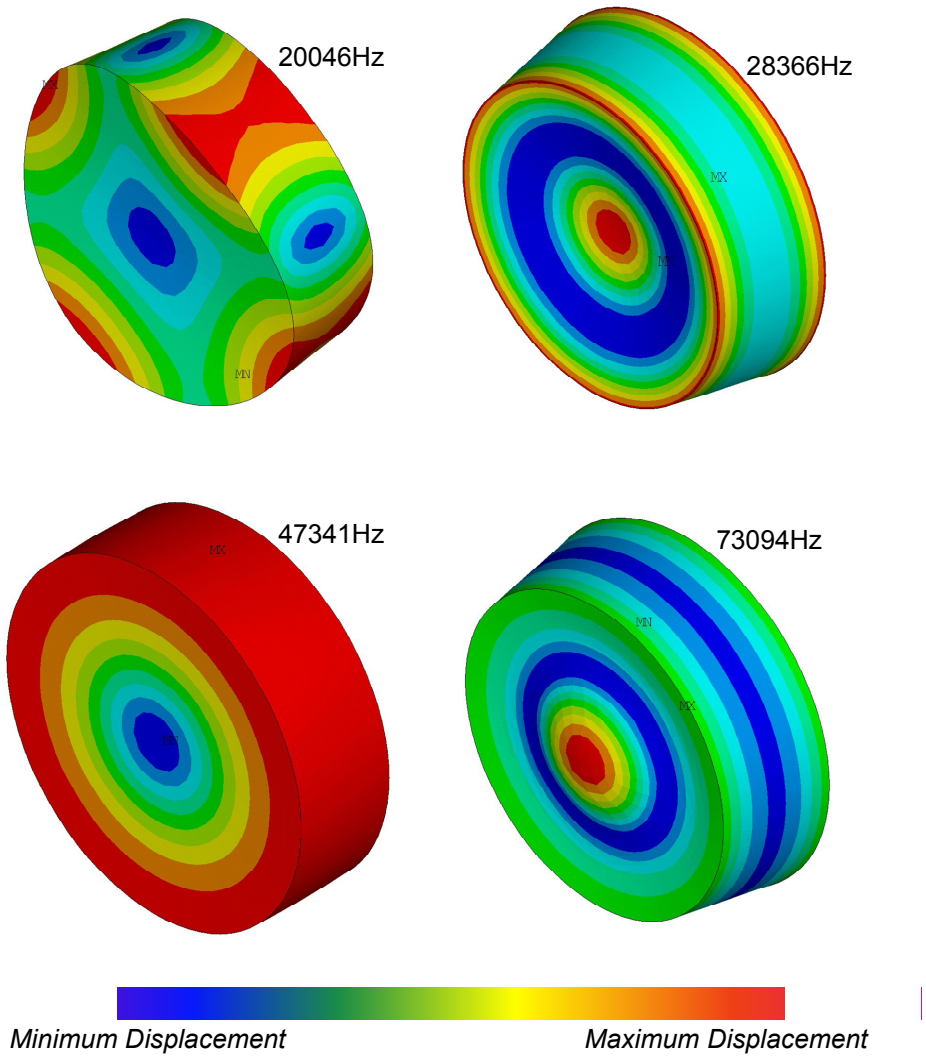

Figure 5.12 ANSYS derived mode shapes for 76.2 mm (3") diameter and 25.4 mm (1") thick test mass sample. Relative displacement vector sums $U = \sqrt{x^2 + y^2 + z^2}$ *are shown in dimensionless units.*

These modes were chosen for measurement of losses as they exhibit motion on the front face of the mass, and only modes with significant displacement on the front face of the test mass can be sensed using an interferometric read out.

5.4 Mechanical Loss of Doped Tantala Coatings

The measured mechanical losses of the three silica samples with doped coatings are shown in Figure 5.13. Also shown for reference are measurements by Murray [162] of a sample with a tantala / silica coating where no doping had been performed on the tantala component.

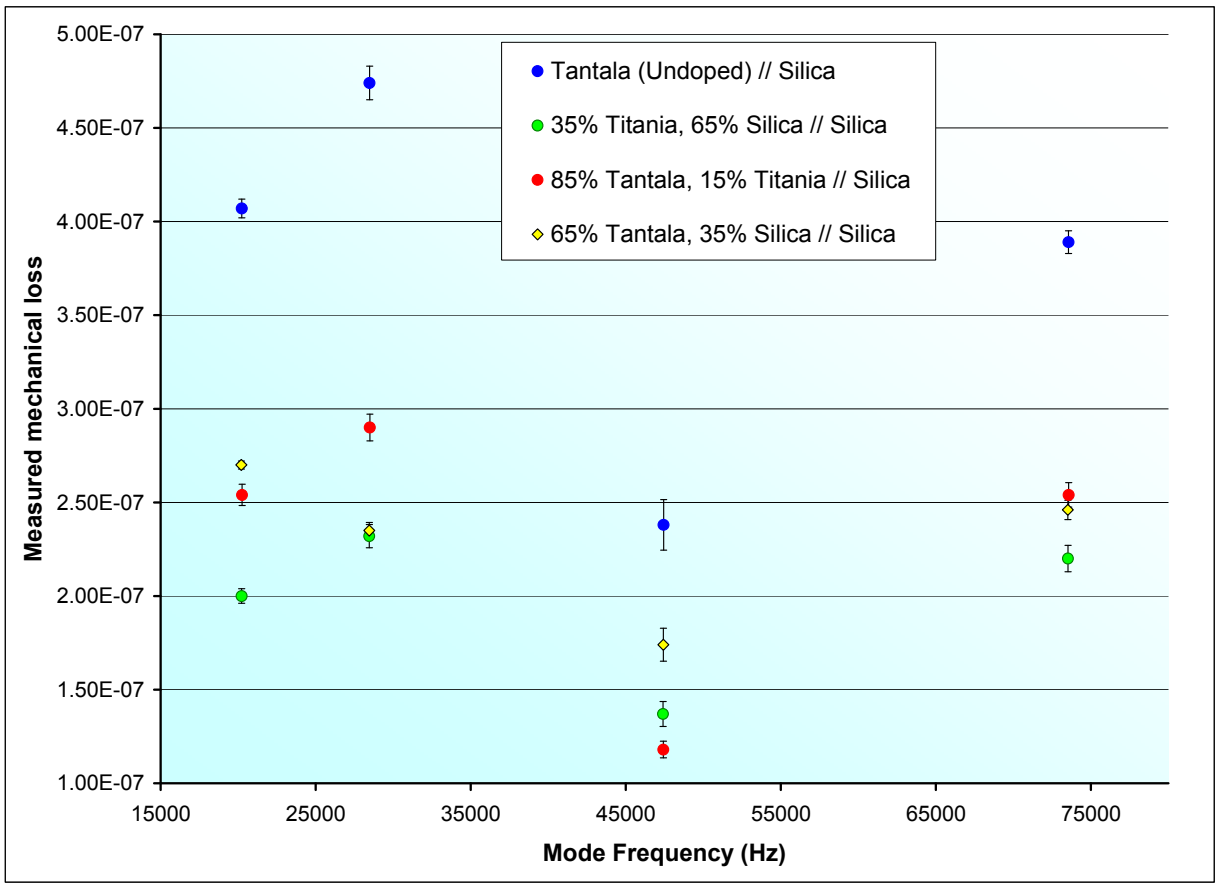

Figure 5.13 Measured mechanical losses of different 30 layer coatinged silica test mass samples manufactured by CSIRO

The ratios of elastic energies calculated using ANSYS are shown in Table 5.6.

Coating	Mode frequency	Elastic energy ratio x 10^{-4}
1 – 35% Titania, 65% Silica / Silica	20047	5.89
	28369	6.38
	47341	2.21
	73092	4.47
2 – 85% Tantala, 15% Titania / Silica	20047	6.90
	28367	7.47
	47340	2.38
	73089	5.23
3 – 65% Tantala, 35% Silica / Silica	20047	5.95
	28368	6.23
	47339	2.15
	73117	4.39

Table 5.6 Ratios of the elastic energy contained in the coating to the total elastic energy in both substrate and coating for the three doped mass samples. Convergence of the solutions was found to be similar to the convergence of the models studied in Chapter 4

The resulting coating losses (which include thermoelastic contribution as shown in equation (5.11)) are shown in Table 5.7.

Coating	Coating loss x 10^{-4}
Tantala (Undoped) / Silica	4.28±0.19
1 - 35% Titania, 65% Silica / Silica	2.06±0.03
2 - 85% Tantala, 15% Titania / Silica	2.49±0.06
3 - 65% Tantala, 35% Silica / Silica	2.70±0.21

Table 5.7 Coating losses for doped coatings, with undoped tantala / silica coating loss also shown.

Residual coating losses (which show the Brownian thermal noise contribution only) were calculated by Peter Murray and are presented in Table 5.8.

Coating	Residual loss x 10^{-4}
Tantala (Undoped) / Silica	4.19±0.13
1 - 35% Titania, 65% Silica / Silica	1.70±0.40
2 - 85% Tantala, 15% Titania / Silica	2.42±0.11
3 - 65% Tantala, 35% Silica / Silica	2.69±0.24

Table 5.8 Residual coating losses for doped coatings, with undoped tantala / silica residual coating loss also shown.

It is clear that both the coating losses and the residual coating losses for all the doped samples are significantly lower than those for an undoped coating.

The first sample showed the greatest change in loss, with a reduction of around a factor of 2.5 over an undoped tantala / silica coating. This is an encouraging result for thermal noise reduction.

However, the two doped tantala coatings (coatings 2 and 3) also exhibit a reduction in loss of around a factor of 2 over the undoped coating sample. Doping tantala with titania also increases the refractive index of the doped layers, meaning that potentially fewer layers may be required to obtain a suitably reflective mirror; whereas the silica doped titania coating (coating 1) has a lower refractive index meaning that the number of layers could not be reduced as much [172]. Use of fewer layers therefore may be another method of reducing the overall mechanical loss of the coating.

The titania doped tantala sample gave a residual loss that was consistent with that measured previously on the nominally identical LMA sample whose residual loss also showed a similar drop to $(2.0 \pm 0.2) \times 10^{-4}$. The LMA sample had slightly lower loss, and it is apparent that the CSIRO coating has some property that is causing this difference. Currently the reason for this difference is unknown and requires further investigation.

5.5 Conclusions

It is clear that significant reductions in mechanical loss associated with tantala / silica multilayer high reflective mirrors can be achieved by doping of the high index tantala layer with small quantities of other materials.

The samples studied in this chapter have demonstrated that use of silica or titania as a dopant can result in a reduction in mechanical loss of around a factor of 2 for the

multilayer coating. Doping with titania also may offer an additional benefit of allowing a reduction in the number of coating layers required, which would also reduce the mechanical loss of the coating.

Work is ongoing by Martin et al [173], investigating the mechanisms for loss within the tantala coating layer which, when the mechanisms have been identified, may provide pointers to ways in which the coating mechanical loss could be further reduced.

Ongoing research will significantly benefit future gravitational wave detectors where a reduction in thermal noise at the most sensitive frequency regime will result in directly increasing the instrument sensitivity and astronomical reach.

Chapter 6

Mechanical Loss of Diffractive Mirrors

6.1 Interferometry Using Diffractive Optics

6.1.1 Introduction

Reduction of photon-shot noise in third generation interferometric gravitational wave detectors will necessitate use of much higher circulating laser powers, using power recycling. Advanced LIGO will have up to 830 kW of arm cavity laser power [125]. Future detectors are likely to increase this further permitting the circulation of megawatts of laser power in the arm cavities. Current interferometer topologies are not ideal for the use of such high powers, due to the use of transmissive optical components - namely the beamsplitters, and the inner test masses that make up the Fabry-Perot cavities. These components experience heating (of both their substrate material and the dielectric coatings) when a high laser power is applied [174]. This in turn can result in thermal deformation of the surface of the optic, which cause wavefront distortions in the laser beam [175]. In addition to the geometric deformations, the heating will result in a temperature gradient through a transmissive optical component producing lensing effects that place a limit on sensitivity [176] [177] [178]. Therefore, to mitigate these effects, use of all-reflective optical components may ultimately be desirable. This can be

achieved by employing mirrors with diffraction gratings on their surfaces, as proposed by Drever in 1996 [113].

6.1.2 Diffractive Interferometer Configurations

Consider a diffraction grating illuminated with a beam incident at angle θ_{in} relative to normal on the grating. Angles of diffracted beams are governed by the grating equation:

$$\sin\theta_m + \sin\theta_{\text{in}} = \frac{m\lambda}{d} \tag{6.1}$$

where d is the pitch of the diffraction grating, θ_m is the angle of the diffracted beam of mth order and λ is the wavelength. An all reflective Michelson interferometer (Figure 6.1b) can be constructed by placing reflective mirrors to intercept the beam reflected from the grating ($m = 0$ order case) and the $m = 1$ diffracted beam. The output beam from arm 1 comprises the $m = 1$ order diffracted beam resulting from the beam returning from mirror 1. The output beam from arm 2 comprises the $m = 0$ order diffracted beam resulting from the beam returning from mirror 2.

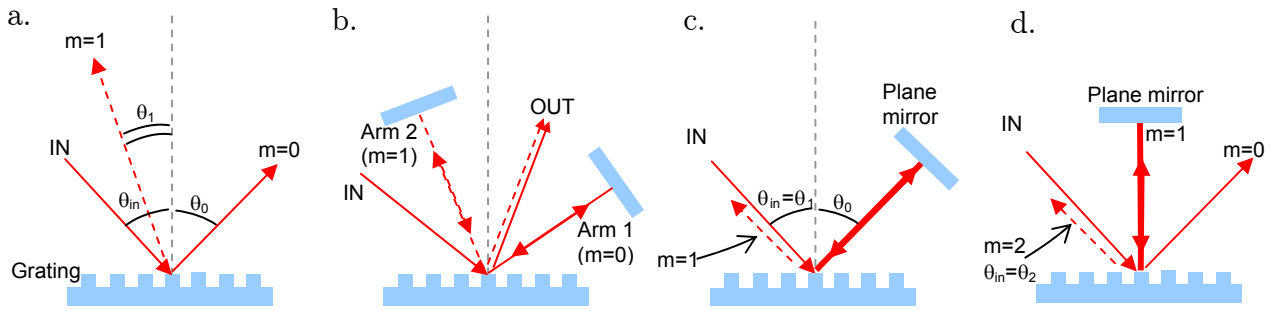

Figure 6.1 Typical grating configurations a. Diffraction from grating surface showing reflected beam m=0, and first order m=1 diffracted beam b. All reflective Michelson interferometer c. Fabry-Perot cavity formed with grating in 1st order Littrow configuration d. Fabry-Perot cavity formed with grating in 2nd order Littrow configuration

A grating is said to be in *first order Littrow* configuration when the incident angle θ_{in} and angle of first order diffraction θ_1 are equal. Placement of a mirror to intercept the reflected beam enables a simple Fabry-Perot cavity to be formed, as the returning beam

from the mirror also strikes the grating in first order Littrow configuration. This allows a build up of laser power in the cavity, with the finesse of the cavity being limited by diffraction efficiency of the grating in first order. Cavities formed in such a manner have been demonstrated by Sun [179].

In second order Littrow configuration ($\theta_{in} = \theta_2$) the first order diffracted beam is always normal to the grating surface, therefore a Fabry-Perot cavity can also be formed by placing a mirror parallel to the surface of the grating as shown in Figure 6.1. Such cavities have been experimentally demonstrated by Bunkowski [180].

6.1.3 Advantages of Diffractive Interferometry

Elimination of transmissive optical components is one of many advantages of use of diffractively coupled interferometers. Reduction of mirror heating has additional benefits for third generation detectors. The quest to reduce thermal noise may ultimately lead to cryogenically cooled detectors and therefore a reduction in mirror heating will permit easier cooling of the mirrors in such detectors.

Additionally, use of all reflective optics will permit the use of alternate ultra low mechanical loss materials as mirror substrates. Materials that have already been demonstrated [107] [115] as having suitably low mechanical loss include single crystal sapphire, and silicon. Silicon in particular has several desirable thermal properties including being highly thermally conductive compared to fused silica, which would again aid the cooling of test masses in cryogenic detectors. Additionally, at 18 K and 120 K silicon has a null in thermal expansion coefficient meaning there is no thermoelastic dissipation at these temperatures, which could allow a further reduction in thermal noise for cryogenic detectors.

The advantages of all reflective optical components have made the characterisation of the properties of the diffraction gratings an important research area [179] [181] [182]. In particular, since the surface of the substrate material is altered by the placement of a grating, it is important to examine if this has a detrimental affect on the mechanical loss of the substrate. Any increase in mechanical loss will result in an increase in thermal noise in the mirror. Additionally, since dielectric mirror coatings will be a limiting factor at mid-range frequencies in second generation detectors, it is important to determine if the mechanical loss of the coating layer is modified by placing it on top of a grating surface. The remainder of this chapter details mechanical loss measurements carried out on disk samples with diffraction gratings on their surfaces. These used fused silica as the substrate. This preliminary work on fused silica will be extended to other materials in the future.

6.1.4 Diffractive Samples

The samples utilised were 75 mm diameter by 1.7 mm thick 'Suprasil 311' fused silica disks, manufactured by Heraeus Quarzglass, with disks from 2 separate production batches used in the experiments.

Diffraction gratings were placed on two disks from the first batch. The gratings were manufactured by the University of Jena, using ion beam etching [183]. In this process, a thin layer of an ultraviolet reactive polymer is deposited on the surface of the disk. The grating structure was written into this polymer layer by laser. This polymer masks the areas of the disk surface which are to remain un-etched. The sample is then placed in a vacuum and exposed to an ion beam, which erodes the silica in the areas where the mask was removed by the laser. This etching process forms structure on the surface of the substrate. A portion of the resulting grating was observed under a VEECO optical

profiler [184] and the profiles are shown in Figure 6.2. The period of the diffraction grating grooves was approximately 1.4 μm, as shown in Figure 6.2c.

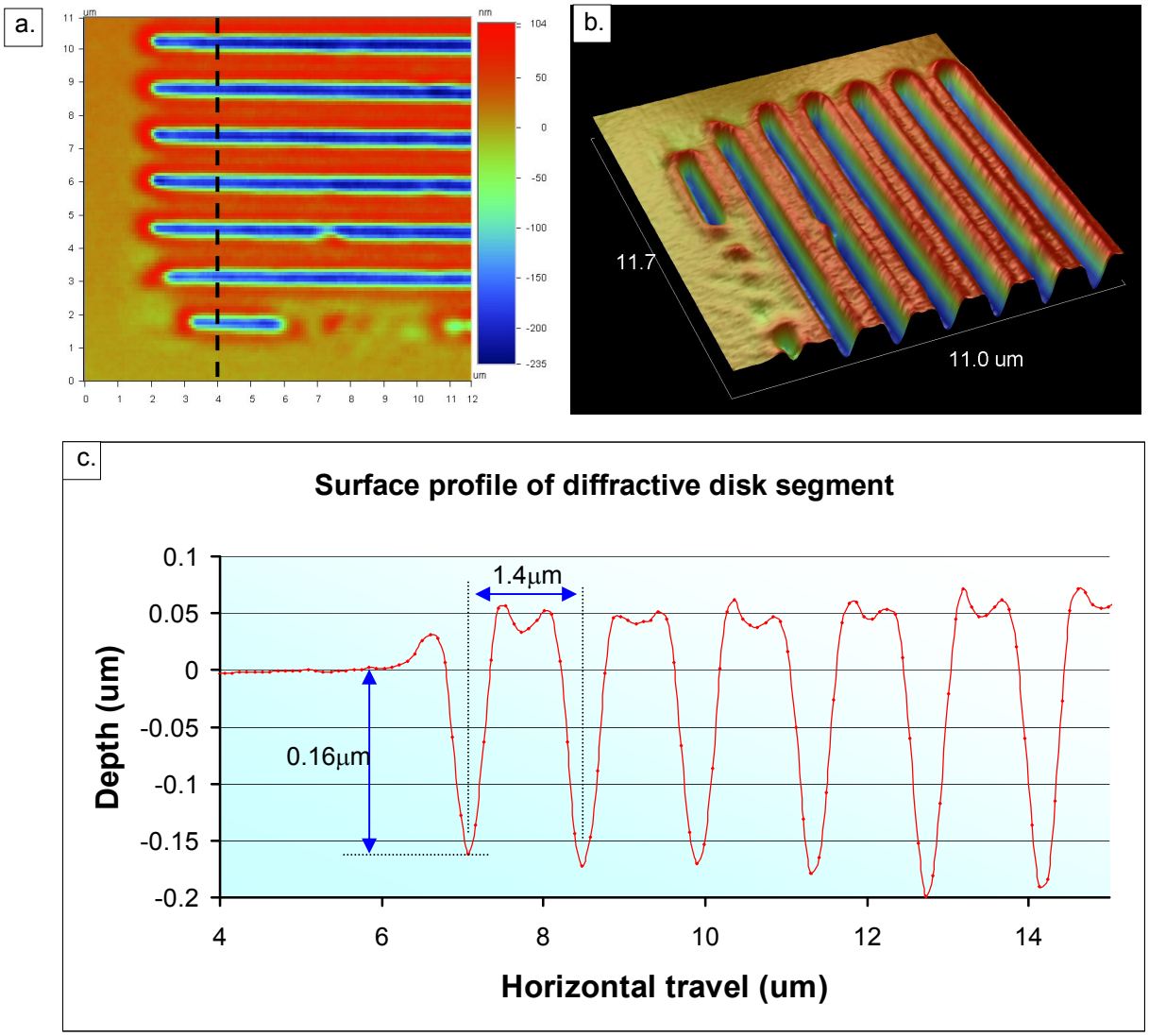

Figure 6.2 a. 2-D Optical profiles of diffraction grating on silica disk substrate, used in the experiments detailed in this chapter b. 3D image of same region c. Surface profile along dashed line

After initial measurements were conducted on the samples a standard high reflective silica doped tantala optical coating in a 30 layer stack was laid down on top of the grating. This was applied by ion beam sputtering, by LMA[2]. The coatings, the same as those studied in chapter 5 serve to enhance the reflectivity of the silica substrate and

[2] Laboratoire des Matériaux Avancés, University Claude Bernard Lyon I, France.

smooth the grating profile allowing softening of sharp edges and rough areas. A typical coating stack as applied to one of the samples is shown in Figure 6.3, showing the smoothing of the edges of the grating.

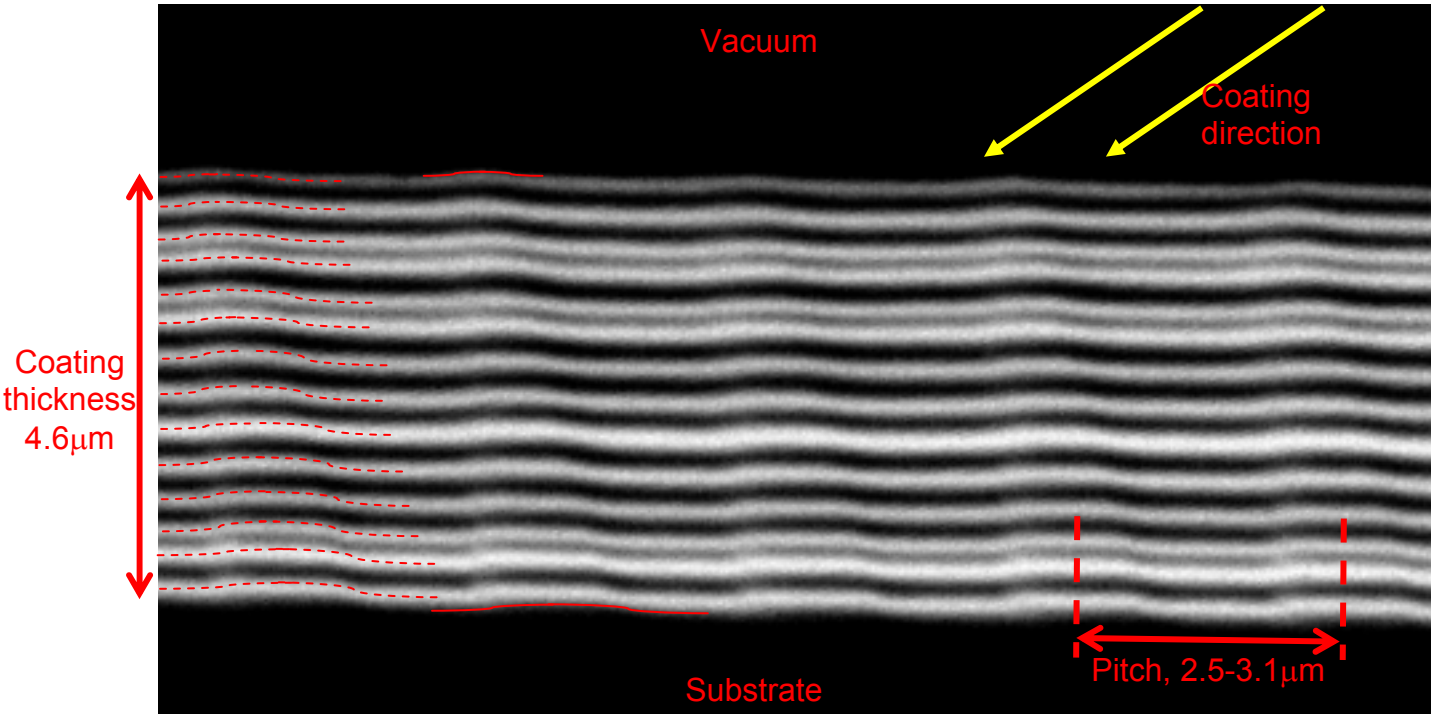

Figure 6.3 S.E.M. image of cross section of diffractive substrate with 30 layer silica-tantala coating stack (only 28 layers visible).

6.2 Mechanical Loss Measurements of Diffractive Samples by Fibre Suspension

The mechanical loss of the samples was determined using the same methods detailed in Chapter 5, by measurement of quality factor of excited resonant internal modes of the sample. Sample motion was sensed by the Michelson interferometer whose construction was detailed in Chapter 5.

6.2.1 FEA Modelling of the Substrates

Prior to commencing measurements of the samples, a FEA model of the substrate was made to observe the types of internal resonant modes of the sample, and also the approximate frequencies at which to search for them.

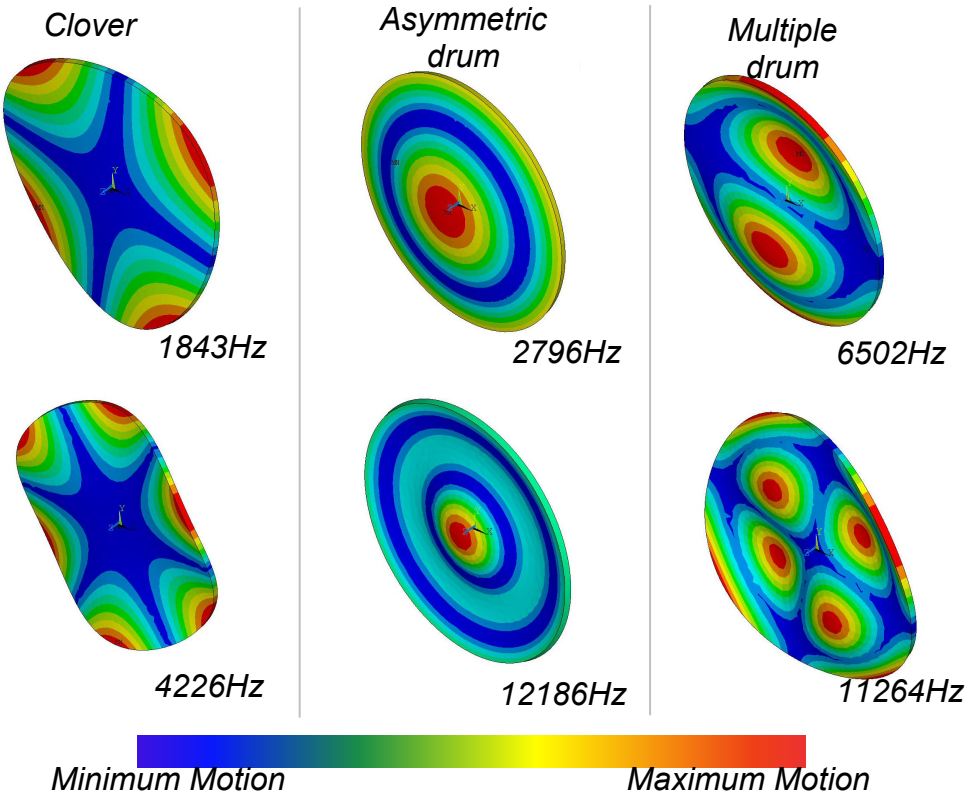

Figure 6.4 ANSYS FEA model mode shapes of silica disks. Relative displacement vector sums $U = \sqrt{x^2 + y^2 + z^2}$ *are shown in dimensionless units.*

Three broad types of mode were seen to exist – *"clover"* where multiple lobes of large motion are observed around the disk edge, *"Asymmetric drum"* with maximal motion at disk centre, these are rotationally symmetric, and *"multi-drum"* modes which can be seen to be a combination of clover and asymmetric drum modes, with points of maximal motion on both edges and at points across the surface of the disk.

The modes measured throughout this chapter comprised 4 to 12 lobe clover modes, the first two asymmetric drum modes and the first four multi-drum modes.

6.2.2 Sample Suspensions Used in Measurement

Support of the sample proved to be the most difficult aspect of the experiment. Initial measurements were performed with the disk suspended from silica fibres in a semi-

monolithic suspension. Seven suspensions of the sample were tried, with details as shown in Table 6.1 and Figure 6.5.

Suspension number	Description
1	Disk held at two points from 2 170 μm diameter, 175 mm long suspension fibres welded to crossbar and isolation mass. Isolation mass held from 330 μm diameter tungsten wire and blade springs
2	Disk held at single point from 2 170 μm diameter, 17.5 cm long suspension fibres welded to crossbar and isolation mass. Upper stage as suspension 1
3	Disk held at single point from 2 170 μm 8.3 cm long suspension fibres welded to crossbar and isolation mass. Upper stage as suspension 1
4	Disk held at single point from a single 170 μm 7.5 cm long suspension fibre welded directly to isolation mass. Upper stage as suspension 1
5	Disk held at single point from a single 170 μm 3 cm long suspension fibre welded directly to isolation mass. Upper stage as suspension 1, but minus cantilever blades
6	Disk held at single point from a single 170 μm 3 cm long suspension fibre welded directly to isolation mass. Upper stage held from thread
7	Disk held at single point from a single 170 μm 3 cm long suspension fibre welded directly to isolation mass, with isolation mass axis orientated vertically. Second fibre held mass from silica ear

Table 6.1 Details of the seven disc suspensions used in measurements.

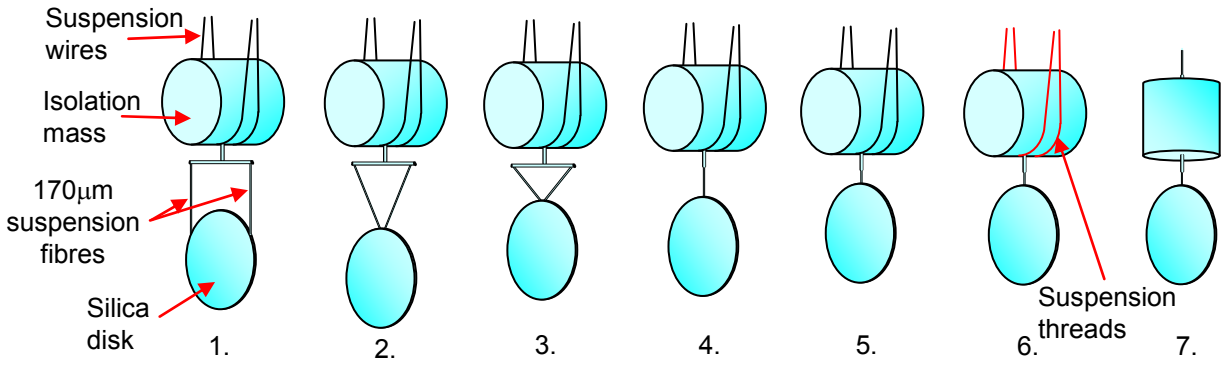

Figure 6.5 Seven silica suspensions used to investigate mechanical loss of silica disk

Initially, the disk was held by two silica fibres (suspension 1). This configuration was chosen to try and reduce the potential for the disk to rotate in the horizontal plane. Additional background isolation was employed in the form of a penultimate mass held

from cantilever blade springs, and this helped reduced motion of the suspension from seismic sources and the vacuum pumps as shown in Figure 6.6.

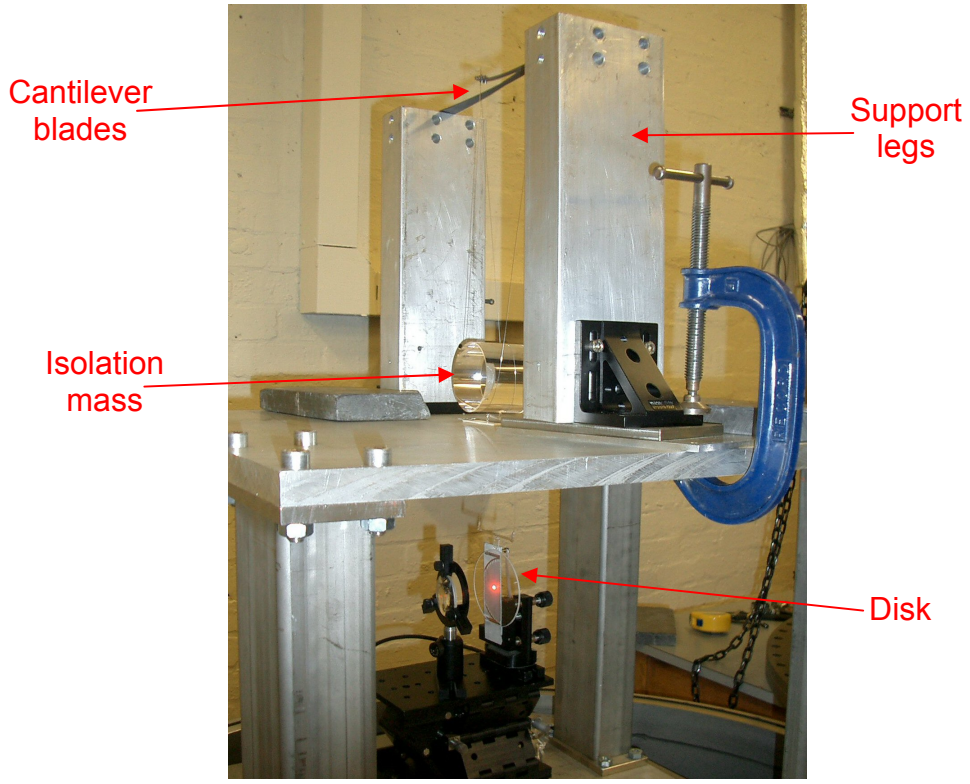

Figure 6.6 Suspension of silica disk, showing blade spring isolation and intermediate isolation mass

The second and third suspensions also utilised two suspension fibres, but welded to a single suspension point on this disk. Several modes were observed to have significant motion around the disk edges in the FE analysis, and reducing the number of suspension points was an attempt to minimise the potential for energy contained in an excited internal mode of the disk to be coupled into other, more dissipative, elements of the suspension. Also, two different lengths of suspension fibre were used to check whether there was coupling of energy to violin modes of the suspension fibres.

Suspensions 4 and 5 used a single fibre between the isolation mass and the disk – this made measurement more difficult with notable rotation of the disk due to twisting of the suspension fibre along its axis, however measurement was possible when great care

was taken to reduce external vibrations near the vacuum tank. Additionally a lens was used to reduce the motion observed at the detector. Again, two suspensions with different fibre lengths were considered. Cantilever blades were removed as a better isolated vacuum tank was used.

Suspension 6 swapped the tungsten wires holding the top stage for thread, which was known to be suitable for suspending test masses as in Chapter 5 [107].

The final suspension tried was similar to that used by Harry [185] in measurements of similarly sized samples. The suspension was fully monolithic with the isolation mass axis orientated vertically with a single fibre welded top and bottom, one to the disk and one to a small silica ear which was then clamped (Figure 6.8).

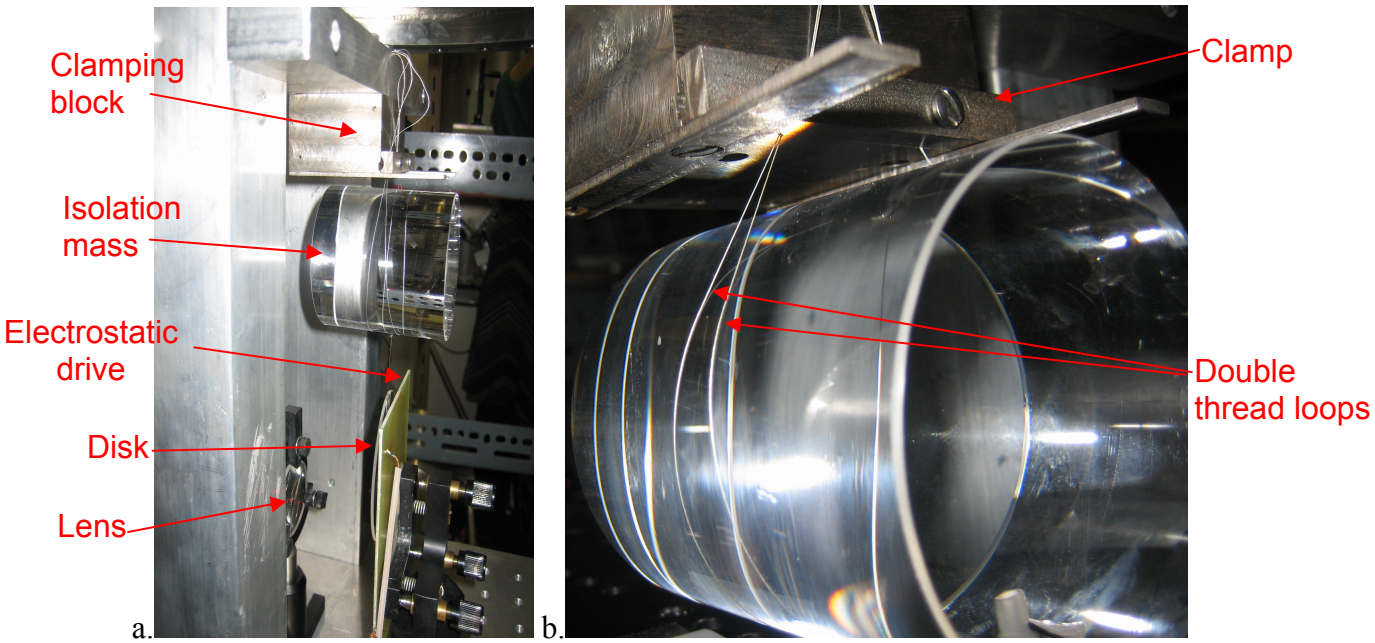

Figure 6.7 a. Suspension 6 with disk held from a single 3 cm fibre, and upper isolation mass held from thread. b. close up of clamping and double thread loop.

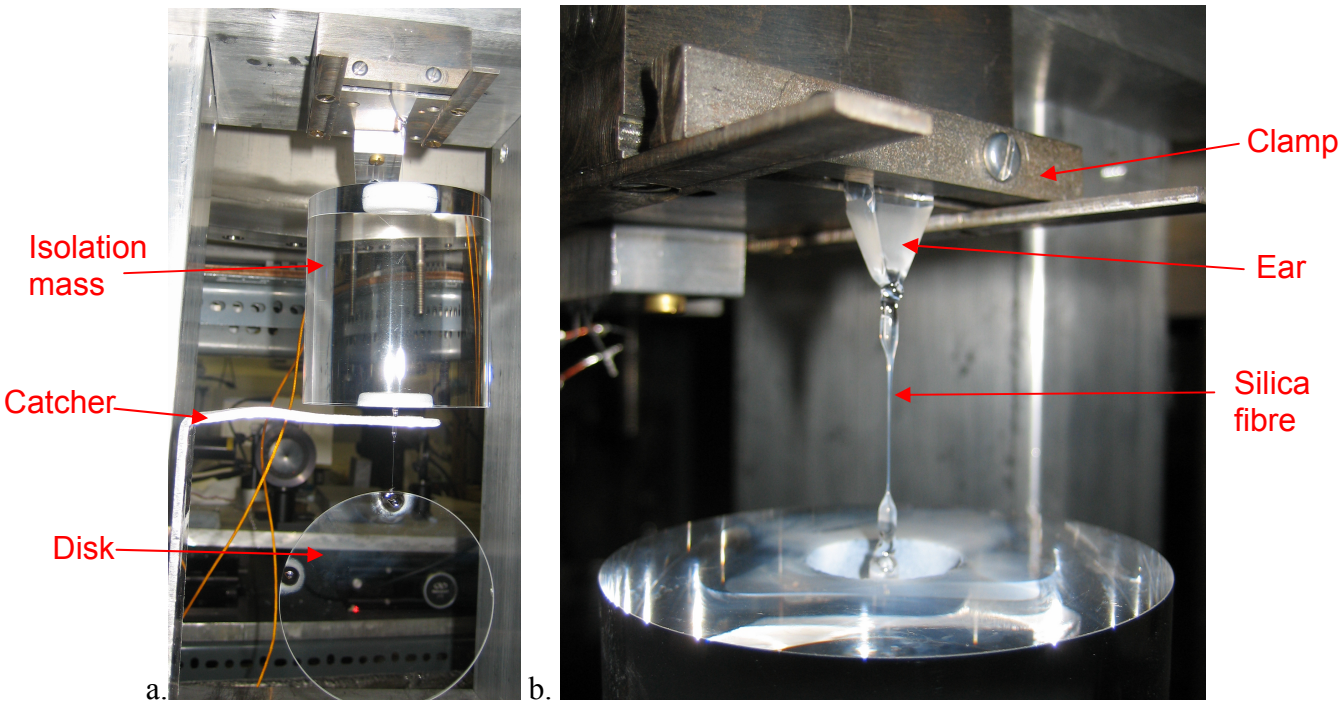

Figure 6.8 a. Suspension 7 with disk held in monolithic suspension. b. Isolation mass held by fibre from clamped ear.

6.2.3 Measured Losses

Mechanical losses were measured for the first eight modes with frequencies ranging from 1.8 – 19 kHz. Results for all seven suspensions are shown in Figure 6.9.

Very little difference in measured loss was observed for the first four suspensions and measured losses were clustered to within a maximum of 10% spread, with the exception of the 11095 Hz ten lobe clover mode which showed a much higher measured loss on the first suspension, indicating significant coupling at this frequency between the motion of the disk and the remainder of the suspension.

Losses were seen to improve with suspensions 5 and 6, which used a very short suspension fibre, which would further decouple violin mode frequencies of the suspension fibres.

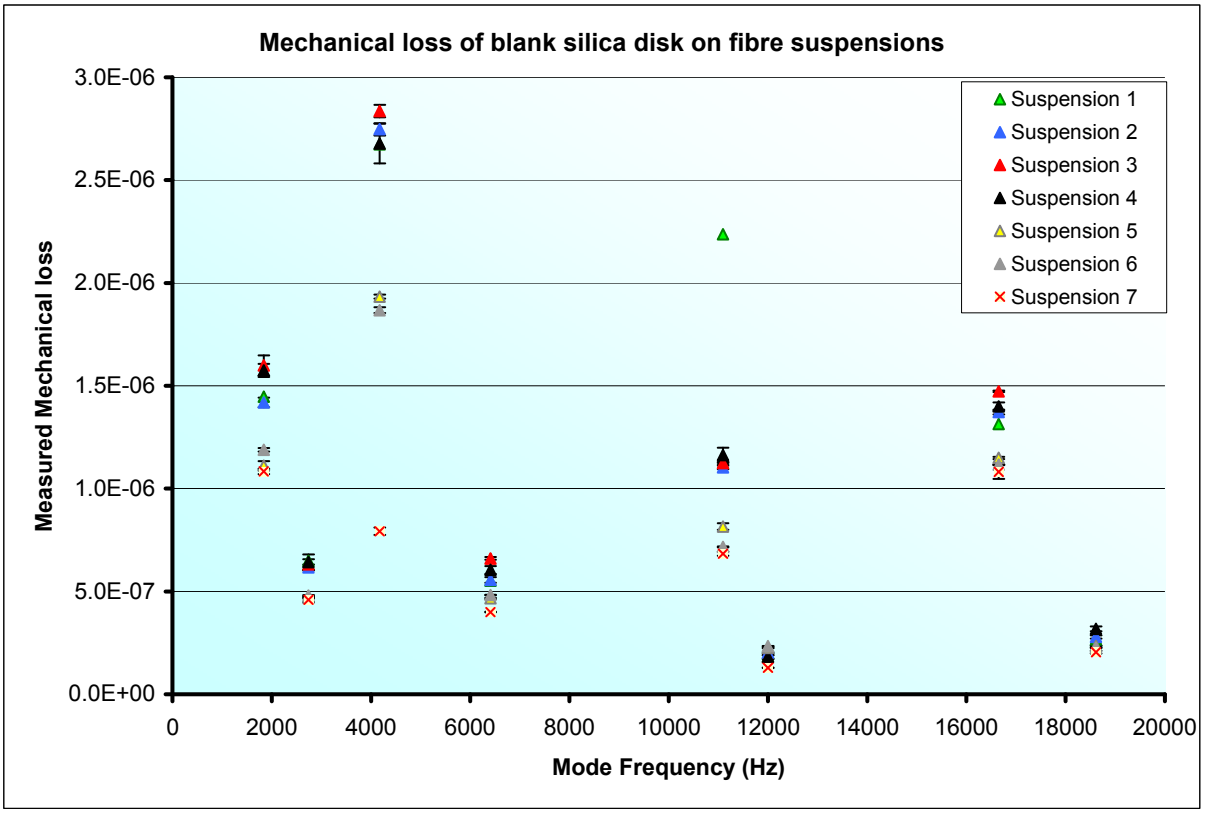

Figure 6.9 Measured mechanical loss using fibre suspensions

The final monolithic suspension gave the lowest measured losses for all modes. This indicated that the previous suspensions (nos. 1 - 6) did have energy contained in upper parts of the suspension, with dissipation into the clamping structure occurring.

However, despite this final suspension being a similar configuration to that used by Harry [185] [186] for similar type samples by and, the measured losses were significantly higher for all modes. Also, the measured losses were greater than those observed on other Suprasil 311 samples measured by Numata [157], by around an order of magnitude. It seemed possible that the explanation for this was the quality of the welds that joined the components of the suspension.

Welding one or more fibres to the disk sample was seen to cause deformation to the area surrounding the weld, and silica vapour deposition, as shown in Figure 6.10. The loss measurements showed evidence of the shapes of the resonant modes being altered

by this deformation, as many separate modes were observed clustered around the resonant frequencies, despite FE modelling of the sample showing only single or double modes are possible at the given frequency. There was also concern about the repeatability of such suspensions. By its nature, this method of suspension construction makes it very difficult to obtain suspensions that are identical each time – each repeated weld to a different disk will result in different deformation and silica vapour deposition. Repeated welding to the same disk will result in deformation and vapour being further accentuated. Furthermore, the quality of the weld is not easily controllable, and it is possible that some welds will have greater mechanical loss than others. This was particularly true for the thin-fibre to disk weld shown in Figure 6.10. Ensuring an identical comparison is particularly important when doing measurements to compare two similar disks, so that any measurable difference in loss between samples can be attributed to sample properties; and not to suspension variables. Therefore, a different form of support was considered, that did not use welding to attach to the disk, in an attempt to mitigate some of these problems.

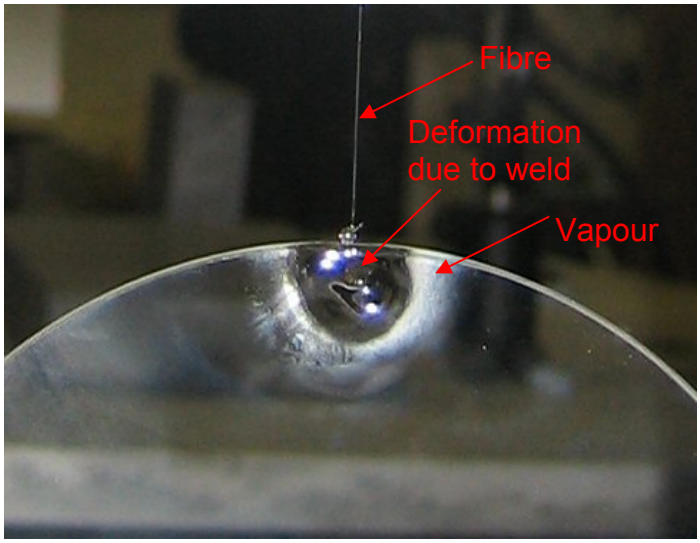

Figure 6.10 Close up of disk weld point showing deformation near the weld and vapour deposition around the weld point.

6.3 Measurements by Nodal Support

For some years it has been known that it possible to measure very low mechanical loss by direct contact clamping of the silica samples at points of minimum resonant motion ("nodes"). Experiments by Numata [155] [157] [187] have demonstrated successful use of this 'nodal' support technique for thicker samples, such as the test mass samples used in Chapter 5. A nodal support was therefore developed as an alternate method of holding the disks, to see if superior clamping could yield lower measured losses.

6.3.1 Design

Previous supports built by Numata, and a similar example being developed at Glasgow [188], both employ the same basic concept. These supports are designed such that the samples are held at points on the centre of the faces, on a line through the centre of mass. This permits measurement of modes with nodes only at face centres – clover type modes – without risk of excess loss being introduced, in the form of frictional grinding against the clamp. It seemed desirable to be able to measure resonant modes that also had motion at their face centres. Holding at the edges was seen to be the only way of achieving this, and therefore it was decided to try and design a support based on this concept. It was realised that thin samples could be held at their edges between thin tensioned threads. This had the advantage of maintaining only a small contact area. This is important as contact with the node should be reduced as much as possible to minimise the potential for energy to be lost at the clamping point.

The initial design concept for a suitable support used three threads clamped in tension between two clamping blocks, as shown in Figure 6.11. The clamping blocks were identical to those used when suspending masses in Chapter 5. These, together with thread, were chosen for suspension since they had already been proven to allow measurement of low losses for test mass sling suspensions as used in Chapter 5.

Resonant modes were again excited by means of an electrostatic drive plate held a few millimetres behind one face of the sample (Figure 6.12b)

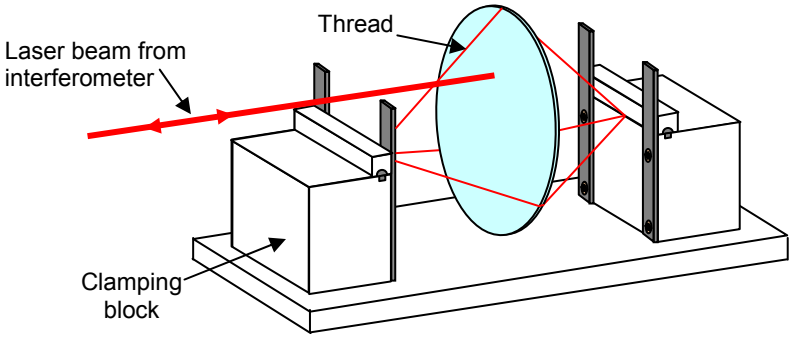

Figure 6.11 Design concept for nodal support using tensioned thread to support thin disks

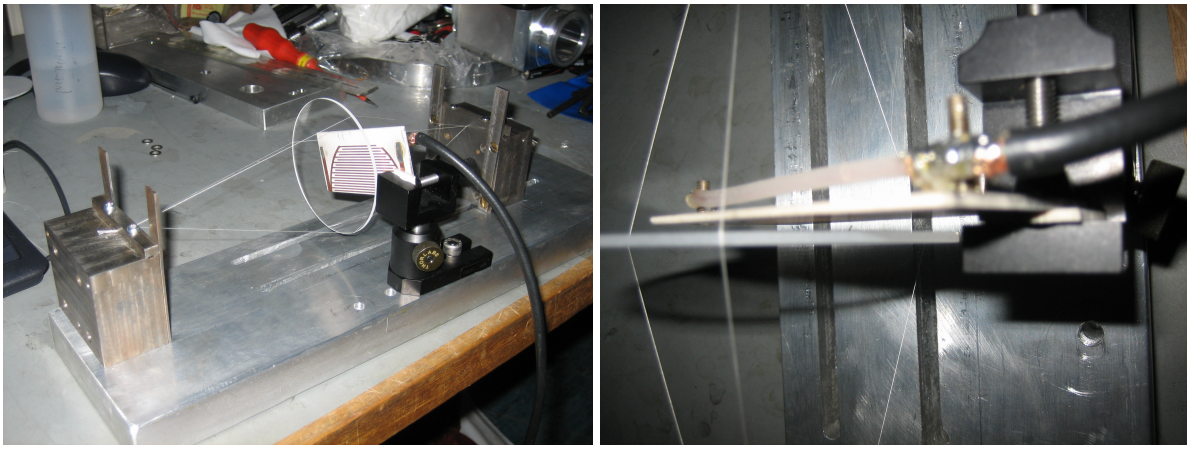

Figure 6.12a. First test nodal suspension using 3 threads b. electrostatic drive plate held behind sample

6.3.2 Nodal Support Initial Testing and Development

Using three threads was quickly abandoned in favour of four, since there were few modes with points of minimum motion at 120° separation around the disk edges.

It could be seen by eye that when tensioned the thread would spread out fractionally at the contact point on the disk, therefore increasing the surface area of contact. The thread could be split into three strands, reducing its thickness and this tendency to spread. Tests confirmed this, showing that improvements in the mechanical loss were gained by reduction of the thickness of the thread from full thickness to 1 strand ($^1/_3$ original thickness), as shown in Figure 6.13. The best losses were achieved when the

disk was supported on 50 μm thick polished tungsten wire. This is almost certainly due to the wire being much more robust against deformation such as that shown in Figure 6.14, and therefore having a reduced contact surface area. Tungsten was previously used successfully in low loss sling suspensions of test masses by Rowan [107].

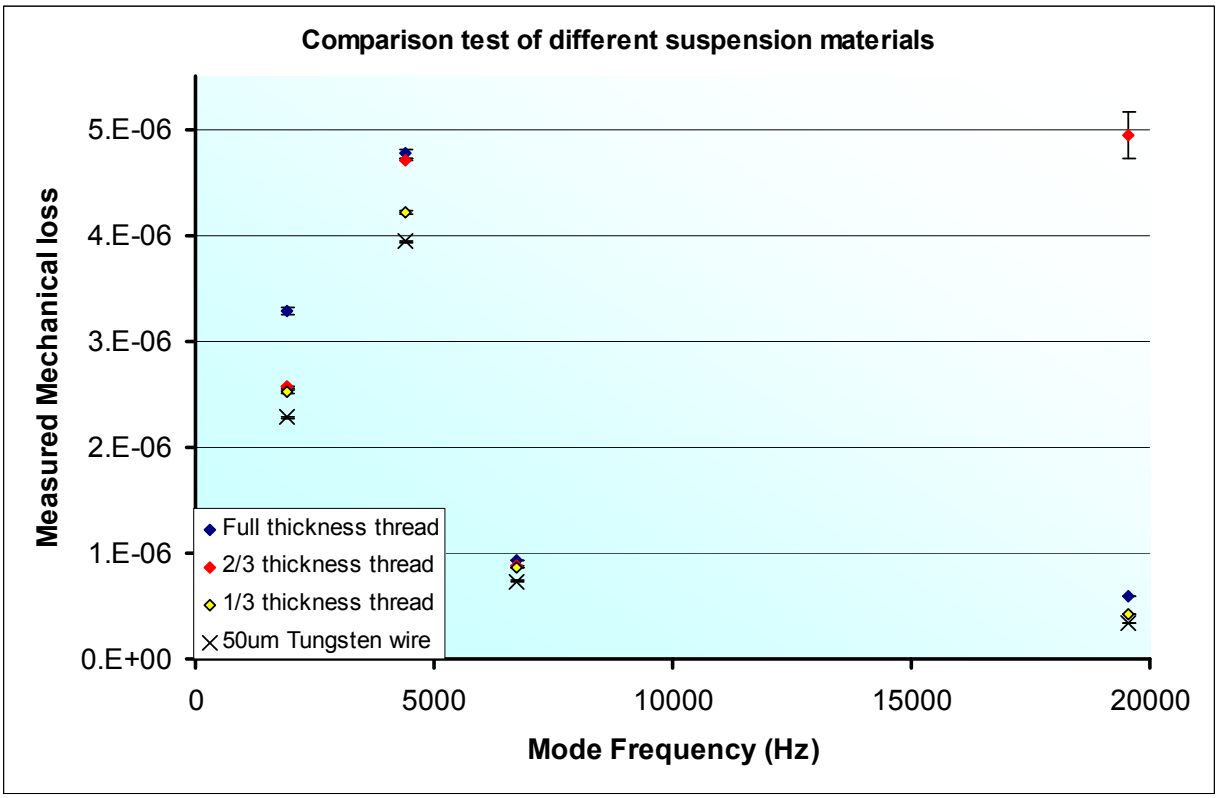

Figure 6.13 Comparison of different suspension materials and configurations

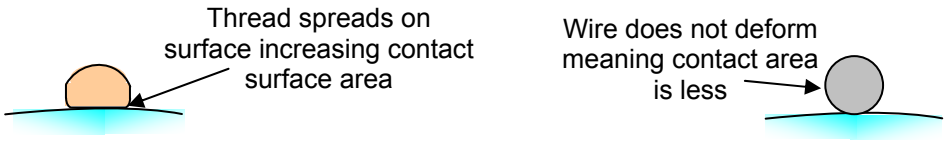

Figure 6.14 Cross section of thread/wire at contact point.

It was soon found that the optimal configuration used only 2 threads contacting at points across a diameter of the disk as shown in Figure 6.15. This minimised the

contact surface area, and therefore the potential for grinding of the sample against the suspension threads.

Additionally, improved isolation from background vibrations (particularly those from the vacuum pumps) was gained by seating the support on rubber o-rings. This helped reduce pitching vibrations of the disk caused by vibrations of the wires, which in turn made it difficult to keep the interferometer locked for long periods.

It was noted that particularly varied losses were measured for the 18839 Hz multi drum mode – a gradual improvement in measured loss was obtained by placement of successive lead blocks each weighing 5 kg on the structure – this idea was prompted by observation that the structure could potentially vibrate on its mounts. The blocks were placed toward the rear of the support where space was available, with the upper ones located closer to the centre, as in Figure 6.15.

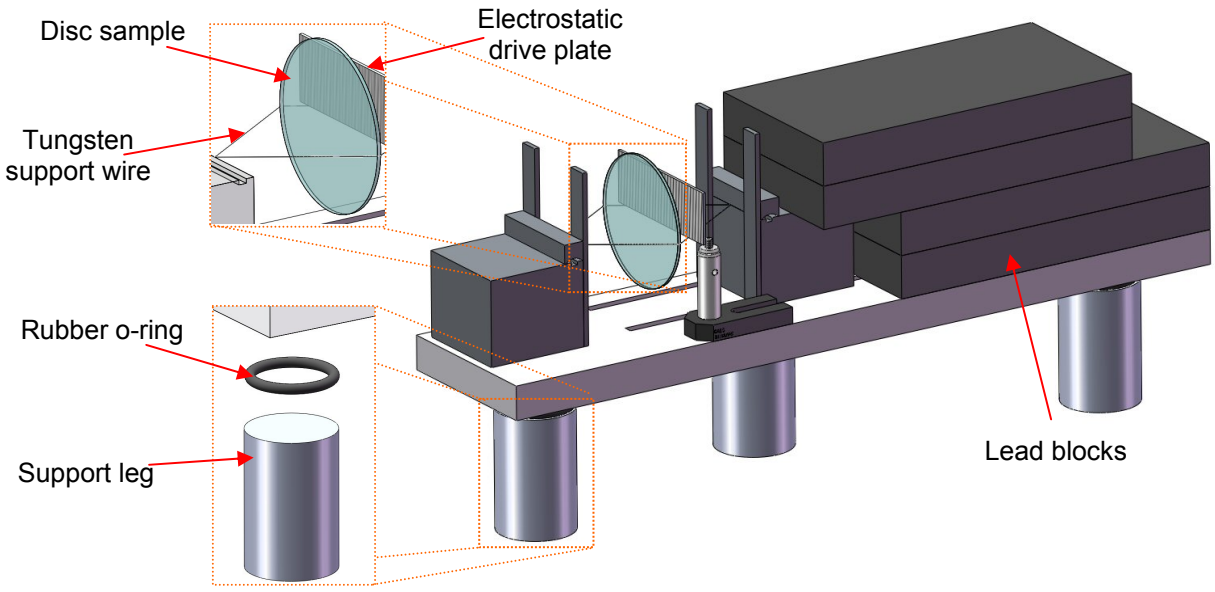

Figure 6.15 Revised nodal support with rubber damping o-rings between legs and base, and lead blocks

The improvement in measured loss (Figure 6.16) indicated energy was being coupled into a resonance of the clamp structure at frequency close to the 18839 Hz mode. The disc was not removed from the suspension during this test. Additional damping was

also tried with a second set of rubber o-rings placed under the legs of the support. Three to four lead blocks were seen to give the best loss measurements without the second set of o-ring dampers, as shown by Figure 6.16, so all further measurements were conducted in this manner.

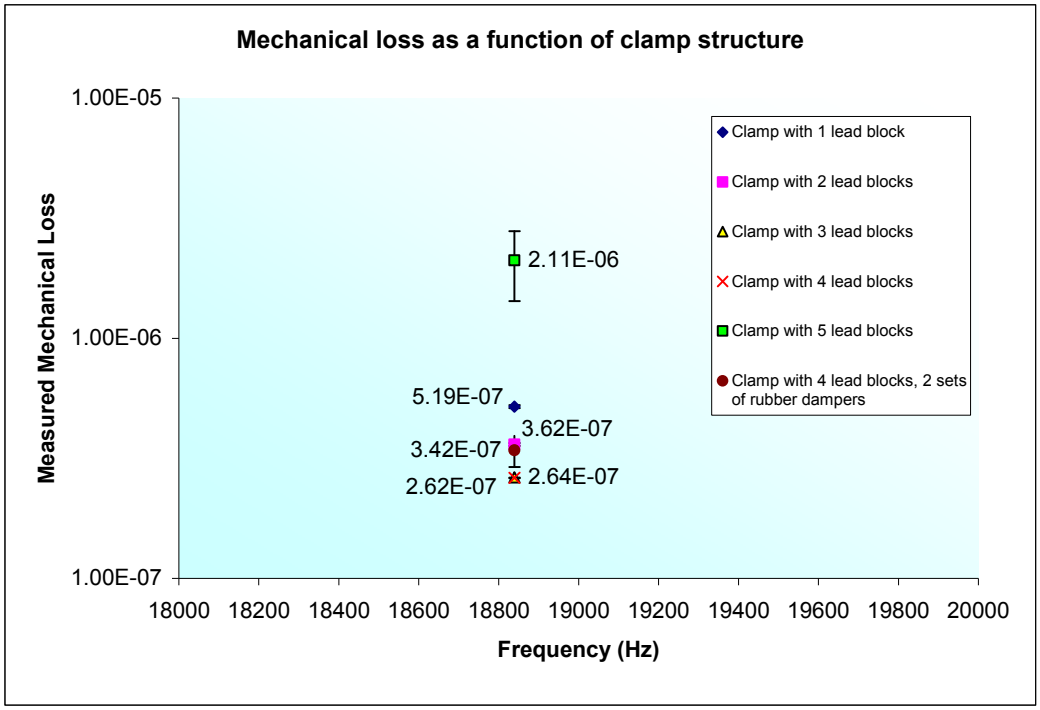

Figure 6.16 Mechanical loss changes when lead blocks added on top of clamping structure

6.4 Sample Surface Quality

A notable observation came when collating the lowest measured losses from the two different production batches of disks. It was observed that the best measured losses from disks from the two batches did not agree closely as would be expected for nominally identical samples, as shown in Figure 6.17. The disks from the first batch had significantly lower measured loss than those from the second batch, over all resonant modes, with the second batch disks having a factor of between 1.45 and 2.88 times greater loss than the first batch disks.

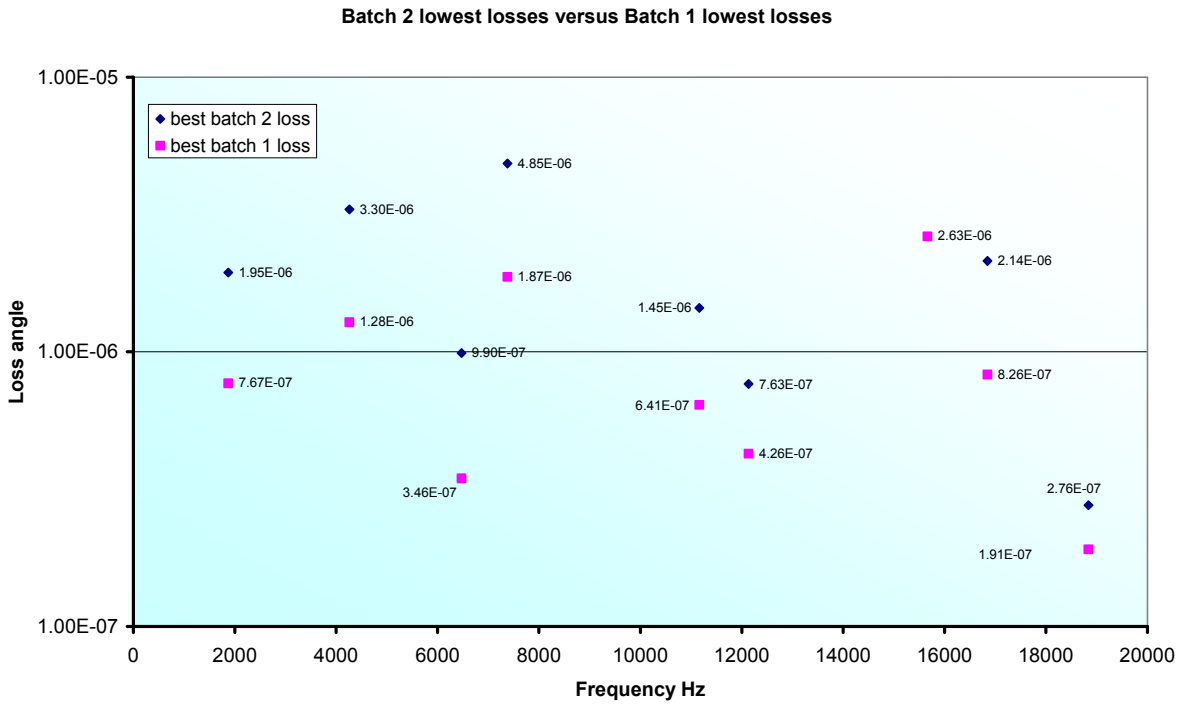

Figure 6.17 Comparison of lowest measured losses for different production batches of disks.

This observation indicated the existence of a difference in properties between the two (supposedly identical) production batches of disk. It seemed likely that this related to the surface finish of the edges of the disks, which were to a rougher ground finish; unlike the faces of the disks which were mechanically polished.

There was also concern about the possibility of frictional grinding between the suspension support wire and the rougher disk edge. To check for grinding between the wires and disk required a change in the frictional properties of one or other. The suspension wire is supplied in a polished state, and tests with further polishing using diamond paste made no measurable difference to the observed losses. Therefore a small area (approximately 5 mm) of the disk edge was polished by hydrogen-oxygen flame, in an attempt to reduce contact friction between the disk and the wire at the suspension point. Flame polishing heats the surface briefly to melting point, with it then being allowed to cool naturally.

Comparison of measured loss showed small improvement for some of the modes. In particular, it was noted that the 'clover' type modes (1872, 4260, 7378 Hz) all showed an improvement – this initially appears consistent with the reduction of grinding between the wire and the disk.

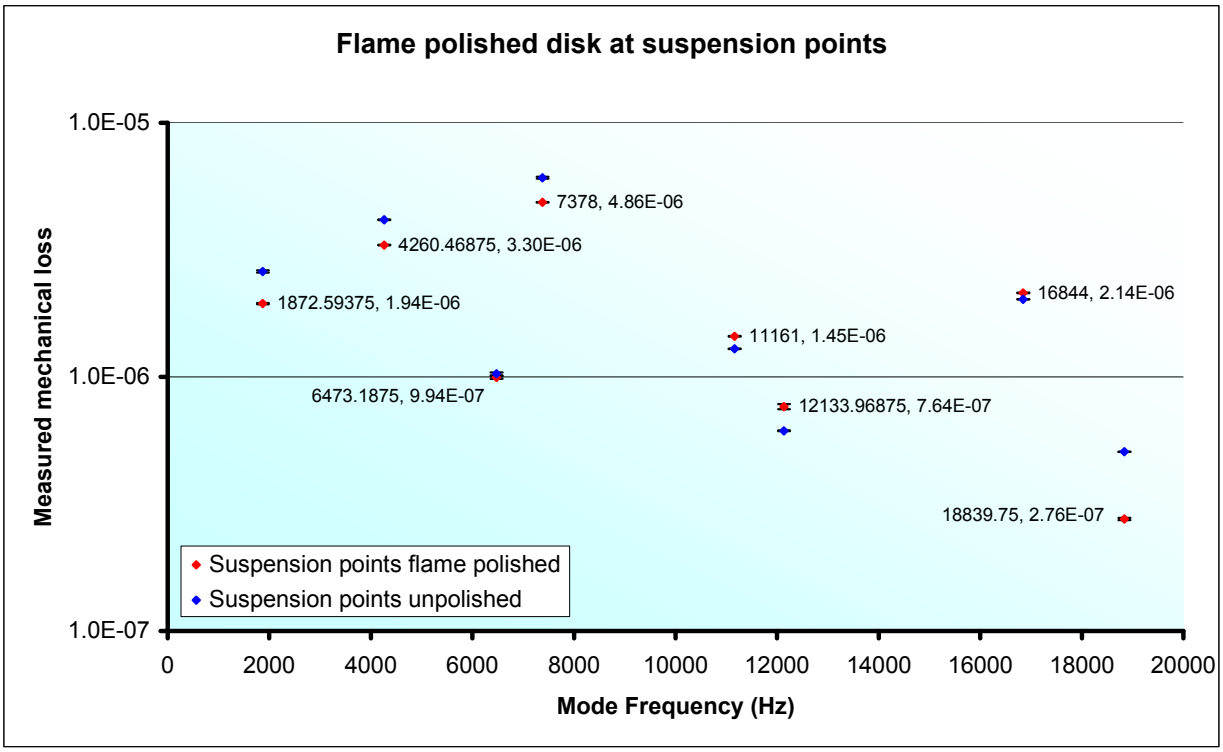

Figure 6.18 Comparison of measured losses with points where suspension wires contact flame polished.

However, it was noted that the second order asymmetric drum mode at 12133 Hz showed an increase in loss, which was unforeseen. This mode has edge motion predicted by ANSYS FEA modelling (see Figure 6.4), so expectation was that the measured loss would decrease significantly when flame polishing contact points, as there would be less friction at those points. Instead the loss increased by approximately 25%.

Furthermore, the greatest improvement was seen in the 18839 Hz mode; yet this had the largest areas of minimum motion, so intuitively should be least affected by grinding. All these observations gave the indication that grinding at the clamp was not the

mechanism that was causing these changes in measured loss. However, these results did indicate that changing the disk's ground surface was influencing the loss.

Therefore, it was decided to flame polish the entire edge of a disk to investigate the role played by the ground surface edge. The process of flame polishing is shown in Figure 6.19.

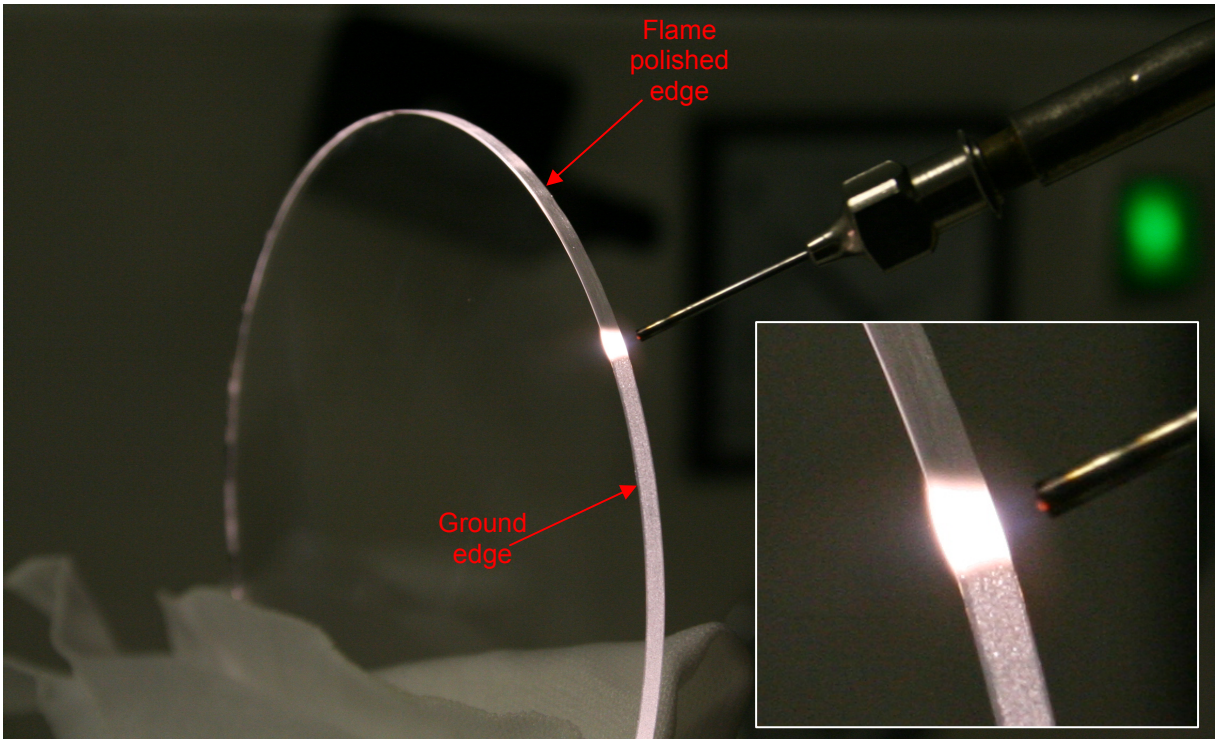

Figure 6.19 Flame polishing of disk edge Inset: Close up of heating of edge showing area heated and proximity and angle of gas torch.

Care is required when polishing the disk as excessive heating can produce silica vapour which can end up being deposited on the surface of the sample. It was found that directing the flame across the ground edge surface at an angle as shown in Figure 6.19 allowed the action of the flame to blow any vapour away from the disk faces.

The measured losses for this sample once polished exhibited a very large reduction, as shown in Figure 6.20. The measurements showed a change in loss ranging from a factor of 7 improvement for the highest frequency mode and a factor of 119 improvement for

the 7.3 kHz mode. This confirmed that the structure of the ground edges of the disk gave a very large dissipation of energy, despite only accounting for 4% of the disk total surface area. The results also follow more closely the trend predicted by the Penn empirical model, although the losses do not reach that magnitude that Penn predicts. This is likely due to other surface effects which including the mechanically polished faces of the discs. The measured losses were however very low and comparable to those measured on similarly dimensioned samples by Harry [185] and larger Suprasil 311 samples by Numata [157].

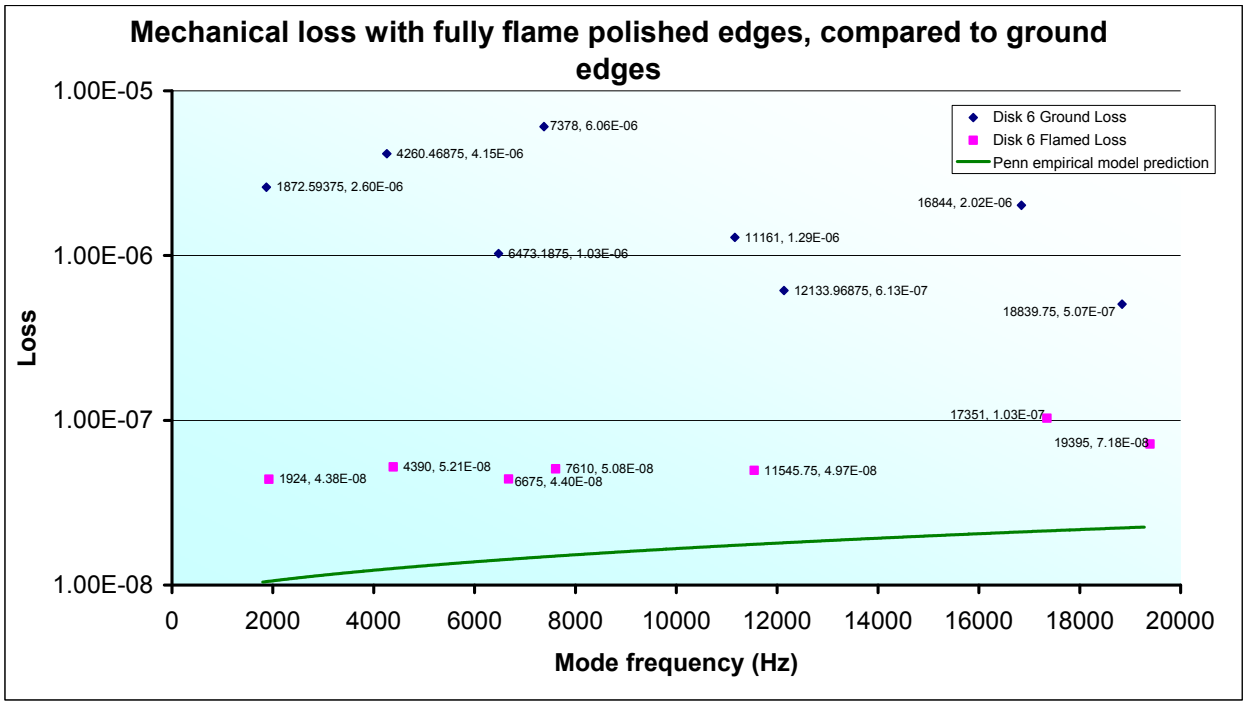

Figure 6.20 Mechanical losses for disk with and without flame polished edges.

In order to confirm that this was indeed an edge effect, the FEA model of the disk was reanalysed, this time focussing on the ratio of the total strain energy in the disk to the strain energy in an annulus around the disk edge. Two annuli were considered, one comprising the outermost 2.5 mm of the disk, the other using the outermost 270 μm. Comparison of the measured mechanical loss and this ANSYS energy ratio (Figure 6.22) showed a very close correlation between the amount of energy contained in the disk

edge and the measured loss. Those modes that had a higher concentration of energy at the edge were seen to have higher measured mechanical loss. This was noted for both size of annulus, further confirming that the measured loss was dominated by the effect of the ground edges.

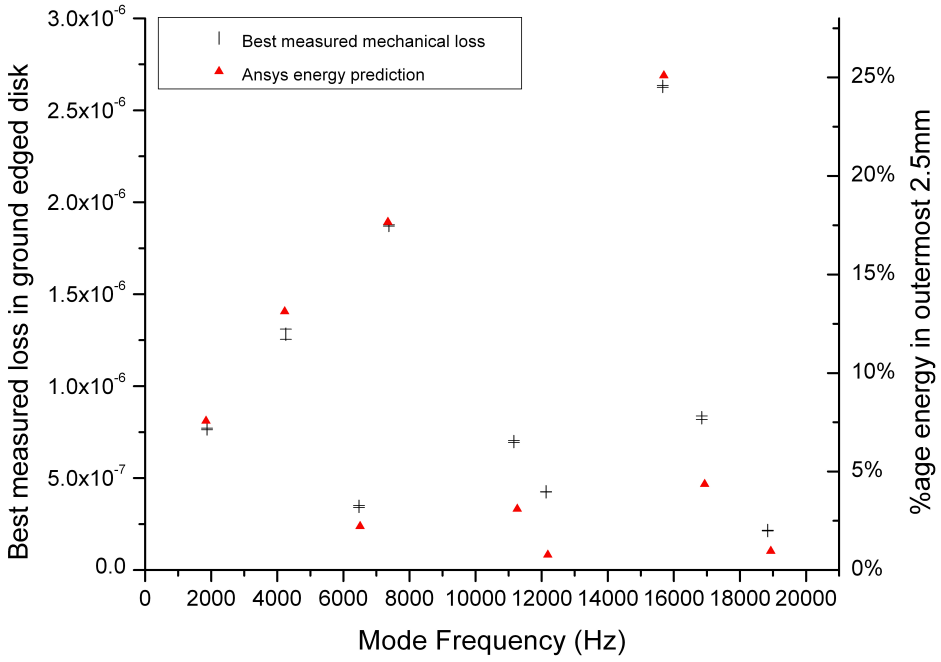

Figure 6.21 Comparison of ratio of energy in disk edge to measured mechanical loss for outermost 2.5 mm of disk edge.

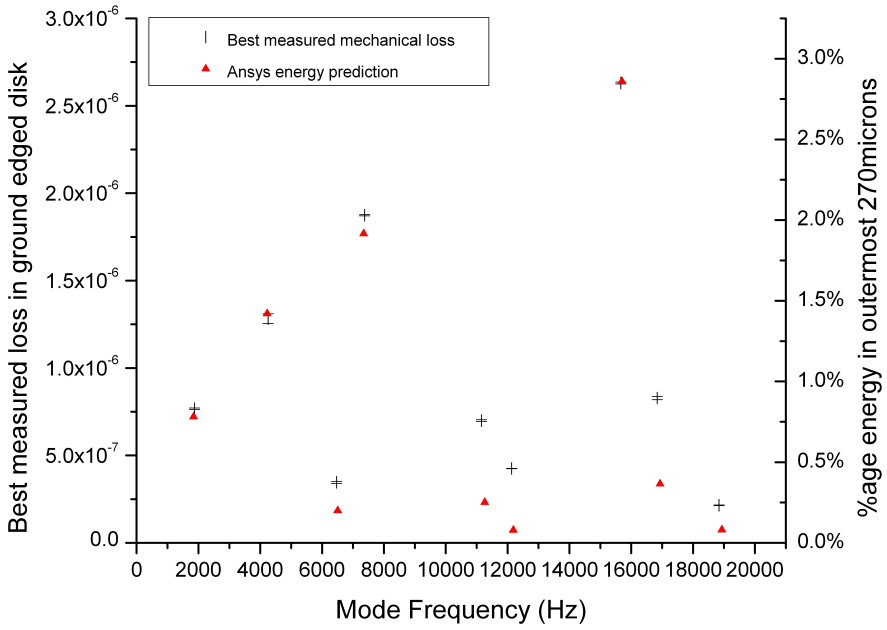

Figure 6.22 Comparison of ratio of energy in disk edge to measured mechanical loss for outermost 270 μm of disk edge.

This finish was clearly a dominant factor in the measured loss, and the prominent loss mechanism for such a surface seems likely to be frictional grinding of material in the microcracks and gaps between grains in the surface [189]. Images across the edge of disks from both production batches were taken using a scanning electron microscope (Figure 6.23 and Figure 6.24) to observe the nature of the surface structure. In both instances much surface structure is observable. The edges appeared smoother at one side of each image – this was due to an edge chamfer on each of the disks. A third image was taken of a disk whose edge was flame polished, and is shown in Figure 6.25.

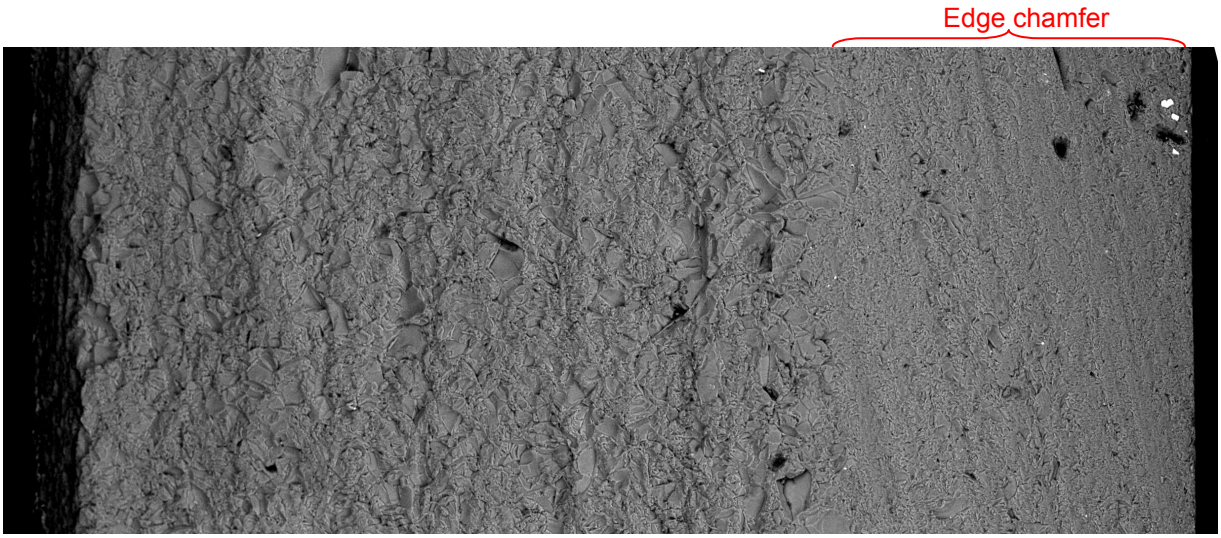

Figure 6.23 SEM image of 1.7 mm cross section of batch 1 disk, showing rough surface.

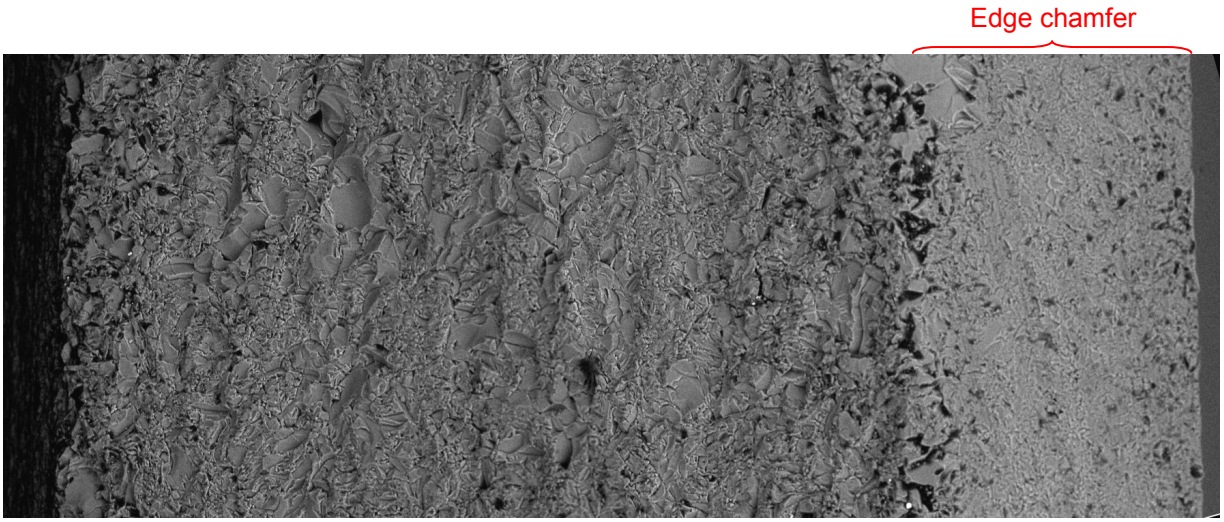

Figure 6.24 SEM image of 1.7 mm cross section of a production batch 2 disk, showing rough surface with more features compared to batch 1 disks.

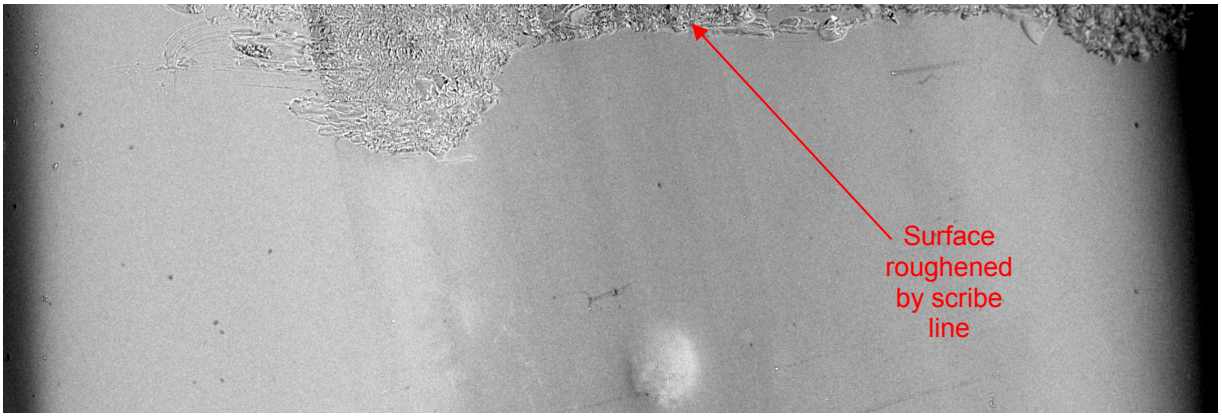

Figure 6.25 SEM image of 1.7 mm cross section of production batch 1 disk, with edge flame polished. The rough surface at top of image is a scribe line, used to verify that image was correctly focussed. The small circular feature visible at the centre bottom of the image is a small chip in the disk edge that left a depression after flame polishing

A spatial Fourier transform was applied to these images, to gauge the frequency of occurrence of different sized features. The transform was applied to individual rows of pixels through the image, with the resulting spectra averaged over the rows. The image of the flame polished disk (Figure 6.25) had the scribe line area cropped out so the transform was applied only to the flame polished section. The resulting Fourier spectrum is shown in Figure 6.26.

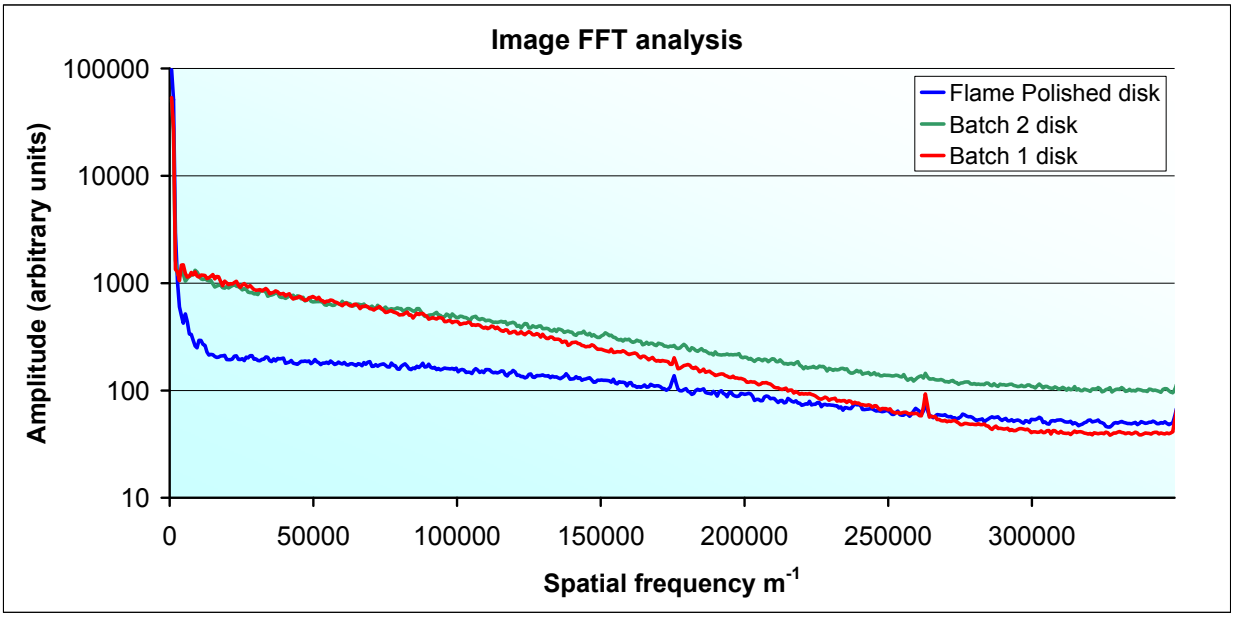

Figure 6.26 FFT analysis of disk edge images.

It is apparent that the flame polished disk has much less structure, which is clear too from the image comparison. Notably, the highest loss batch 2 disk (green curve) had higher amplitude over most of the spectrum, particularly at higher frequency (smaller feature size), with approximately 2.5 times the occurrence of features with spatial frequencies > 250000 m^{-1}. This trend is in broad agreement with the measured losses for the two batches, which have difference which ranges from 1.45 times (18 kHz multiple drum mode) and 2.88 times (6.4 kHz multiple drum mode). It seems likely that this increased occurrence of small scale grained features is the contributor to the difference in measured losses between the two batches of disks.

It should be noted that the flame polished disk image Fourier transform was averaged over fewer pixels, and hence the random noise ($\sqrt{\text{Number of averages}}$) is greater. This explains the apparently increased roughness of the flame polished sample at spatial frequencies greater than 250000 m^{-1}. At such dimensions and smaller, detail cannot be resolved and hence the noise floor of the measured image has been reached.

Comparison of the RMS deviation from the average brightness (namely the deviation in structure height from a mean value) for the 3 image subsections shown in Figure 6.27 was also calculated.

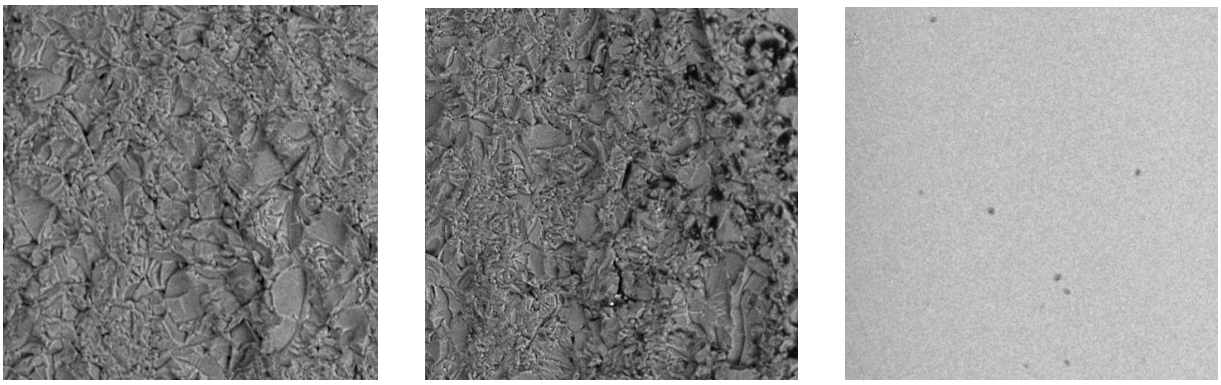

Figure 6.27 Images used in RMS deviation calculation, Batch 1 disk, Batch 2 disk, flame polished disk

The RMS values calculated are shown in Table 6.2.

	RMS about mean
Flame Polished Disk	8.19 ± 0.35
Batch 1 disk	26.35 ± 0.79
Batch 2 disk	29.38 ± 1.32

Table 6.2 RMS about mean of the average brightness values (structure height) for three different disk edge images

It is clear again that the flame polished disk has smoother surface, but there is less distinction between the other two disks. This is possibly due to the inability of the SEM image to resolve the small scale cracks between small surface features. However, the batch 2 disk does shows highest RMS deviation from mean, again in broad agreement with the measured losses being highest for this sample.

These findings made it clear that use of samples with ground edges is not good for ultra low loss measurements, as friction on these ground surfaces becomes the dominant source of dissipation. Therefore, all subsequent measurements were carried out on disks which had flame polished edges.

6.5 Mechanical Loss of Sample With Diffractive Surface

With low mechanical losses now being consistently measured, studies were undertaken on the disk with the diffraction grating etched on it. Two blank disks were measured as control samples – one had pristine finish, the other had significant silica vapour deposition on its surface – this resulted from heating the edges of the disk for too long.

The diffractive disk was seen to have a slightly higher loss than the pristine disk, but lower loss than the poorer quality disk, for all but one mode, as shown in Figure 6.28. The diffractive disk was also seen to have a small amount of vapour deposition, which was a likely contributory factor in its increasing its measured loss. This provided a useful indicator, as the measured loss for this disk was seen to be higher than that of the pristine one, implying that the surface quality of the disk faces was now a limiting factor.

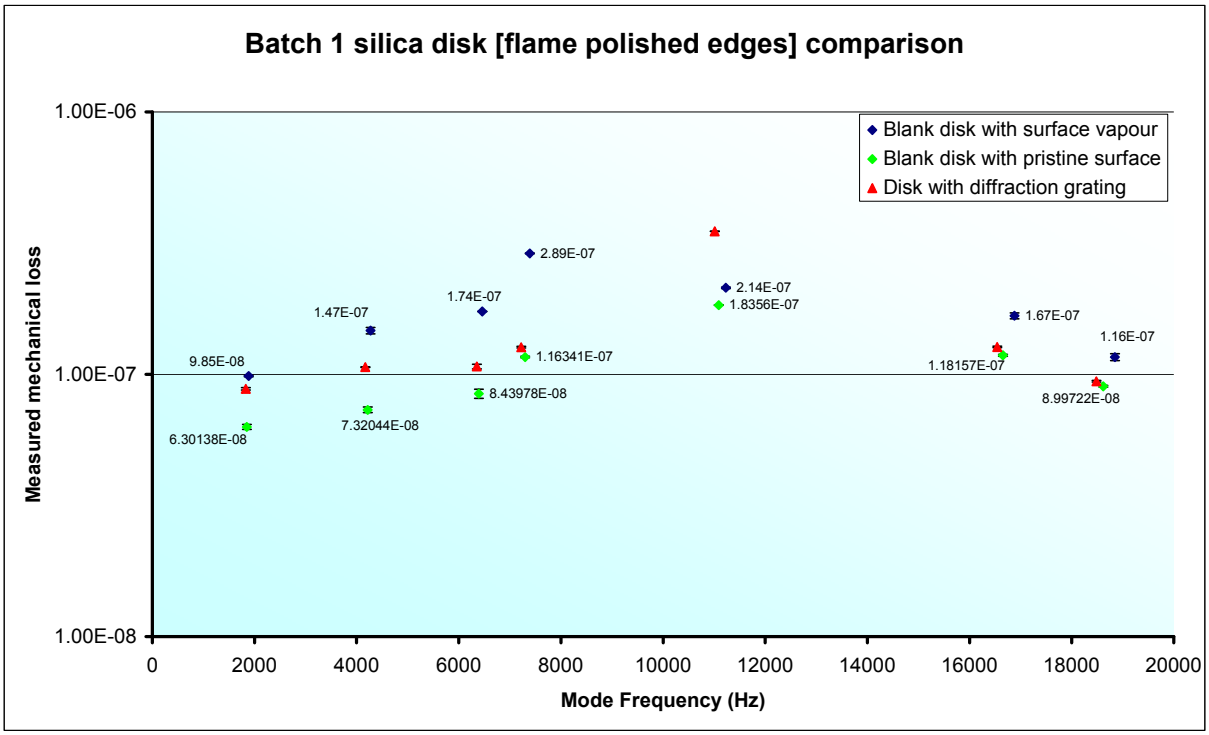

Figure 6.28 Comparison of measured losses of blank disk with vapour deposits, pristine blank disk, and diffractive disk.

It is therefore apparent that the grating does not significantly detrimentally affect the measured mechanical loss at the level being measured. This concurs with similar measurements performed by Nawrodt [190], which showed no change in the measured loss of samples with diffraction gratings; albeit with those samples being test mass samples with a smaller surface to volume ratio which would contain less energy in the material surface.

6.6 Mechanical Loss of Diffractive Optics with Reflective Optical Coating

To simulate the manner in which diffractive mirrors would be used in real interferometers, it was necessary to introduce a reflective coating, similar to those studied in Chapter 5. In order to analyse the mechanical loss of the coatings when applied to a surface that had been altered by the addition of a grating, the three disks whose losses were measured in section 6.5 (one from the first production batch; one

from the second batch, and the third sample with the diffraction grating) were coated with a 30 alternating layer coating silica / tantala coating by LMA, with a high index layer of tantala doped with 14.5% titania.

The mechanical losses were then re-measured, again using the nodal suspension. The resulting measured mechanical losses are shown in Figure 6.29.

The measured losses for the three coated disk show similar trends of mechanical losses for the different modes of the samples, with the greatest spread being 13% for the 11240 Hz mode.

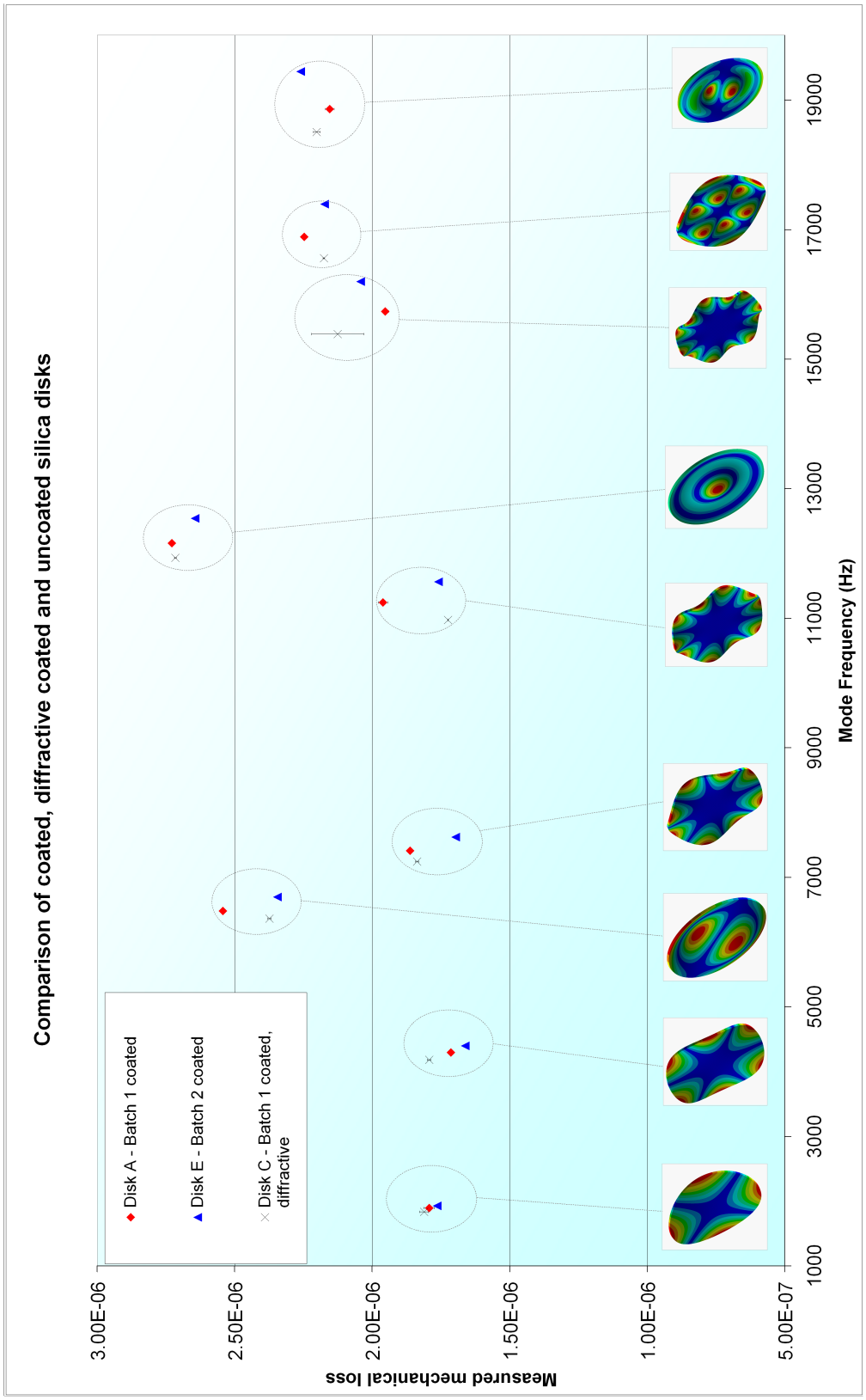

Figure 6.29 Measured coating loss values for three silica disks from two different production batches, with one diffractive sample.

The coating mechanical losses were calculated as in chapter 5 using equation (5.11), and are presented in Table 6.3.

Sample	Coating loss x 10^{-4}
Disk A – Batch 1	2.08±0.23
Disk E – Batch 2	2.07±0.27
Disk C – Batch 1, diffractive	2.01±0.23

Table 6.3 Measured coating losses for silica disks (Note, disks B and D were blank samples, not involved in the coating process).

These results show that the application of a diffractive surface to a substrate surface does significantly change the measured coating loss. This is an encouraging result as it shows that at the level of loss being measured, the benefits of using diffractive mirrors can be exploited with no significant increase in thermal noise from either the diffractive surface or the surface coating.

In addition, use of substrates from different production batches did not result in a different coating loss being measured – this would be expected as the measured loss of the coated samples is over an order of magnitude greater than the equivalent samples when uncoated (compare Figure 6.28 and Figure 6.29), and therefore the effects of the coating dominate.

6.7 Conclusions and Future Work

Samples with surface diffraction gratings have been shown to have insignificant detrimental effect to the mechanical loss of the sample, and introduction of such gratings to test masses would not significantly increase thermal noise.

However, throughout the course of the measurements it became clear that the surface quality of the samples is very important, with the ground edges of the disk samples significantly increasing the measured mechanical loss, even when the ground surface comprised only a small percentage of the total. It became apparent that different

production batches of sample could have different ground edge surface quality, and different resultant mechanical losses.

In the process of conducting the measurements a revised suspension technique was developed, holding the samples at nodes of the resonant modes, which proved capable of measuring low mechanical losses, comparable with those measured by other methods.

Finally, it was observed that a surface coating layer's mechanical loss was not adversely increased at the level of loss measured by also having a diffraction grating on the surface. This means that if such surfaces were applied to future gravitational wave detector mirrors, thermal noise would be dominated by that in the reflective coating, and not the grating.

With these results demonstrated for fused silica substrates, future extension of the work contained in this chapter may include repeating with silicon or sapphire substrates, to investigate if different materials perform similarly. If so, use of diffractive interferometry may prove lucrative for gravitational wave detectors beyond Advanced LIGO and Advanced VIRGO, permitting the reach of such ground based detectors to be yet further extended deeper into the expanse of the Universe.

Chapter 7

Conclusions

Current interferometric gravitational wave detectors are now operating at sensitivities close to their original design goals. The possibility of obtaining a first direct detection of a signal resulting from an astronomical source is now more likely than ever; but still proves elusive. Further increase in sensitivity will require the reduction of many different noise sources, and at mid band frequencies thermal noise is one of the most significant of these.

This thesis aimed to study various aspects of thermal noise that will limit the sensitivity of advanced gravitational wave detectors at mid-band frequencies, and investigate ways of reducing this noise source.

Use of monolithic fused silica suspensions in GEO600 helped reduce the mirror suspension thermal noise, and Advanced LIGO will use and extend this technology further. Crucial parts of the design are the fused silica suspension ribbons. The work presented in chapter 3 of this thesis explored the manufacture and characterisation of these suspension ribbons. The laser pulling machine program was written to permit the capability of producing the desired shape of ribbon.

Characterisation equipment was constructed to measure the dimensions and vertical bounce frequency of the ribbons, and also check their ability to hold the required mass

in Advanced LIGO. The profiler was constructed to be capable of measurements with resolutions in the order of microns, and output data on both the dimensions and shape of the ribbons, in particular their neck regions. The bounce test machine was characterised to ensure that bounce frequency measurements would accurately determine the frequency without systematic error.

Typical ribbons produced with both oversize and approximately correct cross sectional area were seen to have sufficient strength to hold 12.5 kg, meaning they would easily hold the 10 kg that each will be required to hold in Advanced LIGO. The measured vertical bounce frequencies for both oversized and approximately correct cross section ribbons were measured to be below the required upper limit for Advanced LIGO, at 10.5 Hz and 8.3 Hz respectively.

Methods of producing finite element models of ribbons fibres and mirror suspensions were presented in chapter 4. Analysis of the ribbon fibres showed that for simple necked ribbons, the pendulum dilution factor was lower than that for the simple non-necked ribbon, with more bending strain energy occurring in the thicker necked portion. The ribbons were seen to have lower dilution than equivalent cross section fibres for necks longer than around 5.5 mm, and around 3.5 mm for the ribbons proposed for use in Advanced LIGO. The results from chapter 3 had shown that typical necks lengths being produced were of the order of 7.5 mm long or greater. The dilution was seen to also decrease when accurate models of the ears were introduced, with additional bending occurring within the ears, causing an increase in bending strain energy.

The discovery of low pendulum dilution factors when using ribbons with necks prompted a reanalysis of the various mechanical loss contributions within ribbons and fibres, with tapered fibres analysed in detail, to assess their suitability for replacing the ribbons in Advanced LIGO. Tapered fibres aimed to reduce noise primarily through

reduction of thermoelastic noise rather than via high dilution factors. Reduction in mechanical loss of nearly an order of magnitude at 30 Hz was observed for a real tapered fibre when compared to the ideal baseline ribbon, and this work has now prompted the Advanced LIGO design to be changed to use tapered fibres to help further reduce thermal noise.

Measurement of mechanical losses of mirror test mass coatings in chapter 5 showed that doping of the high refractive index layer reduced the measured loss. Reduction in mechanical loss of around a factor of 2.5 was observed when comparing a standard tantala / silica coating to a titania doped tantala / silica coating whose residual coating loss was the lowest of those measured at 1.7×10^{-4}. Doping tantala with both titania and silica also gave reductions in mechanical loss when compared to a standard tantala / silica coating.

The mechanical loss of silica substrates with surface diffraction gratings, as may be employed in future gravitational wave detectors, was studied in chapter 6. Methods for holding the thin disk samples were investigated, with a wire nodal support being constructed for the measurements. Initially, mechanical losses no lower than 1.9×10^{-7} were measured, and this was significantly higher than measurements conducted on similar samples at other institutions. Investigation showed that the ground finish of the edges of the disks was introducing excess mechanical loss, and when the edges were smoothed by flame polishing the measured mechanical losses were reduced by as much as a factor of 119, with the lowest resulting measured loss being 4.38×10^{-8}. Differences in mechanical loss were also consistently observed between disks fabricated in different production batches, with disks of higher mechanical loss having rougher ground edges that displayed more small scale structure.

Introduction of the diffraction grating to the surface did not notably increase the measured mechanical loss, with the measurements lying between those of two control samples of slightly superior and slightly inferior surface quality. Mirror optical coatings were also applied to the disk samples, and the resulting measured coating losses were all around 2×10^{-4}. This showed that the use of a diffraction grating on the substrate surface did not noticeably increase the coating loss at the level of loss being measured.

The experimental work carried out in this thesis has assisted in the production of ultra low loss mirror suspensions for Advanced LIGO, and builds on previous work undertaken in the gravitational wave field carried out on mirror coatings. The use of diffraction gratings has also been shown to be viable for detectors beyond Advanced LIGO. This research is pushing the detector technology to new levels, which will hasten the first direct detection of gravitational waves, and usher in the dawn of a new method of astronomical observation – gravitational wave astronomy.

Appendix A
CO_2 Laser Pulling Machine LabVIEW Control Program

A.1 CO_2 Laser Machine Control

Laser pulling machine control was achieved using National Instruments LabVIEW versions 6, 7.1 and 8. The pulling machine program was written for LabVIEW 7.1. LabVIEW is a C++ programming language with a graphical interface [191].

The "front panel" is the program user interface with which the user interacts during the running of the program. The "block diagram" is the program code, laid out graphically with program "subvi's" linked by lines "wires" in the same way an electrical circuit is. The subvi's are individual sub-programs with an individual purpose, for example a mathematical subvi would be addition. The CO_2 laser machine control program is written in a "state machine" format, where the program will cycle through a number of program states. Different operations are performed in each state. The choice of the next state run is determined at the end of the operation of the current state. This type of programming is versatile in allowing code that would be necessarily repeated in a sequentially run program can be removed and replaced with one single state which is called when required.

The program front panel and code is detailed below.

A.2 Front Panel

A.3 Block Diagram

A.3.1 Main Diagram and Idle State

Block diagram for this state is split over the next 3 pages.

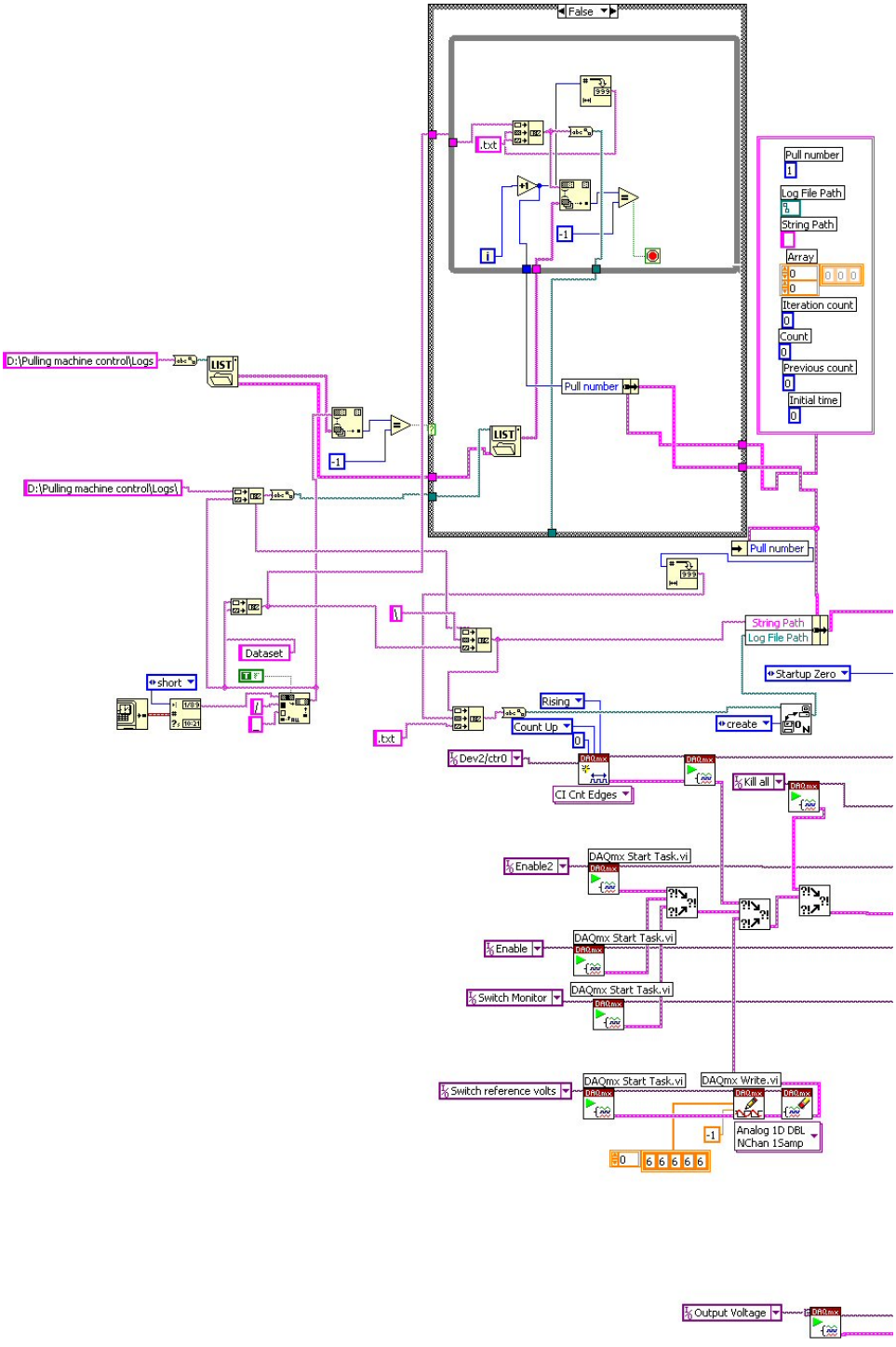

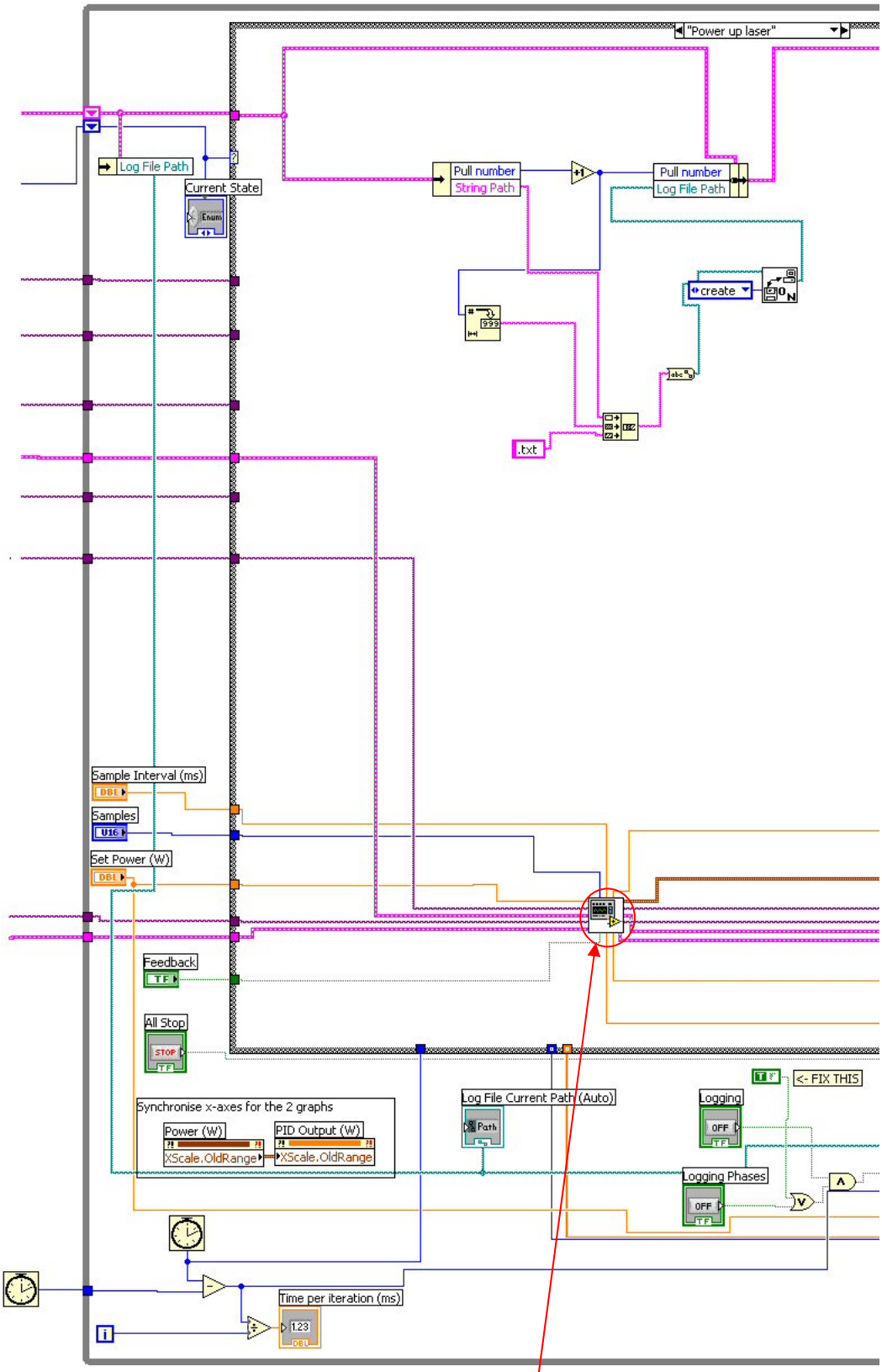

Laser stabilisation vi by Dr. M Barton

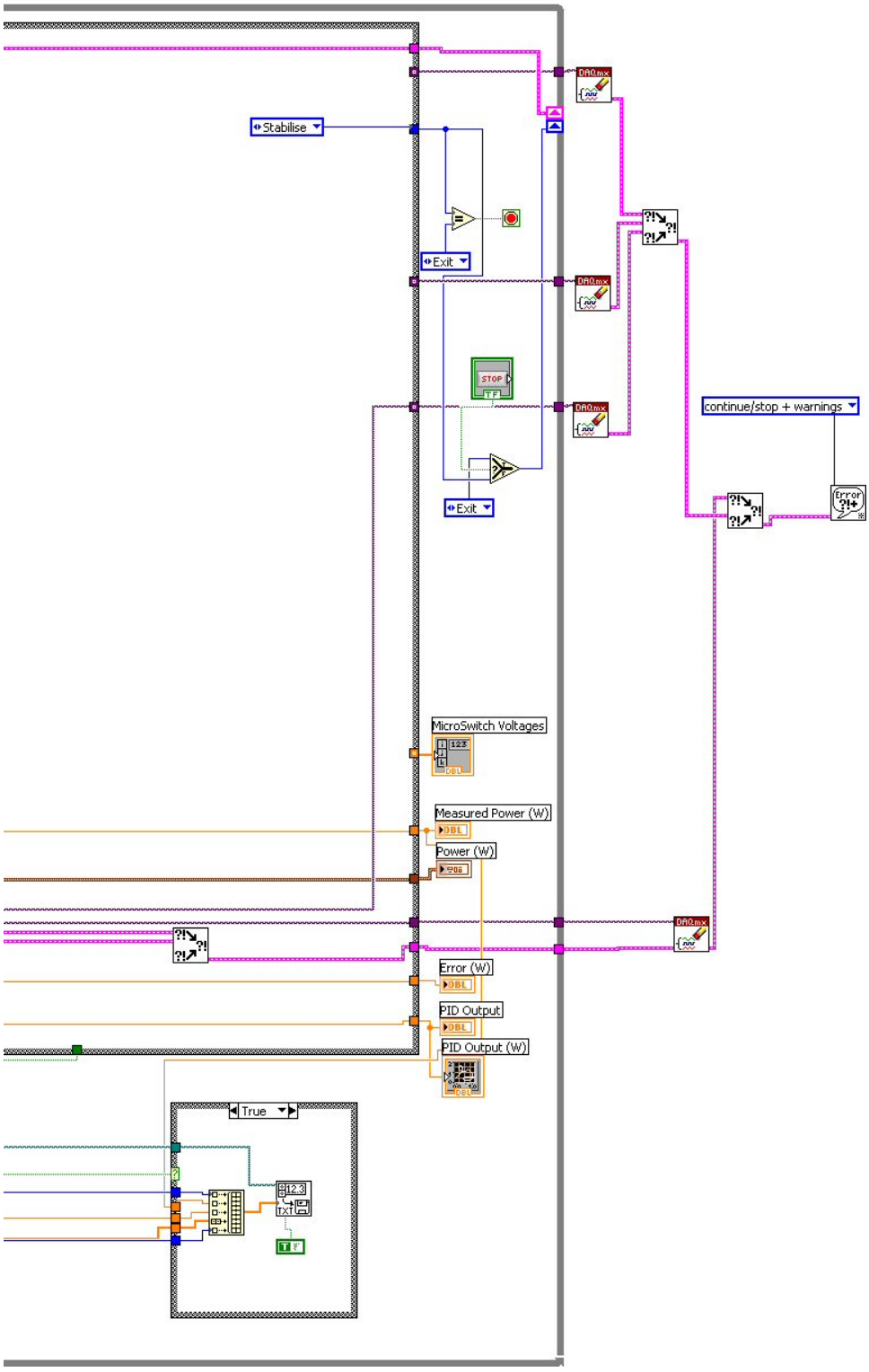
Stabilise
Exit
STOP
TF
Exit
continue/stop + warnings
Error
MicroSwitch Voltages
Measured Power (W)
Power (W)
Error (W)
PID Output
PID Output (W)
True

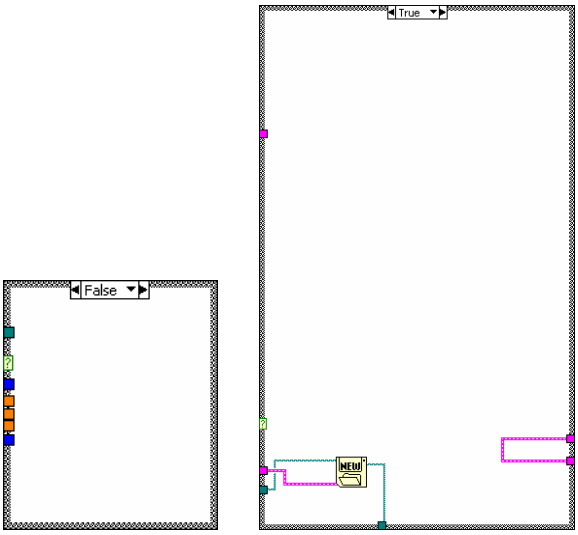
False
True
NEW

A.3.2 Startup Zero State

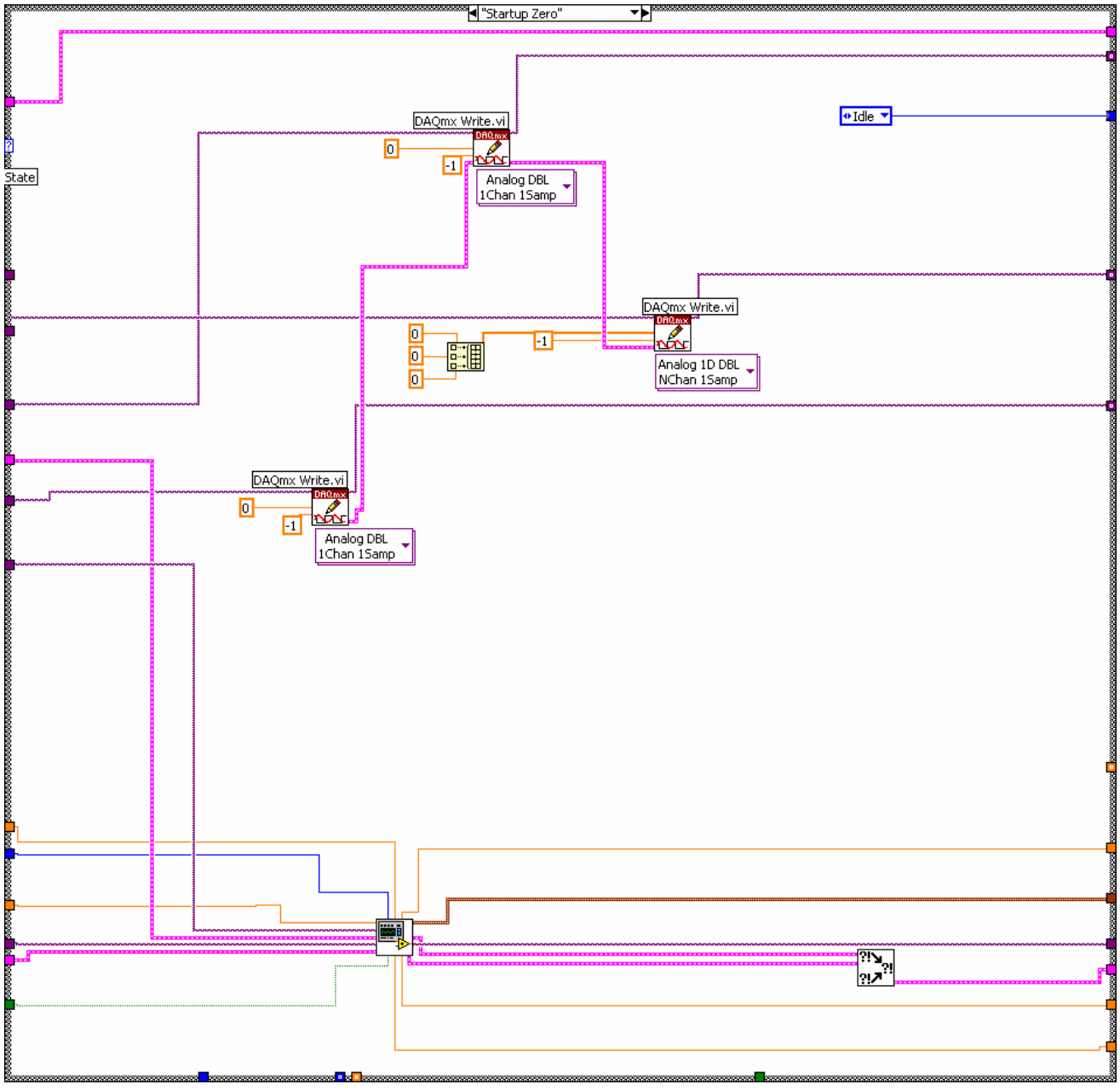

A.3.3 Stabilise State

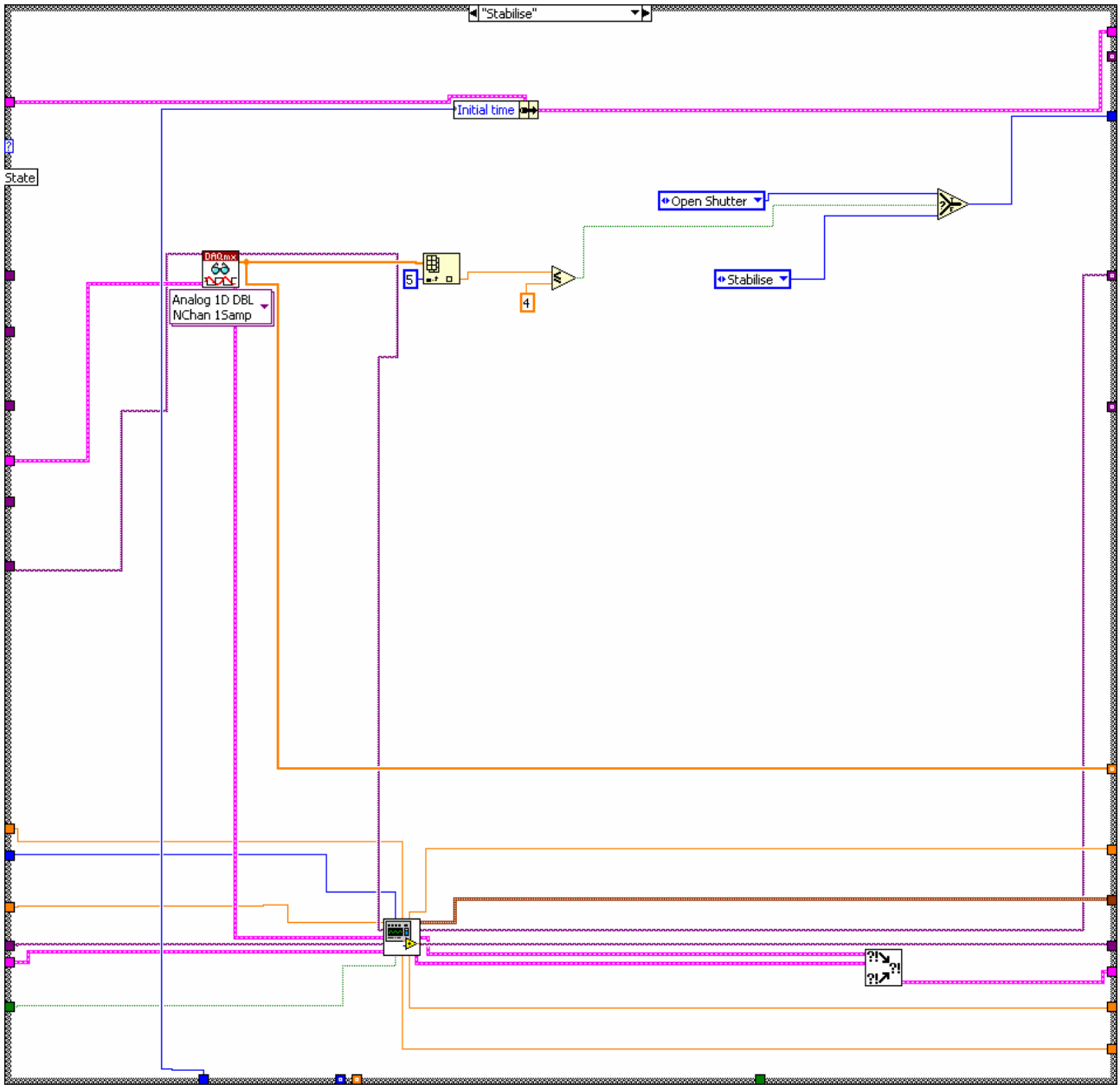

A.3.4 Open Shutter State

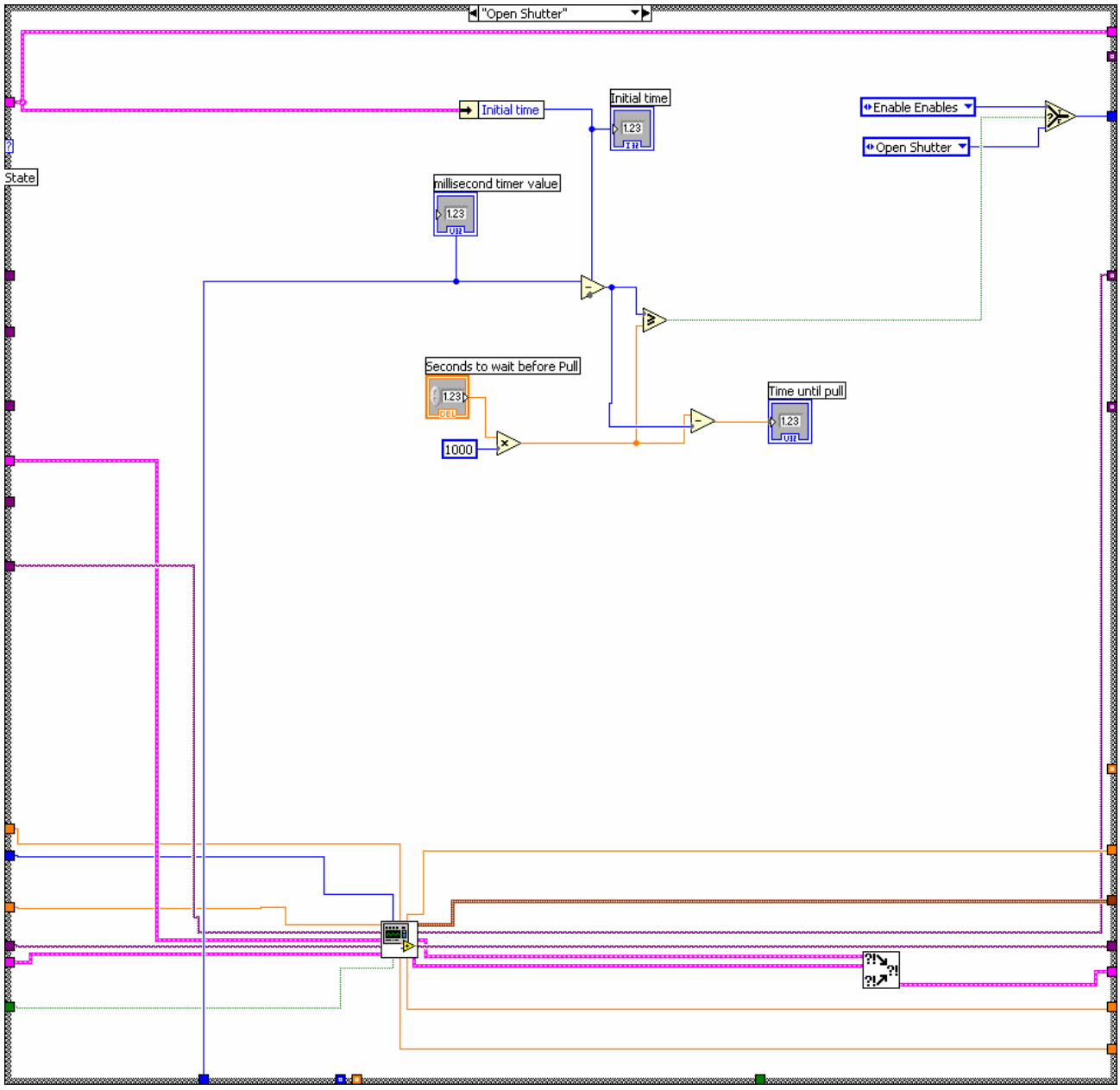

A.3.5 Enable Enables State

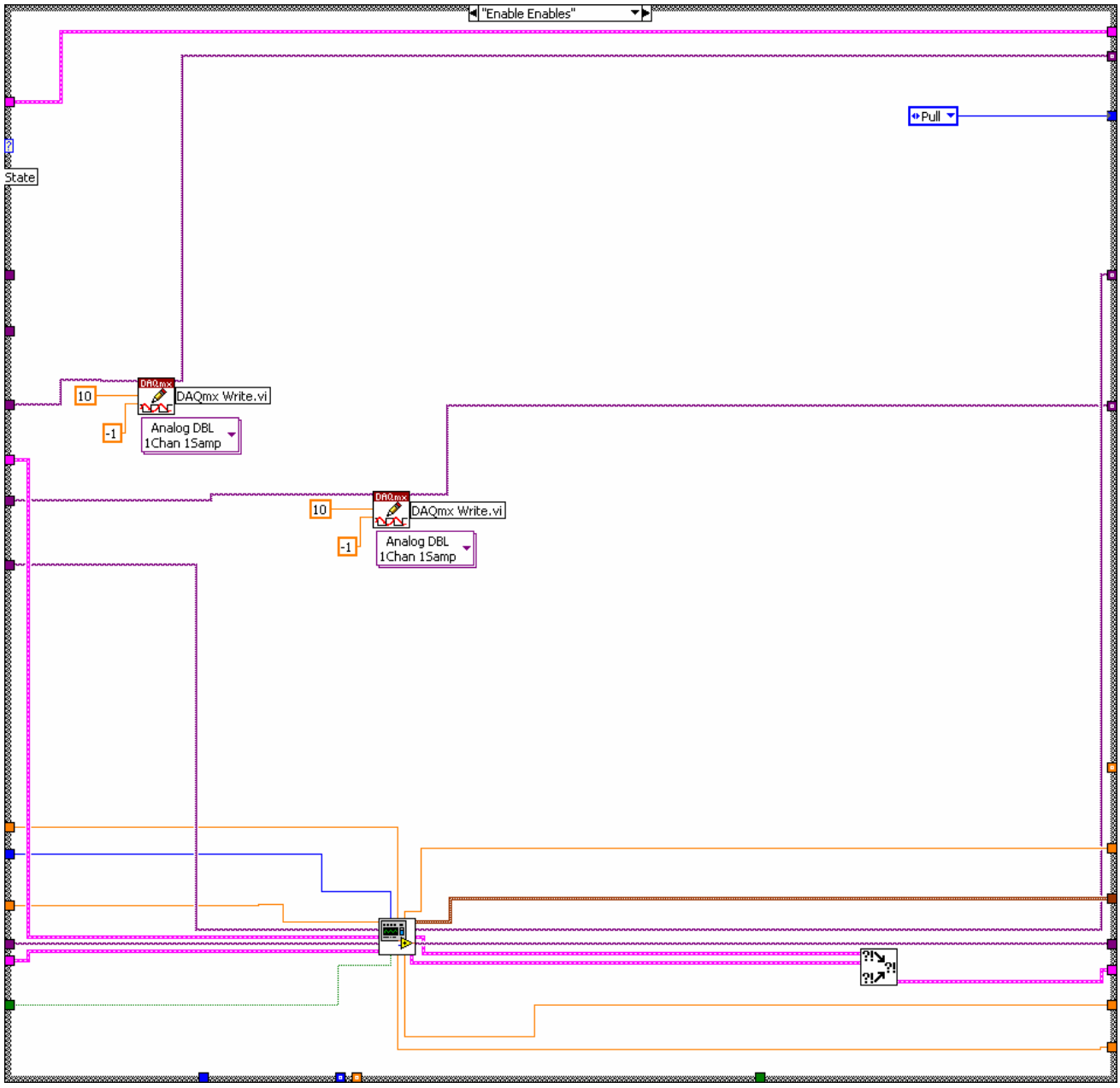

A.3.6 Pull State

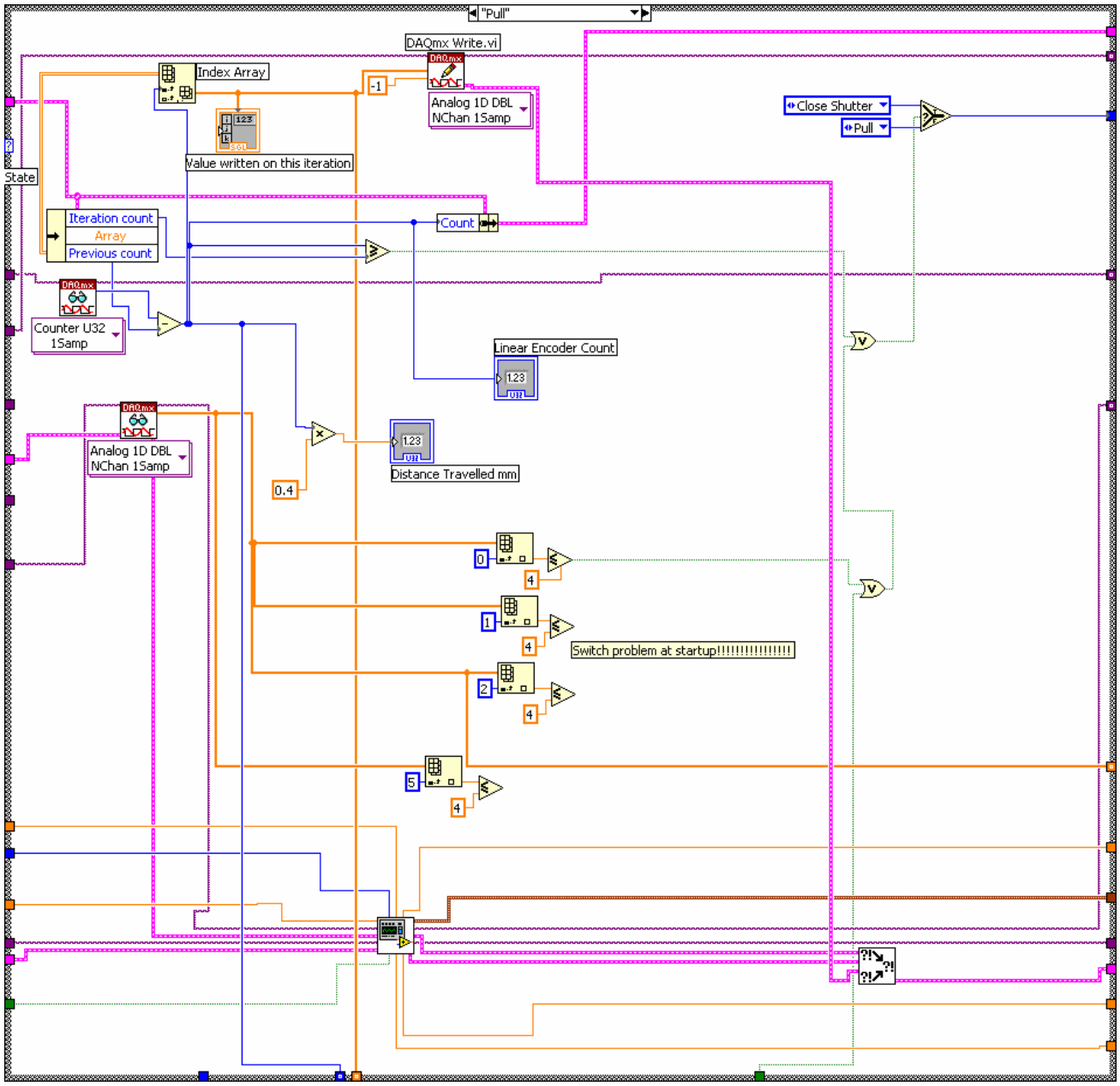

A.3.7 Close Shutter State

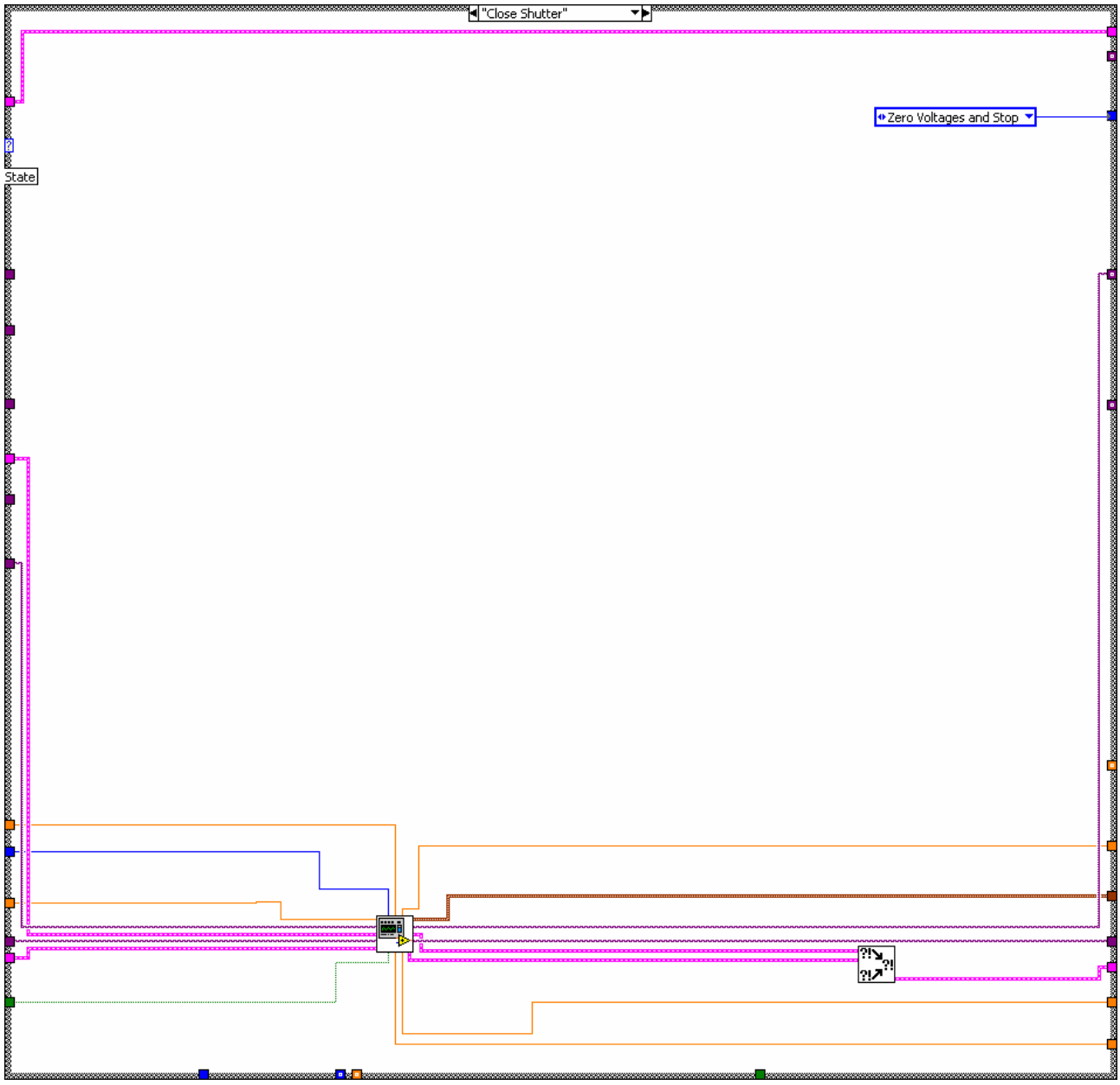

A.3.8 Zero Voltages and Stop State

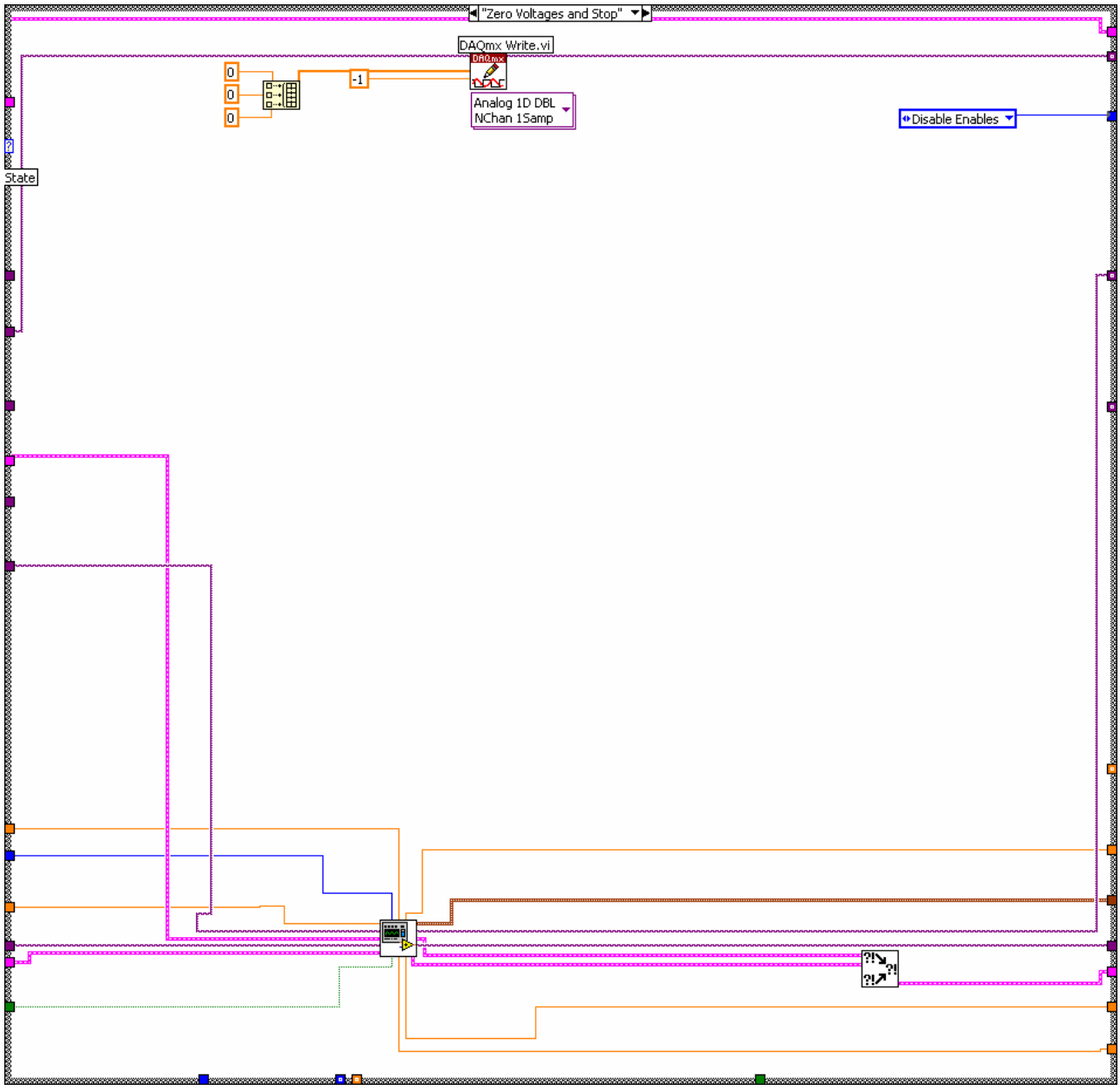

A.3.9 Disable Enables State

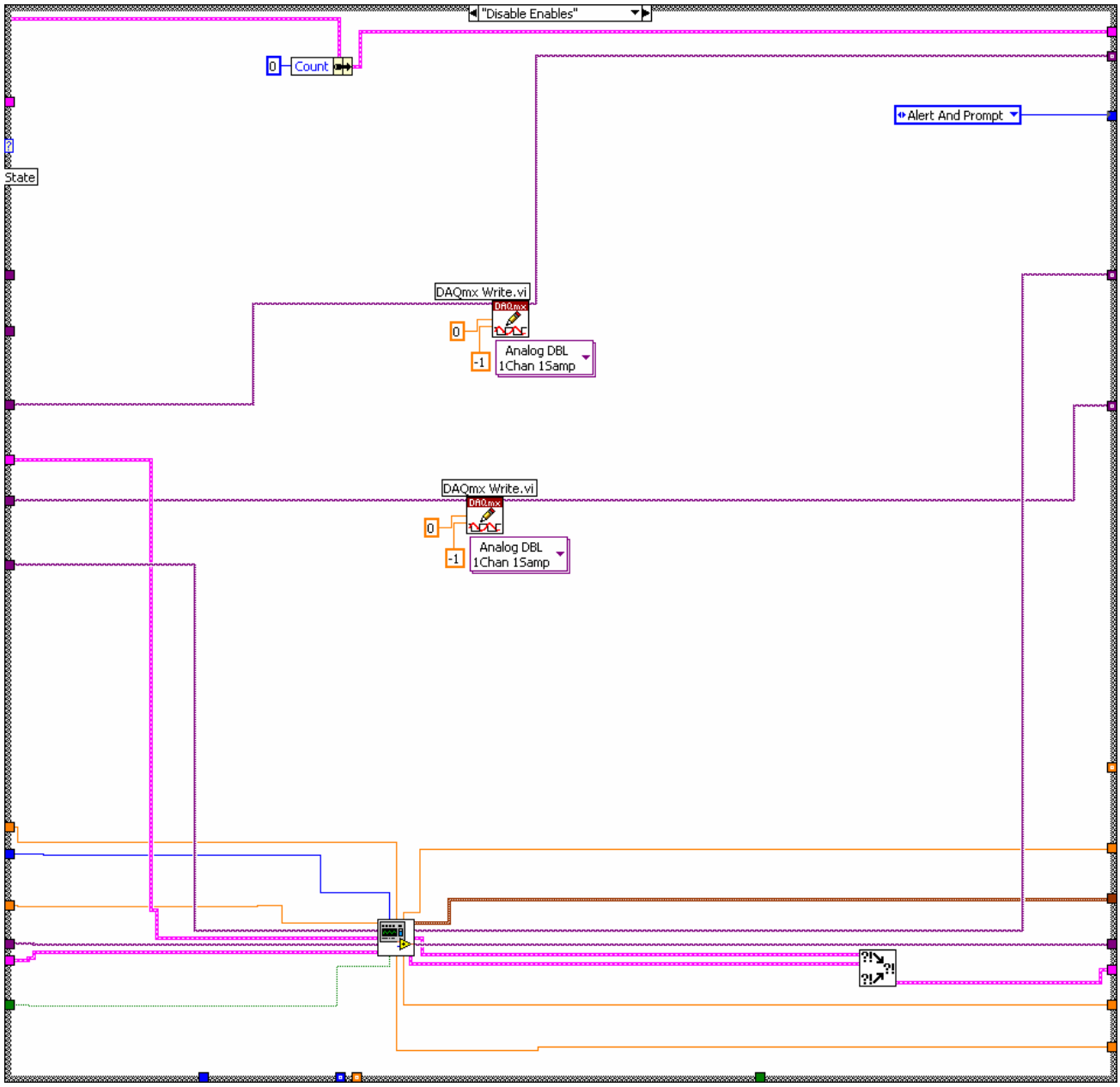

A.3.10 Alert and Prompt State

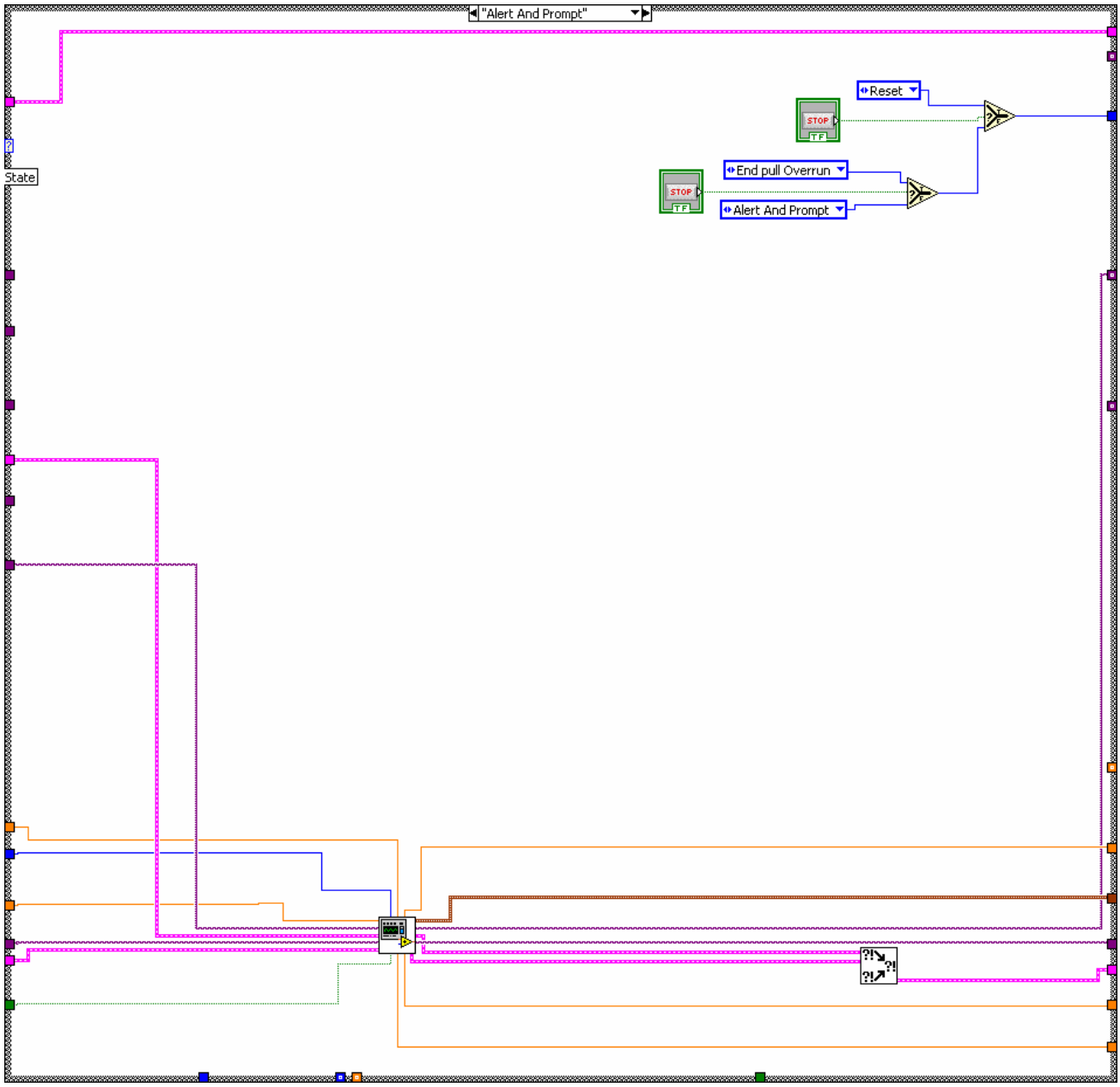

A.3.11 End Pull Overrun State

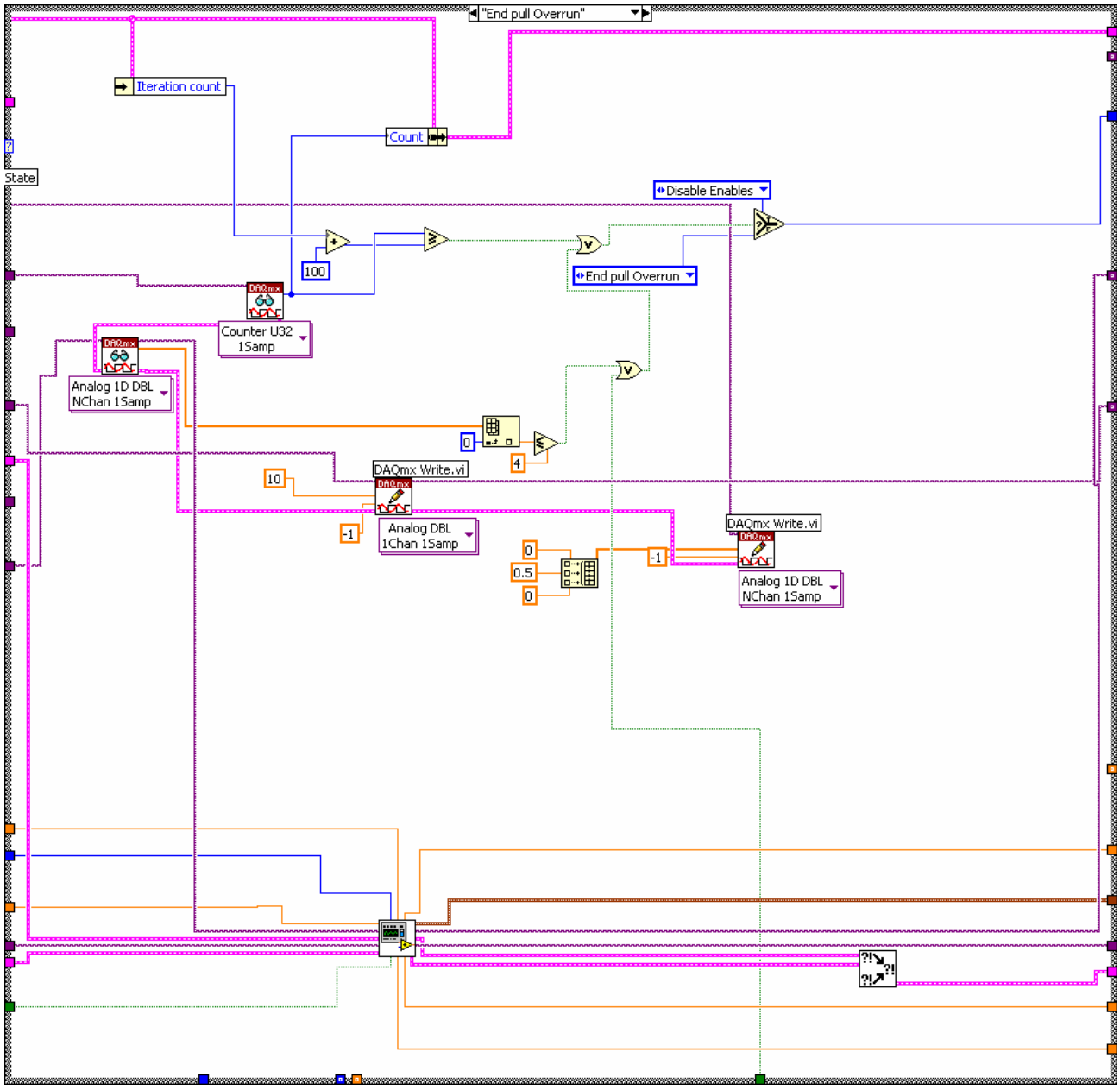

A.3.12 Reset State

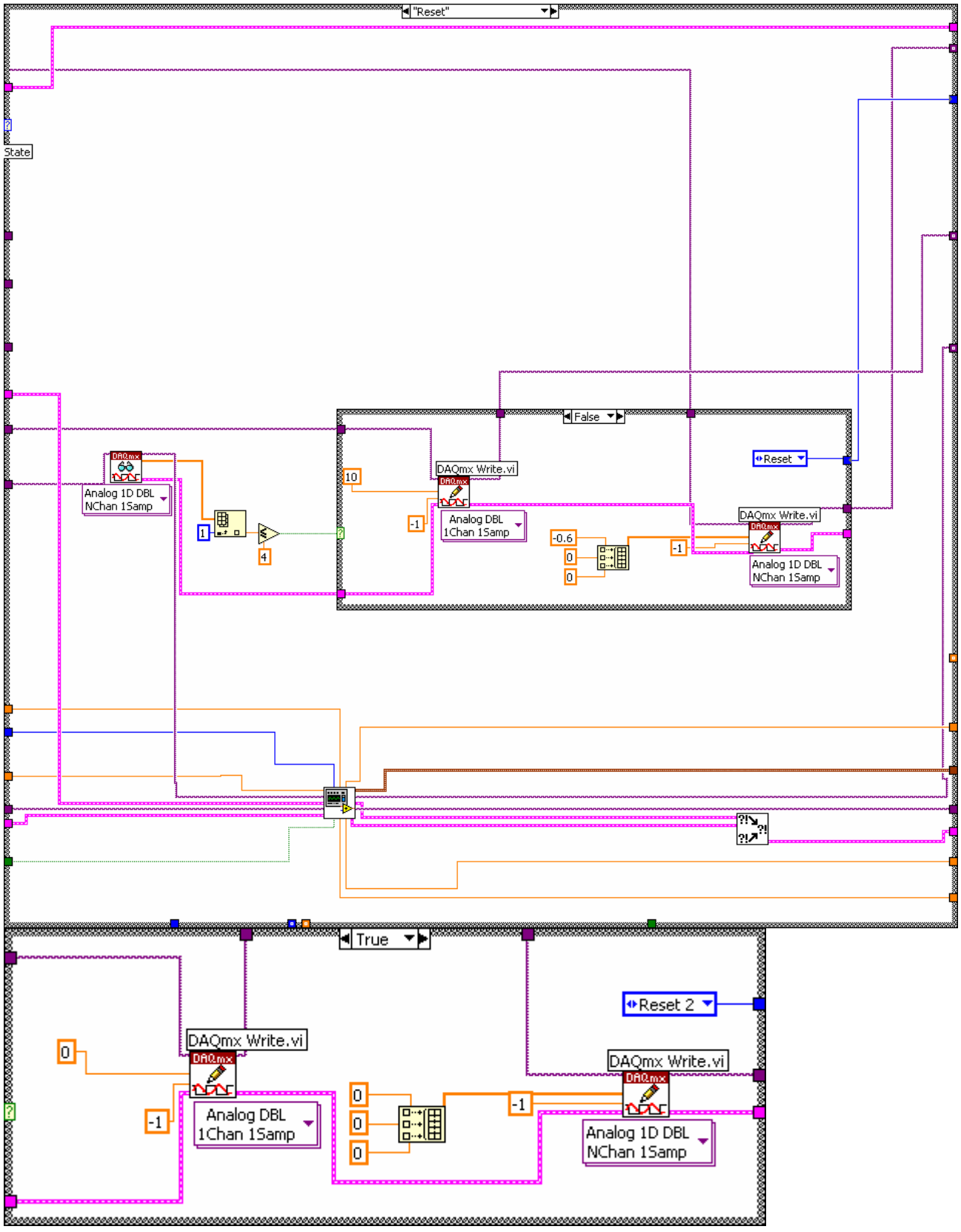

A.3.13 Reset 2 State

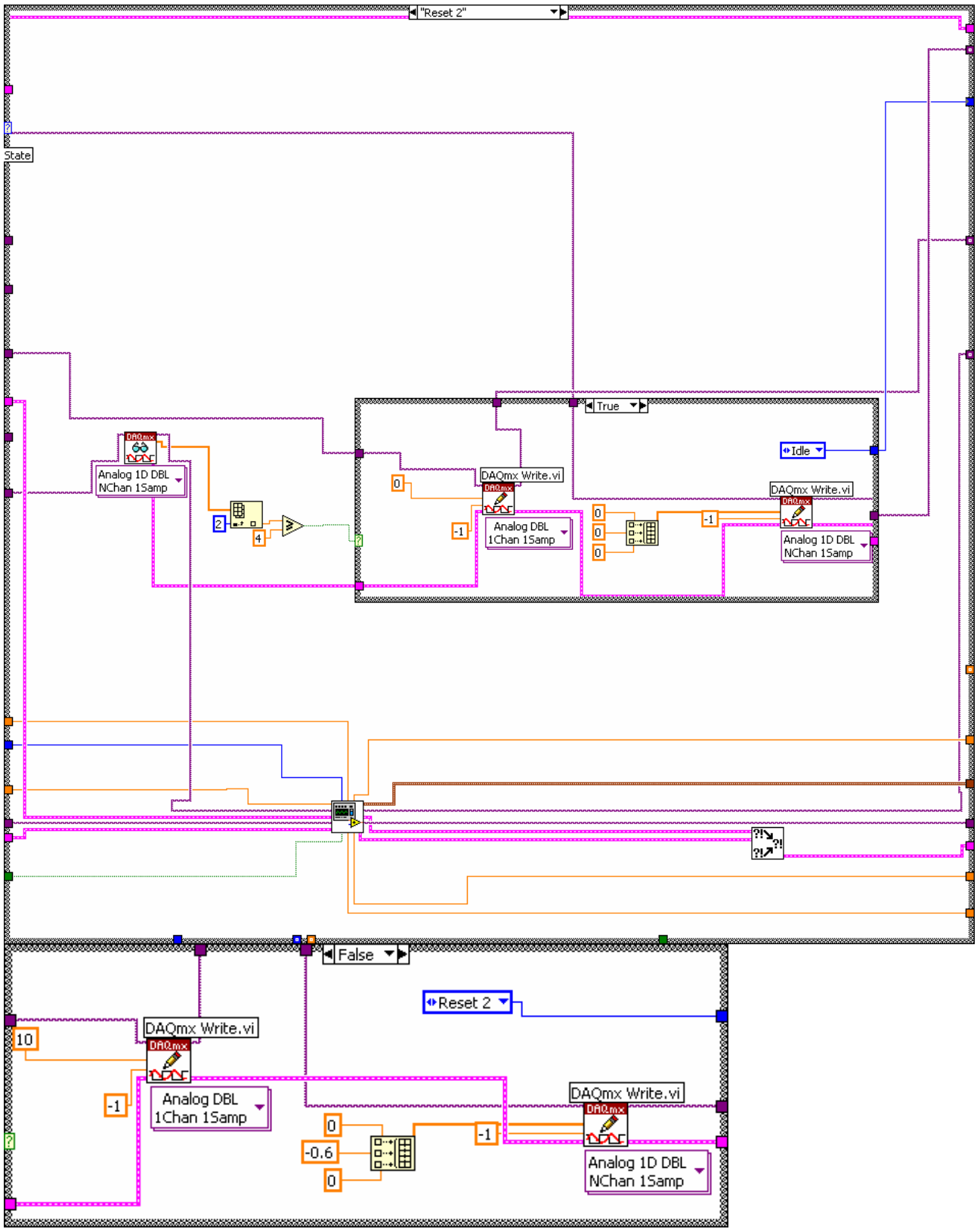

A.3.14 Exit State

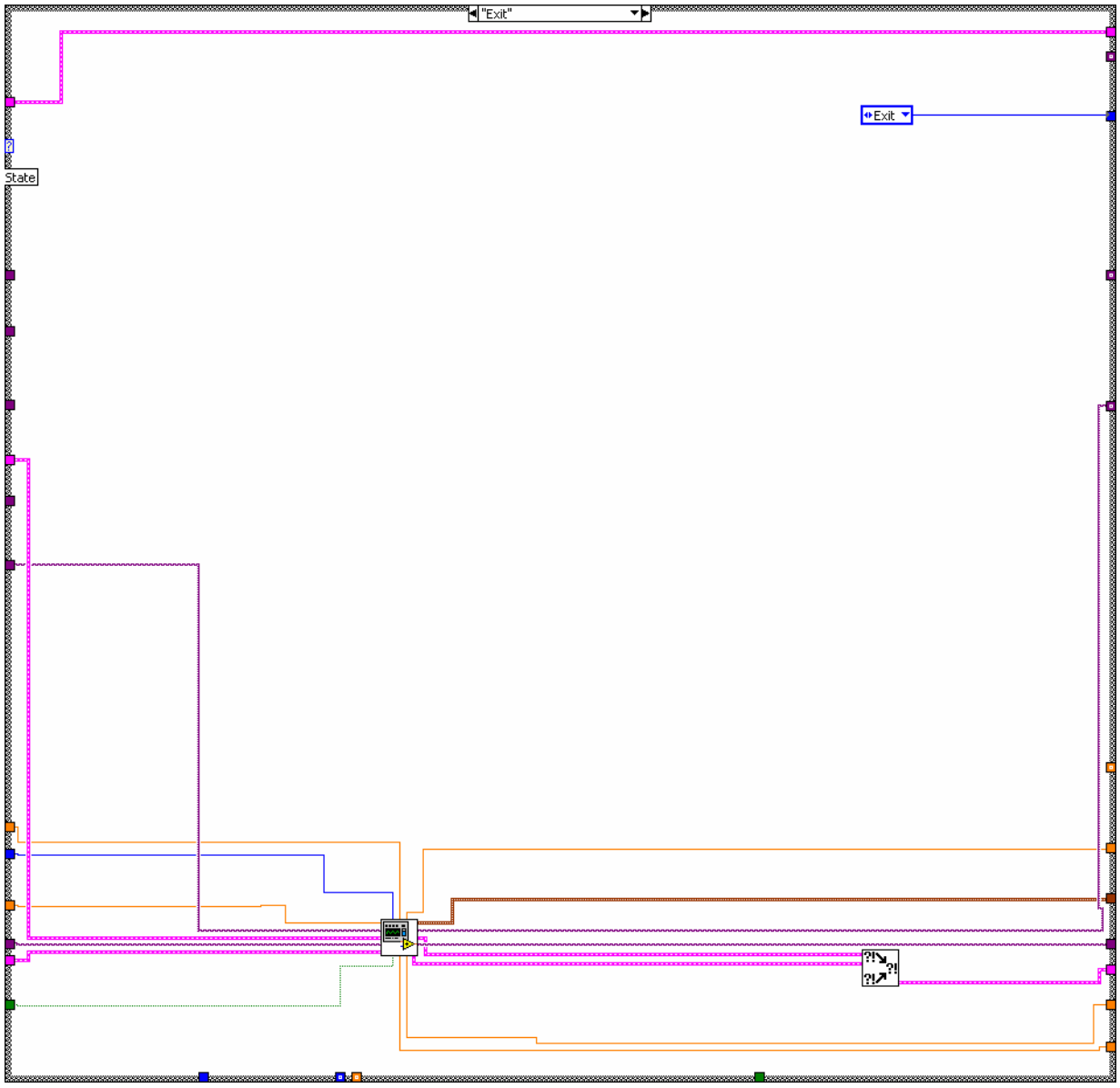

A.4 Input Voltage Dataset

Below is a typical input voltage dataset for the starting neck of a ribbon. The laser power column is zeroed out as this had not been implemented, but has been used as a placeholder for future program versions.

Feed Motor	Pull Motor	Laser power
0.0306	0.0306	0
0.0306	0.0306	0

0.0306	0.0306	0
0.0306	0.0306	0
0.0306	0.0306	0
0.0306	0.0306	0
0.0306	0.0306	0
0.0306	0.0306	0
0.0306	0.0306	0
0.0306	0.0306	0
0.0306	0.0306	0
0.0306	0.0306	0
0.0306	0.0306	0
0.0306	0.0306	0
0.0306	0.0306	0
0.0306	0.045	0
0.0306	0.0594	0
0.0306	0.0738	0
0.0306	0.0882	0
0.0306	0.1026	0
0.0306	0.117	0
0.0306	0.1314	0
0.0306	0.1458	0
0.0306	0.1602	0
0.0306	0.1746	0
0.0306	0.189	0
0.0306	0.2034	0
0.0306	0.2178	0
0.0306	0.2322	0
0.0306	0.2466	0
0.0306	0.261	0
0.0306	0.2754	0
0.0306	0.2898	0
0.0306	0.3042	0
0.0306	0.3186	0
0.0306	0.333	0
0.0306	0.3474	0
0.0306	0.3618	0
0.0306	0.3762	0
0.0306	0.3906	0
0.0306	0.405	0
0.0306	0.4194	0
0.0306	0.4338	0
0.0306	0.4482	0
0.0306	0.4626	0
0.0306	0.477	0
0.0306	0.4914	0
0.0306	0.5058	0
0.0306	0.5202	0
0.0306	0.54	0

0.0306	0.5598	0
0.0306	0.5796	0
0.0306	0.5994	0
0.0306	0.6192	0
0.0306	0.639	0
0.0306	0.6588	0
0.0306	0.6786	0
0.0306	0.6984	0
0.0306	0.7182	0
0.0306	0.738	0
0.0306	0.7578	0
0.0306	0.774	0
0.0306	0.774	0
0.0306	0.774	0
0.0306	0.774	0
0.0306	0.774	0
0.0306	0.774	0
0.0306	0.774	0
0.0306	0.774	0
0.0306	0.774	0

Appendix B
Dimensional Characterisation Machine LabVIEW Measurement and Control Program

B.1 Program Front Panel

The program detailed below was used to perform dimensional measurements and control the profiler. Program is again of state machine structure. Due to large size of front panel (3200 x 1600 pixels) it is split over the next

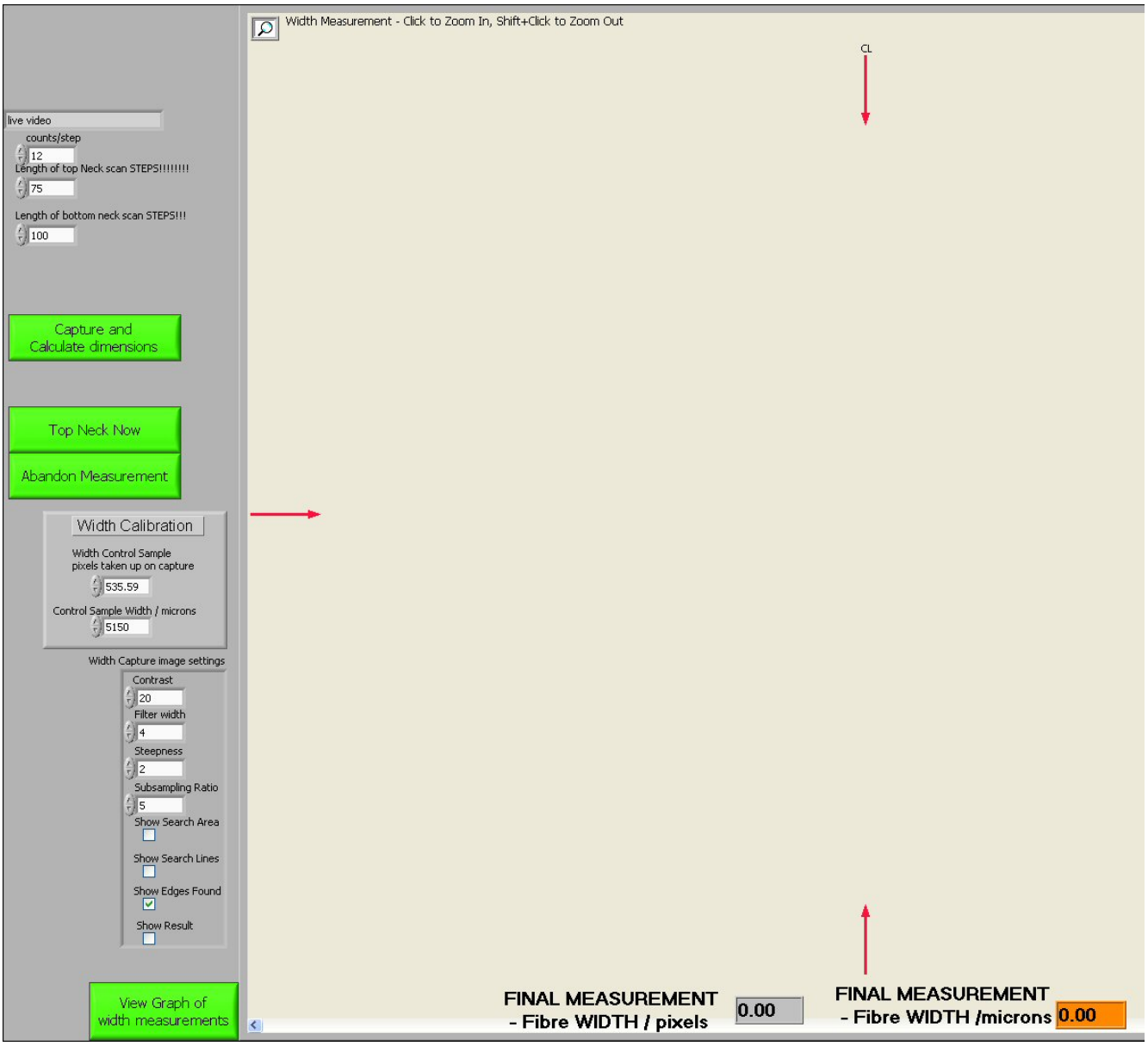
Width Measurement - Click to Zoom In, Shift+Click to Zoom Out
CL
live video
counts/step
12
Length of top Neck scan STEPS!!!!!!!!
75
Length of bottom neck scan STEPS!!!
100
Capture and Calculate dimensions
Top Neck Now
Abandon Measurement
Width Calibration
Width Control Sample pixels taken up on capture
535.59
Control Sample Width / microns
5150
Width Capture image settings
Contrast
20
Filter width
4
Steepness
2
Subsampling Ratio
5
Show Search Area
Show Search Lines
Show Edges Found
Show Result
View Graph of width measurements
FINAL MEASUREMENT - Fibre WIDTH / pixels
0.00
FINAL MEASUREMENT - Fibre WIDTH /microns
0.00

Thickness Measurement - Click to Zoom In, Shift+Click to Zoom Out
CL
FINAL MEASUREMENT
- Fibre THICKNESS / pixels
0.00

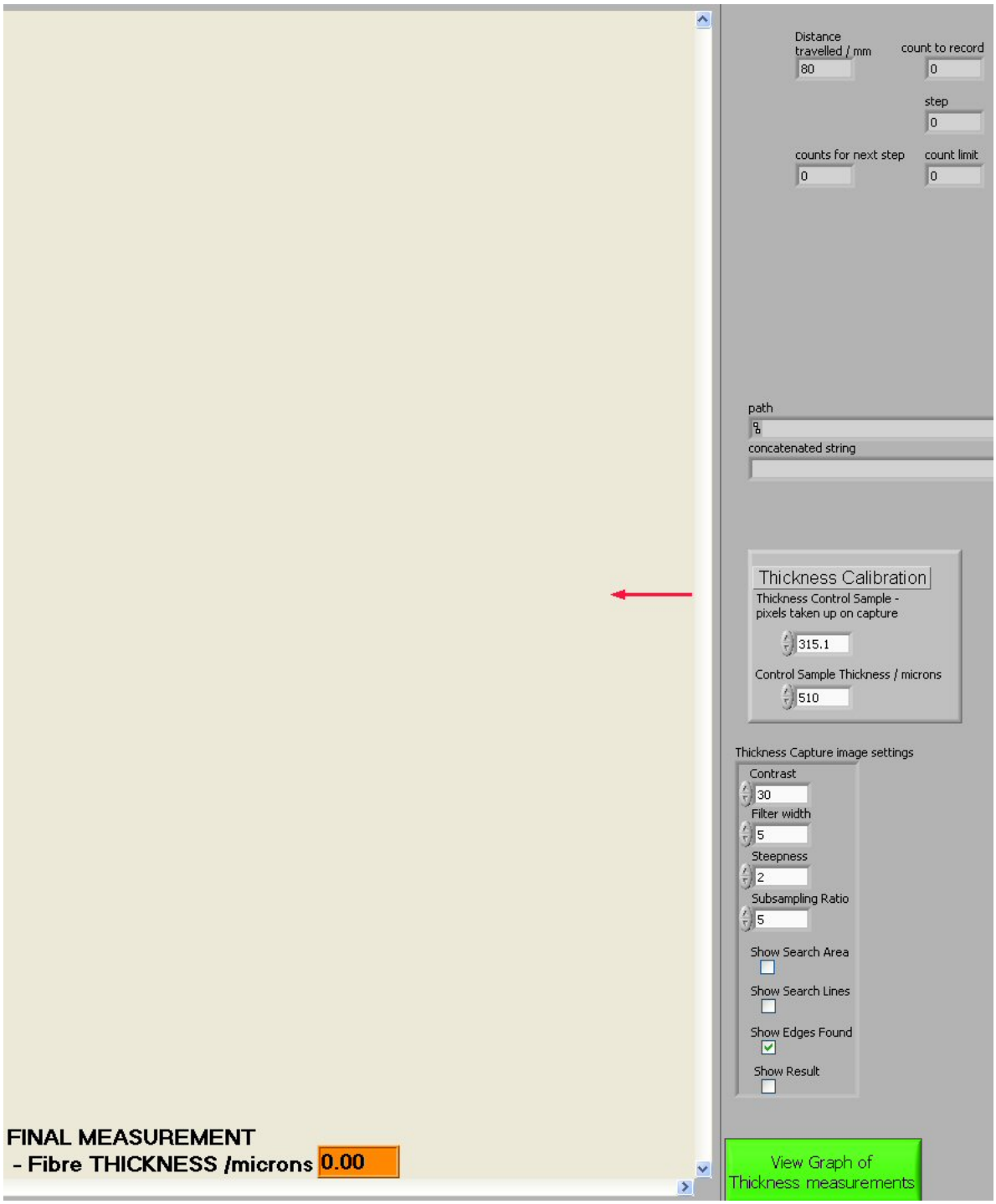
Distance travelled / mm
80
count to record
0
step
0
counts for next step
0
count limit
0
path
concatenated string
Thickness Calibration
Thickness Control Sample - pixels taken up on capture
315.1
Control Sample Thickness / microns
510
Thickness Capture image settings
Contrast
30
Filter width
5
Steepness
2
Subsampling Ratio
5
Show Search Area
Show Search Lines
Show Edges Found
Show Result
FINAL MEASUREMENT
- Fibre THICKNESS /microns
0.00
View Graph of Thickness measurements

B.2 Block Diagram

B.2.1 Main Diagram and Measurement State

Block diagram for this state is split over the next 4 pages.

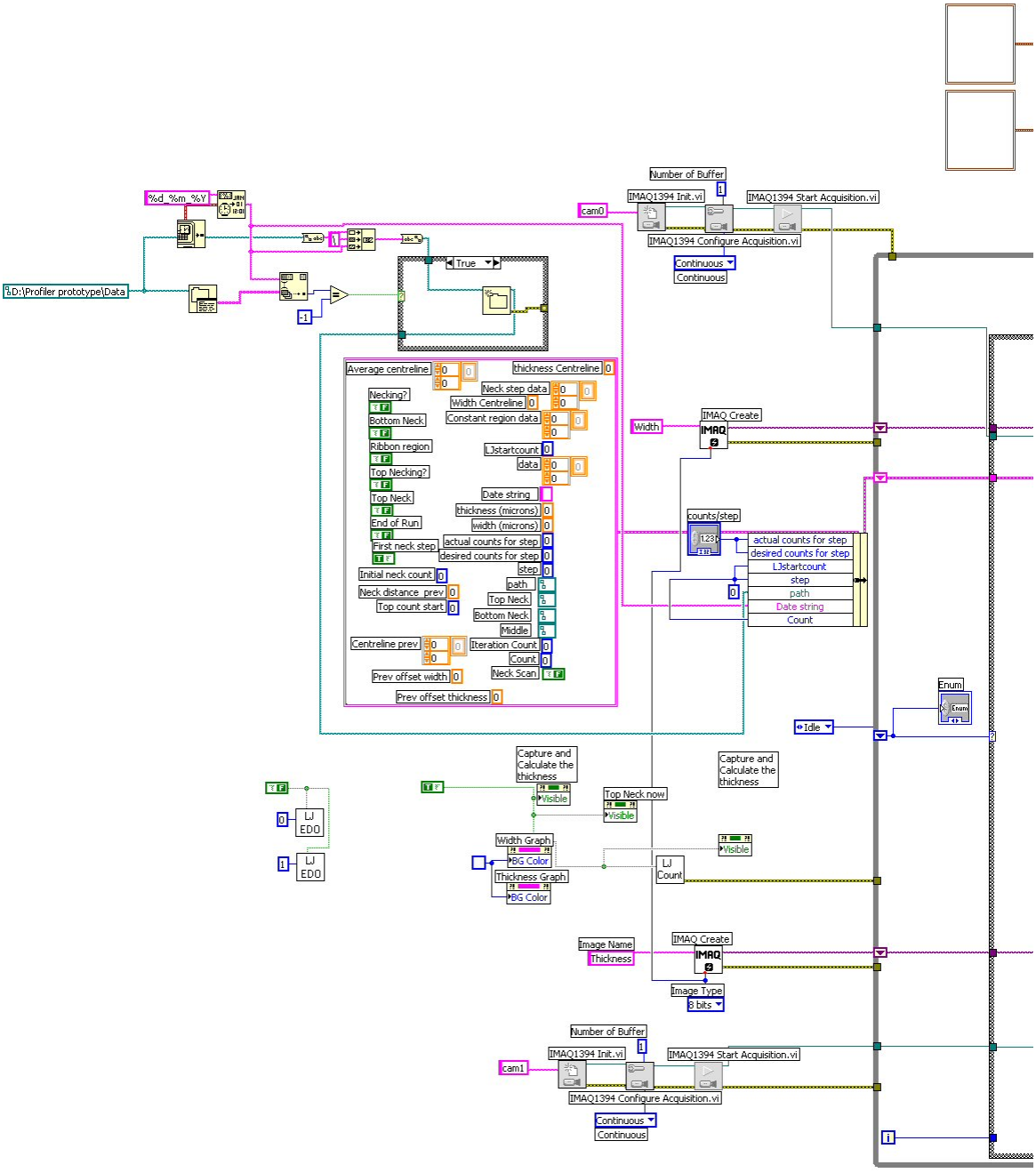

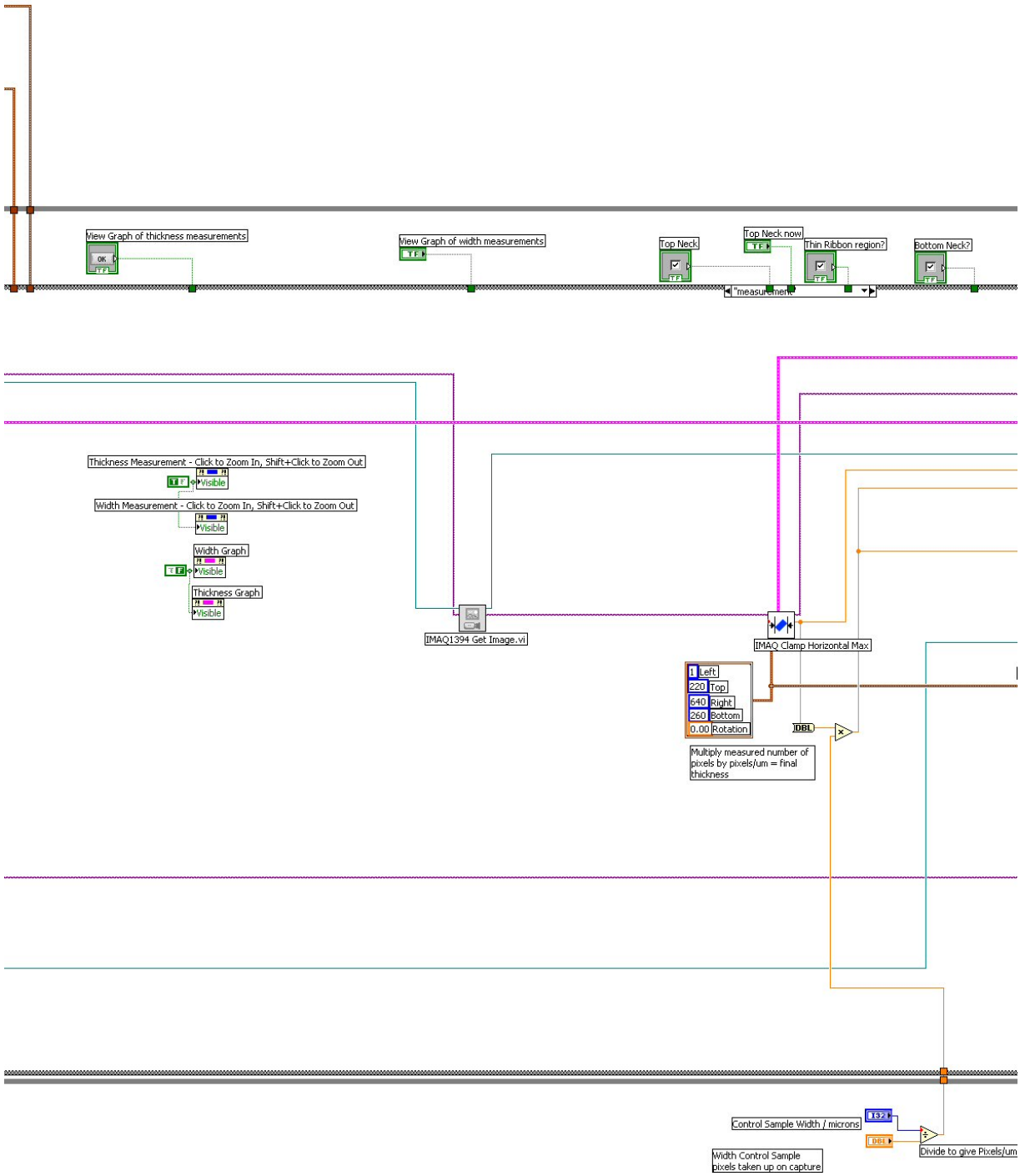
View Graph of thickness measurements
View Graph of width measurements
Top Neck
Top Neck now
Thin Ribbon region?
Bottom Neck?
"measurement"
Thickness Measurement - Click to Zoom In, Shift+Click to Zoom Out
Visible
Width Measurement - Click to Zoom In, Shift+Click to Zoom Out
Visible
Width Graph
Visible
Thickness Graph
Visible
IMAQ1394 Get Image.vi
IMAQ Clamp Horizontal Max
1 Left
220 Top
640 Right
260 Bottom
0.00 Rotation
DBL
Multiply measured number of pixels by pixels/um = final thickness
Control Sample Width / microns
I32
DBL
Divide to give Pixels/um
Width Control Sample pixels taken up on capture

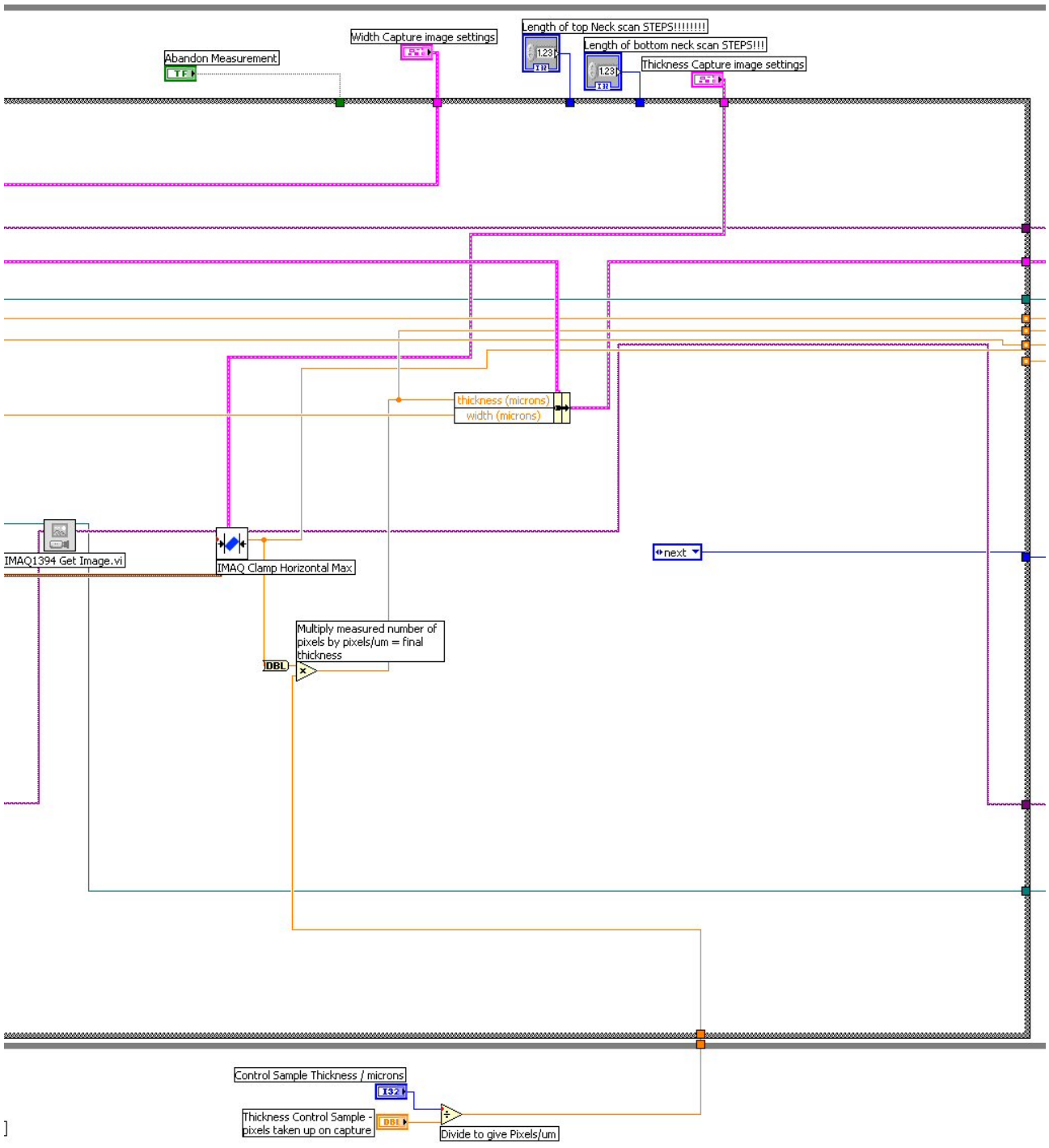
Abandon Measurement
Width Capture image settings
Length of top Neck scan STEPS!!!!!!!!
Length of bottom neck scan STEPS!!!
Thickness Capture image settings
thickness (microns)
width (microns)
IMAQ1394 Get Image.vi
IMAQ Clamp Horizontal Max
next
Multiply measured number of pixels by pixels/um = final thickness
DBL
Control Sample Thickness / microns
I32
Thickness Control Sample - pixels taken up on capture
DBL
Divide to give Pixels/um

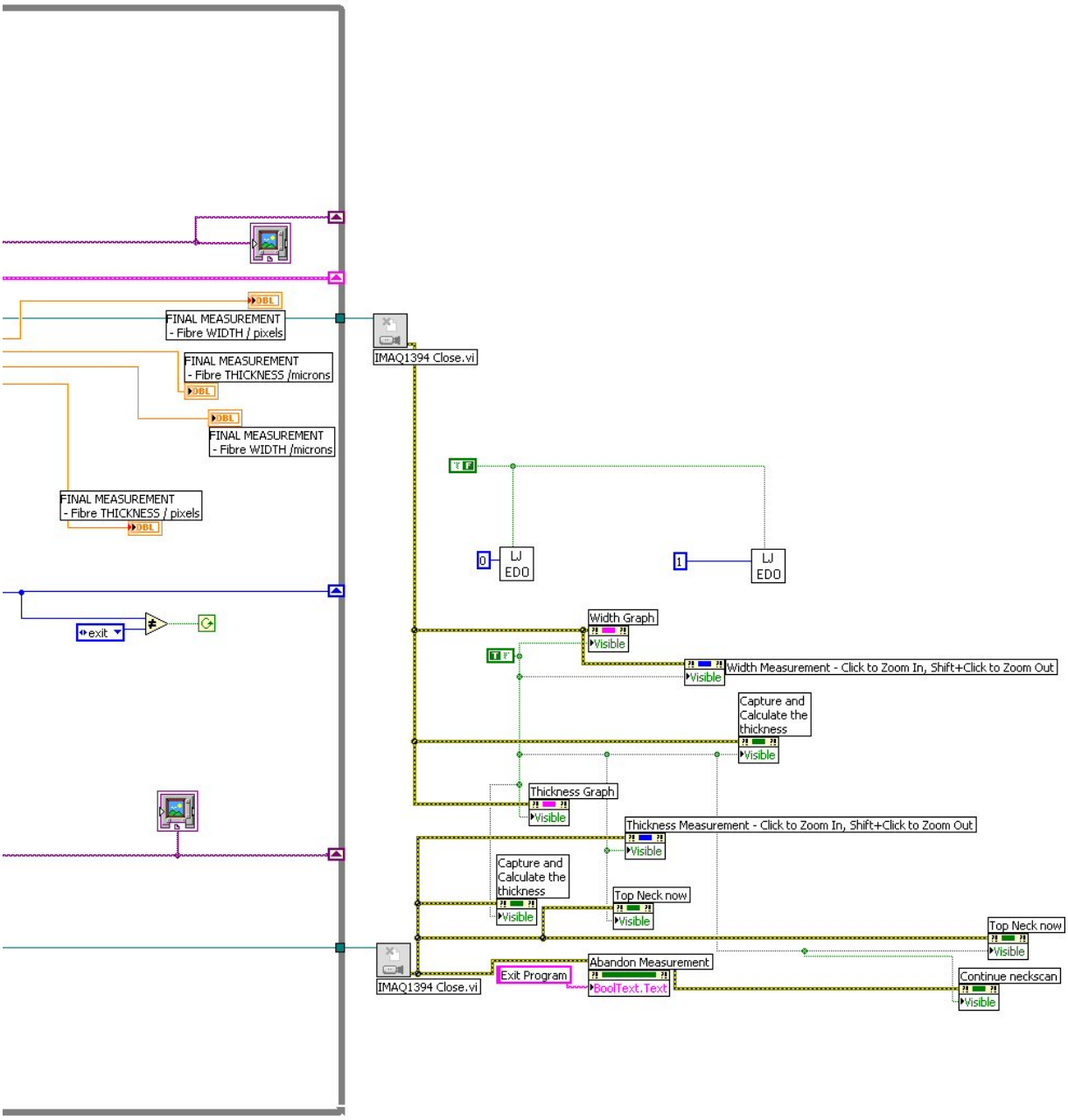
FINAL MEASUREMENT
- Fibre WIDTH / pixels
FINAL MEASUREMENT
- Fibre THICKNESS /microns
FINAL MEASUREMENT
- Fibre WIDTH /microns
FINAL MEASUREMENT
- Fibre THICKNESS / pixels
IMAQ1394 Close.vi
exit
LJ
EDO
LJ
EDO
Width Graph
Visible
Visible
Width Measurement - Click to Zoom In, Shift+Click to Zoom Out
Capture and
Calculate the
thickness
Visible
Thickness Graph
Visible
Thickness Measurement - Click to Zoom In, Shift+Click to Zoom Out
Visible
Capture and
Calculate the
thickness
Visible
Top Neck now
Visible
Top Neck now
Visible
IMAQ1394 Close.vi
Exit Program
Abandon Measurement
BoolText.Text
Continue neckscan
Visible

B.2.2 Motor Off State

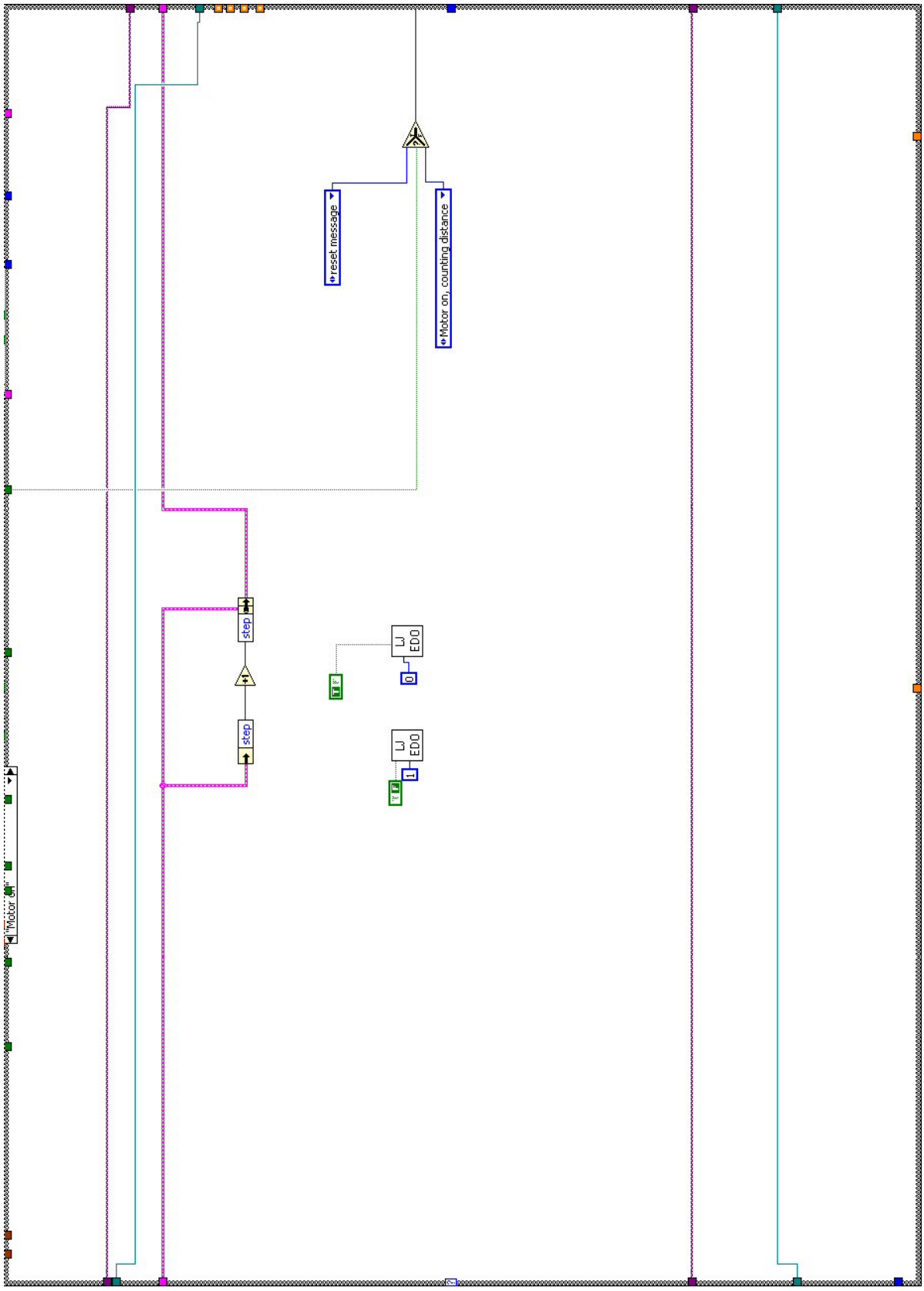

B.2.3 Motor On, Counting Distance State

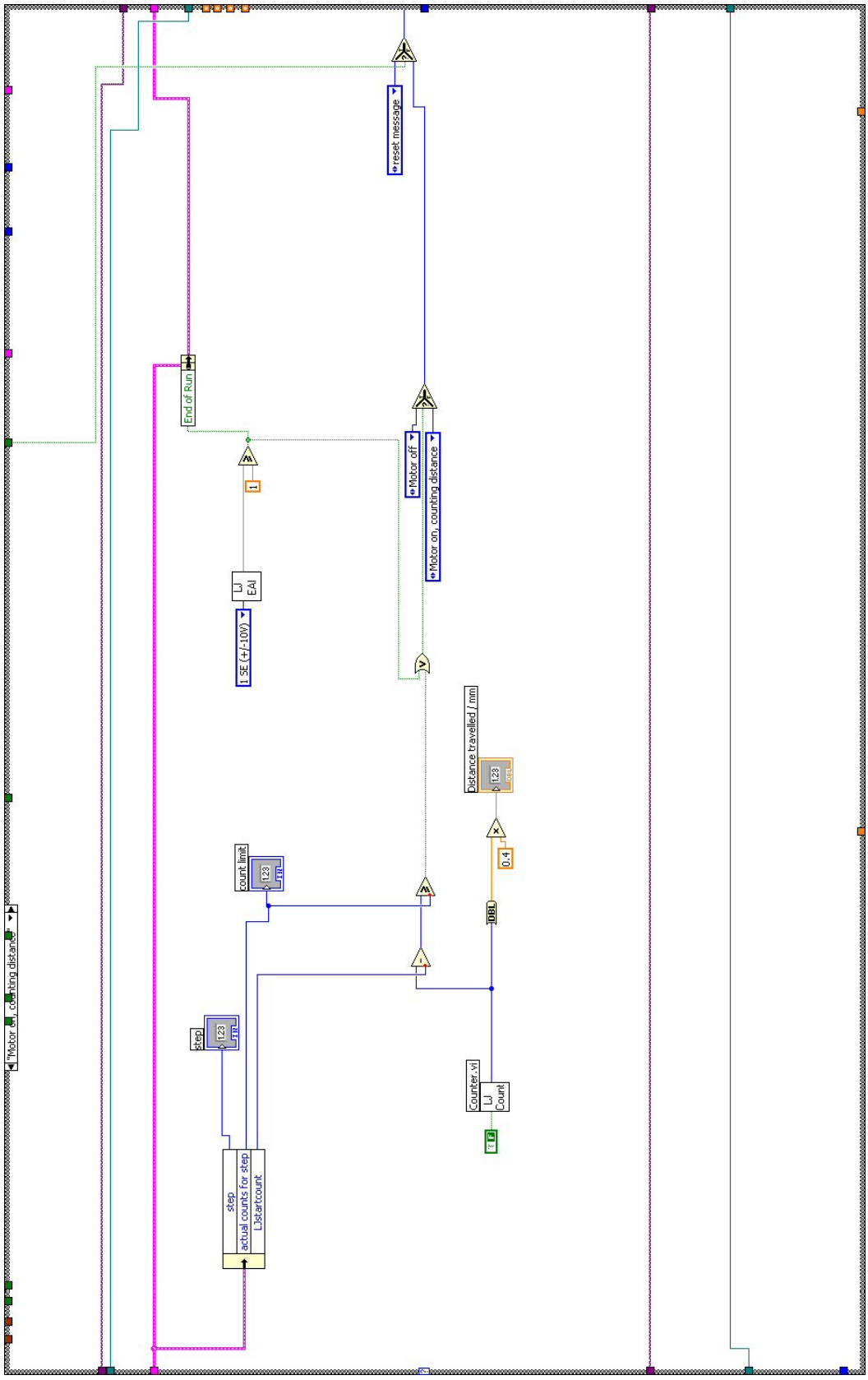

B.2.4 Motor On State

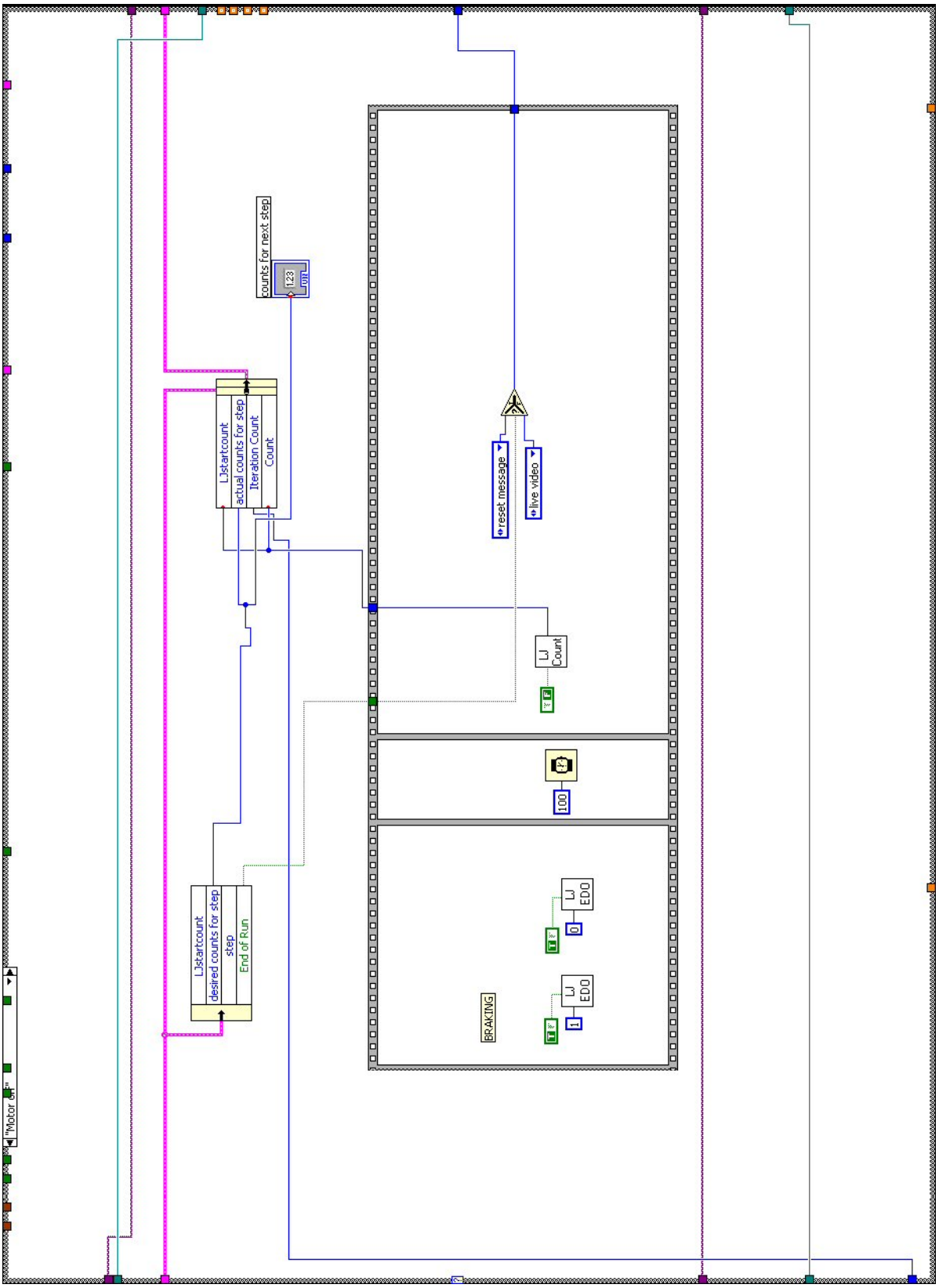

B.2.5 Reset Message State

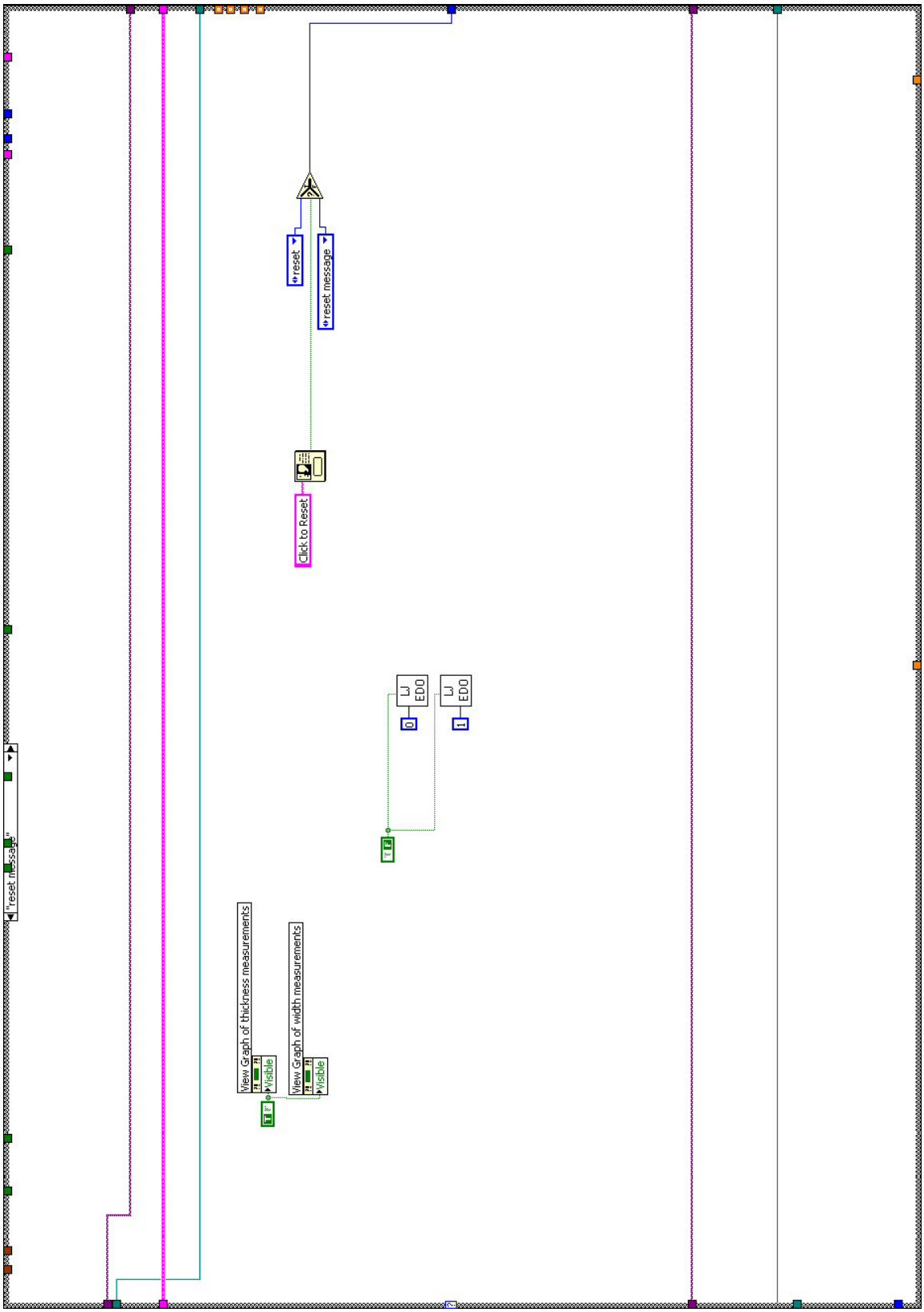

B.2.6 Idle State

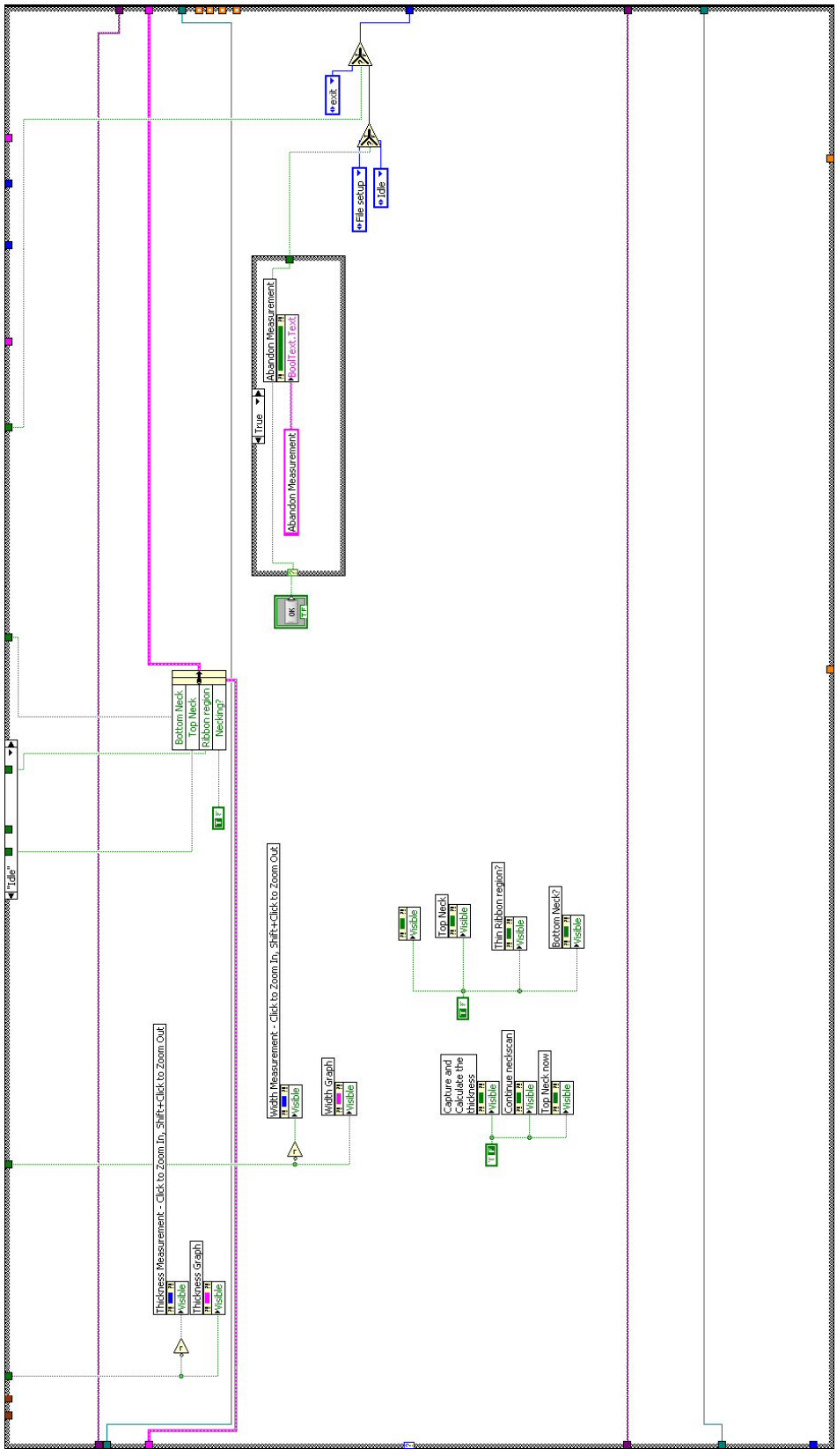

B.2.7 File Setup State

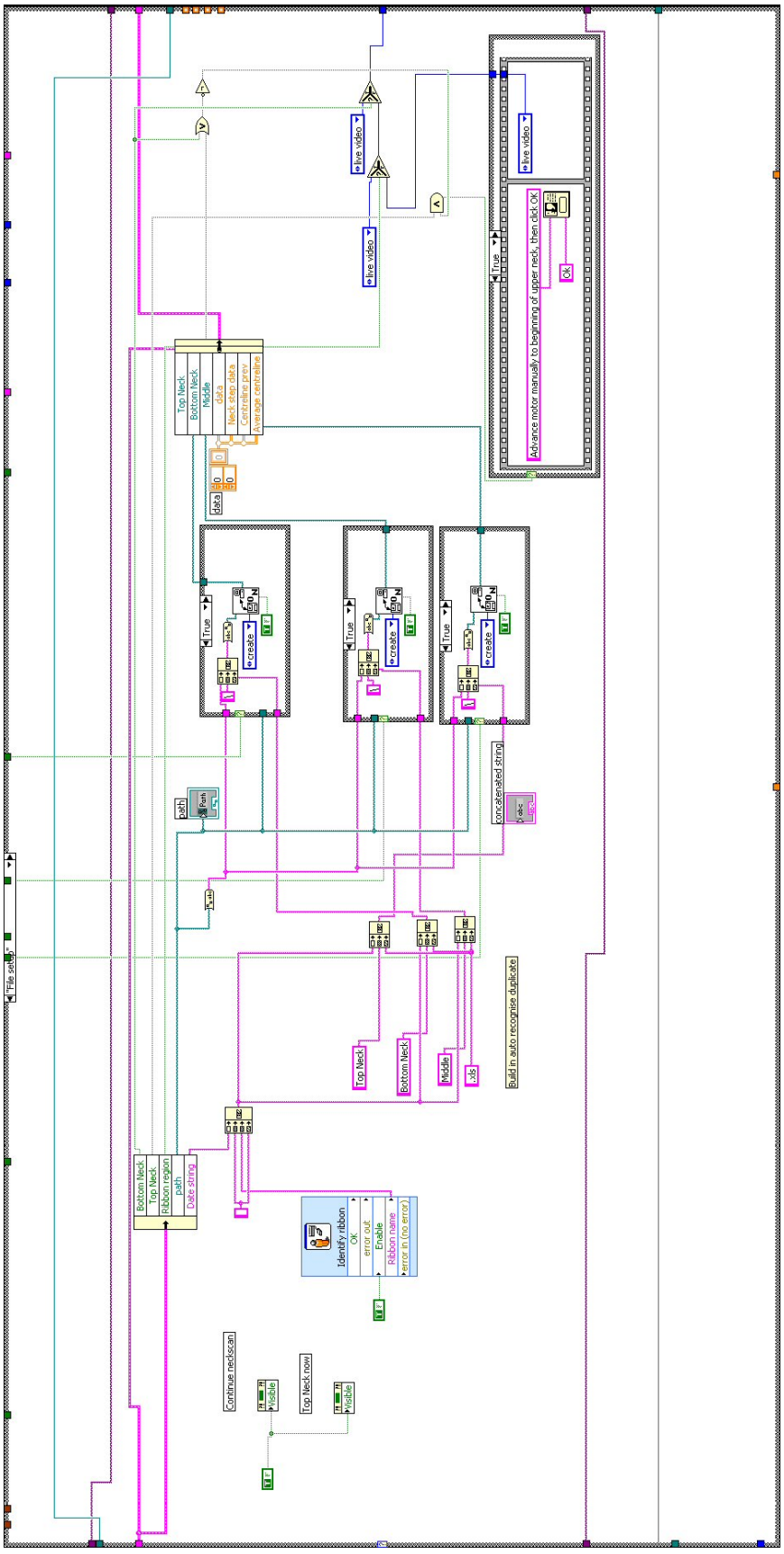

B.2.8 Snap for Neck Scan State

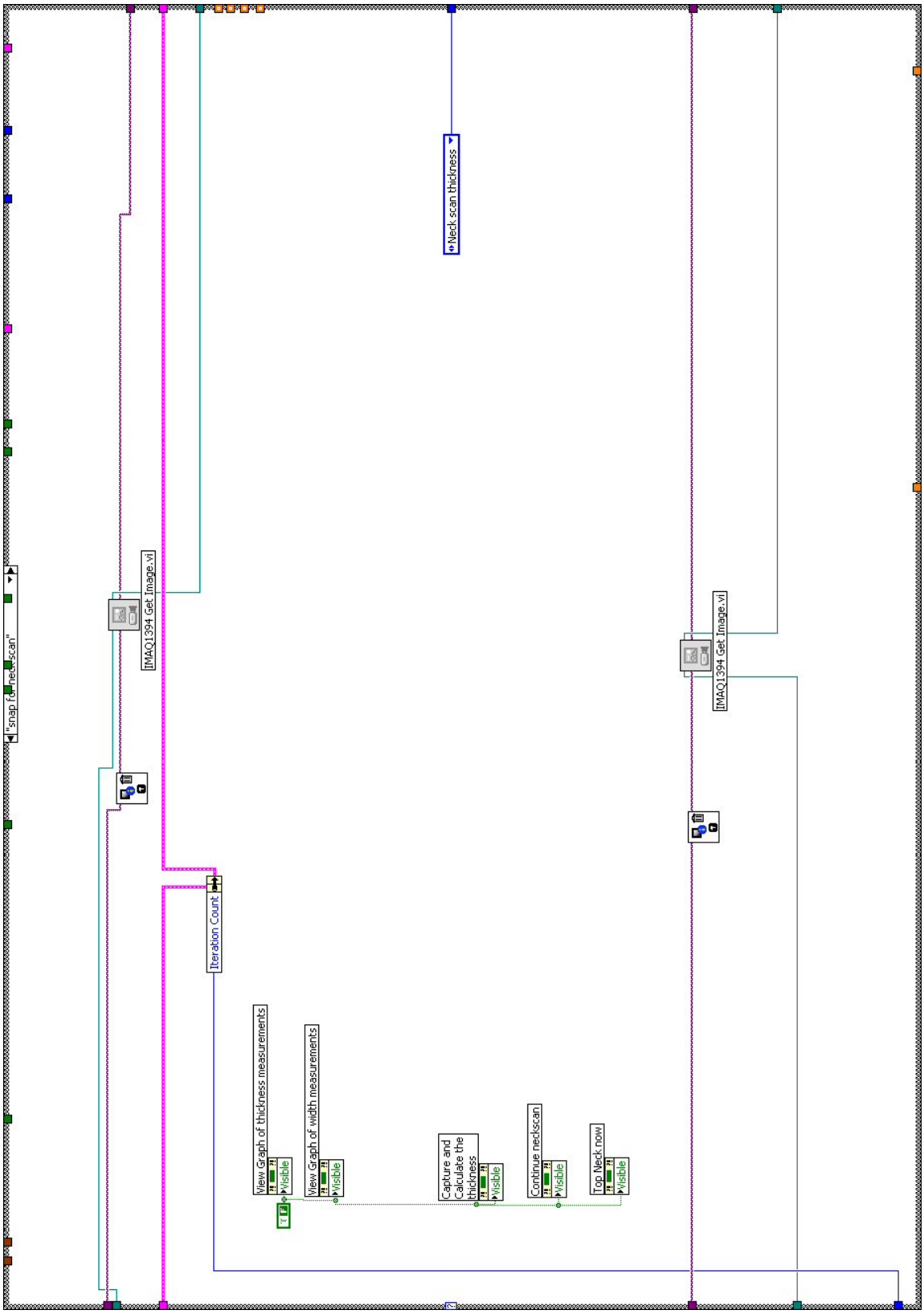

B.2.9 Neck Scan Top State

Block diagram for this state is split over the next two pages.

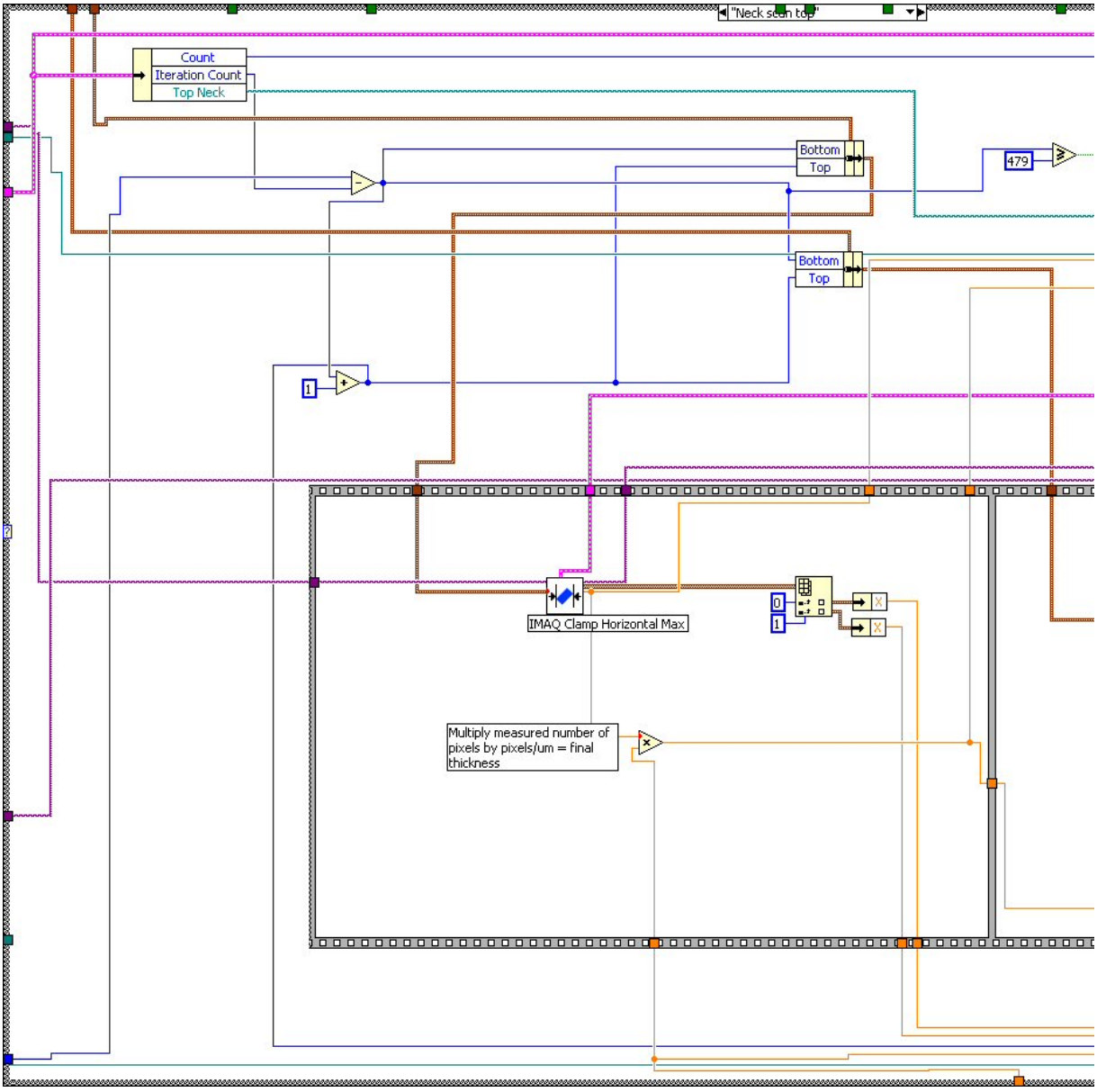

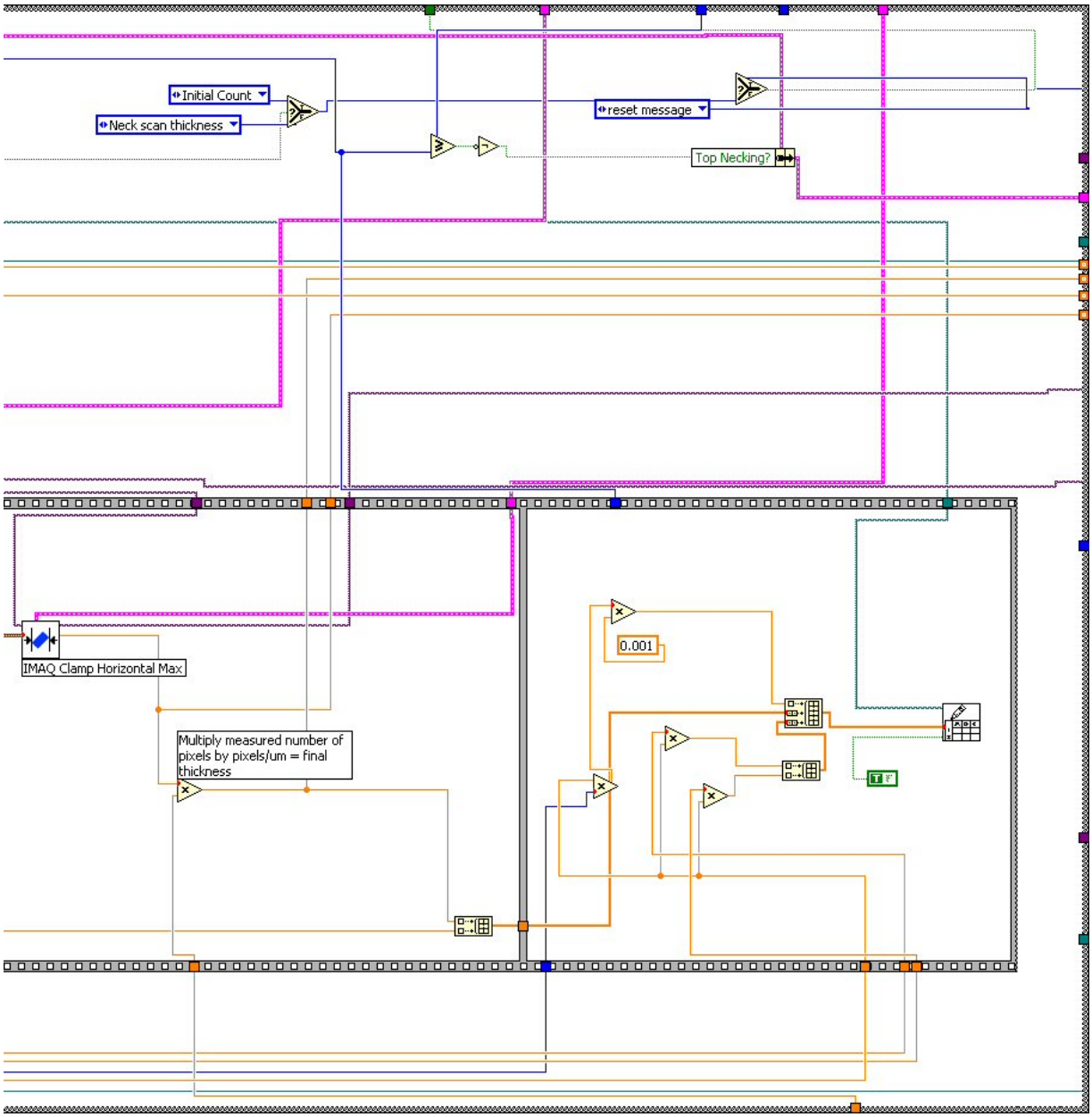

B.2.10 Initial Count State

This large state' block diagram is split over the next 4 pages.

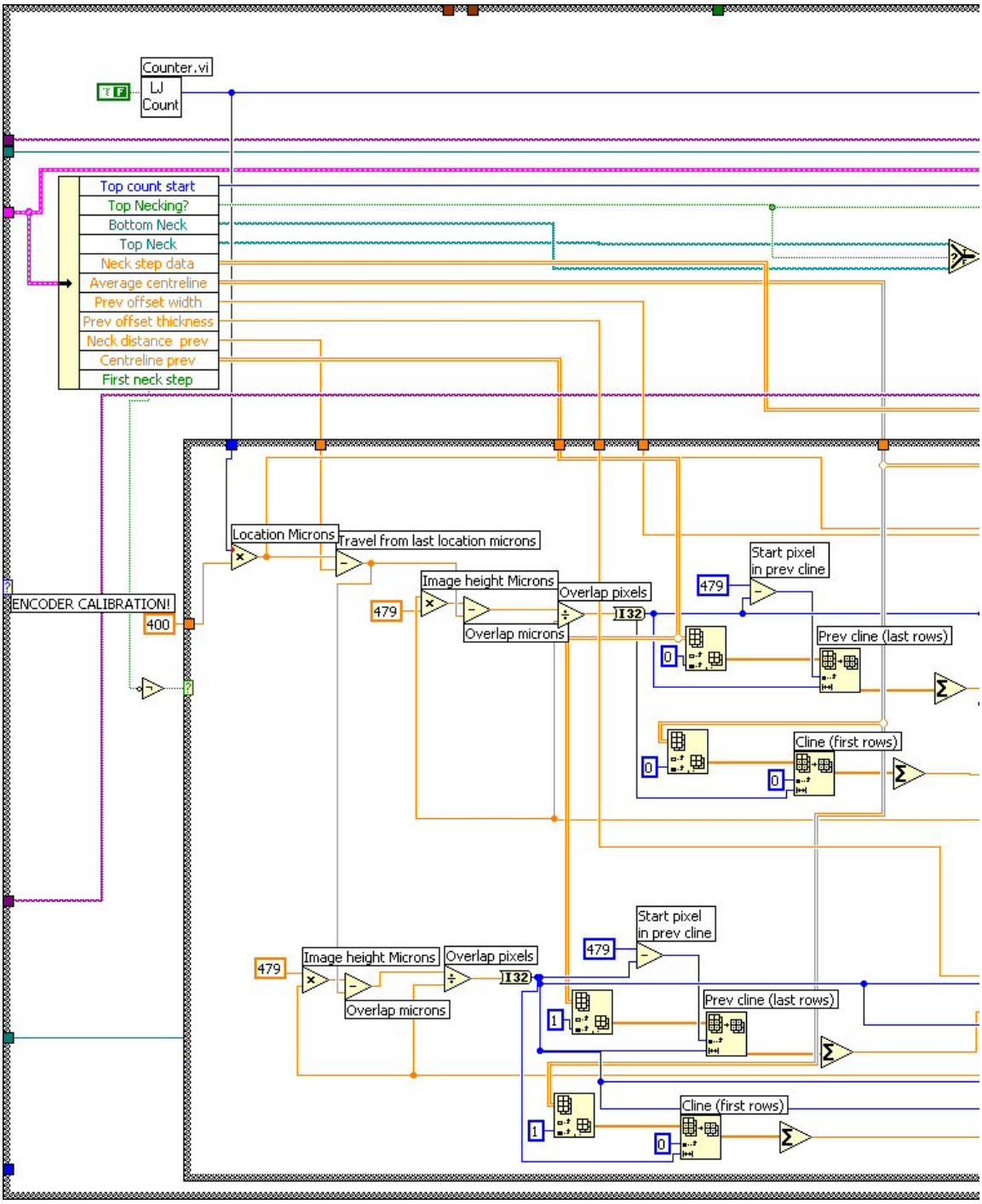
Counter.vi
LJ
Count
Top count start
Top Necking?
Bottom Neck
Top Neck
Neck step data
Average centreline
Prev offset width
Prev offset thickness
Neck distance prev
Centreline prev
First neck step
ENCODER CALIBRATION!
400
Location Microns
Travel from last location microns
Image height Microns
479
Overlap microns
Overlap pixels
I32
Start pixel
in prev cline
Prev cline (last rows)
Cline (first rows)
0
1

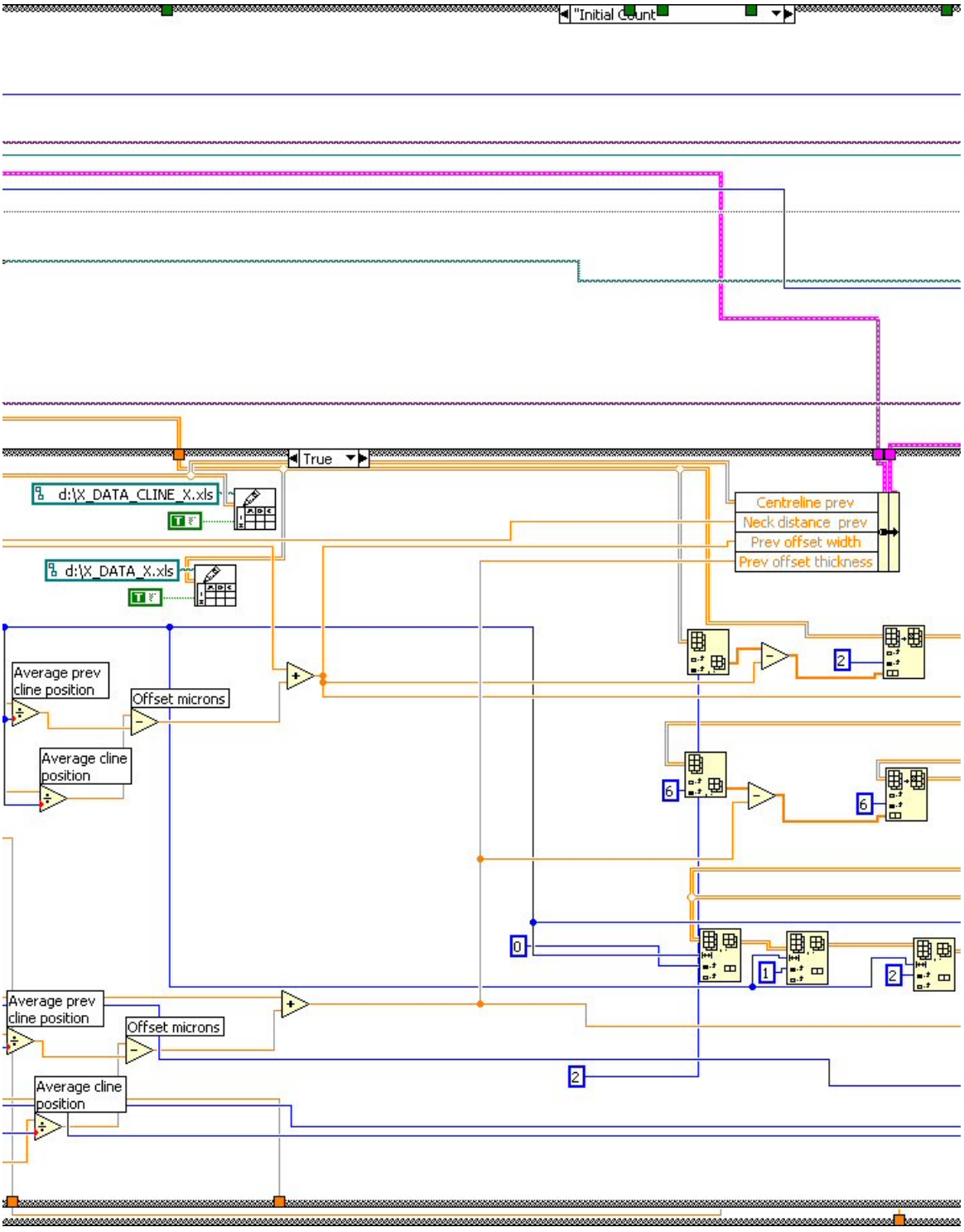
"Initial Count"
True
d:\X_DATA_CLINE_X.xls
d:\X_DATA_X.xls
Centreline prev
Neck distance prev
Prev offset width
Prev offset thickness
Average prev cline position
Offset microns
Average cline position
Average prev cline position
Offset microns
Average cline position
0
1
2
2
6
6

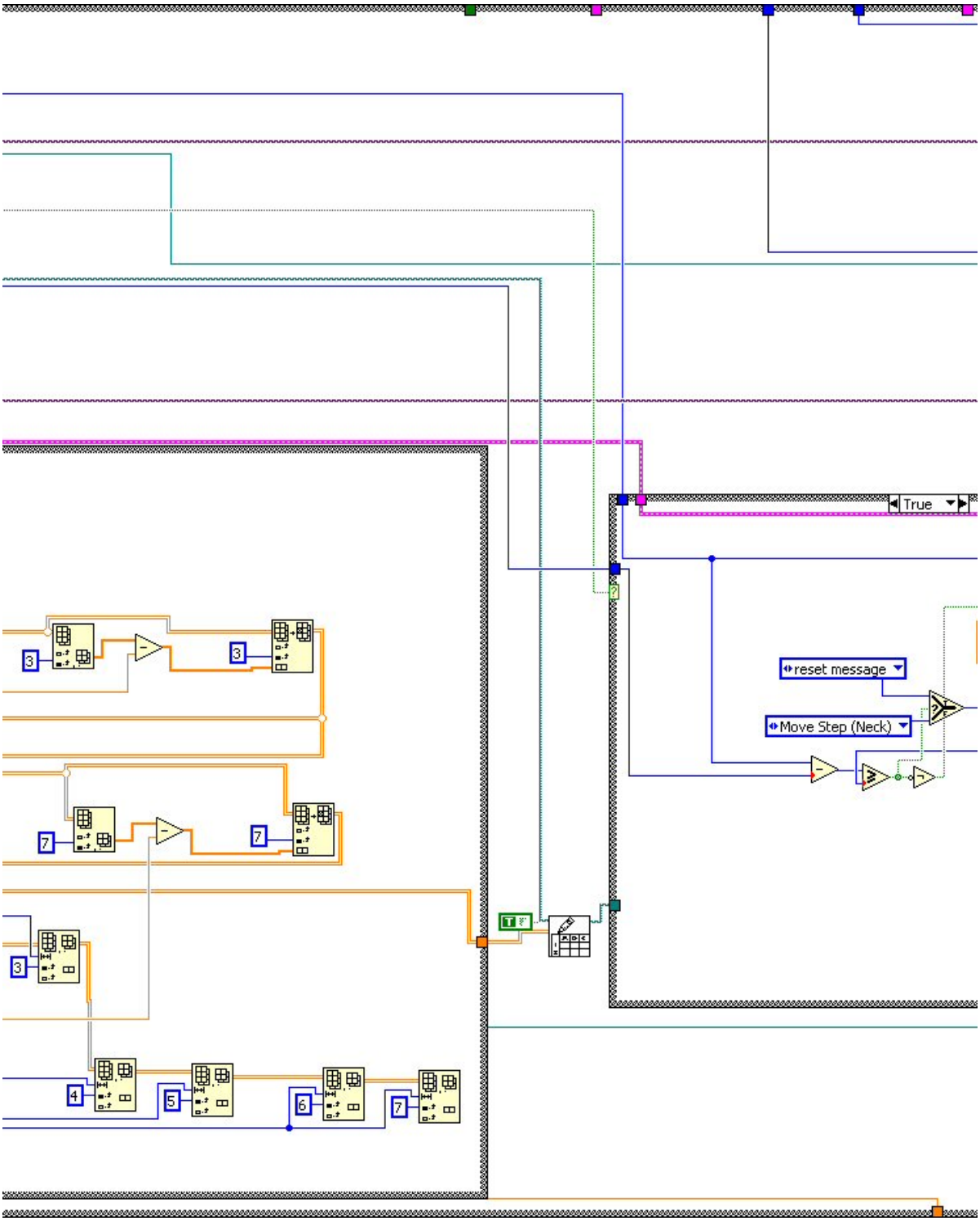
True
reset message
Move Step (Neck)
3
3
7
7
3
4
5
6
7

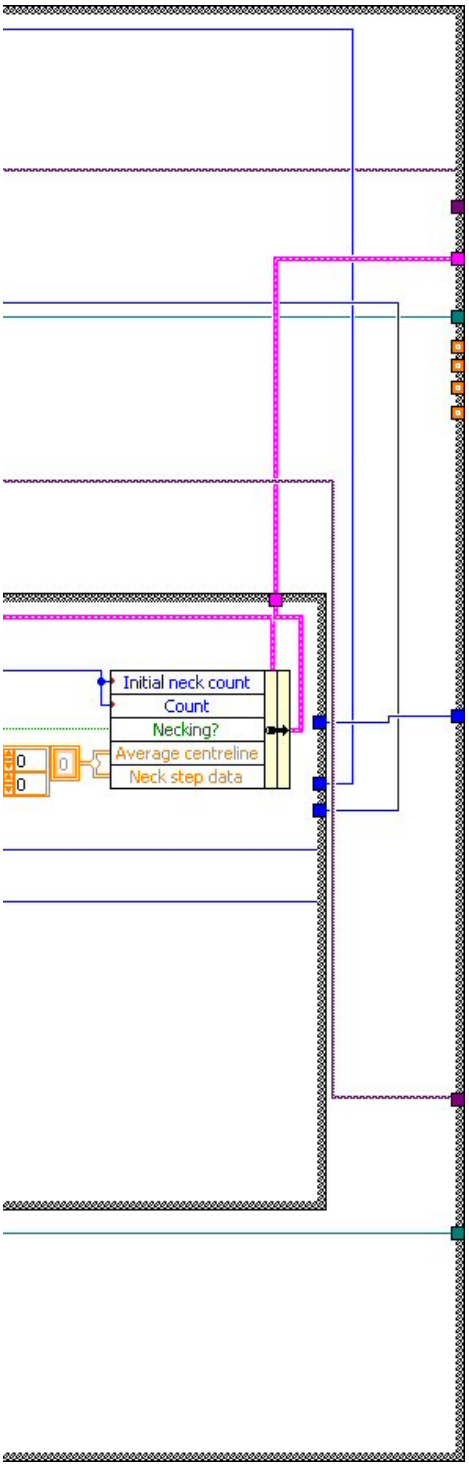

B.2.11 Reset State

Block diagram for this state is split over the next two pages.

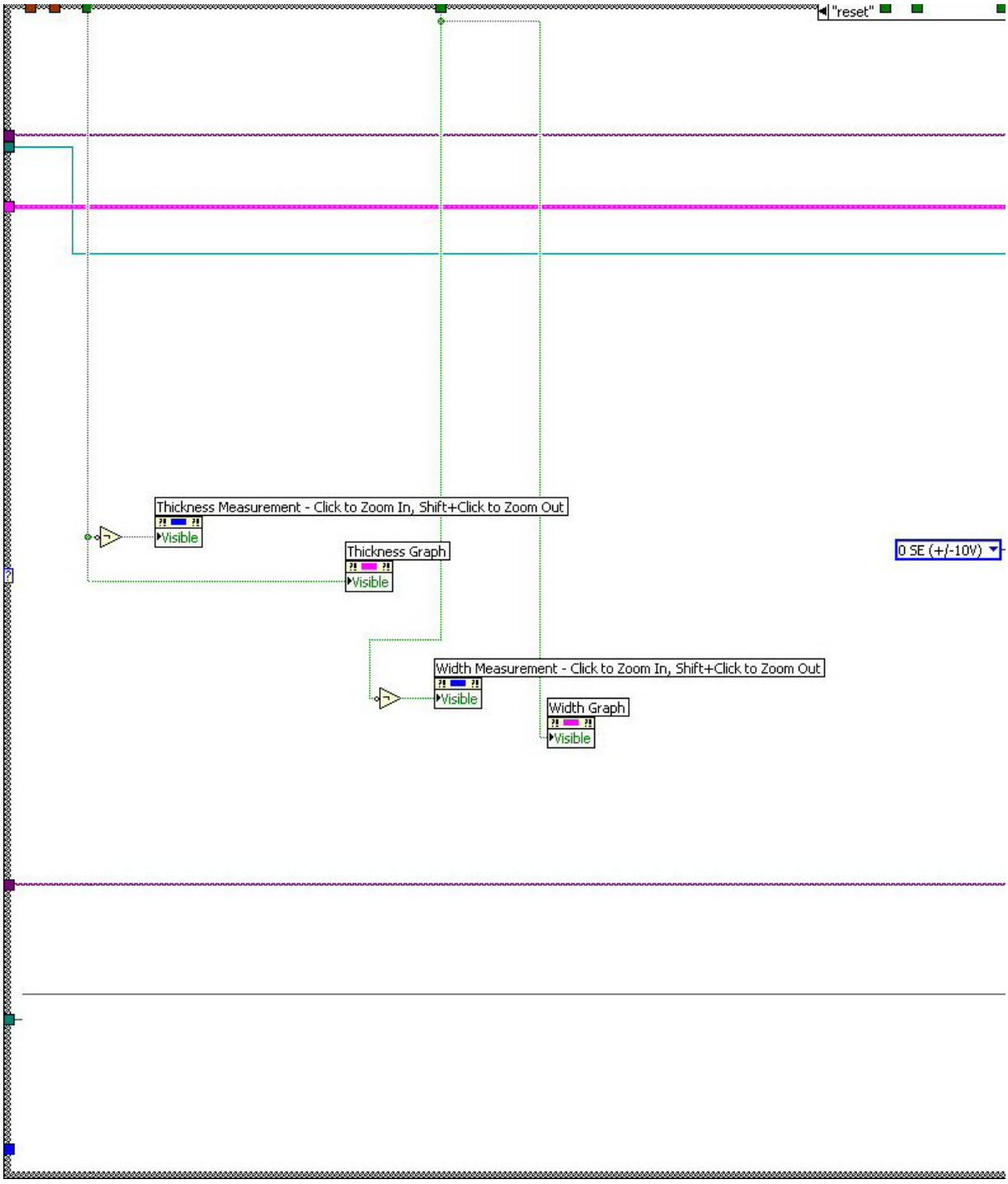
"reset"
Thickness Measurement - Click to Zoom In, Shift+Click to Zoom Out
Visible
Thickness Graph
Visible
0 SE (+/-10V)
Width Measurement - Click to Zoom In, Shift+Click to Zoom Out
Visible
Width Graph
Visible

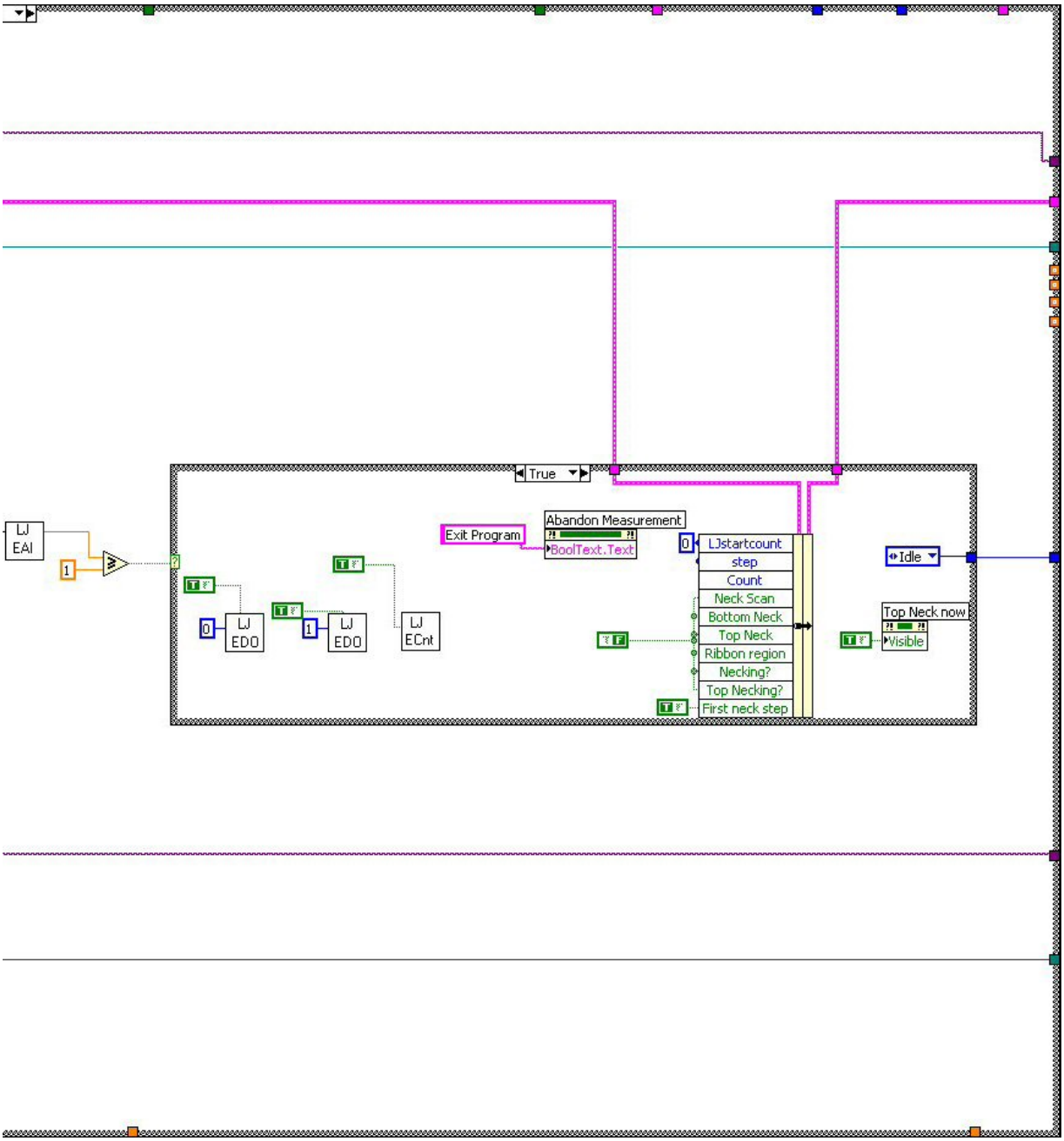

B.2.12 Exit state

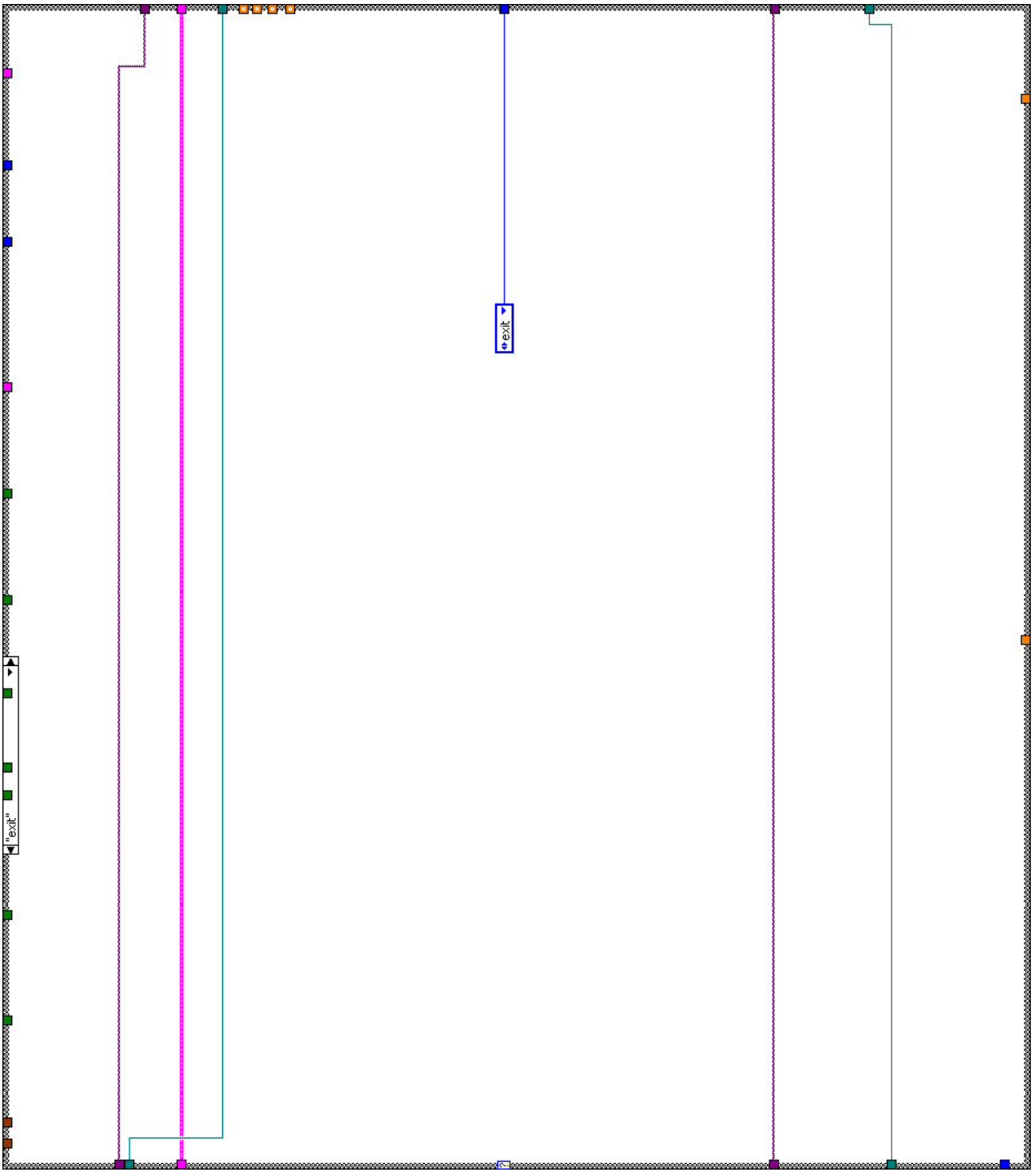

B.2.13 Live Video State

Block diagram for this state is split over the next two pages.

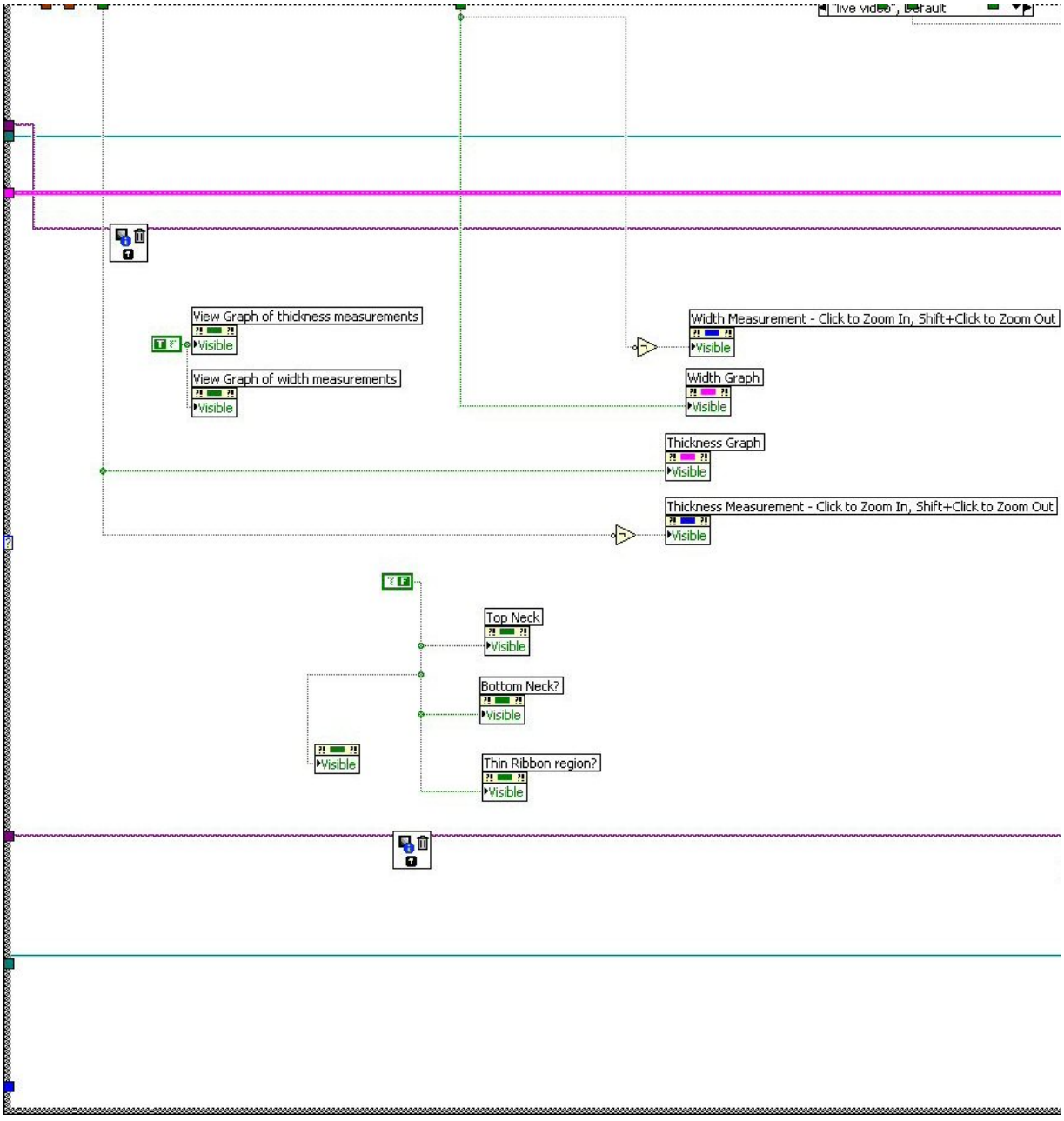
View Graph of thickness measurements
Visible
View Graph of width measurements
Visible
Width Measurement - Click to Zoom In, Shift+Click to Zoom Out
Visible
Width Graph
Visible
Thickness Graph
Visible
Thickness Measurement - Click to Zoom In, Shift+Click to Zoom Out
Visible
Top Neck
Visible
Bottom Neck?
Visible
Visible
Thin Ribbon region?
Visible

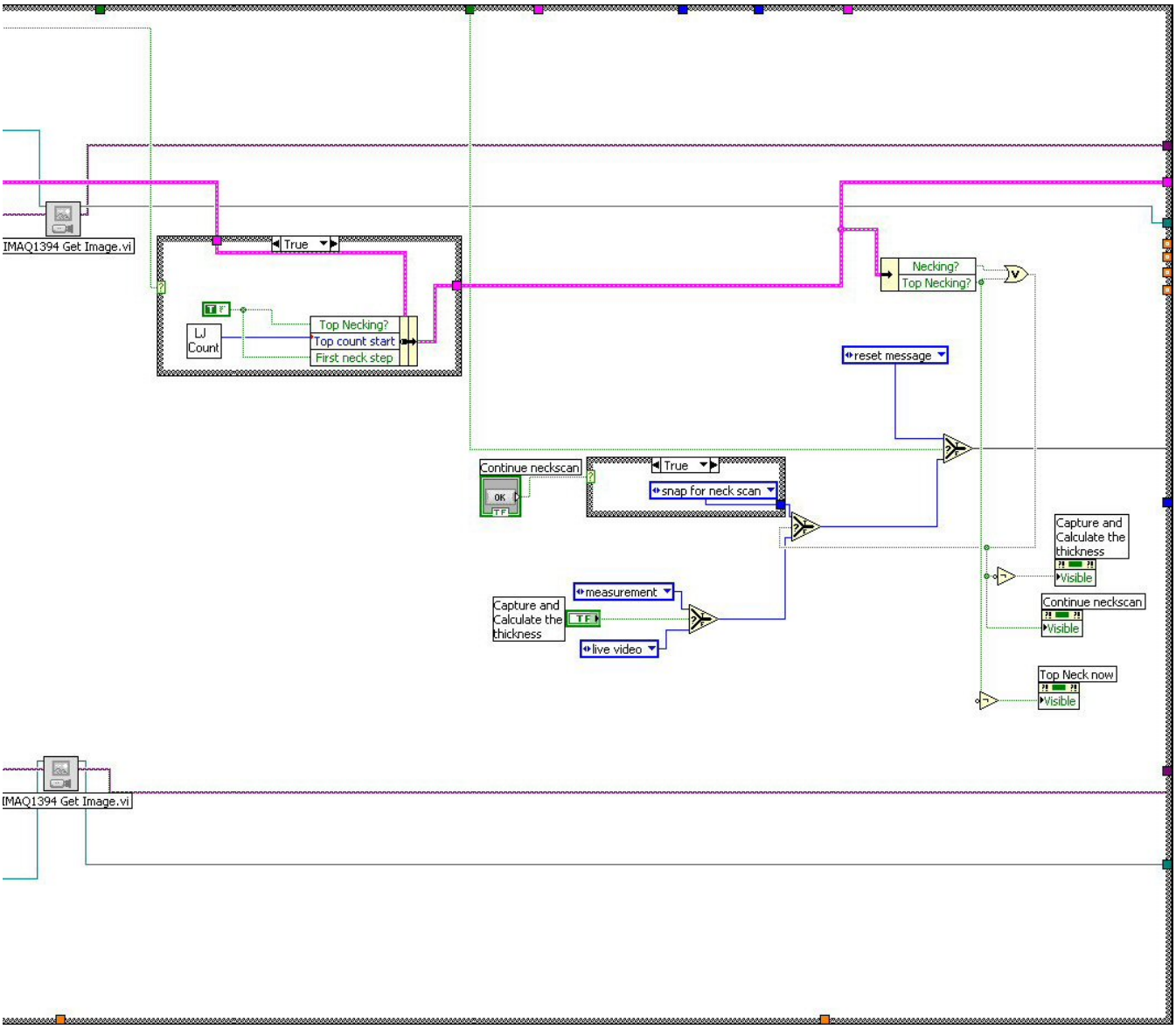
IMAQ1394 Get Image.vi
True
LJ Count
Top Necking?
Top count start
First neck step
Necking?
Top Necking?
reset message
Continue neckscan
OK
True
snap for neck scan
Capture and Calculate the thickness
measurement
live video
Capture and Calculate the thickness
Visible
Continue neckscan
Visible
Top Neck now
Visible
IMAQ1394 Get Image.vi

B.2.14 Next State

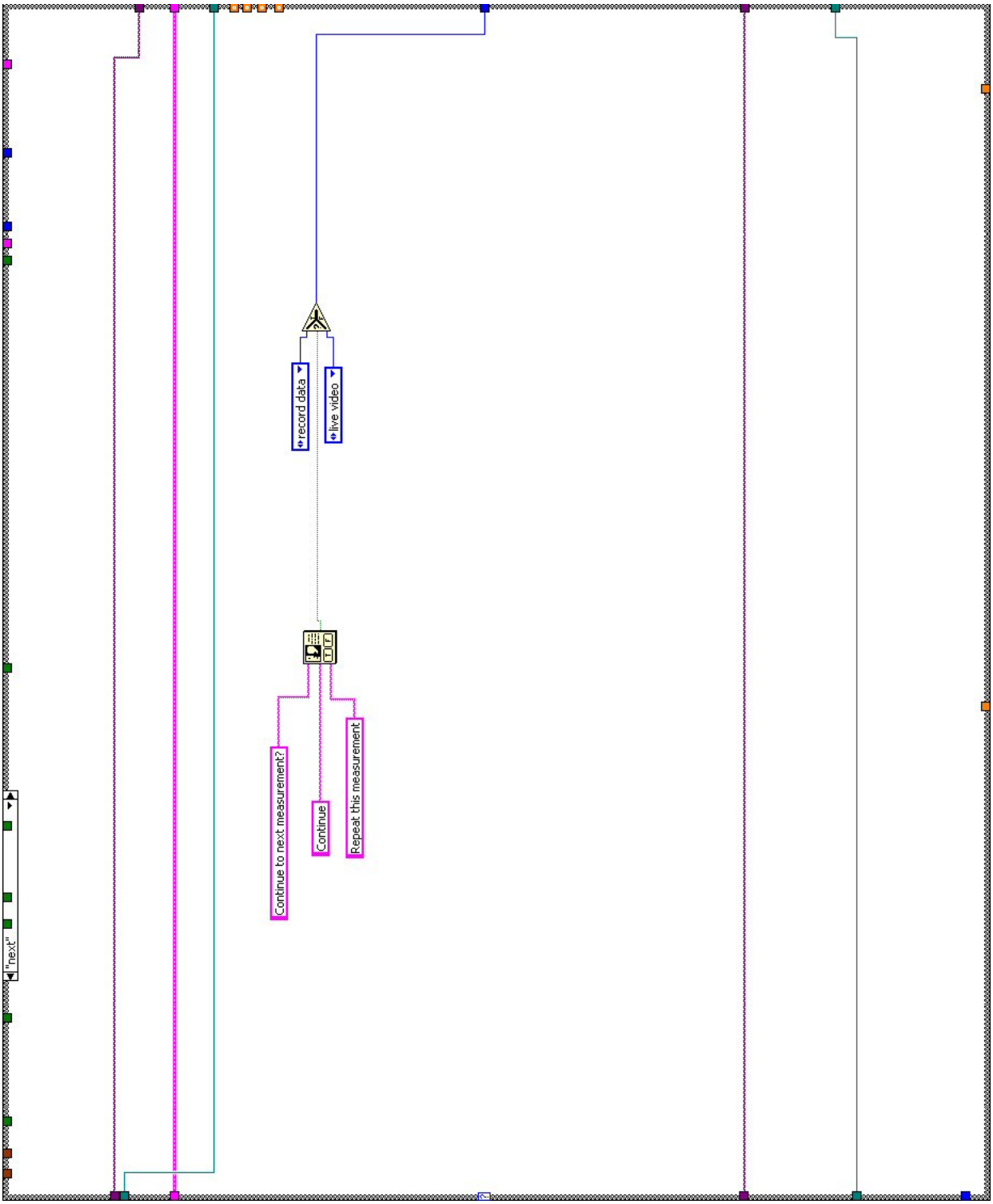

B.2.15 Record Data State

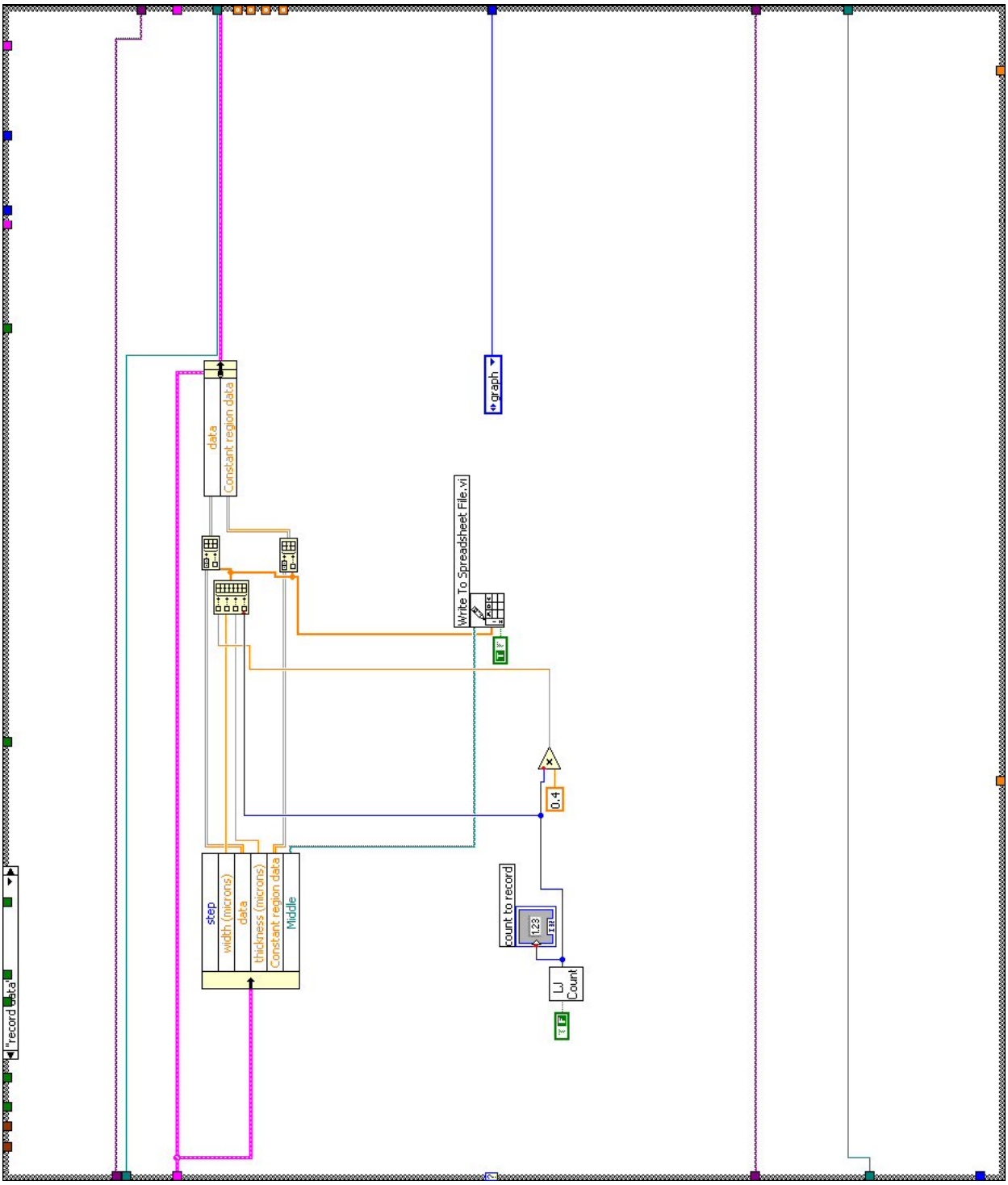

B.2.16 Graph State

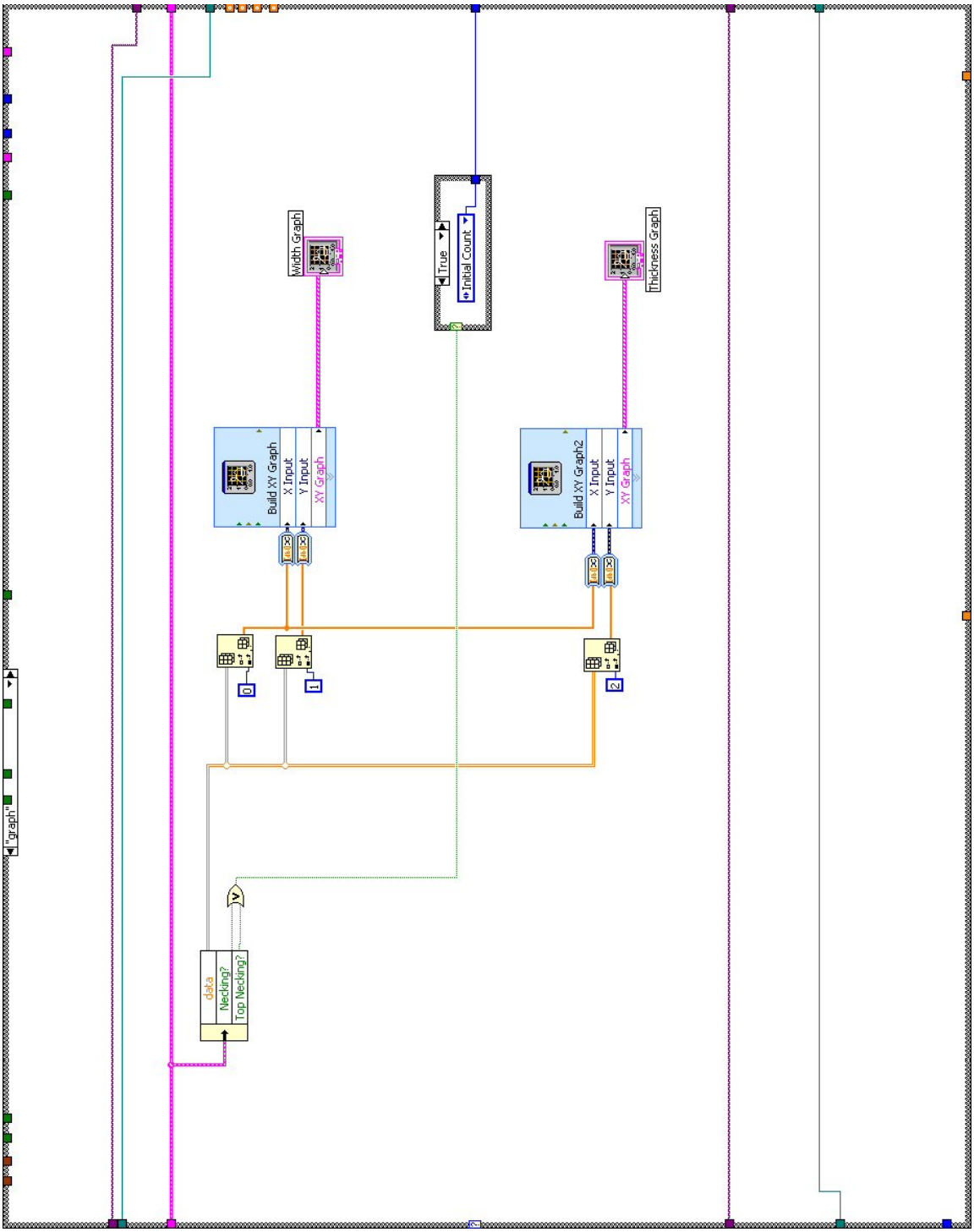

Appendix C
Installation of Ribbon Characterisation Equipment at LASTI, LIGO Test Facility

Below is photo of characterisation equipment installed at LASTI lab, Boston.

Appendix D
LabVIEW Program for Producing Command Line ANSYS Code

D.1 Front Panel

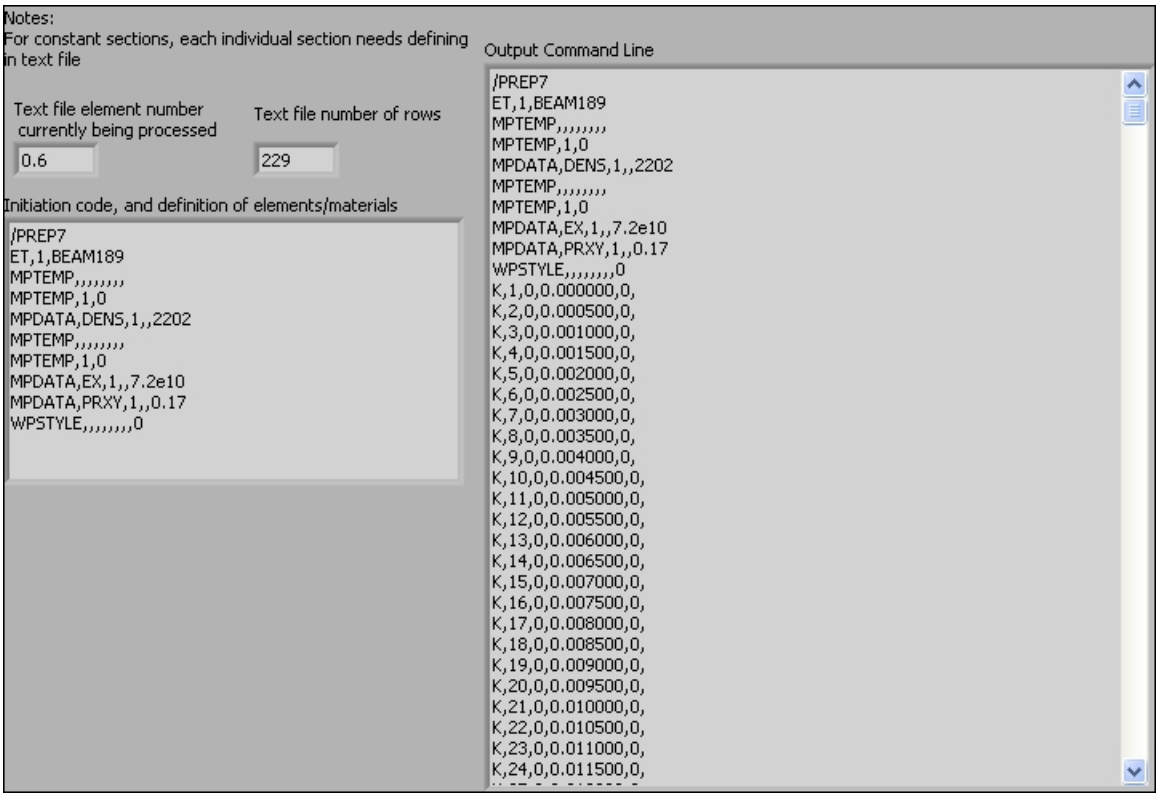

D.2 Block Diagram

Block diagram is split over the next two pages.

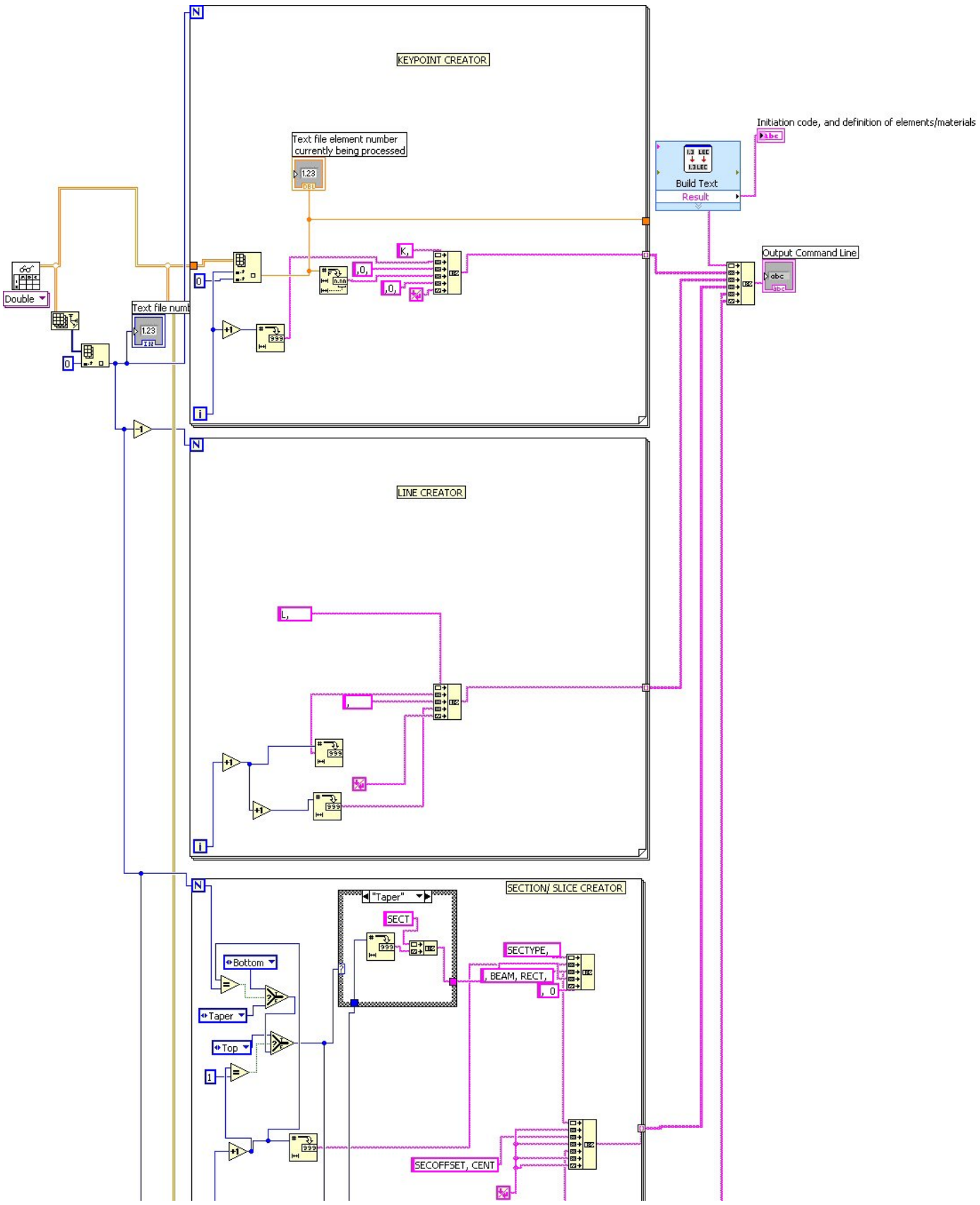
KEYPOINT CREATOR
Text file element number currently being processed
Initiation code, and definition of elements/materials
Build Text
Result
Output Command Line
Double
Text file numb
K,
,0,
,0,
LINE CREATOR
L,
,
SECTION/ SLICE CREATOR
"Taper"
SECT
Bottom
Taper
Top
SECTYPE,
, BEAM, RECT,
, 0
SECOFFSET, CENT

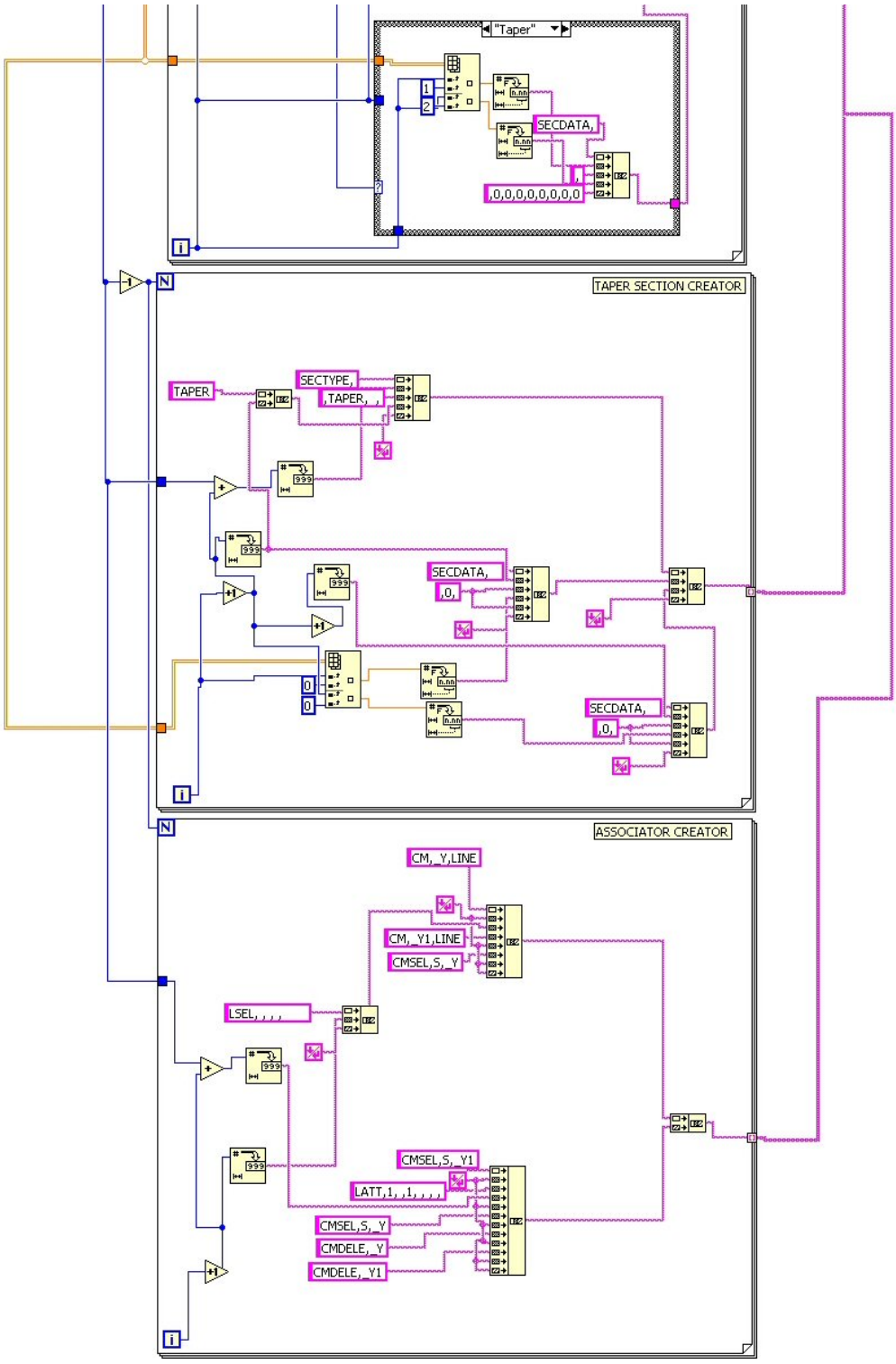
"Taper"
SECDATA,
,0,0,0,0,0,0,0,0
TAPER SECTION CREATOR
TAPER
SECTYPE,
,TAPER, ,
SECDATA,
,0,
SECDATA,
,0,
ASSOCIATOR CREATOR
CM, Y,LINE
CM, Y1,LINE
CMSEL,S, Y
LSEL, , , ,
CMSEL,S, Y1
LATT,1, ,1, , , ,
CMSEL,S, Y
CMDELE, Y
CMDELE, Y1

Appendix E
LabVIEW Exponential Voltage Decay Program

E.1 Exponential Decay Drive of Function Generator

Program uses a while loop structure.

E.1.1 Front Panel

E.1.2 Block Diagram

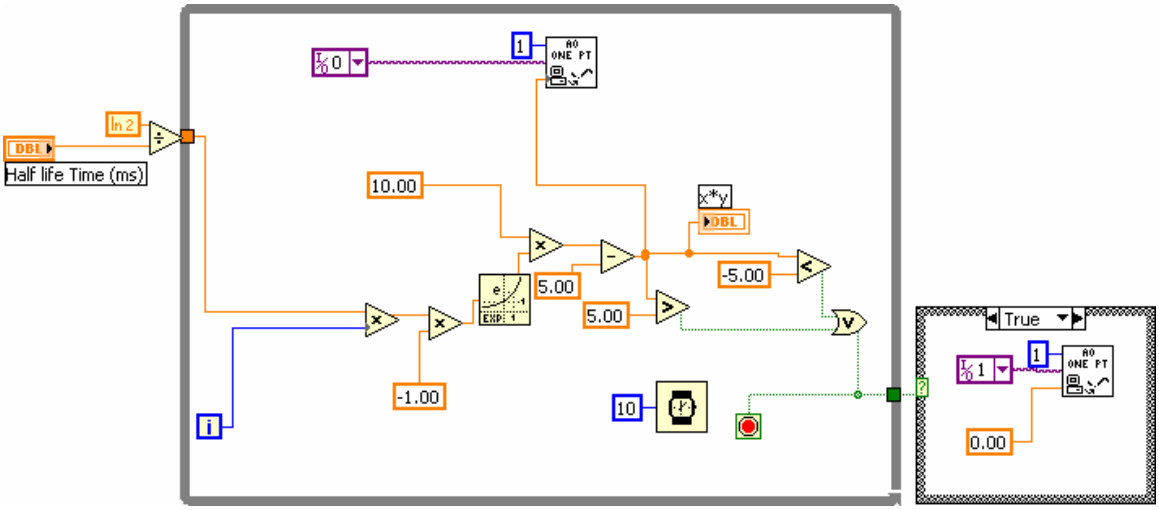

Appendix F
LabVIEW Data Acquisition and Mechanical Loss Calculation Program

F.1 Front Panel

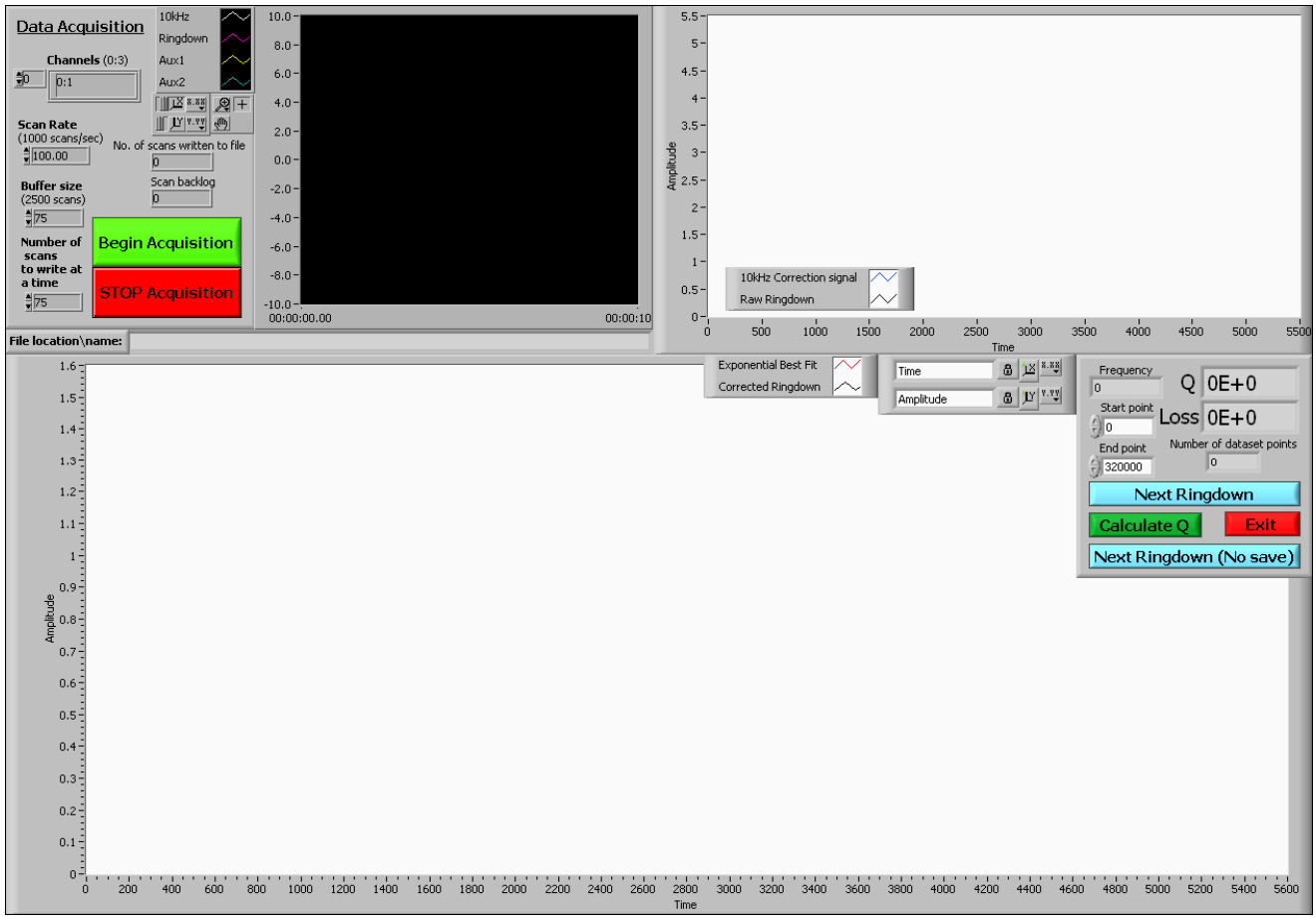

F.2 Block Diagram

F.2.1 Main Diagram and Idle State

Block diagram for this state is split over next two pages.

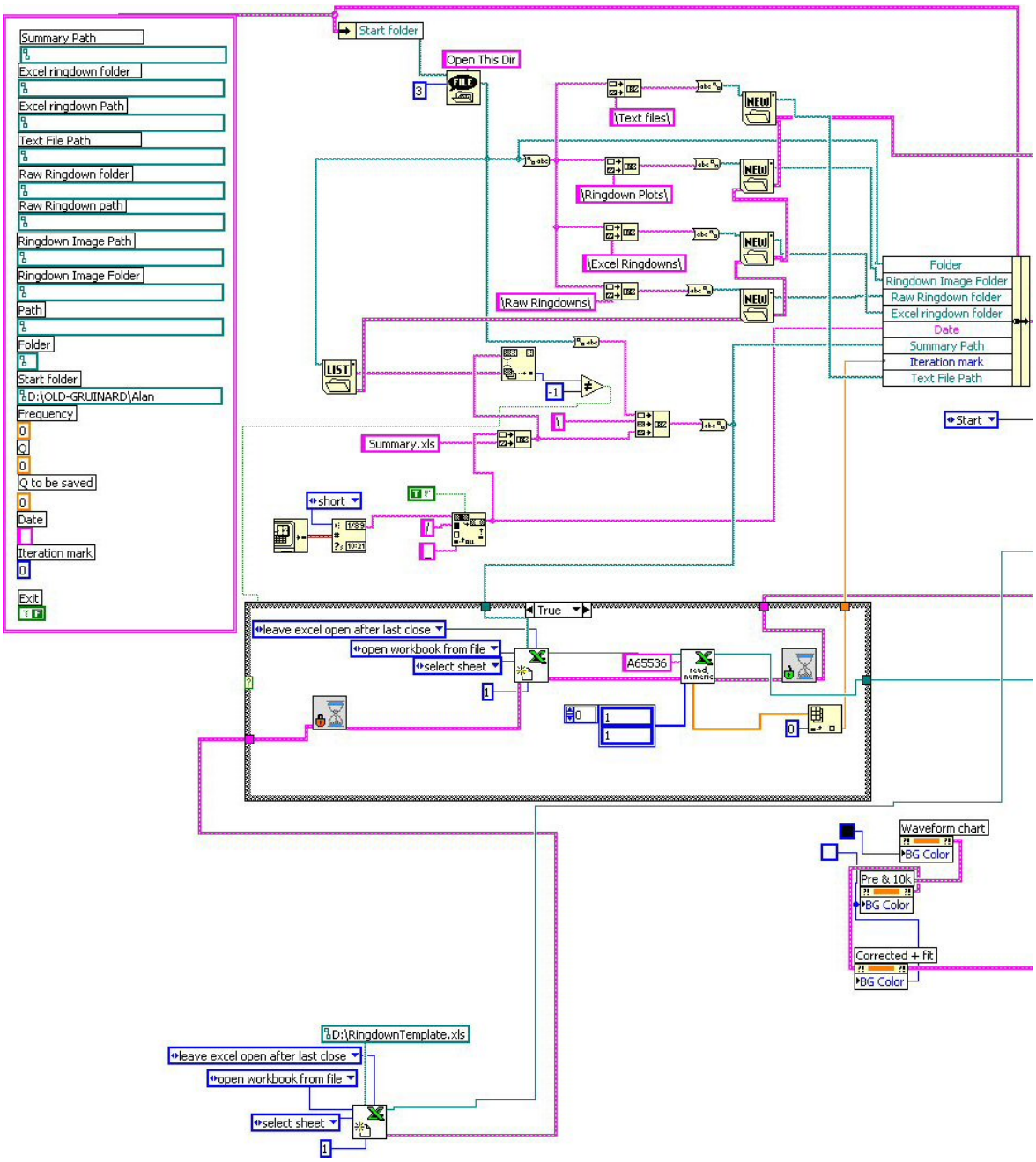

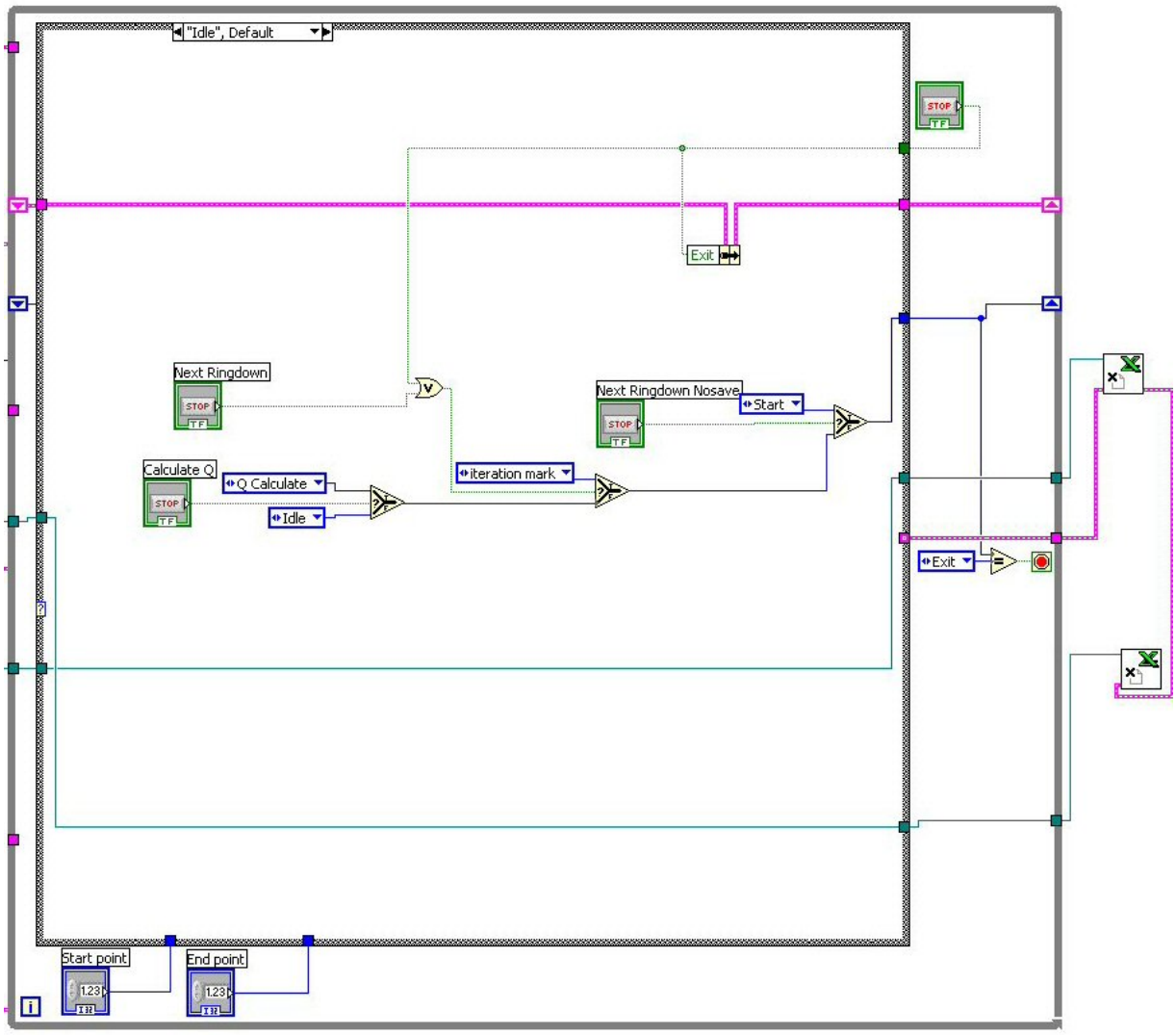
"Idle", Default
STOP
TF
Exit
Next Ringdown
Next Ringdown Nosave
Start
Calculate Q
Q Calculate
Idle
iteration mark
Exit
Start point
End point
123

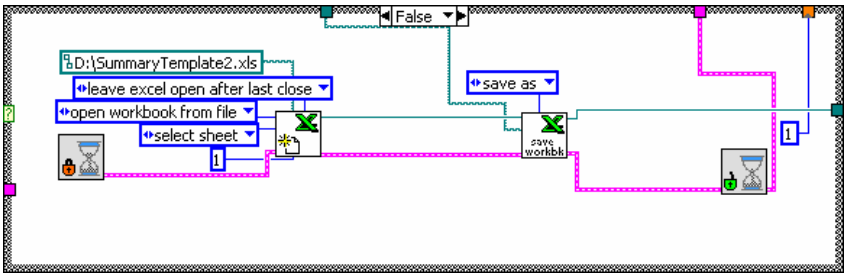
False
D:\SummaryTemplate2.xls
leave excel open after last close
open workbook from file
select sheet
save as
save workbk

F.2.2 Start State

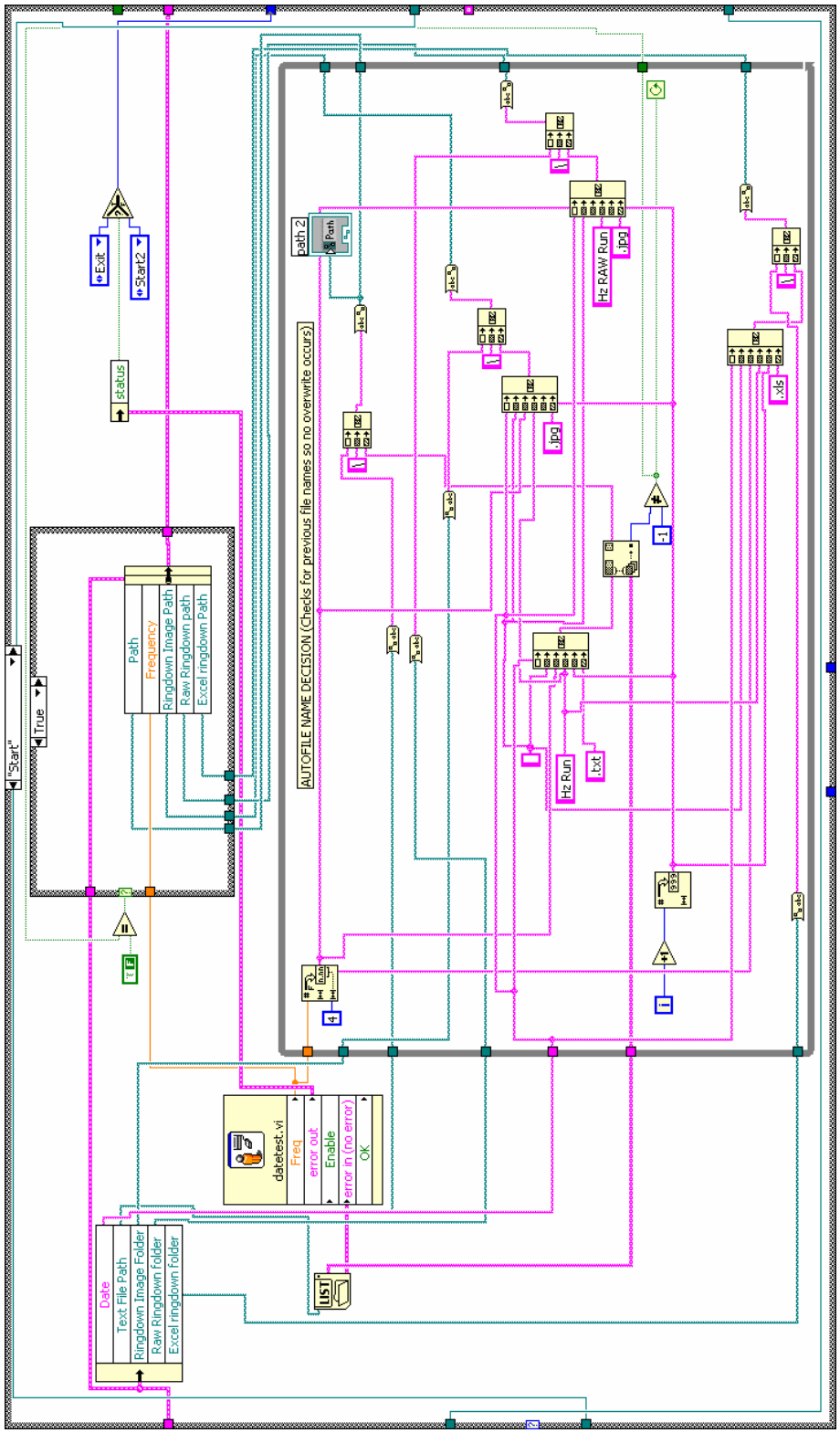

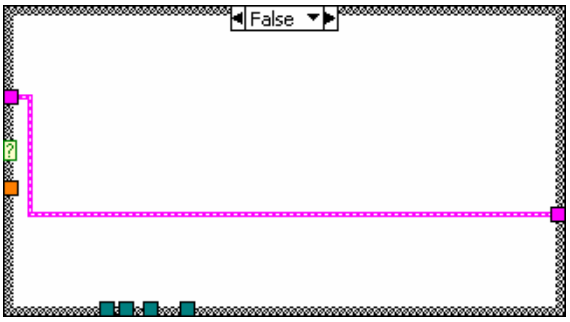

F.2.3 Data Acquisition State

State was adapted from original program written by Jenifer Lotz [108].

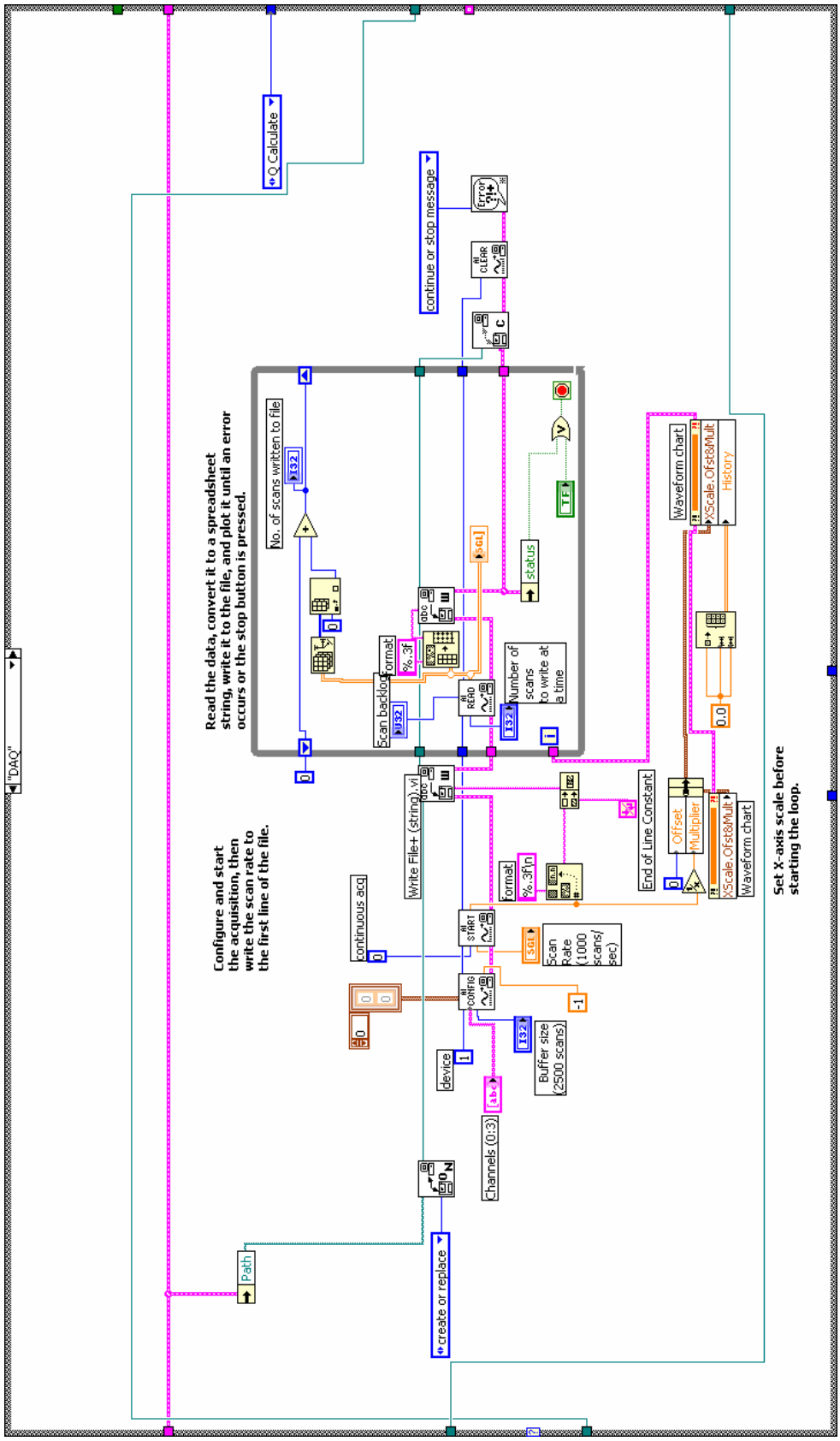
"DAQ"
Q Calculate
continue or stop message
Error
CLEAR
c
Read the data, convert it to a spreadsheet string, write it to the file, and plot it until an error occurs or the stop button is pressed.
No. of scans written to file
I32
status
TF
Scan backlog
format
%.3f
Number of scans to write at a time
READ
Write File+ (string).vi
Waveform chart
XScale.Ofst&Mult
History
0.0
End of Line Constant
Offset
Multiplier
Configure and start the acquisition, then write the scan rate to the first line of the file.
continuous acq
format
%.3f\n
START
Scan Rate (1000 scans/sec)
CONFIG
-1
device
Buffer size (2500 scans)
channels (0:3)
Path
create or replace
Set X-axis scale before starting the loop.

F.2.4 Calculation of Q Value / Mechanical Loss State

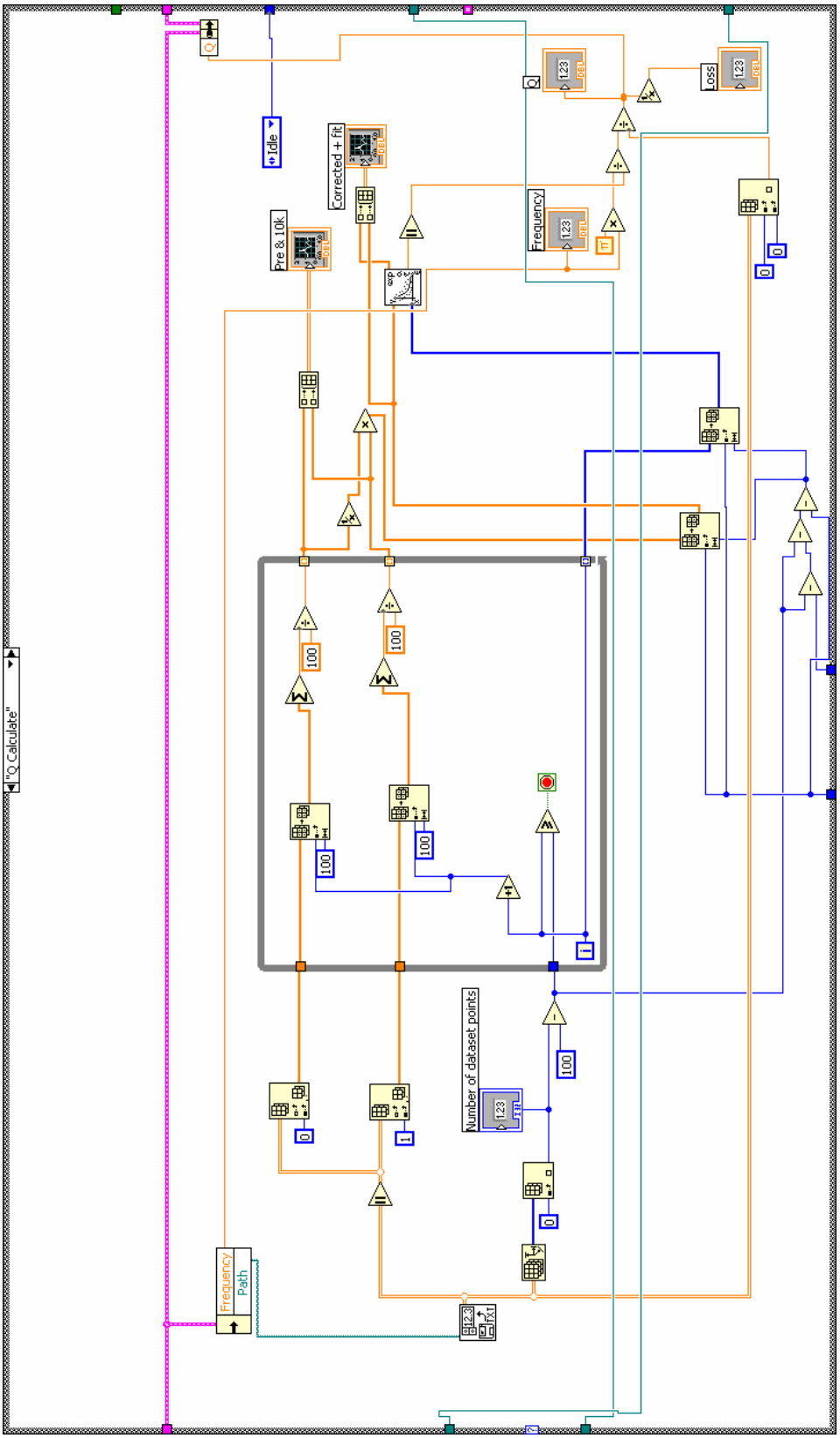

F.2.5 Iteration Mark State

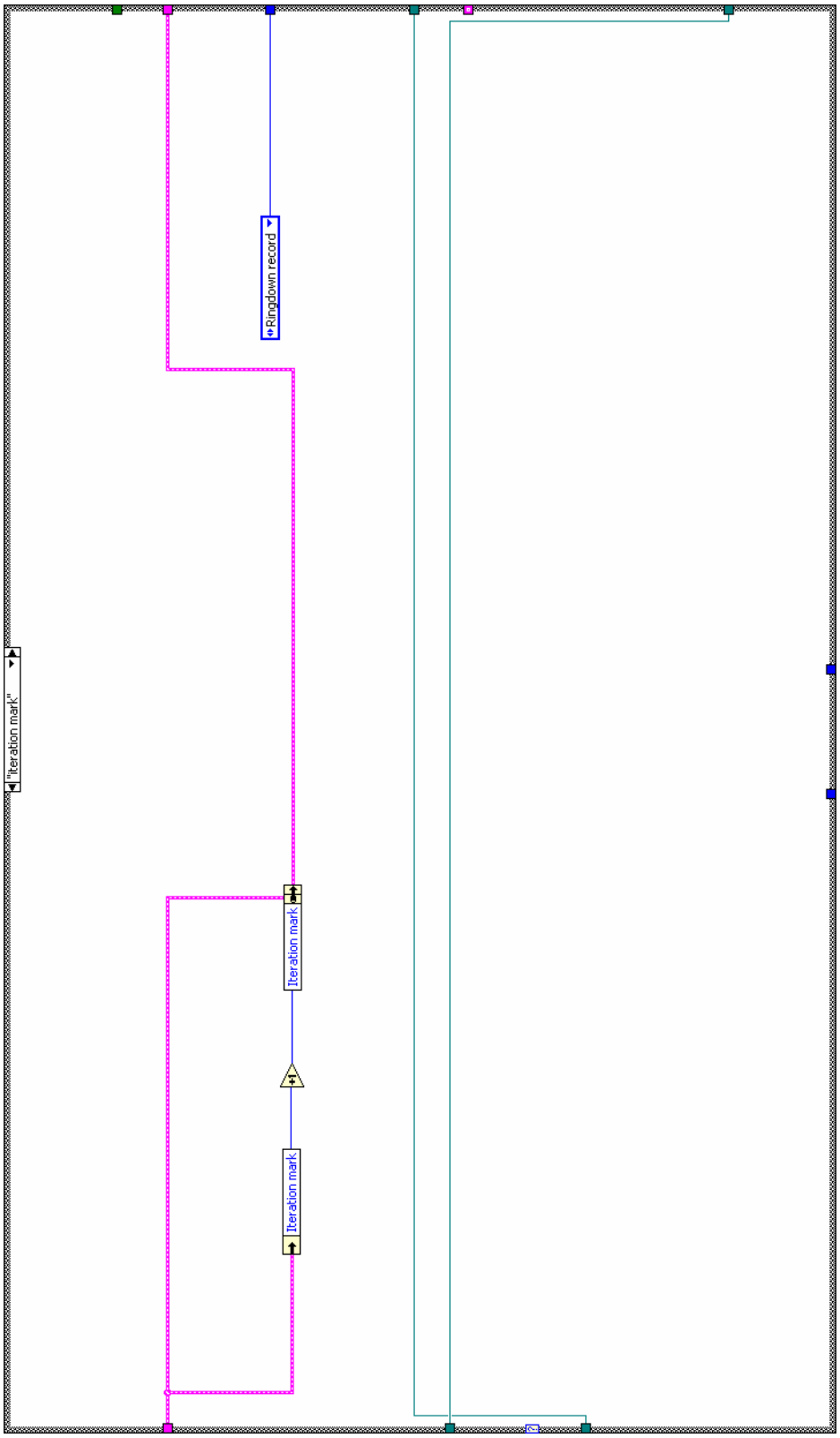

F.2.6 Recording of Ringdown State

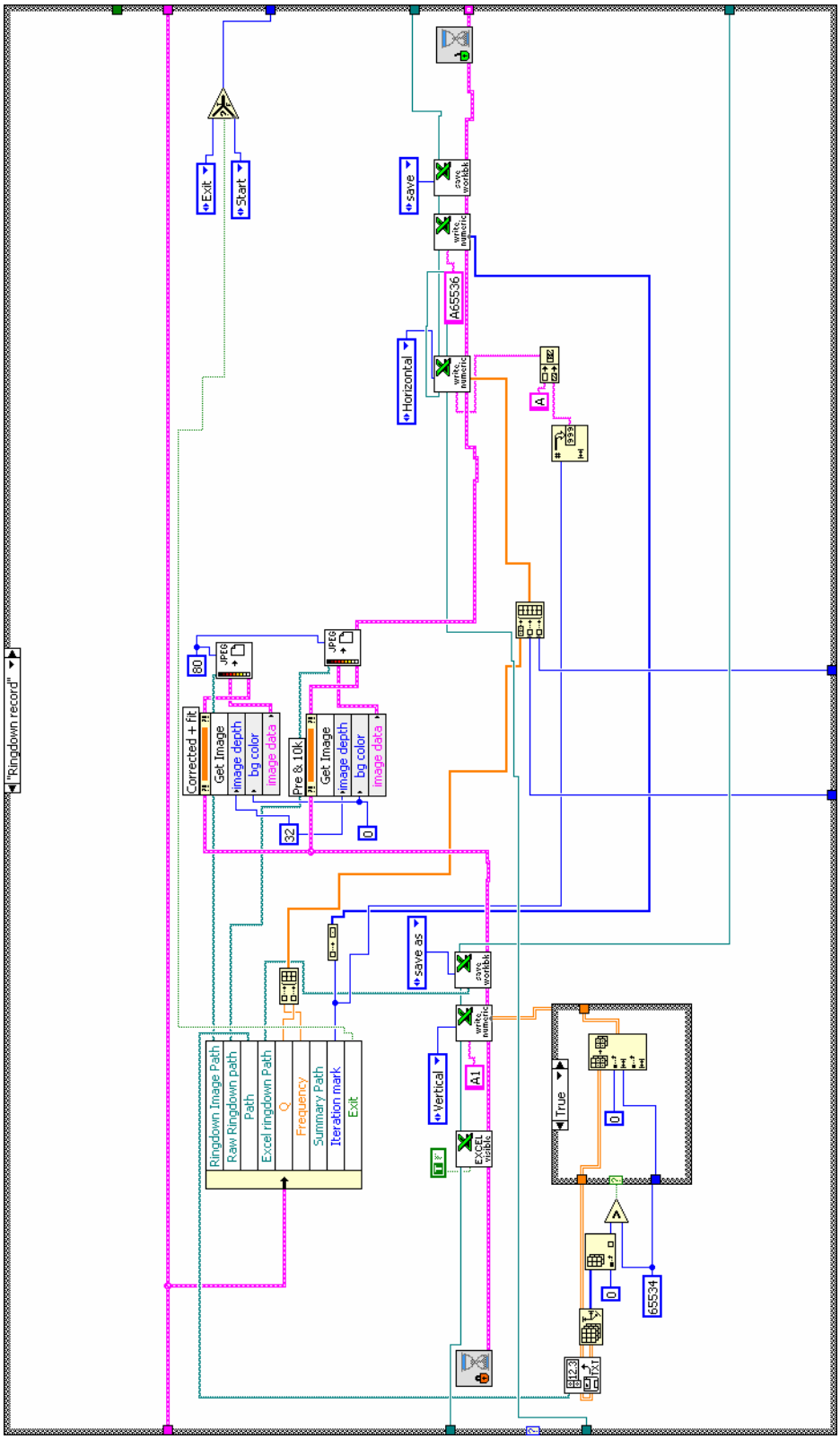

F.2.7 Start2 State

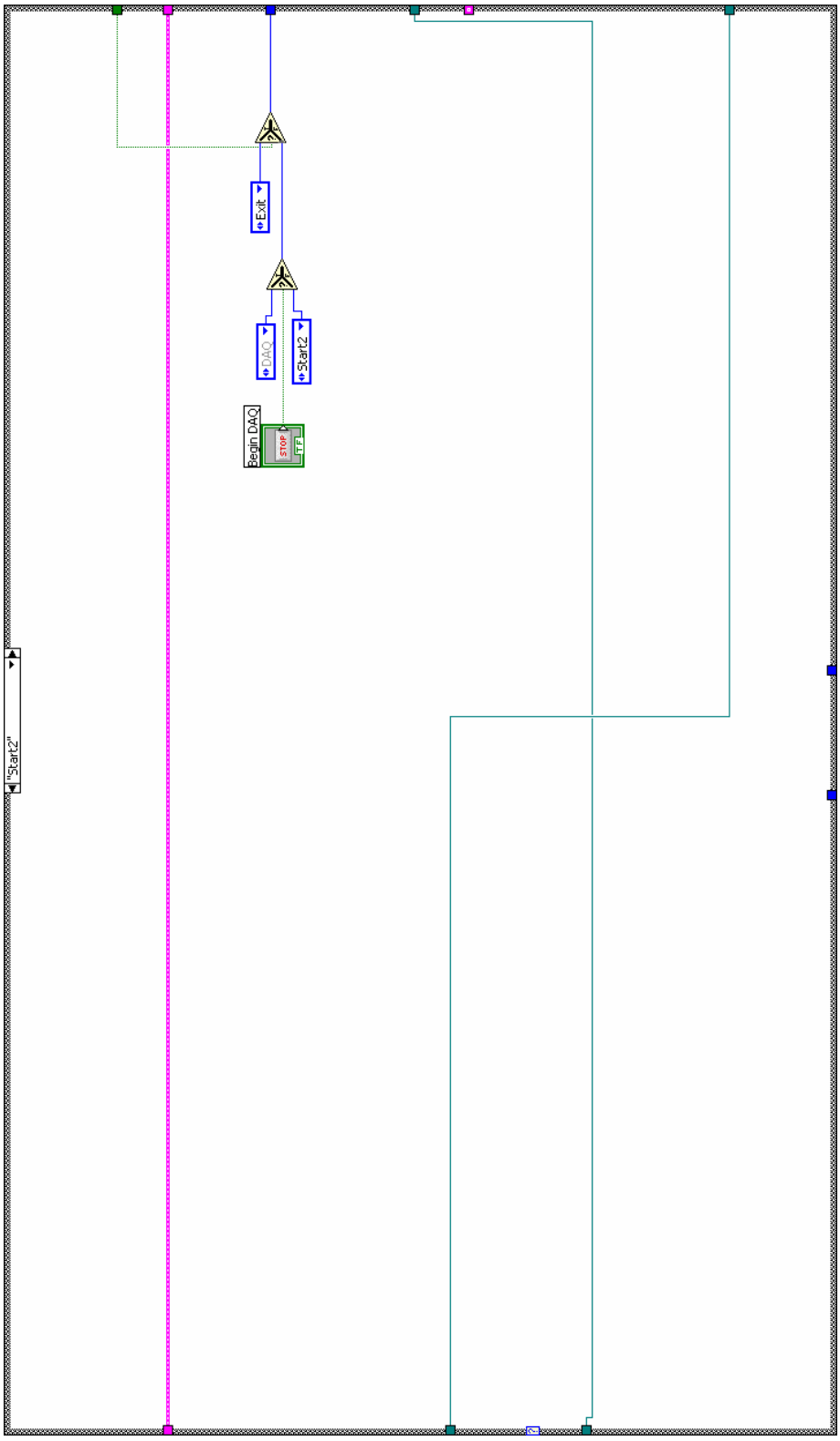

F.2.8 Exit State

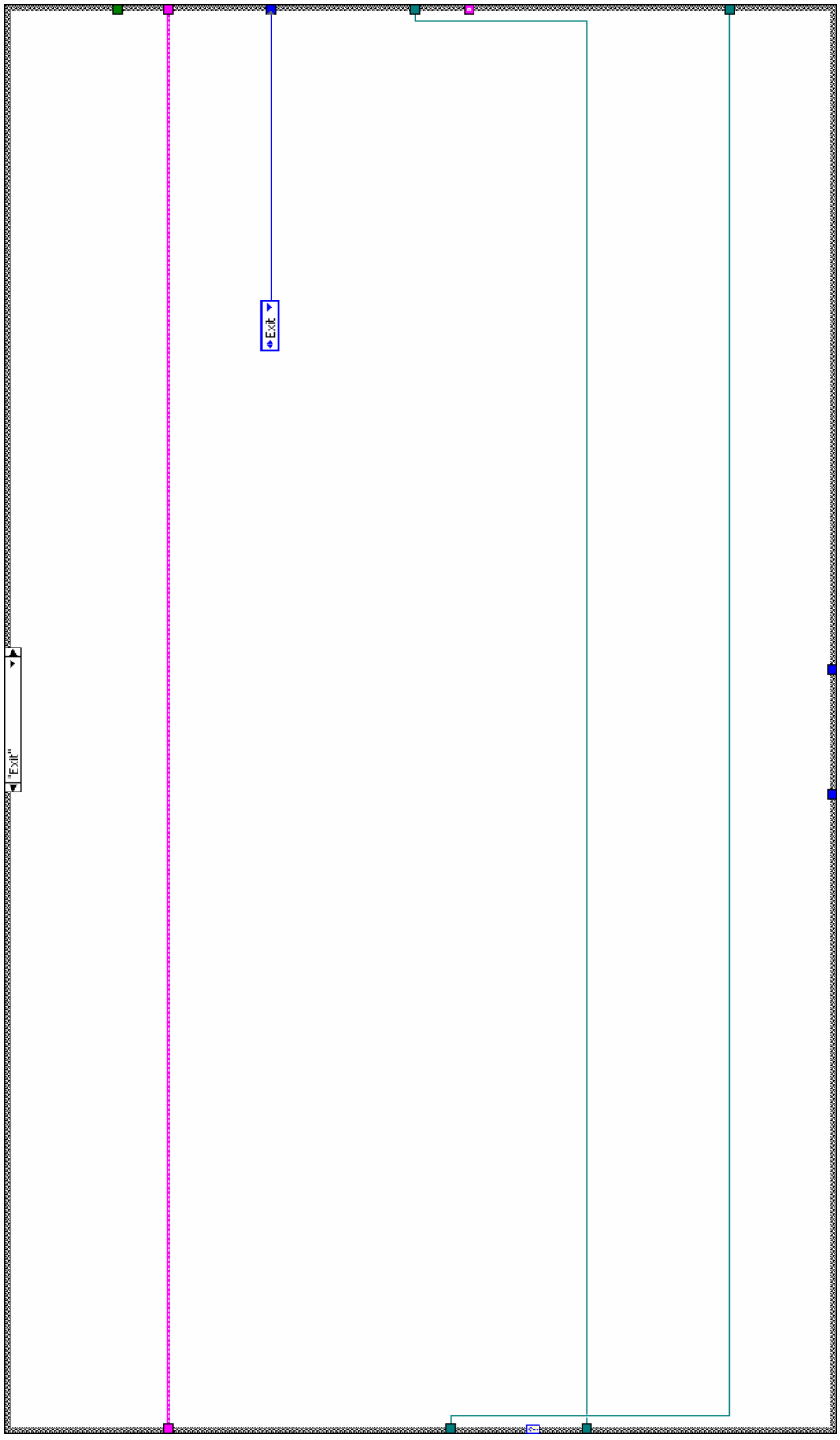

Bibliography

[1] A. Einstein, *"The Foundation of the General Theory of Relativity"*, Annalen de Physik **49**, 6769, (1916).

[2] P. R. Saulson, *"Fundamentals of Interferometric Gravitational Wave Detectors"*, World Scientific, London, (1994).

[3] R. A. Hulse, *"Discovery of a pulsar in a binary system"*, The Astrophysical Journal **195**, L51, (1975).

[4] R. A. Hulse, *"The discovery of the binary pulsar"*, Reviews of Modern Physics **66**, 699, (1994).

[5] J. H. Taylor, *"Binary Pulsars and relativistic gravity"*, Reviews of Modern Physics **66**, 711, (1994).

[6] J. M. Weisberg and J. H. Taylor, *"Relativistic Binary Pulsar B1913+16: Thirty Years of Observations and Analysis"*, Astronomical Society of the Pacific Conference Series **328, Binary Radio Pulsars**, 25, (2004).

[7] M. Kramer, et al., *"Tests of General Relativity from Timing the Double Pulsar"*, Science **314**, 97, (2006).

[8] J. Tyson and R. Gifford, *"Gravitational-Wave Astronomy"*, Annual Review of Astronomy and Astrophysics **16**, 521, (1978).

[9] J. Weber, *"Evidence for discovery of gravitational radiation"*, Physical Review Letters **22**, 1320, (1969).

[10] R. W. P. Drever, *"Search for Short Bursts of Gravitational Radiation"*, Nature **246**, 340, (1973).

[11] J. Hough, *"Search for continuous gravitational radiation"*, Nature **254**, 498, (1975).

[12] V. Vali and R. C. Bostrom, *"Some Earth strain observations with a thousand meter laser interferometer"*, Earth and Planetary Science Letters **4**, 436, (1968).

[13] V. Vali and R. C. Bostrom, *"One Thousand Meter Laser Interferometer"*, Review of Scientific Instruments **39**, 1304, (1968).

[14] S. Chandrasekhar, *"Stellar configurations with degenerate cores"*, The Observatory **57**, 373, (1934).

[15] S. E. Woosley and A. Heger, *"The evolution and explosion of massive stars"*, Reviews of Modern Physics **74**, 1015, (2002).

[16] C. Cutler and K. S. Thorne, *"An Overview of Gravitational-Wave Sources"*, arXiv:gr-qc/0204090, (2002).

[17] B. F. Schutz, *"Gravitational-wave sources"*, Classical and Quantum Gravity **13**, A213, (1996).

[18] E. Muller, et al., *"Toward gravitational wave signals from realistic core-collapse supernova models"*, the Astrophysical Journal **603**, 221, (2004).

[19] B. F. Schutz, *"Determining the Hubble constant from gravitational wave observations"*, Nature **323**, 310, (1986).

[20] K. S. Thorne, in *Proceedings of the Snowmass 95 Summer Study on Particle and Nuclear Astrophysics and Cosmology*, 1995).

[21] R. V. Wagoner, *"Gravitational radiation from accreting neutron stars"*, The Astrophysical Journal **278**, 345, (1984).

[22] J. Weber, *"Detection and Generation of Gravitational Waves"*, Physical Review **117**, 306, (1960).

[23] J. Weber, *"Observations of the thermal fluctuations of a gravitational-wave detector"*, Physical Review Letters **17**, 1228, (1966).

[24] J. Weber, *"Gravitational-wave-detector events"*, Physical Review Letters **20**, 1307, (1968).

[25] J. Weber, *"Anisotropy and Polarization in the gravitational-radiation experiments"*, Physical Review Letters **25**, 180, (1970).

[26] J. L. Levine, *"Absence of Gravity-Wave signals in a bar at 1695 Hz"*, Physical Review Letters **31**, 173, (1973).

[27] P. Astone, *"Long-term operation of the Rome "Explorer" cryogenic gravitational wave detector"*, Physical Review D **47**, 362, (1993).

[28] P. Astone, *"Increasing the Bandwidth of Resonant Gravitational Antennas: The case of Explorer"*, Physical Review Letters **91**, 111101, (2003).

[29] P. Astone, *"The next science run of the gravitational wave detector NAUTILUS"*, Classical and Quantum Gravity **19**, 1911, (2002).

[30] A. d. Waard, *"MiniGRAIL, the first spherical detector"*, Classical and Quantum Gravity **20**, S143-S151, (2003).

[31] A. d. Waard, *"Preparing for science run 1 of MiniGRAIL"*, Classical and Quantum Gravity **23**, S79, (2006).

[32] A. d. Waard, *"Cooling down MiniGRAIL to milli-Kelvin temperatures"*, Classical and Quantum Gravity **21**, S465, (2004).

[33] M. Cerdonio, *"The ultracryogenic gravitational-wave detector AURIGA"*, Classical and Quantum Gravity **14**, 1491, (1997).

[34] F. Acernese, *"First joint Gravitational Waves search by the AURIGA-EXPLORER-NAUTILUS-Virgo collaboration"*, arXiv:0710.3752v1 [gc-qc], (2007).

[35] L. Baggio, *"A joint search for gravitational wave bursts with AURIGA and LIGO"*, Classical and Quantum Gravity **25**, 095004, (2008).

[36] M. Bassan, *"A new capacitive read-out for EXPLORER and NAUTILUS"*, Journal of Physics: Conference Series **32**, 89, (2006).

[37] M. Cerdonio, *"Wideband Dual Sphere Detector of Gravitational Waves"*, Physical Review Letters **87**, 031101, (2001).

[38] M. Cerdonio, Private communication, (2007).

[39] M. E. Gertsenshtein and V. I. Pustovoit, Soviet Physics JETP **16**, 433, (1962).

[40] R. L. Forward, *"Wideband laser-interferometer gravitational-radiation experiment"*, Physical Review D **17**, 379, (1978).

[41] A. A. Michelson, *"On the Relative Motion of the Earth and the Luminiferous Ether"*, The American Journal of Science **34**, 333, (1887).

[42] D. Herriott, *"Off-Axis Paths in Spherical Mirror Interferometers"*, Applied Optics **3**, 523, (1964).

[43] B. J. Meers, *"Recycling in laser-interferometric gravitational-wave detectors"*, Physical Review D **38**, 2317, (1988).

[44] K. A. Strain, *"Experimental Demonstration of Dual Recycling for Interferometric Gravitational-Wave Detectors"*, Physical Review Letters **66**, 1391, (1991).

[45] K. A. Strain, *"Sensing and control in dual-recycling laser interferometer gravitational-wave detectors"*, Applied Optics **42**, (2003).

[46] W. A. Edelstein, *"Limits to the measurement of displacement in an interferometric gravitational radiation detector"*, Journal of Physics E: Scientific Instruments **11**, 710, (1978).

[47] J. Hough, *"Prospects for gravitational wave detection with laser interferometer detectors"*, Proceedings of the fifth Marcel Grossmann meeting on General Relativity, p265, (1989).

[48] C. M. Caves, *"Quantum-Mechanical Radiation-Pressure Fluctuations in an interferometer"*, Physical Review Letters **45**, 75, (1980).

[49] C. M. Caves, *"Quantum-mechanical noise in an interferometer"*, Physical Review D **23**, 1693, (1981).

[50] R. Loudon, *"Quantum Limit on the Michelson Interferometer used for Gravitational-Wave Detection"*, Physical Review Letters **47**, 815, (1981).

[51] V. B. Braginsky, *"Nonlinear meter for the gravitational wave antenna"*, Physics Letters A **218**, 167, (1996).

[52] V. B. Braginsky, *"Optical bars in gravitational wave antenna"*, Physics Letters A **232**, 340, (1997).

[53] J. Hough, *"The search for gravitational waves"*, Journal of Physics B: Atomic, Molecular and Optical Physics **38**, S497, (2005).

[54] *"LIGO II Suspension: Reference Designs"*, LIGO Technical Document T000012, (2000).

[55] N. A. Robertson, *"Advanced LIGO Suspension System Conceptual Design"*, LIGO Technical Document T010103, (2006).

[56] P. R. Saulson, *"Terrestrial gravitational noise on a gravitational wave antenna"*, Physical Review D **30**, 732, (1984).

[57] S. A. Hughes, *"Seismic gravity-gradient noise in interferometric gravitational-wave detectors"*, Physical Review D **58**, 122002, (1998).

[58] V. B. Braginsky, *"Thermo-refractive noise in gravitational wave antennae"*, Physics Letters A **271**, 303, (2000).

[59] www.geo600.uni-hannover.de/geocurves/.

[60] http://www.geo600.uni-hannover.de/geocurves/files/theoretical/all˙250˙v4.png.

[61] H. Billing, *"An argon laser interferometer for the detection of gravitational radiation"*, Journal of Physics E: Scientific Instruments **12**, (1979).

[62] R. W. P. Drever, *"Gravitational wave detectors"*, Proceedings of Royal Society London A **368**, 11, (1979).

[63] D. I. Robertson, *"The Glasgow 10m prototype laser interferometric gravitational wave detector"*, Review of Scientific Instruments **66**, 4447, (1995).

[64] A. Abramovici, *"Improved sensitivity in a gravitational wave interferometer and implications for LIGO"*, Physics Letters A **218**, 157, (1996).

[65] http://www.ligo.caltech.edu/~jzweizig/distribution/LSC_Data/.

[66] B. Willke, *"The GEO 600 Gravitational wave detector"*, Classical and Quantum Gravity **19**, 1377, (2002).

[67] H. Lück, *"Status of the Gravitational-Wave Detector GEO600"*, LIGO Document P070061, (2007).

[68] C. Bradashia, *"The VIRGO project: a wide band antenna for gravitational wave detection"*, Nuclear Instruments and Methods in Physics Research **A289**, 518, (1990).

[69] F. Acernese, *"The Virgo 3 km interferometer for gravitational wave detection"*, Journal of Optics A: Pure Applied Optics **10**, 064009, (2008).

[70] S. Braccini and e. al, *"Measurement of the seismic attenuation performance of the VIRGO Superattenuator"*, Astroparticle Physics **23**, 557, (2005).

[71] F. Acernese, *"Results of the Virgo central interferometer commissioning"*, Classical and Quantum Gravity **21**, S395, (2004).

[72] http://wwwcascina.virgo.infn.it/MonitoringWeb/General/archive/VSR1/.

[73] G. Heinzel, *"Status and first results of TAMA300"*, Classical and Quantum Gravity **18**, 4113, (2001).

[74] M. Ando, *"Current status of TAMA"*, Classical and Quantum Gravity **19**, 1409, (2002).

[75] R. Takahashi, *"Status of TAMA300"*, Classical and Quantum Gravity **21**, S403, (2004).

[76] O. Puncken, *"Status of the advanced LIGO laser"*, LIGO Document G080230, (2008).

[77] R. Abbott, *"Seismic isolation enhancements for initial and Advanced LIGO"*, Classical and Quantum Gravity **21**, S915, (2004).

[78] B. Willke, *"The GEO-HF project"*, Classical and Quantum Gravity **23**, S207, (2006).

[79] R. Flaminio, *"Advanced VIRGO White Paper"*, (2005).

[80] M. Punturo, *"ET: Einstein Telescope"*, ILIAS General meeting, Jaca, (2008).

[81] J. E. Faller, in *Proceedings of Colloquium "Kilometric Optical Arrays in Space"*, Corsica, 1984).

[82] K. Danzmann, *"LISA-an ESA cornerstone mission for a gravitational wave observatory"*, Classical and Quantum Gravity **14**, 1399, (1997).

[83] K. Danzmann, *"LISA technology-concept, status and prospects"*, Classical and Quantum Gravity **20**, S1, (2003).

[84] R. Brown, *"Microscopical observations on the particles contained in the pollen of plants"*, Edinburgh new Philosophical Journal, 358, (1828).

[85] A. Einstein, *"Investigations on the theory of the Brownian Movement"*, Annalen de Physik **17**, 549, (1905).

[86] A. Einstein, *"The elementary theory of the Brownian motion"*, Zeit für Electrochemie **14**, 235, (1908).

[87] H. B. Callen, *"Irreversibility and Generalised Noise"*, Physical Review **83**, 34, (1951).

[88] H. B. Callen, *"On a Theorem of Irreversible Thermodynamics"*, Physical Review **86**, 702, (1952).

[89] P. R. Saulson, *"Thermal noise in mechanical experiments"*, Physical Review D **42**, 2437, (1990).

[90] H. J. Pain, *"The Physics of Vibrations and Waves"*, Wiley, New York, (2000).

[91] S. Rowan, *"The quality factor of natural fused quartz ribbons over a frequency range from 6 to 160 Hz"*, Physics Letters A **227**, 153, (1997).

[92] C. Zener, *"Elasticity and anelasticity of metals"*, University of Chicago Press, (1948).

[93] A. L. Kimball, *"Internal friction in solids"*, Physical Review **30**, 948, (1927).

[94] C. Zener, *"Internal Friction in Solids"*, Physical Review **52**, 230, (1937).

[95] A. Nowick and B. Berry, *"Anelastic Relaxation in Crystalline Solids"*, Academic Press, London, (1972).

[96] V. B. Braginsky, "*Thermodynamical fluctuations and photo-thermal shot noise in gravitational wave antennae*", Physics Letters A **264**, 1, (1999).

[97] Y. T. Lui, "*Thermoelastic noise and homogeneous thermal noise in finite sized gravitational-wave test masses*", Physical Review D **62**, 122002, (2000).

[98] A. D. Gillespie, "*Thermal Noise in the Initial LIGO Interferometers*", Phd Thesis, (1995).

[99] Y. Levin, "*Internal thermal noise in the LIGO test masses: A direct approach*", Physical Review D **57**, 659, (1998).

[100] H. Young and R. Freedman, "*University Physics*", Addison-Wesley, New York, (2000).

[101] A. Gillespie and F. Raab, "*Thermal noise in the test mass suspensions of a laser interferometer gravitational-wave detector prototype*", Physics Letters A **178**, 357, (1993).

[102] E. Gustafson, "*LSC White Paper on Detector Research and Development*", LIGO Document T990080, (1999).

[103] S. Hild, "*Measurement of a low-absorption sample of OH-reduced fused silica*", Applied Optics **45**, 7269, (2006).

[104] S. D. Penn, "*Frequency and surface dependence of the mechanical loss in fused silica*", Physics Letters A **352**, 3, (2006).

[105] S. Reid, "*Studies of materials for future ground-based and space-based interferometric gravitational wave detectors*", Phd Thesis, (2006).

[106] P. Murray, "*Measurement of the Mechanical Loss of Test Mass Materials for Advanced Gravitational Wave Detectors*", Phd Thesis, (2007).

[107] S. Rowan, "*Investigation of mechanical loss factors of some candidate materials for the test masses of gravitational wave detectors*", Physics Letters A **265**, 5, (2000).

[108] P. Sneddon, "*Investigations of Internal Mechanical Loss Factors of Test Mass Materials for Interferometric Gravitational Wave Detectors*", Phd Thesis, (2001).

[109] M. Fine, "*Low-Temperature Internal Friction and Elasticity Effects in Vitreous Silica*", Journal of Applied Physics **25**, 402, (1953).

[110] A. Schroeter, "*On the mechanical quality factors of cryogenic test masses from fused silica and crystalline quartz*", arXiv:0709.4359v1 [gr-qc], (2007).

[111] T. Uchiyama, *"Mechanical quality factor of a cryogenic sapphire test mass for gravitational wave detectors"*, Physics Letters A **261**, 5, (1999).

[112] T. Uchiyama, *"Mechanical quality factor of a cryogenic sapphire test mass for gravitational wave detectors"*, Physics Letters A **261**, 5, (1999).

[113] R. W. P. Drever, *"Some new concepts for laser interferometer gravitational wave detectors"*, Moriond Workshop on Dark Matter and Cosmology, Quantum measurements and Experimental Gravitation, (1996).

[114] D. Rugar, *"Force Detection of Nuclear Magnetic Resonance"*, Science **264**, 1560, (1994).

[115] S. Reid, *"Mechanical dissipation in silicon flexures"*, Physics Letters A **351**, 205, (2005).

[116] R. Frey, *"LIGO: Status and Recent Results"*, C2CR07 proceedings, LIGO Document P070079-01-Z, (2007).

[117] http://geo600.aei.mpg.de/general-information/technical-principles/sensitivity/image/image˙view˙fullscreen.

[118] R. Adhikari, *"Enhanced LIGO"*, LIGO Technical Note T060158, (2006).

[119] S. Kawamura, *"Suspension Design Requirements"*, LIGO Document T950011, (1996).

[120] G. Cagnoli, *"Low-frequency internal friction in clamped-free thin wires"*, Physics Letters A **255**, 230, (1999).

[121] A. Gretarsson, *"Dissipation of mechanical energy in fused silica fibers"*, Review of Scientific Instruments **70**, 4081, (1999).

[122] A. Gillespie, *"Suspension losses in the pendula of laser interferometer gravitational-wave detectors"*, Physics Letters A **190**, 213, (1994).

[123] M. V. Veggel, *"ALIGO NP-type: - Report on Ear Bonding at LASTI"*, LIGO Document T070223, (2007).

[124] *"LIGO II Conceptual Project Book"*, LIGO Document M990288-A-M, (1999).

[125] P. Fritschel, *"Advanced LIGO Systems Design"*, LIGO Document T010075, (2001).

[126] P. Fritschel, *"Low-frequency Cutoff for Advanced LIGO"*, LIGO Document T020034, (2002).

[127] N. Robertson, *"Quadruple suspension design for Advanced LIGO"*, Classical and Quantum Gravity **19**, 4043, (2002).

[128] N. Robertson, private communication, (2008).

[129] J. Hough, private communication, (2008).

[130] K. Strain, private communication, (2008).

[131] G. Cagnoli, *"Effects of nonlinear thermoelastic damping in highly stressed fibres"*, Physical Review B **65**, 174111, (2002).

[132] A. Heptonstall, *"Characterisation of Mechanical Loss in Fused Silica Ribbons for use in Gravitational Wave Detector Suspensions"*, Phd Thesis, (2004).

[133] G. Cagnoli, *"Silica suspension and coating developments for Advanced LIGO"*, Journal of Physics: Conference Series **32**, 386, (2006).

[134] R. K. Brow, et al., *"Structure and the Intrinsic Strength of Glass"*, Proceedings of 7th International Otto Schott Colloquium 2002, Glastech Ber. Glass Sci. Technology **75**, 133, (2002).

[135] B. Proctor and I. Whitney, *"The strength of fused silica"*, Proceedings of the Royal Society of London. Series A, Mathematical and Physical Sciences **297**, 534, (1967).

[136] M. Barton, *"Ribbon/Fibre Length Budget"*, LIGO Document T070138, (2007).

[137] J. Smith, *"Feedforward correction of mirror misalignment fluctuations for the GEO600 gravitational wave detector"*, Classical and Quantum Gravity **22**, 3093, (2005).

[138] G. Cagnoli, *"Damping dilution factor for a pendulum in an interferometric gravitational wave detector"*, Physics Letters A **272**, 39, (2000).

[139] C. Cantley, *"Flexure point calculator"*, LIGO Document D040183, (2004).

[140] http://www.unibrain.com/Products/VisionImg/Fire¨i¨BC.htm.

[141] D. Crooks, Private communication., (2005).

[142] http://www.lumileds.com/products/line.cfm?lineId=1.

[143] N. Robertson, *"Notes on Design of ETM Reaction Chain and ITM Reaction Chain in Advanced LIGO"*, LIGO Document T060283, (2006).

[144] R. Kumar, *"Finite element analysis of suspension elements for gravitational wave detectors"*, MSc thesis (in preparation), (2008).

[145] http://www.solidworks.com/.

[146] A. Heptonstall, Private communication, (2007).

[147] P. Willems, "*Increased thermal noise in nonuniform fiber suspensions*", Physics Letters A, 16, (1999).

[148] A. Heptonstall, private communication, (2008).

[149] http://www.maplesoft.com.

[150] A. Gretarsson, "*Pendulum mode thermal noise in advanced interferometers: a comparison of fused silica fibers and ribbons in the presence of surface loss*", Physics Letters A **270**, 108, (2000).

[151] A. Heptonstall, "*Characterisation of mechanical loss in synthetic fused silica ribbons*", Physics Letters A **354**, 353, (2006).

[152] BENCH - Matlab program to calculate the strain sensitivity of LIGO interferometers, http://www.ligo.mit.edu/bench/bench.html.

[153] M. Barton, "*Proposal for baseline change from ribbons to fibres in AdvLIGO test mass suspension monolithic stage*", LIGO Document T080091, (2008).

[154] G. Harry, "*Thermal noise from optical coatings in gravitational wave detectors*", Applied Optics **45**, 1569, (2006).

[155] K. Numata, "*Intrinsic losses in various kinds of fused silica*", Classical and Quantum Gravity **19**, 1697, (2002).

[156] P. Willems and D. Busby, "*Report to the April 25, 2003 Core Optics Downselect Committee Meeting*", LIGO Document T030087, (2003).

[157] K. Numata, "*Systematic measurement of the intrinsic losses in various kinds of bulk fused silica*", Physics Letters A **327**, 263, (2004).

[158] V. B. Braginsky, "*Thermodynamical fluctuations in optical mirror coatings*", Physics Letters A **312**, 244, (2003).

[159] D. R. M. Crooks, "*Excess mechanical loss associated with dielectric mirror coatings on test interferometric gravitational wave detectors*", Classical and Quantum Gravity **19**, 883, (2002).

[160] S. D. Penn, "*Mechanical loss in tantala/silica dielecric mirror coatings*", Classical and Quantum Gravity **20**, 2917, (2003).

[161] D. Crooks, "*Experimental measurements of coating mechanical loss factors*", Classical and Quantum Gravity **21**, S1059, (2004).

[162] P. Murray, "*Measurement of the Mechanical Loss of Test Mass Materials for Advanced Gravitational Wave Detectors*", Phd Thesis, (2008).

[163] http://www.csiro.au/science/AstronomyTechnologiesOverview.html#6.

[164] "*CSIRO Progress Report June 2006*", (2006).

[165] "*CSIRO Progress report 8-Dec 2006*", LIGO Document C060162, (2006).

[166] http://lma.in2p3.fr/Lmagb.htm.

[167] I. Martin, Private communication, (2008).

[168] V. B. Braginsky, "*Systems with Small Dissipation*", The University of Chicago Press, (1985).

[169] M. M. Fejer, "*Thermoelastic dissipation in inhomogeneous media: loss measurements and displacement noise in coated test masses for interferometric gravitational wave detectors*", Physical Review D **70**, 082003, (2004).

[170] K. Srinivasan, "*Coating Strain Induced Distortion in LIGO Optics*", LIGO Document T970176, (1997).

[171] P. Murray, Private communication, (2008).

[172] G. Harry, "*Coating Project Update*", LIGO Document G060384, (2006).

[173] I. Martin, "*Measurements of a low-temperature mechanical dissipaton peak in a single layer of Ta_2O_5 doped with TiO_2*", Classical and Quantum Gravity **25**, 055005, (2008).

[174] W. Winkler, "*Heating by optical absorption and the performance of interferometric gravitational-wave detectors*", Physical Review A **44**, 7022, (1991).

[175] R. Savage, "*Measurement of thermally induced test mass surface curvature changes in a LIGO 4-km interferometer*", LIGO Document G050362, (2005).

[176] R. Lawrence, "*Active Wavefront Correction in Laser Interferometric Gravitaional Wave Detectors*", Phd Thesis, (2003).

[177] R. Lawrence, "*Adaptive thermal compensation of test masses in advanced LIGO*", Classical and Quantum Gravity **19**, 1803, (2002).

[178] C. Zhao, "*Compensation of Strong Thermal Lensing in High-Optical-Power Cavities*", Physical Review Letters **96**, 231101, (2006).

[179] K.-X. Sun, "*All-reflective Michelson, Sagnac and Fabry-Perot interferometers based on grating beam splitters*", Optics Letters **23**, 567, (1998).

[180] A. Bunkowski, "*Diffractive Optics for Gravitational Wave Detectors*", Journal of Physics: Conference Series **32**, 333, (2006).

[181] T. Clausnitzer, "*Ultra low-loss low-efficiency diffraction gratings*", Optics Express **13**, 4370, (2005).

[182] A. Bunkowski, "*High reflectivity grating waveguide coatings for 1064nm*", Classical and Quantum Gravity **23**, 7297, (2006).

[183] S. M. Sze, "*Semiconductor devices*", Wiley, New York, (2002).

[184] http://www.veeco.com/default.aspx.

[185] G. M. Harry, "*Thermal noise in interferometric gravitational wave detectors due to dielectric optical coatings*", Classical and Quantum Gravity **19**, 897, (2002).

[186] G. M. Harry, "*Coating Loss Measurements on Thin Fused Silica Substrates*", LIGO Document G020119, (2002).

[187] K. Numata, "*Measurement of the intrinsic mechanical loss of low-loss samples using a nodal support*", Physics Letters A **276**, 37, (2000).

[188] E. Chalkley, private communication, (2007).

[189] B. S. Lunin, "*Physical and chemical bases for development of hemispherical resonators for solid-state gyroscopes*", Moscow Aviation Institute Publishing, Moscow, (2005).

[190] R. Nawrodt, "*Mechanical Q-factor measurements on a test mass with a structured surface*", New Journal of Physics **9**, 225, (2007).

[191] http://www.ni.com/labview/.